DEGRADATION – SAFETY ANALYTICS IN ENERGY STORAGE

by

Daniel Juarez-Robles

A Dissertation

Submitted to the Faculty of Purdue University

In Partial Fulfillment of the Requirements for the degree of

Doctor of Philosophy

School of Mechanical Engineering

West Lafayette, Indiana

December 2019

THE PURDUE UNIVERSITY GRADUATE SCHOOL
STATEMENT OF COMMITTEE APPROVAL

Dr. Partha P. Mukherjee, Chair
School of Mechanical Engineering

Dr. Steven F. Son
School of Mechanical Engineering

Dr. Vilas G. Pol
Davidson School of Chemical Engineering

Dr. Jason K. Ostanek
School of Engineering Technology

Dr. Judith A. Jeevarajan
Underwriter's Laboratories

Approved by:

Dr. Jay P. Gore
Head of the Graduate Program

Dedicated to my first Teachers, my Parents
and my Muse, Shesy

"It is not knowledge, but the act of learning,
not possession but the act of getting there,
which grants the greatest enjoyment."
- Carl Friedrich Gauss

ACKNOWLEDGMENTS

I would like to express my special appreciation and thankfulness to my advisor Prof. Partha P. Mukherjee for encouraging my research and allowing me to grow professionally. I would also like to thank Dr. Judith Jeevarajan for her insightful comments and for sharing with me her tremendous experience with safety in the energy storage field. I would also like to thank my committee members, Dr. Vilas Pol, Dr. Jason Ostanek, and Dr. Steven Son for providing their expertise and insights on my thesis. It is impossible not to mention Dr. Abel Hernandez who was the one who sowed the seed that today bears its first fruit.

Financial support from Underwriters Laboratories (UL) and CONACyT (Mexican National Council of Science and Technology) is gratefully acknowledged.

The completion of this project could not have been accomplished without the support of the ETSL research group members. I will never cease to be amazed at your ability to break down equipment.

The adventure will not be complete without my friends, Mistry, Ankit, Neto, Nohemí, Bere, Jendry, Aaron, Homar, Clau, Celaya and Frank. With your help and support, I managed to reach the end of the doctorate.

I want to especially thank Shesy, the harvest moon that guided me in the darkest moments and illuminated my path to move forward on this journey.

Last but not least, I would like to thank my parents, Ma. de Lourdes Robles-Perez & Luis Juarez-Prieto; and my brothers, Alfredo & Roberto. This journey would not have been possible without their love and endless support.

TABLE OF CONTENTS

LIST OF TABLES

LIST OF FIGURES

ABSTRACT

Author: Juarez - Robles, Daniel. PhD
Institution: Purdue University
Degree Received: December 2019
Title: Degradation –Safety Analytics in Energy Storage
Committee Chair: Dr. Partha P. Mukherjee

The lucrative characteristics of high energy and power density from lithium-ion batteries have also become drawbacks when they are not handled appropriately. The reactive and flammable materials present within the cell raise safety concerns which need to be addressed. Aging of the cell components occurs in a natural way due to continuous cycling. Constant intercalation/deintercalation of Li-ions into the active materials induces stresses that in the long-term cycling mechanically modify the electrodes in an irreversible way. Also, electrode/electrolyte side reactions diminish the Li-ion inventory reducing the cell capacity and lifetime. Along with cell aging, intentional/unintentional abuse tests can occur at the hands of the final user. Improper handling and operation may lead the Li-ion cell to failure and possibly going into thermal runaway. This condition represents a threat to safety not only for cell integrity but also for user safety. Failure event can occur not only in brand new cells but also in aged cells. Current degradation studies focus either on the long-term aging degradation mechanisms or on fresh new cells' abuse test. And few of them focused on the combination of both of them.

In this work, the degradation of Li-ion cells is investigated at different levels. First, at the electrode level, the effect of electrode processing and the intercalation properties of an anode and cathode materials is investigated. Then, at the cell level, abuse conditions such as external short, overcharge and overdischarge are studied in fresh and aged cells with different levels of degradation. Last but not least, the cells are assembled in a module configuration to investigate how a minor difference from one cell to another can affect the long-term performance. The aim is accomplished via a controlled lab test approach in order to get insights about the electrochemical, thermal and morphological changes that take place when the cell degrades.

1. INTRODUCTION

1.1 Energy Storage

The production and consumption of energy dependent on the combustion of fossil fuels has proven to negatively impact the ecology. Electrochemical energy production is under intensive research in order to offer an environmentally benign alternative to the growing demand for energy and power sources[1]. Energy storage is a critical and increasing need in the quest to improve the efficiency and effectiveness of power systems. In the pursuit of higher fuel efficiency, energy storage plays a progressively significant role specially in the ground transportation sector [2-3]. Currently, there exists a wide variety of energy storage devices such as fuel cells [4], supercapacitors [5], redox flow batteries [6], fly-wheels [7], and Li-ion cells [5].

Li-ion batteries are commanding a greater market share attributed to their high energy density and size scale adaptability increasing their attractiveness for applications determined by weight or volume, long life cycle, and low self-discharge rate [8]. An electrochemical battery is a self-contained unit that store chemical energy and, when required, converts it directly into electrical energy to power a variety of applications. The electrochemical battery is composed of multiple cells. Each cell has a positive electrode (cathode), a negative electrode (anode), and an electronically insulating but ionically conductive layer separating the electrodes [9]. In Li-ion batteries, electrical energy is generated by the conversion of chemical energy via redox reactions at the anode and cathode. Oxidation is the loss of electrons or an increase in oxidation state, while reduction is the gain of electrons or decrease in oxidation state. During discharge, positive charge moves from the anode to the cathode through the electrolyte and separator. Negative charge flows in the opposite direction through the external circuit. The anode accumulates negative charge and the cathode accumulates positive charge, creating an electrode voltage difference.

1.2 Li-Ion Cells

Li-ion cells are a member of the secondary (rechargeable) battery type in which lithium ions have the ability to move from the anode to the cathode and/or vice versa depending on the discharge or charge process. In order to acquire a reversible chemical system, intercalation reaction occurs.

Intercalation reactions involve the reversible insertion and extraction of an atom into a crystal lattice with minimal alterations to the host crystal [10]. While electrolyte serves as the Li-ions transportation medium. To preserve electrical neutrality, during charge process, for every electron that moves through an external pathway from the cathode to anode, a Li-ion deintercalates from cathode and internally travels in the same direction as the electron until it eventually intercalates in the anode.

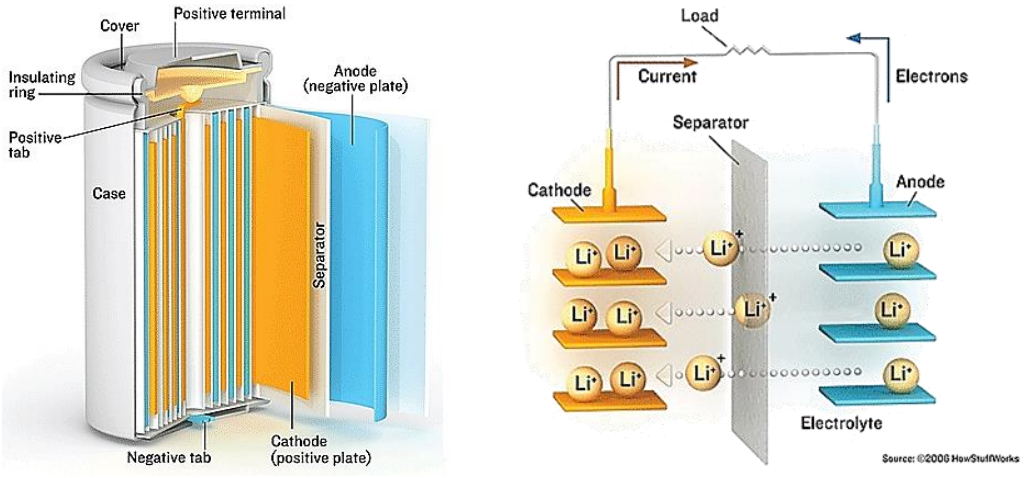

Fig. 1.1 Schematic of a Li-ion cell [11]. (a) Cylindrical cell, (b) intercalation/deintercalation processes.

The anode and cathode serve as a charge transfer medium and participate actively in the redox reaction as active masses. Anode is the negative electrode of a cell associated with oxidative electrochemical reactions that release electron into the external circuit. The cathode, contrarily, is the positive electrode of a cell associated with reductive electrochemical reactions [9]. These electrodes are commonly porous structures. A porous electrode increases the surface area for the electrochemical reaction to take place and reduces the diffusion distances within the active materials. The electrochemical reaction takes place at the phase boundary of the electrode/electrolyte interface throughout the volume of the porous electrode. A typical electrode is a composite of powders constituted of particles of the active material (see Table 1.1 and Table 1.2), a conductive additive, and a binder (see Table 1.3) to hold the mix together and bond the mix to a conductive current collector.

Table 1.1 Common active materials for anode.

Material	Voltage vs. Li/Li^+ [V]	Theoretical Specific Capacity [mAh/g]
Graphite (*C*) [12]	0.0 – 1.5	372
Lithium Titanium ($Li_4Ti_5O_{12}$ or *LTO*) [12]	1.0 – 2.5	175
Silicon (*Si*) [12-13]	0.0 – 1.2	3579
Germanium (*Ge*) [12-13]	0.2 – 2.1	1600
Tin (*Sn*)	0.2 – 1.0	994

Table 1.2 Common active materials for cathode.

Material	Voltage vs. Li/Li^+ [V]	Theoretical Specific Capacity [mAh/g]
Lithium Cobalt Oxide ($LiCoO_2$ or *LCO*) [12]	3.8	274
Lithium Manganese Oxide ($LiMn_2O_4$ or *LMO*) [12]	4.1	148
Lithium Iron Phosphate ($LiFePO_4$ or *LFP*) [12]	3.4	170
Lithium Titanium Disulfide ($LiTiS_2$) [12]	1.9	225
Lithium Nickel Manganese Cobalt ($LiNi_{0.33}Mn_{0.33}Co_{0.33}O_2$ or *NMC*) [12]	3.7	280
Lithium Nickel Cobalt Aluminum Oxide ($LiNi_{0.8}Co_{0.15}Al_{0.05}O_2$ or *NCA*) [12]	3.7	279

Table 1.3 Common electrode binder materials.

Material
Polyvinylidene Difluoride (*PVDF*) [14-15]
Styrene Butadiene Rubber (*SBR*) [14]
Sodium Carboxyl Methyl Cellulose (*CMC*) [14-15]
Acrylamide Co-Diallyldimethyl Ammonium (*AMAC*) [14]
Polyacrylic Acid (*PAA*) [14]
Polypyrrole (*PPy*) [14]

The separator is a physical barrier between the anode and cathode acting as an electronic insulator [16] without participating in the electrochemical reaction. In other words, the separator prevents electrons from flowing through the electrolyte, but allows anions and cations to migrate between the two electrodes. The separator is usually a gelled electrolyte, a microporous plastic film or other porous inert material filled with electrolyte [9] , see Table 1.4 for common materials. Even though they are inert, they must be thermally stable over a wide temperature range in order to maintain the physical and electronical barrier.

Table 1.4 Common separator materials.

Material
Polyethylene (*PE*) [17]
Polypropylene (*PP*) [17]
Polyethylene Terephthalate (*PET*) [17]
Polyvinylidene Fluoride (*PVdF*) [17]
Polytetrafluoroethylene (*PTFE*) [17]

An electrolyte is an ion-conductor solution, consisting of a solvent and a salt, that provides pure ionic conductivity between the positive and negative electrodes of a cell [9]. The electrolyte consists of multiple components: salts, solvents, and additives, refer to Table 1.5, Table 1.6, and Table 1.7 for common materials.

Table 1.5 Common electrolyte salt materials.

Material
Lithium Tetrafluoroborate $(LiBF_4)$ [18]
Lithium Hexafluorophosphate $(LiPF_6)$ [19-20]
Lithium Perchlorate $(LiClO_4)$ [18]
Lithium Bis-oxalatoborate $(LiB(Cr_2O_4)_2$ or $LiBOB)$ [18]
Lithium Bis(trifluoromethylsulfonyl)imide $(LiN(SO_2CF_3)_2$ or $LiTFSI)$ [18]

A salt is a substance that when placed into a solvent results in an electrolyte solution, as the components in the salt dissociate in a process called solvation. A solvent's primary objective, as

mentioned before, is to dissolve electrolyte salt and thus enable lithium-ion transport. Electrolyte additives are used to improve the performance and stability of lithium-ion battery systems.

Table 1.6 Common electrolyte solvent materials.

Material
Ethylene Carbonate (*EC*) [21]
Dimethyl Carbonate (*DMC*) [21]
Diethyl Carbonate (*DEC*) [21]
Ethyl Methyl Carbonate (*EMC*) [21]
Propylene Carbonate (*PC*) [21]

Apart from their primary roles, a crucial characteristic of an electrolyte is the ability to form an effective solid electrolyte interphase (SEI) on the anode of a Li-ion battery. If the solvent mixture itself is not able to form an effective SEI, electrolyte additives need to be incorporated in order to allow the operation of the battery [15]. There are countless ways to combine these elements and create different electrolyte formulations.

Table 1.7 Common electrolyte additive materials.

Material
Vinyl Ethylene Carbonate (*VEC*) [18]
Fluoroethylene Carbonate (*FEC*) [18]
Vinylene Carbonate (*VC*) [22]
Propylene Sulfite (*PS*) [18]
Trimethoxyboroxine (*TMOBX*) [18]

Once a set of materials for each of the components is selected they must be assembled in a sealed tight cell to avoid any side reaction of the electrolyte/electrodes with the oxygen and water from the environment. These cells are classified in two main categories

1. Primary cells [16] or non-rechargeable cells. In this kind of cells, the electrochemical reactions taking place within the cell are irreversible. Thus, when the reactive active material is depleted the cell cannot longer provide energy and it cannot be used again.

2. Secondary cells or rechargeable cells. The analysis presented in this work is focused on this kind of cells on which the electrochemical reactions are quasi-reversible. In order to reuse these cells, an external driving force (current) reverses the electrochemical processes. Consequently, the electrodes are restored to the initial state and energy can be reused.

1.3 Degradation and Safety

The growing interest in powering electric vehicles (EVs) and portable electronics have spurred not only the development of a wide variety of cells with increased energy densities [23] but also a pursuit to investigate the tolerance response to abuse and the implications on safety. Regardless of the advantages over other energy storage devices, Li-ion cells contain volatile and flammable materials which under abnormal conditions may be interpreted as a threat to safety [24].

Unfortunately, the increased energy storage capabilities of lithium-ion cells have been overshadowed by the frequent occurrence of accidents, revealing several safety concerns that require further investigation [25]. For instance, UPS Flight 6 was a Boeing 747 cargo plane that was believed to have crashed in 2010 due to autoignition of the contents of a cargo pellet containing a significant number of lithium type batteries [26]. Samsung was forced to recall nearly 1 million Galaxy Note 7 phones in September 2016 after numerous reports of the devices going into thermal runaway during charging or use [27]. It was later revealed that the issue stemmed from two independent cell design flaws by the two different manufacturers, causing them to short circuit. In February 2017, a Dell Inspiron laptop powered by a LIB violently combusted while charging and proceeded to burst into flames three more times after being unplugged [28]. These examples illuminate the fragility of the Li-ion chemistry and demonstrate the necessity of understanding the response of Li-ion cells to abnormal conditions [29-30].

One of the most frequent safety issue found among all the failure events is thermal runaway. For every anode/cathode/electrolyte combination, a stability window for voltage and temperature is defined [31]. If the cell is operated outside of the stability window, undesired side reactions can occur inducing an additional heat generation. Thermal runaway happens when the cell temperature increases beyond the safe thermal limits in an uncontrolled way leading to a catastrophic event and in some cases to cell ignition.

The reaction of the negative active material is usually the strongest one [32]. A comprehensive study of the thermal behavior of each of the cell components was presented by Spotnitz et al. [33]. The SEI passivating layer that forms on the graphite electrode [34], typically assumed as metastable, decomposes at high temperatures and under some abusive conditions between 90 to 120 ºC [33]. Without the SEI, the electrolyte solvent molecules can cross through the surface to intercalate into graphite and subsequently decompose between graphite planes, which can lead to exfoliation, a mechanism that describes the depletion of material layers after solvent intercalation [35]. The SEI decomposition has been proven to raise the cell temperature by 2 ºC and it strongly depends on the solvents present on the electrolyte. Even though the constituent solvents are known, percentage variations and additives presence can affect the final thermal response. Roth et al. presented a study of the role of electrolyte solvent decomposition on thermal abuse response the role of electrolyte solvent decomposition on thermal abuse response was investigated for two compositions: ethylene carbonate: ethyl methyl carbonate (EC:EMC) (3:7)\1.2M and ethylene carbonate: propylene carbonate: dimethyl carbonate (EC:PC:DMC)(1:1:3)\1.2M with a $LiPF_6$ salt [36] in order to study the electrolyte additives effect on low-temperature stability, flammability and overcharge protection. The ARC analysis revealed that the EC:PC:DMC solvent showed the lowest reaction rate. This study was further extended to explore the solvent effects for different cell chemistries of NCO, NCAO and LCO. Once again the cells with electrolyte containing PC showed reduced heating rates for all three cathode chemistries.

Feng et al. incorporated the use of methylbenzenes as possible electrolyte additives for improving the cell overcharge tolerance [37-39]. From a series of methyl-substituted benzenes in 1M $LiPF_6$/EC-DMC electrolyte, xylene was selected and tested as an electrolyte additive for overcharge protection of Li-ion cells. From the overcharge curves, cyclic voltammetry and SEM observations of the cells in the presence of xylene, it was found that the additive can polymerize during the overcharged test to form a dense layer of isolating polymer film at the cathode surface, which blocks off further oxidation of the electroactive material and electrolyte and, therefore, improves the overcharge tolerance of the Li-ion cell. In addition, the xylene additive showed to only slightly influence the cycling behaviour of the cells.

The reaction of the positive active material is usually the weakest one. The heat released from the anodic reactions triggers the decomposition of the positive active material. The decomposition of the cathode and subsequent oxidation reaction with the electrolyte/solvent is considered to be the most exothermically abusive reaction which can lead to a temperature rise of greater than 100 °C. The solvent oxidation and the cathode decomposition are considered as a coupled reaction because the oxygen release from the cathode oxidizes the solvent. Abuse tests done on prismatic Li-ion cells in the work by Leising et al. [40] identifies and confirms the cathode to be the source of major heat production in the cell. A similar conclusion was derived from the work by Zhang et al. based upon DSC analysis. The study indicated significant exothermic reaction between the electrolyte and common cathode materials such as LNO, LCO, and LMO. The reactions had contributions from the solvents and the salt in the electrolyte. Depending on the stoichiometry, the material and the degree of delithiation, the onset temperatures were reported to be between 200-230 °C [37-39].

1.4 Abuse Tests

Controlled safety test is a valuable method used to get insights about the cell behavior under abnormal and abuse conditions. Safety tests not only emulate the cell performance under abuse scenarios but they can also reveal the potential hazards that could take place. In particular, thermal runaway can take place during each of the tests listed on the schematic from Fig. 1.2. They are usually classified based on their nature as: electrochemical, thermal and mechanical safety tests.

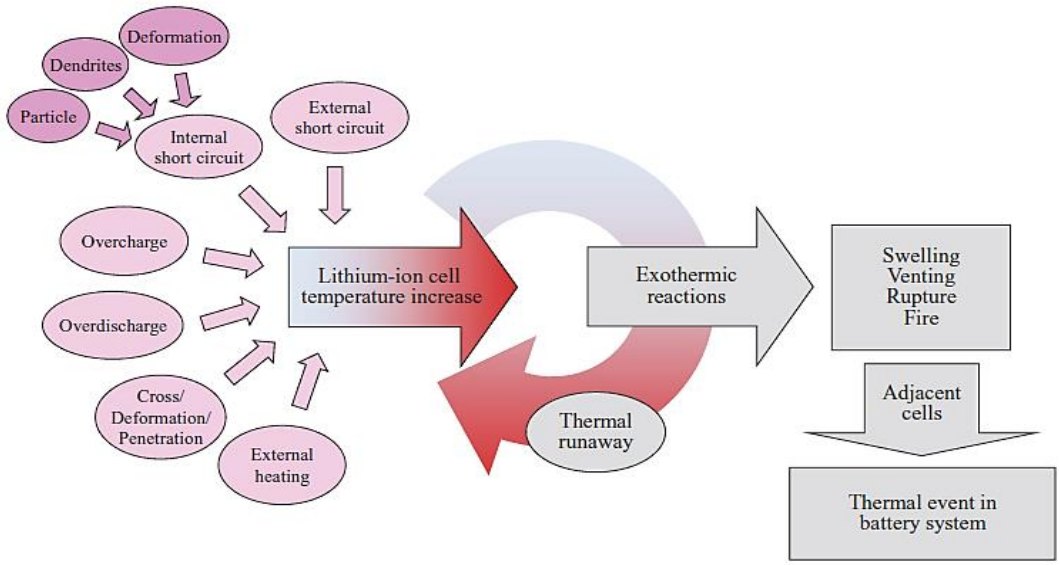

Fig. 1.2 Schematic of the various degradation mechanisms [33, 36, 41] and the typical cell response [24].

1.5 Thermal Abuse Test

Thermal abuse scenario occurs when the Li-ion cells are heated to an excessive temperature (100~190 ^{o}C) or directly exposed to fire. The test is typically applied on fresh new cells in order to characterize the thermal tolerance of the materials. The test is aimed to drive the cell out of the safe thermal limits and find out the onset of failure based on the cell capacity and configuration, the electrode materials and the SOC of the cell.

1.5.1 Heating Test

Tobishima et al. varied the heating temperature in 5 °C increments followed by a constant temperature step until the cell temperature started to decrease [42]. The highest temperature at which the cell did not smoke was defined as the thermal stability limit of the cell. The test was conducted in a 1.27 Ah commercial cylindrical cells with two set temperatures, 150 °C and 155 °C. They found that 150 °C was the thermal stability limit for this type of cells. Further analysis of the evolution of the thermal stability point is necessary when aging is involved [43]. Larsson et al. conducted a heating test in 18650 cells [24]. They found a thermal runaway temperature onset of 220 °C. After that the cell reached a maximum skin temperature of 743 °C. A differential analysis of the temperature profile revealed that the temperature increased at a rate of 5000 K/min. Golubkov et al. conducted a thermal runaway in three cathode materials, LFP, LCO, NMC. They found that LFP has the highest thermal runaway onset temperature, 195 ^{o}C, among the three materials. [44]

1.5.2 Fire Test

Electrolytes for Li-ion cells contain flammable organic solvents. Some of them are volatile even a relatively low temperatures of 100 °C or less. $LiPF_6$ salt also has a limited window of thermal stability [45-46]. It can react with even the slightest traces of moisture to form toxic gases such as lithium fluoride (LiF) and hydrogen fluoride (HF). The reactivity and stability of these gases has been studied under normal temperatures, but not under high temperatures simulating the event of a fire or explosion as Larsson et al. did [47]. Six cells with LFP cathodes were exposed to a controlled propane fire in order to evaluate the rate of heat release (HRR), emission of toxic gases as well as cell temperature and voltage under this type of abuse. The results showed that cells at high SOC

gave high HRR peaks. The thermal and electrochemical response confirmed that the cells with higher SOC exhibited more reactive response.

1.6 Mechanical Abuse Test

Mechanical abuse tests are conducted in order to determine how the mechanical deformation of the cell impacts its integrity. Cells can be mechanically deformed due to an improper handling or by crashing [26], directly or indirectly, the casing where they are contained. The most common mechanical abuse tests include nail penetration and deformation due to impact. Cell failure, in most of the cases, occurs due to an induced internal short circuit driven by the modifying external force.

1.6.1 Deformation Test

In a typical lab controlled crush test, a slab is used to deform the battery initiating an internal short circuit in the cell[48]. Sahraei et al. tested 18650 lithium-ion cells indenting them with an hemispherical punch, lateral indentation by a cylindrical rod, compression between two flat plates and three point bending [49]. The results from the test included force, displacement, voltage and temperature versus time. Lam et al. performed mechanical abuse experiments on commercially obtained 18650 Li-ion batteries and pouch cells [50]. Blunt rod indentation was performed in both the axial (parallel to the cylindrical axis) and transverse (normal to the cylindrical axis) directions of cylindrical cells as well as horizontally (through the flat face of the cell) and vertically (through the side of the cell) through prismatic pouch cells. Through CT imaging, it was shown that extensive damage to the cell components was necessary in order to cause a failure to the cell.

1.6.2 Nail Penetration

Nail penetration testing is a safety test aimed to emulate internal short circuit. In the test, the cell is penetrated with a nail while and then is monitored to verify if the cell goes into thermal runaway. Nail penetration tests are no longer described in the UL 1642 standard [51].

1.7 Electrochemical Abuse Test

Electrochemical abuse test consists of driving one of the main cell components out of the safe electrochemical operating condition (voltage limits, limiting current, SOC). The condition can be

achieved accidentally by mean of a mechanical and thermal abuse or indirectly as a consequence of another reaction happening in the cell.

1.7.1 External Short Circuit

External short induced circuit test happens when the terminals get in direct contact with a low resistance (<5 mΩ) is connected across the terminals of the battery. In this test, current flows through the battery generating heat. The cell gets internally heated due to Joule heating effect associated to the ionic resistance, and the external circuit can dissipate heat also [33]. New and old cells with different architectures were tested in an external short circuit test done by Larsson et al. [24]. It was found that the results did not vary among the two different designs of the cell. Events such as swelling and burning of the cell tabs were noticed in the test, but the cell was not found to reach thermal runaway. The peak current reached at the beginning of the discharge was almost 900 A. Chapter 5 gives a more detail description of the physics behind the external short test.

1.7.2 Overdischarge

Overdischarge is a phenomenon that occurs when a cell is discharged beyond the lower electrochemical voltage limit. The lower limit in this case is determined by chemistries on the cell. Consider three lithium-ion cells at arbitrary states of charge, two fully charged and one 50% discharged. If these are connected in series and then connected to an electrical load, the partially discharged cell will fully discharge before the other two, and will be forced into polarity reversal by the other cells if the load is left on. Although this does not necessarily cause a safety hazard, it forces electrodes outside their normal potential range and adversely affects the cycle life [52]. Several works have been done where redox shuttles have been reviewed, tested and employed in order to improve the overdischarge as well as overcharge performance of the cells [37-39]. Chapter 7 gives a more detail description of the physics behind the overdischarge phenomenon.

1.7.3 Overcharge

In this safety test, the cell is allowed to charge beyond the fully charge condition up to a predetermined maximum voltage limit or until the failure event occurs. Prevention of overcharge is critical to achieving long lifetimes and averting catastrophic failure events in lithium-ion batteries [53]. Chapter 6 gives a more detail description of the physics behind this phenomenon.

1.8 Objective

The overall objective of the present work is to study the degradation mechanisms behind failure or bad electrochemical performance in lithium-based energy storage systems. The aim is accomplished via a systematic and comprehensive approach. The goal is to correlate the electrochemical and thermal response of the cells with the physical and chemical changes occurring within the cell.

Degradation-Safety-Analytics (DSA) is the methodology proposed in this work and consisted first on designing and testing the safety abuse test of interest. The electrochemical properties are collected simultaneously with thermal measurements. Then, a differential analysis of both property sets complements the work. Once the electrochemical test is complete, the cell is subjected to a careful Destructive Physical Analysis (DPA). Finally, evidence of morphological and chemical changes is contrasted with the external measurable properties to unveil the cause of failure of the cell. DSA methodology can be applied to any cell architecture or electrochemical coupling.

1.8.1 Electrode Level Degradation

Degradation in LIBs is usually associated with external factors or a malfunction of the cell. However, the intrinsic mechanical properties of the active materials can directly affect cell performance. In order to increase the energy density, two different approaches to increase the capacity of the cell are investigated. First, a high capacity anode material, copper-tin, is investigated as well as the degradation mechanisms hindering its commercial use, see Chapter 2. It is hypothesized that mechanical degradation is the main cause of bad electrochemical performance. Second, thick NMC electrodes are made using a novel aqueous electrode processing with SBR and CMC as a binder. It is hypothesized that a thick electrode will provide a larger capacity while the presence of cracks will hinder its full use, see Chapter 3.

1.8.2 Cell Level Degradation

Degradation of two LIBs architectures, cylindrical (Chapter 4, 5, 6, 7) and pouch cell (Chapter 8, 9), under different safety abuse tests is investigated. The objective is to study the interaction between aged and fresh cells and the electrochemical abuse test (overcharge, overdischarge and external short) and their implication on the safety aspects. The aim is accomplished by applying

the DSA methodology on single cells and modules. The analysis will provide insights about how the different degradation mechanisms affect the microstructural, electrochemical and thermal response of the cell and if the combination of those effects makes the cell more or less prone to fail and go into thermal runaway. It is hypothesized that degradation due to aging plays a benign factor if the cells go into a failure event.

1.8.3 Module Level Degradation

An analogous analysis is conducted on 3P9S cylindrical fresh and aged modules without a battery management system. The effect of the voltage window on the cycling life is investigated. The degradation-safety interaction is investigated by conducting an overcharge safety test at the end of the cycle life. It is hypothesized that the cycle life from the single cells will be extended to the modules. However, it is expected that the cell-to-cell variation influences even more the electrochemical and thermal response. The results are presented in Chapter 10.

2. ELECTRODE LEVEL DEGRADATION: HIGH CAPACITY ANODE

Relevant Publications and/or Working Papers

1. D. Juarez-Robles, H. J. Gonzalez-Malabet, M. L'Antigua, X. Xiao, G. J. Nelson, P.P. Mukherjee, 2019, *Elucidating Lithium Alloying-Induced Degradation Evolution in High-Capacity Electrodes*, ACS Appl. Mater. Interfaces, 2019, 11, 563-577 (doi: 10.1021/acsami.8b14242)

Alloy electrode materials offer high capacity in lithium ion batteries; however, they exhibit rapid degradation resulting in particle disintegration and electrochemical performance decay. In this study, the evolution of lithium alloying induced degradation due to electrochemo-mechanical interactions is examined based on a multi-pronged electrochemical and microstructural analysis. Copper-tin (Cu_6Sn_5) is chosen as an exemplary alloy electrode material. Electrodes with compositional variations were fabricated and electrochemical performance was examined under varying conditions, such as voltage window, C-rate, and short- and long-term cycling. Morphology and composition analyses of pristine and cycled electrodes were conducted using micrography and spectroscopy techniques. Alloying induced electrode microstructural evolution was probed using X-ray microtomography. The rapid capacity fading was found to be caused by mechanical degradation of the electrode. Driving the electrode to a lower potential ($E \approx 0.2$ V vs. Li/Li^+) induced Li-Sn alloy formation and provided the characteristic large capacity; however, this lead to a large volume expansion and active particle cracking and disintegration. Copper expulsion was found to be a consequence of the alloy formation; however, it was not the primary contributor to the dramatic electrochemical performance decay.

2.1 Introduction

Energy is a fundamental asset to the economic and social progress of every country. The disjunctive obstacle of the demand-generation binomial, on which the demand is hard to predict and production exhibits an intermittent behavior [54], can be addressed in a simple, effective and rational way by invoking a third agent, energy storage. One of the most popular ways to store energy is in batteries. In this era where more and more devices work without cables or "wireless", the use of batteries has become habitual. In addition, the introduction of new electric and hybrid

vehicles has facilitated research in batteries with high energy and power density as well as high capacity retention, which has drawn the attention especially to lithium ion batteries [55-56].

In a typical single electrochemical lithium-ion cell, there are three main components: the anode, the cathode, and the electrolyte with lithium-ions (Li^+) as charge carriers. Intercalation and deintercalation are the processes of moving lithium in and out, respectively, of the electrodes. During discharge, Li^+ deintercalates from the anode and intercalates into the cathode, while during charge this process is reversed. Simultaneously, electrons follow an analogous path but in the external circuit. The most common active material of the positive electrode, the cathode, is usually a transition metallic oxide ($LiCoO_2$, $LiNi_{1/3}Mn_{1/3}Co_{1/3}O_2$, $LiMn_2O_4$, $LiFePO_4$) [23] cast on an aluminum sheet current collector [57]. The most common active material in the negative electrode, the anode, is a graphitic carbon cast on a copper sheet current collector. The combination of both chemistries and their active material load determines the energy density of the cell. In commercial lithium-ion cells, the energy density is limited by the cathode capacity but its performance is dominated by the intrinsic electrochemical stability of anode.

2.1.1 Anode Materials

Ever since the early 1990s, lithium-ion cells have used two kinds of materials: carbon-based intercalation anodes [58-59] and metal-based alloying anodes [60]. Carbon-based anodes do not exhibit a large volume expansion as compared to the metallic ones; however, their theoretical capacity is much lower, 372 mAh/g [58]. The pursuit for an alternative anode material has led to a persistent research on materials with a larger energy density.

2.1.1.1 Silicon

Silicon (Si) seemed to address the large theoretical capacity of 4200 mAh/g requirement for the anode material [61]. However, it has a noteworthy drawback; it significantly shrinks and expands during the charge and discharge process. The severe volume expansion (~300%) [62] leads to cracking and pulverization in the short-term cycling, and a steep capacity fading in the long-term.

2.1.1.2 Tin

Tin (Sn) forms an alloy with lithium which can be reversible during the charge and discharge process. This property coupled with its high theoretical capacity of ~990 mAh/g [12-13], obtained at

the maximum uptake of lithium ($Li_{17}Sn_4$), have resulted in its consideration as a prospective anode material. However, the high capacity of the pure tin cannot be achieved in long-term cycling due to losses associated to slow diffusion and reaction kinetics. These losses along with the breakdown of the lithiated-tin phase, caused by a large volume expansion on the order of ~250% [63], represent the main drawbacks that impede its widespread use as an anode material [64-65].

2.1.1.3 Copper-Tin

The material breakdown exhibited by tin due to successive and drastic volume changes can be buffered by introducing a binary $Sn_{1-x}M_x$ amorphous alloy, where M is a 3d transition metal and x its concentration [66]. Dahn et al. studied the electrochemical properties of these Sn-transition metal alloys [67]. They showed that the achieved specific capacity for Sn-Cu alloys was increased when the Cu content ranged between $x = 0.5 \sim 0.6$ with still significant capacity retention. Subsequently, a noteworthy number of studies with a common composition, Cu_6Sn_5, corresponding to a Cu content of $x = 0.5\overline{454}$, had been developed aiming to implement it as an anode material.

The overall reactions for Cu_6Sn_5 electrodes consist of the initial protective irreversible copper matrix formation followed by a reversible electrochemical operation. The matrix copper formation is an irreversible process aimed to buffer the drastic volume changes and provide structural support to the electrode. The electrochemical operation consists of the lithiation/delithiation processes. The Cu_6Sn_5 theoretical capacity strongly depends on the Li-Sn composition. Han et al. presented an electrochemical performance comparison of different copper-tin alloys paired either with lithium metal, carbon or silicon [68]. They found that the experimental reversible capacity could range from 200 mAh/g [69] to 605 mAh/g [68].

Despite the large amount of work around the Cu_6Sn_5 composite as an anode electrode, there is not a full consensus on the intermediate reactions that occur during the lithiation and delithiation processes. Formation of different possible stoichiometries for Li-Cu-Sn and Li-Sn alloys makes it difficult to establish the intermediate reactions [70]. In general terms, the electrochemical reactions [68] for the Cu_6Sn_5 composite depends upon the state of charge as described in Eq. 2.1 and Eq. 2.2.

$$xLi^{+} + xe^{-} + \alpha_x Cu_6Sn_5 \underset{Delithiation}{\overset{Lithiation}{\rightleftharpoons}} \beta_x Li_2CuSn + Cu \qquad 0 \le x \le 10 \qquad \text{Eq. 2.1}$$

$$(x-10)Li^{+} + (x-10)e^{-} + \beta_x Li_2CuSn \underset{Delithiation}{\overset{Lithiation}{\rightleftharpoons}} \sum_{0<y\le 5} \gamma_{x,y} Li_xSn_y + 5Cu \qquad 10 < x \le 22 \qquad \text{Eq. 2.2}$$

The α_x, β_x and $\gamma_{x,y}$ coefficients depend upon the lithium content and the alloys (*e.g.*, Li_7Sn_2, $Li_{17}Sn_4$, $Li_{22}Sn_5$, ...) present in the reaction.

In order to improve the Cu_6Sn_5 composite electrodes, performance changes based on: (*i*) morphological changes, (*ii*) mixtures composition, and (*iii*) electrode processing have been proposed. Shin and Liu fabricated a highly porous three-dimensional foam structure of Cu_6Sn_5 alloy using an electrochemical deposition process [71]. They studied the long-term cycling performance of this material at high C-rates. Their experimental results showed a reversible specific capacity of 400 mAh/g when cycling at 1C-rate in the E = [0.0, 1.5] voltage range after 30 cycles. The irreversible capacity exhibited was attributed to mechanical degradation due to drastic volume change, formation of lithium oxides, solid electrolyte interphase (SEI) formation, and inability of copper to reincorporate in the reaction.

Trahey et al. presented a similar approach with a three-dimensional microporous prepared by electrodeposition of Cu and Sn onto sintered foam substrates [72]. They obtained a reversible capacity of 670 mAh/g when the cells were cycled between E = [0.0, 2.0] V. The large capacity developed was also accompanied with a sudden onset of capacity fade after 30 cycles possible due to the loss of electronic contact between the Cu foam substrate and the Cu-Sn particles.

Algul et al. [73] fabricated Cu_6Sn_5 electrodes with a porous nickel foam substrate fabricated by a pulse electrodeposition process. In this work, the authors correlated the electrode morphology with the electrochemical performance. They found that the best electrochemical performance was obtained on the alloy electrodes with a dendritic morphology. The mesoporous structure of the electrode buffered the volume expansion occurred during cycling.

2.1.1.4 Electrode Processing

Despite the huge number of publications related to the development of new Cu_6Sn_5 anode materials, there are few studies related with their synthesis-processing-performance interaction. Previous works on cathode materials had shown how the electrode processing [74], composition (active material + binder-solvent + conductive additive) [75], and drying conditions [76] lead to different microstructures, and hence different electrochemical properties and performance. The interplay of all the electrode processing factors could explain the wide range of reversible capacities found in the technical literature, for the Cu_6Sn_5 active material.

In this work, Cu_6Sn_5 active material is prepared via a sintering of pellets followed by a size reduction to a powder via a ball milling process. Non-aqueous electrode processing is carried out with Cu_6Sn_5 powder as the anode active material. Key parameters to the final electrode microstructure such as the drying temperature and the powders composition are studied. The electrochemical performance and its correlation with the operating voltage window are also studied. Copper expulsion phenomenon is analyzed as one of the main factors for degradation at the short and long-term cycling.

2.2 Experimental Details

2.2.1 Alloy Synthesis

The copper-tin active material was synthesized following the methods of Kepler et al. [69]. Briefly, this process involved mixing copper and tin powders in stoichiometric proportions, pressing pellets of the mixed powder, and sintering the pellets under an argon atmosphere. The sintered pellets were ground under an argon atmosphere and sieved to yield an alloy powder of 400-500 mesh size. These steps are illustrated in Fig. 2.1. X-ray Diffraction (XRD) was performed on the powders and it was found that a significant majority of the powder sample was Cu_6Sn_5 with smaller amounts of Cu_3Sn, Sn, and Cu. No significant quantities of Sn or Cu oxides were observed. Further details of the alloy synthesis XRD, and electrode fabrication are given in Ausderau et al. [77]. For electrochemical testing, two forms of electrodes were produced: pellets electrodes (13 mm diameter and 1 mm thick) and composite electrodes. Here, testing of composite electrodes is

addressed. For composite electrodes, alloy powders were ball milled for size reduction prior to electrode fabrication.

2.2.2 Electrode Processing

Copper-tin electrodes were prepared with Cu_6Sn_5 composite powder as active material (AM). Super C65 (carbon black, Timcal) was used as conductive additive (CA). Binder solution (B) was prepared by dissolving polyvinylidene fluoride (PVDF, Kynar) powder on N-methyl-2-pyrrolidone (NMP, Sigma Aldrich) in a 1:10 %*wt* ratio. First, the dry powders, super C65, and Cu_6Sn_5 were mixed in mortar and pestle until a uniform mixture was obtained. The mixture was transferred to a stirring tube device (IKA) with the binder solution and 16 glass balls. The AM, CA, and binder solution were then mixed for 30 minutes. The slurry was poured and then cast onto the dull side of a copper sheet substrate, (9 μm thickness, MTI) previously cleaned with acetone and isopropanol. The film applicator (Elcometer) with a doctor blade set to a 200 μm thickness was used to cast the slurry on the substrate. The electrode was dried in an oven (MTI) at 70 ^{o}C for 12 hours. The electrode composition denoted, from hereafter, as AM:CA:B = $\%\omega_{AM}$: $\%\omega_{CA}$: $\%\omega_{B}$, where $\%\omega_{AM} + \%\omega_{CA} + \%\omega_{B} = 100\%$ and $\%\omega_x = \omega_x/\omega_{Total}$ and $\omega_{AM} + \omega_{CA} + \omega_B = \omega_{Total}$. Electrodes with two different compositions were studied, $(AM:CA:B)_1$ = 80:10:10 and $(AM:CA:B)_2$ = 70:20:10.

2.2.3 Cell Performance

The electrochemical performance of the synthesized Cu_6Sn_5 anode material was characterized using the 2032 coin cell architecture half-cells [78]. They included a lithium metal (Sigma Aldrich, 99.9% purity) electrode disk (14.29 mm diameter, 0.75 mm thickness) and a Cu_6Sn_5 electrode disk (12.7 mm diameter) punched out from the in-house made electrode. The average electrode mass, after drying, is 16.0 mg. The amount of dried slurry, obtained by subtracting the substrate mass, 11.5 mg, is 4.5 mg. This corresponds to an active material mass loading of 3.60 mg (26.5 μm dry slurry thickness) and 3.15 mg (25.8 μm dry slurry thickness), for the $(AM:CA:B)_1$ = 80:10:10 and $(AM:CA:B)_2$ = 70:20:10, respectively. The Li and Cu_6Sn_5 electrodes were separated by a membrane (Celgard 2500, polypropylene (PP)) separator disk (15.875 mm diameter, 25 μm thickness). The cell was flooded with electrolyte (BASF) composed of 1.0M $LiPF_6$ in ethylene carbonate (EC)/diethyl carbonate (DEC) (1:1 by volume) solvent. The cells were crimped at 4.82

MPa pressure in a hydraulic crimping machine (Model MSK-110, MTI). Assembly of the cells was conducted in an Argon-filled Glovebox (MBraun), where water and oxygen levels are kept under 0.5 ppm. The cycling tests were conducted on an Arbin battery testing system (BT2000).

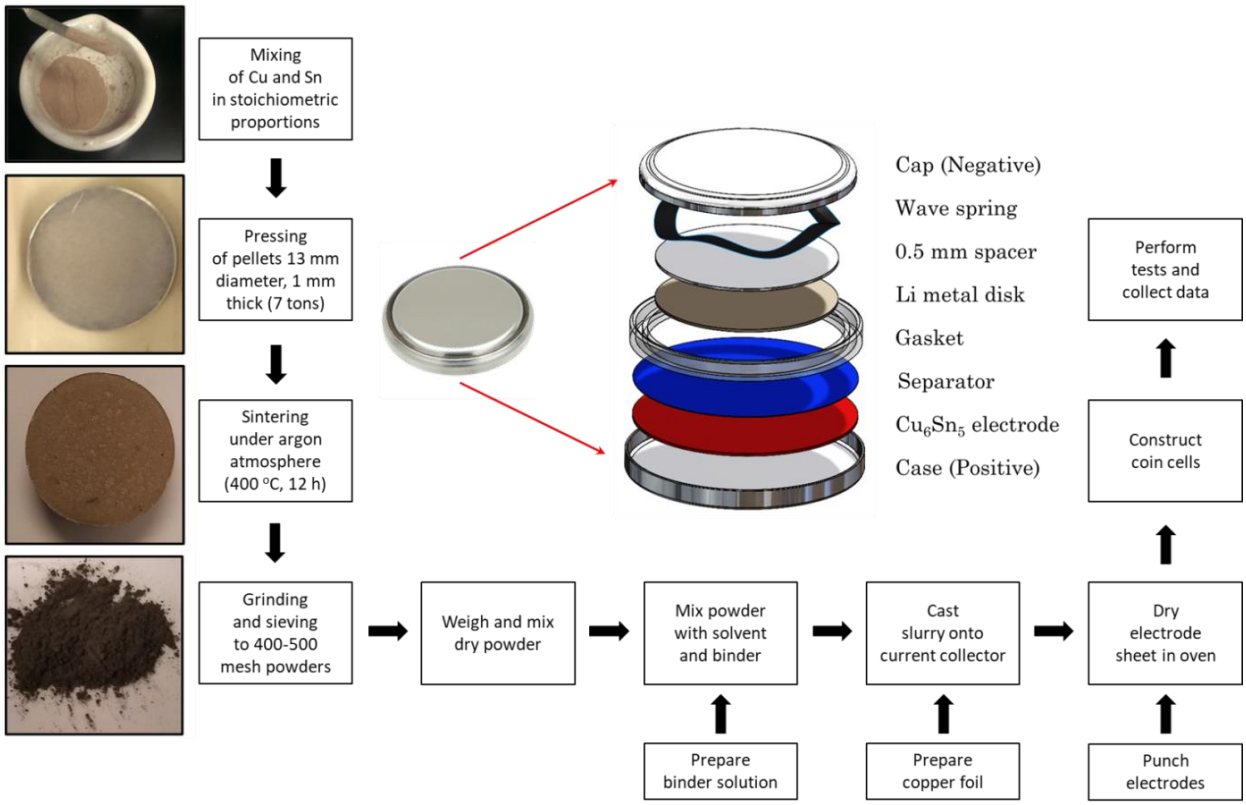

Fig. 2.1 Schematic of synthesis process used to prepared the Cu_6Sn_5 powder based electrode and coin cell assembly. The overall electrochemical tests were done using the 2032 coin cell architecture (half-cells).

Cyclic voltammetry (CV) was carried out on a multichannel potentiostat (Bio-Logic, VMP3). All the electrochemical tests are conducted at ambient temperature, $T_{amb} \approx 25\ ^{o}C$. Cyclic voltammograms for the first three cycles are obtained with a potential sweep rate of 1 mV/s between 0.0 and 2.0 V vs. Li/Li^{+}. The CV test is carried out in order to identify the nature of the reactions and the phase change transition.

2.2.4 Maximum Theoretical Capacity

Fresh cells were rested for 8 hours, after being crimped and removed from the glovebox. The resting time allows the electrodes and the electrolyte to reach a chemical equilibrium. The cells

were then cycled three times in the operating window, E = [0.0, 2.5] V vs. Li/Li^+ using a constant current (CC) protocol at a low current density, 86.8 $\mu A/cm^2$ (C-rate ≈ 1/20) with a 30-minute rest between the charge and discharge process. This test provided the maximum experimental theoretical capacity of each of the electrodes.

2.2.5 Short-Term Cycling

The effect of drying temperature, operating voltage window, and composition on the cell performance was also studied. The first test was run on cells with electrodes dried at 30, 50 and 70 ^oC. Cells were cycled 5 times between 0.0 and 1.5 V vs. Li/Li^+ at a C/2-rate. These results provided the composition and drying temperature under which the largest reversible capacity is obtained. Electrodes prepared under these conditions were the baseline to study the effect of composition, drying temperature, and the operating voltage window on the performance of the cell. The electrochemical window effect was studied by cycling cells between [0.0, 1.5] and [0.2, 1.5] V vs. Li/Li^+.

2.2.6 Coulombic Efficiency Test

Rate capability of the composite electrode was done for two electrodes, dried at 70 ^oC, with each of the compositions. Half-cells were cycled 10 times at each of the four different selected C-rates between [0.0, 2.5] V vs. Li/Li^+ with no resting in between the charge and discharge processes.

2.2.7 Long-Term Cycling Test

Long-term cycling performance and capacity fading were also investigated. Half-cells with electrodes dried at 70 ^oC for each of the two compositions were cycled at three different C-rates (C/2, 1C, 2C) by applying a constant current charge and discharge protocol. Cells were cycled 100 times in the range of [0.0, 2.5] V vs. Li/Li^+ and they were not allowed to rest in between the charge and discharge processes.

2.2.8 X-Ray Microtomography

To better understand the coupling of microstructural changes and cycling for the Cu_6Sn_5 anode active material an x-ray microtomography (μCT) study was performed with Cu_6Sn_5 composite electrodes as the working electrode in half-cells with lithium metal as the counter electrode. Samples were extracted from pristine and cycled composite electrodes after 5 cycles after been

discharged at the corresponding cut-off voltage. In total, samples from six electrodes were examined. These samples corresponded to pristine and cycled electrodes of each composition, 70:20:10 and 80:10:10. Two cut-off voltages were applied, 0.0 and 0.2 V vs. Li/Li^+.

After cycling, the half-cells were disassembled in a controlled atmosphere glove box. Samples were cut from these coin cell electrodes and sealed between two pieces of Kapton tape. The samples did receive some exposure to the external atmosphere during transit and processing for μCT studies. However, a comparison of chemical and structural characteristics for samples exposed to ambient conditions and those strictly handled under inert atmosphere have shown no significant differences [77]. Synchrotron-based μCT was performed on samples extracted from the composite electrodes at a resolution of 1.3 μm (0.65 μm pixel size) using beamline 2-BM-A at the Argonne National Laboratory Advanced Photon Source (APS). The μCT scans were performed in white beam mode with an exposure time of 50 ms per projection image. Each tomographic scan contained 1500 projection images equally spaced over 180^o of rotation.

2.2.9 Microstructural Analysis

The projection image data were reconstructed using the *TomoPy* software developed by APS [79]. First, an appropriate center for each sample was determined by reconstructing a central slice of the tomogram with a series of test center. The sample centers were selected based on visual inspection and the minimization of fan artifacts in the test reconstructions. Once the sample centers were found, regions 175.5 μm thick were reconstructed for each sample. These regions corresponded to 270 vertical slices within the 3D image. During reconstruction, stripe removal [80] and phase retrieval [81] of phase contrast data were performed. After reconstruction, the images were segmented and analyzed using *FIJI* [82], an open source platform for image analysis [77]. It was noted that the images were affected by slight beam hardening due to the presence of higher attenuating Sn, Cu_6Sn_5, and Cu. In this case, attenuation became more prevalent towards the center of the reconstructed image. Based on visual inspection sub-regions with a lower variation in frequency were selected as representative volumes. To minimize variation, sub-regions were selected such that the lowest value of the Cu current collector attenuation was within 25% of the maximum value of the Cu current collector attenuation for the sub-region.

The sample sub-regions selected, Fig. 2.2 and Table 2.1, show a range of particle sizes with varied attenuation due to the presence of copper, Cu_6Sn_5, and tin. In general, there is a low level of noise in these images, particularly relative to the Cu and Sn containing regions. These characteristics facilitated segmenting the metallic active material (Cu, Cu_6Sn_5, and Sn) from the supporting pore/carbon/binder regions in the electrode samples. In this analysis, the Cu, Cu_6Sn_5, and Sn materials are treated as a single solid active material phase.

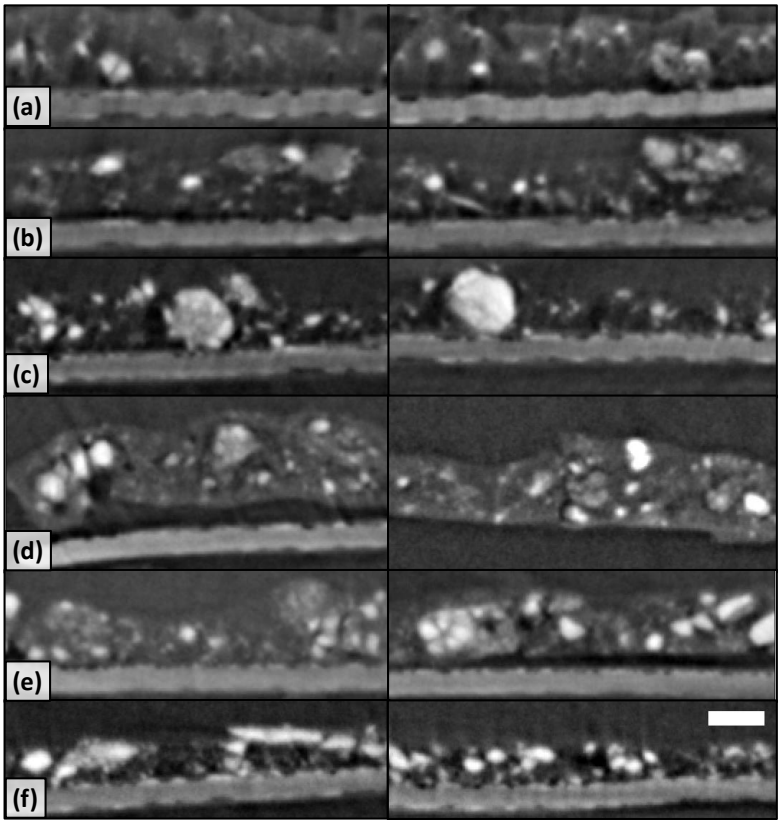

Fig. 2.2 Representative cross-sections from the composite Cu_6Sn_5 electrode samples with (AM:CA:B) composition (a) – (c) 70:20:10 and (d) – (f) 80:10:10. Cycling conditions for each pair of cross-sections are (a) and (d) cycled between [0.0, 1.5] V vs. Li/Li^+, (b) and (e) cycled between [0.2, 1.5] V vs. Li/Li^+, and (c) and (f) uncycled. Electrodes were analyzed in a discharged condition at their corresponding lower cutoff voltage. Scale bar at the lower right represents 25 μm and applies to all images.

Table 2.1 Sample set overview for x-ray microtomography tests and microstructural analysis.

Sample Number	Composition (AM:CA:B)	Cycling Condition: Lower Cutoff Voltage	Number of RVEs Analyzed	D_{50} Solid [μm]	D_{50} Pore/Carbon/Binder [μm]
1	70 : 20 : 10	0.0 V vs. Li/Li^+	2	2.82	17.36
2	70 : 20 : 10	0.2 V vs. Li/Li^+	2	3.32	14.29
3	70 : 20 : 10	Uncycled	2	3.78	11.82
4	80 : 10 : 10	0.0 V vs. Li/Li^+	3	2.51	10.07
5	80 : 10 : 10	0.2 V vs. Li/Li^+	2	2.85	8.86
6	80 : 10 : 10	Uncycled	2	2.88	8.44

After identifying the sub-regions in Fig. 2.2 and Table 2.1, the metallic phases (Cu, Cu_6Sn_5, and Sn) were segmented from the lower attenuating phases (Kapton tape, carbon, binder, and pore). As a first step, a mean filter was applied to reduce noise in the acquired images. The image resulting from this filter operation and its histogram are shown in Fig. 2.3 (a). Two regions are highlighted in this histogram. The red box region contains values indicative of the background, Kapton tape, and supporting matrix (*i.e.*, pore/carbon/binder) regions. The green circle region contains values indicative of solid regions associated with the active material. These regions are expected to be primarily Cu, Cu_6Sn_5, and Sn. Following the filtering step, the histogram values smaller than the peak associated with the Kapton tape and supporting matrix were removed using a minimum operation. This step effectively eliminated the noise and isolated the tape, supporting matrix, and solid particles from the background. The resulting image and its histogram are shown in Fig. 2.3 (b).

To segment the metallic phases, the mean grayscale value from the Cu foil region was assessed. Histograms of the copper current collector, seen at the bottom of five of the six sample regions in Fig. 2.2, were used to identify a value for the grayscale threshold within each given sub-region. This step treats the copper current collector, a known material, as an internal reference within each electrode sample. The gray values smaller than the Cu foil mean were removed from the images using a minimum operation. An iterative visual inspection was used to optimize this minimum value to include all of the copper within the sub-region. This step effectively removed the supporting matrix and Kapton tape regions along with lower attenuation reaction products. These newly separated particles represent the Cu, Cu_6Sn_5, and Sn particles present in the analyzed image

shown in Fig. 2.3 (c) and their associated gray values are highlighted by the green region in the accompanying histogram.

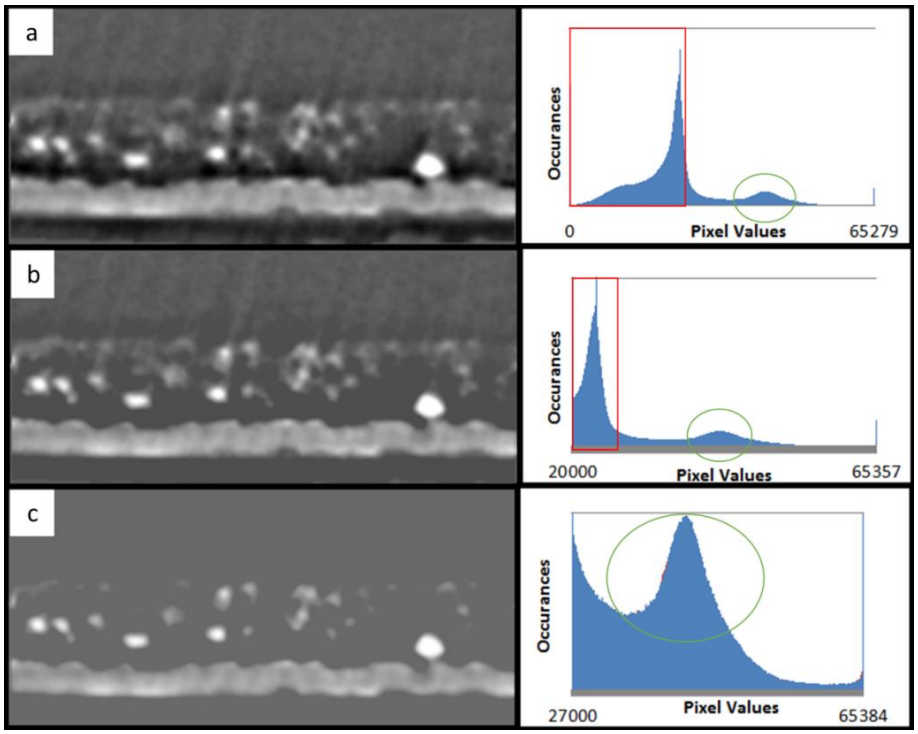

Fig. 2.3 Image of Cu_6Sn_5 70:20:10 electrode cycled between [0.2, 1.5] V and extracted after been discharged to 0.2 V vs. Li/Li^+. (a) Image following application of a mean filter. (b) Image after background removal. (c) $Cu/Cu_6Sn_5/Sn$ particles and Cu foil current collector segmented from non-metallic phases.

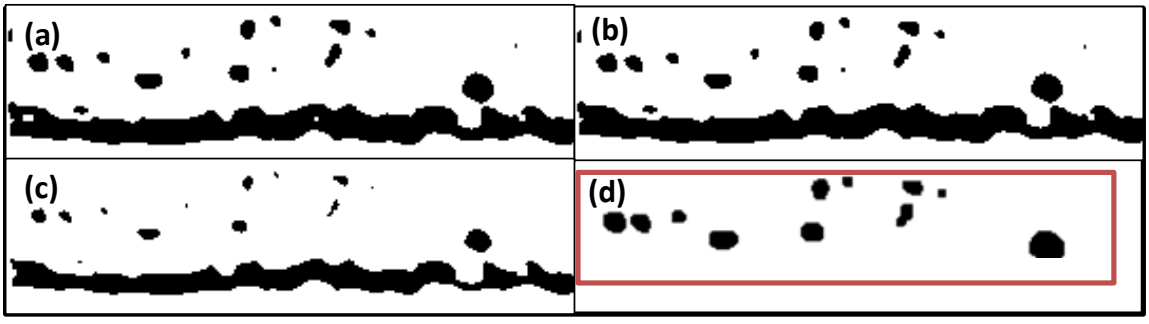

Fig. 2.4 Image of Cu_6Sn_5 70:20:10 electrode cycled between [0.2, 1.5] V and extracted after been discharged to 0.2 V vs. Li/Li^+ after threshold. (a) Image after initial threshold. (b) Image after filling holes. (c) Image after erosion and watershed techniques. (d) Dilated and cropped region for further PSD analysis. The black spots represent the Cu, Cu_6Sn_5, Sn particles related to the active material while the white regions represent the non-reactive carbon/binder components.

Following the initial filtering outlined above, a threshold process was applied to generate a binary image of the metallic phases for subsequent analysis, see Fig. 2.4. Once the binary images were obtained, a hole filling routine in *FIJI* was used to fill out holes present in some of the particles shown in Fig. 2.4 (a). The resulting image is shown in Fig. 2.4 (b). Following the hole filling, an erosion process was done to remove pixels in the particle boundaries and further aid in segmenting the remaining particles that are connected at edges, as shown in Fig. 2.4 (c). The particles were then separated using watershed segmentation tools available in *FIJI*. This added step helped to separate distinct particles for further analysis of particle size distributions, specifically the characterization of particle surface area and volume. The watershed process does result in a net removal of the solid material. To mitigate this over-segmentation a dilation step was performed on the binary image following watershed segmentation, Fig. 2.4 (d). This dilation results in a marginal increase of 2~3% on the particle size estimates compared to estimates based on the original thresholding step. Finally, the holes filled prior to segmentation and the boundaries between particles from the watershed segmentation were reincorporated into the binary image data.

Once segmentation of the Cu/Cu_6Sn_5/Sn regions was complete, the Cu foil current collector, seen in the lower part of the images in Fig. 2.3 (a)-(c) and Fig. 2.4 (a)-(c), was removed by cropping the image to obtain the final image with the Cu, Cu_6Sn_5, and Sn particles related to the active material, and the lower attenuating regions that represent the pore/carbon/binder, see Fig. 2.4 (d). The binary image data, representing Cu, Cu_6Sn_5, and Sn particles, was then characterized. Using the continuous phase size distribution (PSD) and discrete particle size distribution calculation methods developed by Münch and Holzer [83-85], the radius, volume, and surface area are found for the active material particles that were segmented. The continuous PSD of the regions in between the active material particles was also calculated to determine representative sizes of the pore/carbon/binder regions of the samples.

2.3 Results and Discussion

2.3.1 Theoretical Capacity

The analysis started with the active material synthesis, followed by the electrode casting and the assembly of coin cells. In these half cells, Cu_6Sn_5 (2.6 ~ 2.8 V vs. Li/Li^+ at the fully delithiated

condition) acts as the positive electrode, while, lithium metal (0.0 V vs. Li/Li^+) acts as the negative electrode. First, it was necessary to determine the maximum reversible capacity that could be obtained from these electrodes. Results shown in Fig. 2.5 correspond to the second cycle, which is a more representative result for a full cycle. During the first cycle, a long CC discharging occurs since it accounts not only for the reversible but also the irreversible lithium. The maximum delivered discharge capacity by the half-cells with the 70:20:10 and 80:10:10 compositions were 531.9 and 469.4 mAh/g, respectively, which is in agreement with previously reported values [68].

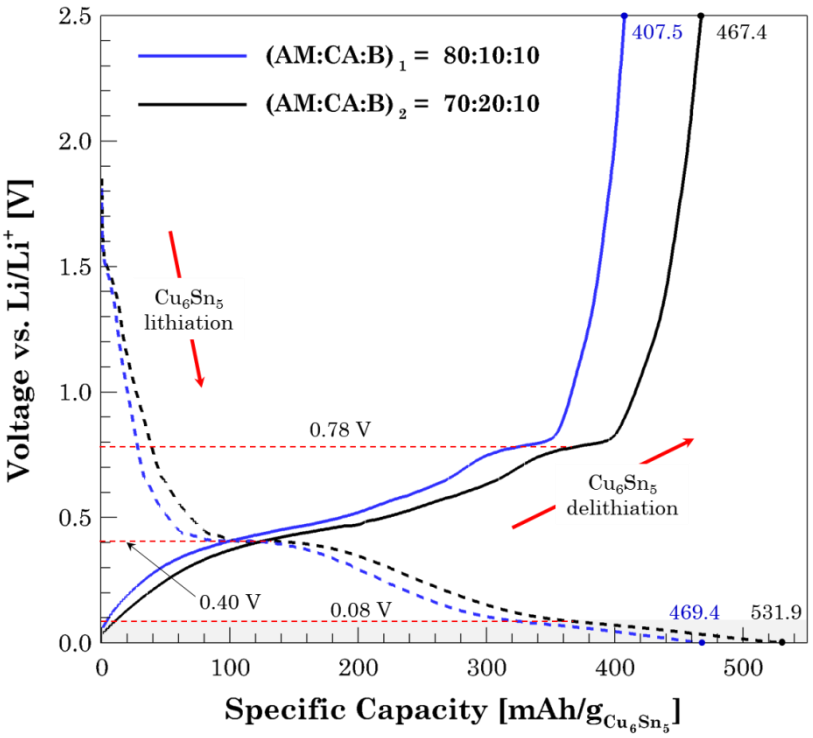

Fig. 2.5 Maximum achievable experimental capacity: charge and discharge profile at a low C-rate (C/20). During the lithiation process, the plateau voltages (red dashed lines) indicate the phase transition from Cu_6Sn_5 to Li_2CuSn (0.40 V vs. Li/Li^+) and then to the alloys formation, Li_xSn_y + Cu, (0.08 V vs. Li/Li^+).

The effect of the secondary phase turned out to be more significant than the percentage of active material. In terms of the performance, two different plateaus are found in the charge and discharge profiles at 0.78 V and 0.40 V, respectively. These correspond to the Li_2CuSn phase transition described by the electrochemical reaction described by the Eq. 2.1. The results show that the electrode with the 70:20:10 composition has a better performance, in terms of capacity, by

achieving almost ~14% more capacity than the cell with the 80:10:10. The electron transport resistance is higher in the 80:10:10 cell due to a lower binder-conductive additive amount in the electrode. During the discharge, a second plateau voltage is found around 0.08 V corresponding to the Li-Sn alloy formation accompanied with the matrix copper expulsion. The irreversible nature of this reaction is reflected in the immediate charge process with a specific capacity reduction larger than 10%, even though the initial cycling is done at a low C-rate.

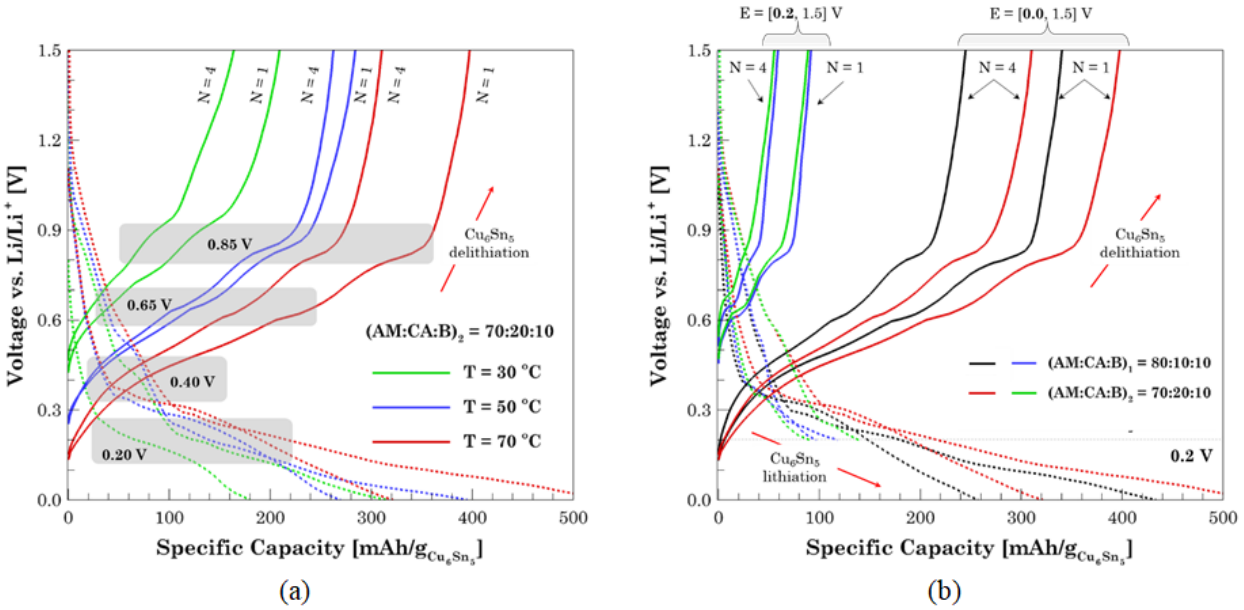

Fig. 2.6 (a) Effect of the drying temperature during the electrode processing on the cell performance. Gray zones represent the potential at which phase change occurs in the charge and discharge processes. (b) Cell performance of electrodes with different compositions cycled in two operating voltage windows. The lower cutoff voltage is selected between 0.0 and 0.2 V vs. Li/Li^+. Cells are cycled 5 times and representative results for cycle 1 and 4.

Electrode Drying Temperature Effect. The microstructural properties of the electrode were modified by two variables: electrode composition and drying temperature. From Fig. 2.5, it was obtained that the 70:20:10 composition had a larger reversible capacity than the 80:10:10 composition when cycled at a low C-rate. Hence, the drying temperature effect on cell performance was studied by using the 70:20:10 composition as a baseline. The results for the half-cells cycled at C/2-rate are shown in Fig. 2.6 (a) and Table 2.2.

Table 2.2 Maximum charge and discharge specific capacity for cells with different electrode's composition and cycled at different voltage window. The specific capacities listed correspond to the charge and discharge specific capacities from Fig. 2.6 (b). The capacity retention, calculated with respect to the initial specific discharge capacity, is also listed in the table as a percentage.

	$(AM:CA:B)_1$ = 80:10:10				**$(AM:CA:B)_2$ = 70:20:10**			
	Cycle 1		**Cycle 4**		**Cycle 1**		**Cycle 4**	
Voltage Window	Specific Capacity [mAh/g]		Specific Capacity [mAh/g]		Specific Capacity [mAh/g]		Specific Capacity [mAh/g]	
	Discharge	Charge	Discharge	Charge	Discharge	Charge	Discharge	Charge
Extended [**0.0**, 1.5]	**434.15**	**340.33**	**257.83**	**244.64**	**527.66**	**397.39**	**322.17**	**310.29**
	100.0 %	78.4 %	59.3 %	56.3 %	100.0 %	75.3 %	61.0 %	58.8 %
Reduced [**0.2**, 1.5]	**117.75**	**91.63**	**97.25**	**58.77**	**138.78**	**88.64**	**90.59**	**55.34**
	100.0 %	77.8 %	82.6 %	49.9 %	100.0 %	63.8 %	65.2 %	39.8 %

First, the phase transition potential was identified for all three drying temperatures. During the discharging (lithiation), the transition from Cu_6Sn_5 to Li_2CuSn occurs at ~0.40 V vs. Li/Li^+. A further lithiation exhibits a second plateau voltage around 0.20 V, indicating the formation of Li-Sn alloys. The capacity delivered after this plateau voltage is comparable to half of the total capacity, independent of the temperature at which the electrode was dried. In terms of the overall performance, the electrodes dried at 70 ^oC provide the largest specific capacity (527.66 mAh/g) during the first cycle. Similarly, the lowest initial capacity (316.22 mAh/g) is obtained with the electrodes dried at 30 ^oC. This is in agreement with previous studies by Liu et al. and Stein et al. where it was shown that the electrode morphology [86] and the electrochemical performance[76], respectively, could be modified by the drying temperature. Initially, NMP solvent evaporation dominates the electrode drying until the air-solvent interface reaches the sediment surface. During the second regime, the air-solvent meniscus in between the particles produces a capillary pressure inducing stresses on the dry electrode. At a higher temperature, the evaporation rate is faster and the onset for the capillary-driven regime occurs early. The higher drying temperature coupled with a lower solvent content reduces the elapsed time for the capillary-pressure drying regime. Consequently, the stress-inducing time on the electrode microstructure also decreases [87]. The volume expansion of the electrode coupled with the drying stress reduces the capacity and lifetime of the electrode. In particular, at low temperature (30 ^oC) the drying time for both regimes is longer,

induces more stress on the electrode and reduces the capacity that can be obtained from the electrode.

2.3.2 Operating Voltage Window

The operating voltage window delineates the electrochemical reactions that will take place in the electrode. From the results shown in Fig. 2.5, it is known the potentials at which the phase transitions happen. Based on this data, two voltage windows were selected: the extended ([0.0, 1.5] V vs. Li/Li^+) and the reduced one ([0.2, 1.5] V vs. Li/Li^+). By extending the voltage window, the delivered capacity increased as well as the production of Li-Sn alloys and the expulsion of copper from the microstructure. The aim of the reduced voltage window is to study how much the performance changes when the cell overpasses the Li-Sn alloys formation.

The results for the first and fourth cycle of the electrodes cycled in each of the two operating windows are shown in Fig. 2.6 (b) and Table 2.2. The extension of the voltage window from 0.2 to 0.0 V vs. Li/Li^+ delivers four times as much capacity. This implies that the large capacity obtained from the Cu_6Sn_5 active material originates from the phase transition of Li_2CuSn to Li-Sn alloy. However, due to the irreversible nature of the Li-Sn alloy phase, the large capacity cannot be held for multiple cycles. In fact, the capacity fades to almost 50% of the initial capacity after four cycles for both compositions and both voltage windows. According to these results, see Table 2.2, almost 12.5% of the lithium alloyed during the discharge is lost in the Li-Sn alloys formation per cycle. From Fig. 2.6 (b) and Fig. 2.7 (b), it is evident that the 70:20:10 composition provides a higher capacity in the 0.0-1.5 V window. However, in the 0.2-1.5 V window, both compositions showed a similar trend. It is also counterintuitive that the cells with the lower active material content exhibits a higher capacity. This suggests that the structural changes occurring during the Li_xSn_y formation interact with the electrode structure. That is, the electrode composition/structure strongly influences the available capacity on full lithiation. However, expanding the voltage window from 0.2 to 0.0 V has weaker influence on the performance.

Table 2.3 Maximum charge and discharge specific capacity of cells with different electrode's composition tested at multiple C-rates between [0.0, 2.5] V vs. Li/Li^+.

	Charge Capacity [mAh/g]		Discharge Capacity [mAh/g]	
Composition / C-rate	**$(AM:CA:B)_1$ = 80 : 10 : 10**	**$(AM:CA:B)_2$ = 70 : 20 : 10**	**$(AM:CA:B)_1$ = 80 : 10 : 10**	**$(AM:CA:B)_2$ = 70 : 20 : 10**
C/2	377.511	238.105	457.669	260.317
1C	69.166	101.025	82.689	109.414
2C	11.395	51.004	11.513	56.700
3C	4.603	24.138	3.216	24.934

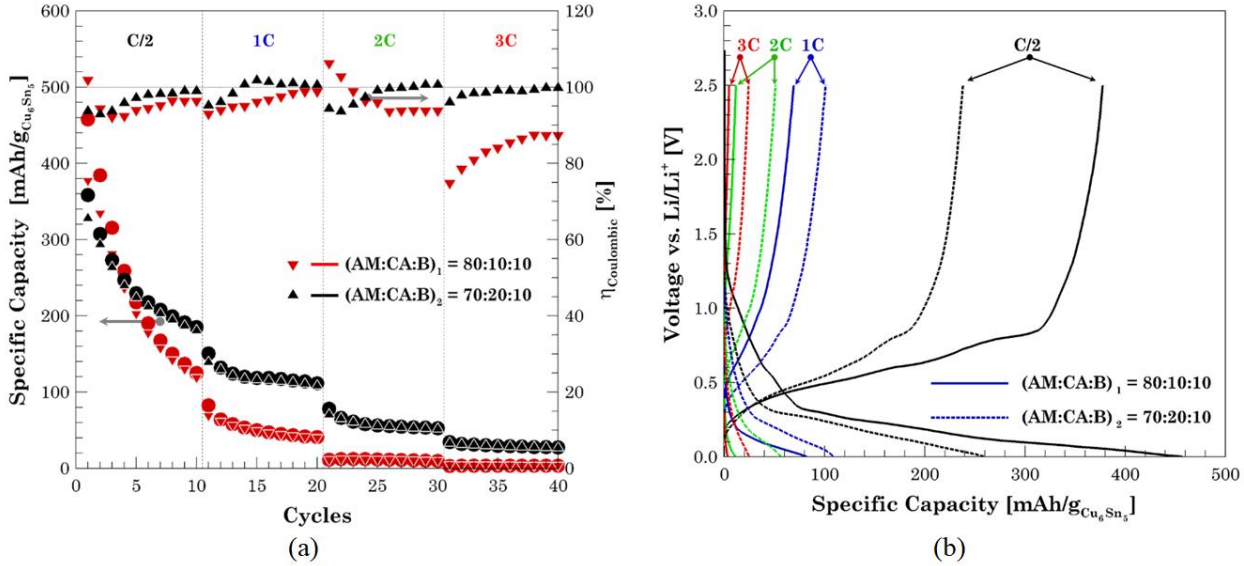

Fig. 2.7 Effect of the C-rate in the half-cell performance. (a) Cells are charged and discharged (left axis) between [0.0, 2.5] V vs. Li/Li^+, at the corresponding C-rate and the corresponding coulombic efficiency (right axis). Circle and triangle markers represent the discharge and charge capacity, respectively. (b) First cycle for each of the four C-rates.

2.3.3 Rate Capability and Coulombic Efficiency

The rate capability of the electrodes is shown in Fig. 2.7 (a). The capacity delivered by the 80:10:10 cell is larger than the capacity delivered by the 70:20:10 cell, but only for the first 4 cycles at C/2-rate. This increased capacity is due the greater amount of active material. From thereafter the trend

inverted and remained unchanged for the remaining C-rates that were tested. Table 3 lists the initial charge and discharge capacity for each of the compositions. For all C-rates and both compositions there is a clear drop in the charge and discharge capacity. This decreasing trend is more evident for the C/2-test than for the other three C-rates and can be associated to two factors: the operating voltage window and the cumulative cycling degradation. Copper expulsion accompanied with mechanical degradation of the dried cast slurry happen when the cells are lithiated below 0.2 V vs. Li/Li^+. An extreme lithiation of the Cu_6Sn_5 composite leads to an irreversible formation of Li-Sn alloys. This degradation increases the cell internal resistance, which combined with the increasing current leads to the largest overpotential during cycling. During cycling, a large overpotential drives the cell faster to the set voltage limits hindering a proper cell charge or discharge. The reduction of the capacity to less than 1% of the initial capacity, for both compositions, is a consequence of these two factors.

The Coulombic efficiency, defined as the ratio of the discharge capacity to the charge capacity [88], exhibits a characteristic increasing trend for each. At the initial cycles, lithium-ions are consumed by the parasitic reactions between the electrode and the electrolyte, forming the SEI and reducing the Coulombic efficiency. Once the electrode forms a steady SEI film the columbic efficiency increases again to 100%.

Representative charge/discharge curves, for the first cycle, at the four selected C-rates, are shown in Fig. 2.7 (b). As expected, the largest capacity is obtained when the cell is cycled at a low C-rate (C/2). The capacity also decreases as the C-rate increases. Through the test, the cell is initially discharged (i.e., the electrode is fully lithiated) and then immediately charged without rest. In this initial cycle, the Coulombic efficiency is roughly 85%, i.e., not only is 15% of the reversible lithium consumed in the Li-Sn formation, but also some percentage of Cu_6Sn_5 anode material becomes permanently unavailable to alloy reversibly with lithium in further cycles. As cycling continues, the consumption of lithium and Cu_6Sn_5 material exhibits an avalanche effect, where degradation from the initial cycles is carried onto the subsequent cycles. Thus, the performance curve for the 3C-rate test accumulates the electrode degradation from the previous 30 cycles, increasing the cell internal resistance and consequently the overpotential. Even though the carrying

phenomenon is intrinsic for all anode materials, the rate at which it occurs in Cu_6Sn_5 composite electrodes is faster than the rate from the conventional graphite electrodes.

2.3.4 Long-Term Cycling Test

Long-term cycling performance for three C-rates (C/2, 1C, 2C) was also studied. Fig. 2.8 shows the specific discharge capacity and the capacity retention, computed as the ratio of the cycle capacity to the initial capacity. The initial largest capacity (394 mAh/g) was obtained with the 80:10:10 cell cycled at C/2-rate. The discharge capacity reduced to 198 and 107 mAh/g when the electrodes were cycled at 1C and 2C-rate, respectively. The delivered capacity quickly decayed to less than 50% of the initial capacity after the first 15 cycles. A similar analysis for the 70:20:10 cells showed relatively better capacity retention than the 80:10:10 cells. For these cells, it took 20~25 cycles before the capacity dropped down below 50% of the initial capacity. No matter the composition or the cycling C-rate, all the cells showed an extreme fast degradation during the initial cycles. After 60 cycles, the capacity retention is at most 30%, corresponding to a specific discharge capacity of ~60 mAh/g. This capacity is still far away from the capacity that could be obtained from a graphite electrode. Also, in a real application, a cell with capacity retention lower than 80% is considered as dead and must be replaced.

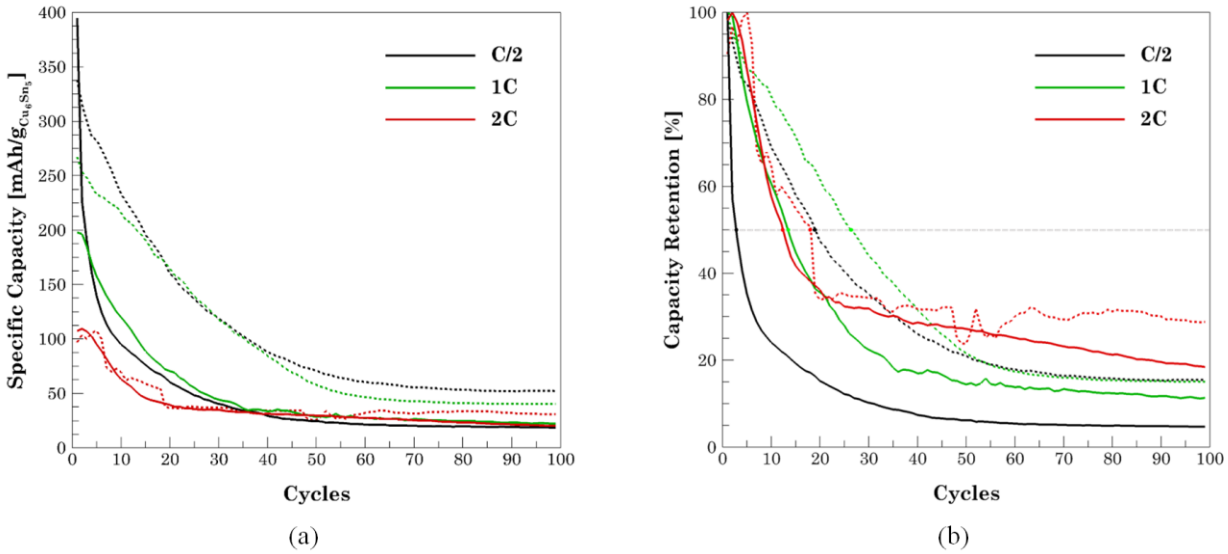

Fig. 2.8 Cycling of cells between [0.0, 2.5] V vs. Li/Li^+ with different compositions. (a) Discharge capacity through cycling and (b) percentage of capacity retention at different C-rates (C/2, 1C, 2C). Solid and dashed lines correspond to the $(AM:CA:B)_1$ = 80:10:10 and $(AM:CA:B)_2$ = 70:20:10, respectively.

2.3.5 Cyclic Voltammetry

Cyclic voltammograms for the 3 initial cycles are shown in Fig. 2.9. The cathodic peak at ~1.23 V, for both compositions, corresponds to the electrode-electrolyte reaction with and subsequently SEI film formation at the electrode surface [89]. The peak shifting along the voltage-axis indicates that the SEI formation reaction is irreversible. As the number of cycles increases, the peak amplitude decreases becoming undistinguishable after the third cycle. This indicates that during the initial cycle the SEI film formed becomes not only uniform but stable. As voltage keeps decreasing (E<0.5 V), the cathodic current increases and lithium alloys with the Cu_6Sn_5 composite. The peak below 0.5 V represents the alloying reaction forming Li_2CuSn. An extensive lithiation (E<0.2 V) of the Cu_6Sn_5 composite leads to Li-Sn alloys (Li_xSn_y, $10 < x \leq 22$, $0 < y \leq 5$) formation, as described in Eq. 2.2, and hence the expulsion of copper from the microstructure.

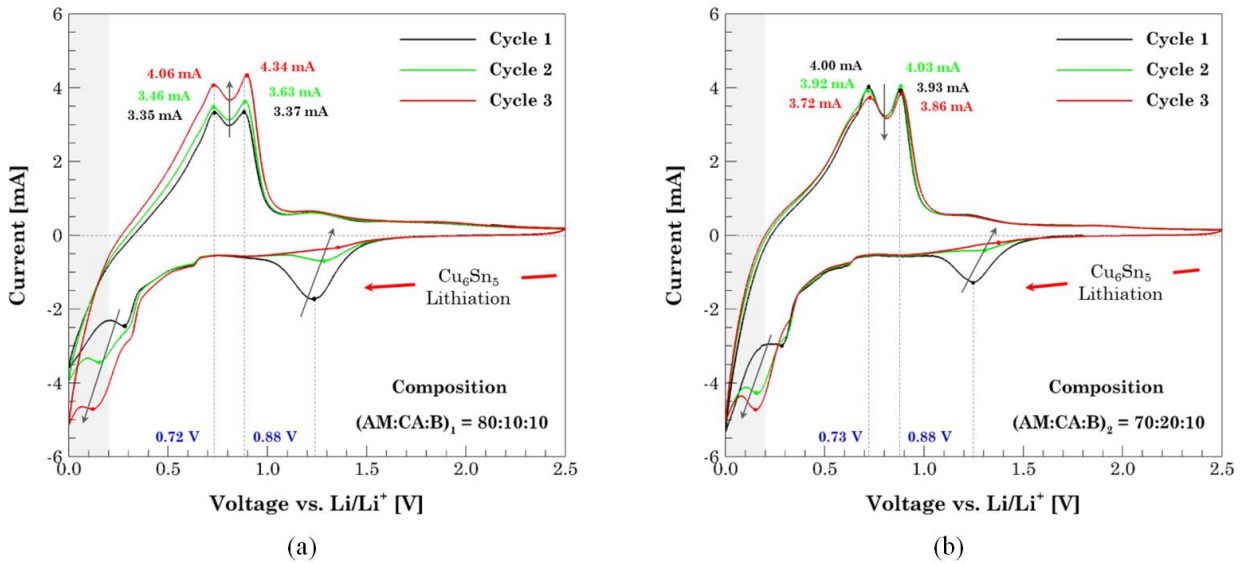

Fig. 2.9 Cyclic voltammograms for the initial three cycles of the Cu_6Sn_5 electrodes between [0.0, 2.5] V vs. Li/Li^+ with a potential sweep rate of 1 mV/s for the composition: (a) $(AM:CA:B)_1$ = 80:10:10 and (b) $(AM:CA:B)_2$ = 70:20:10.

The horizontal shifting of the peaks during the cathodic sweep to a lower voltage indicates the irreversible nature of this reaction and confirms the negative impact of the copper expulsion phenomena. During the anodic sweep, lithium dealloys from Li_2CuSn and two reduction peaks appear at ~0.72 and 0.88 V vs. Li/Li^+ corresponding to the phase transitions $Li_xSn_5 \rightarrow Li_2CuSn$, and $Li_2CuSn \rightarrow Cu_6Sn_5$, respectively. Vertical alignment of the anodic peaks indicates the

reversible nature of the electrochemical reaction. Whereas vertical shifting of anodic current peaks indicates the increasing presence of electrochemically inactive species (expulsed copper and SEI growth from fractured zones), preceding the lithium deintercalation. The fast 80:10:10 electrode degradation comes along with a greater presence of the inactive species and a larger shift of the anodic peak.

2.3.6 Electrode Surface Morphology

In order to study how the first lithiation distresses the microstructure, pristine electrodes were discharged to four voltages: 2.75, 1.75, 0.25, and 0.00 V vs. Li/Li^+. Voltages were selected based upon the CV results shown in Fig. 2.9, and they are common to both compositions. The open circuit potential of pristine electrodes is ~2.75 V prior to lithiation. The first reaction, associated with SEI formation, occurred at 1.25 V. Lithiated electrodes, prior to this reaction (1.75 V), were also analyzed. At this potential, a combination of Cu_6Sn_5 and Li_2CuSn phases are present in the electrode. The third potential, ~0.25 V, corresponds to the point where the Li-Sn alloys start forming. Two phases coexist at this condition: Li_2CuSn and Li_xSn_y plus the presence of the copper released. Finally, at the fully lithiated condition, ~0.0 V, Li_2CuSn converts to Li_xSn_y and more copper is expelled. Here it should be noted that both unreacted Li_2CuSn and Li_xSn_y may be present, but there is a larger presence of the Li-Sn alloys. The unreacted Li_2CuSn may result from electrically or chemically isolated regions created by the evolving microstructure. The micrographs, shown in Fig. 2.10, exhibit uniform smooth surfaces, for the pristine electrodes.

The dark background corresponding to the porous secondary phase (CA+B) covers a larger area in the 70:20:10 electrode due to the larger conductive additive content. As lithiation progresses, the electrode surfaces exhibit some protuberances (through-plane expansion) and some cracks (in-plane expansion). At the fully lithiated condition the electrode expansion creates large cracks and detachment from the substrate, which becomes visible at the bottom of the crack. It's important to highlight that all the Scanning Electron Microscopy (SEM) images correspond to the first lithiation of pristine electrodes at low C-rate. Degradation will worsen if the C-rate increases and the cell is cycled multiple times. This mechanical degradation explains the fast capacity fading of all cells no matter the composition of the way the electrode was processed.

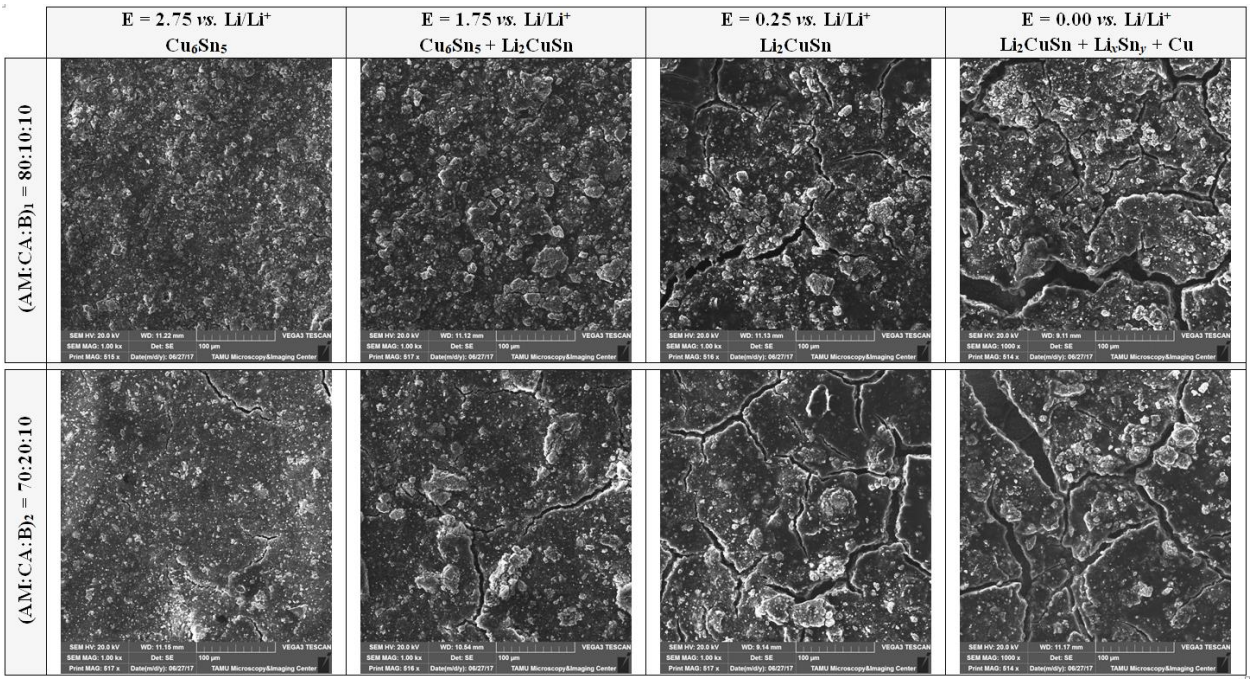

Fig. 2.10 Micrographs of the phases present in the electrode lithiation. By increasing the lithium content, the volume expansion creates a mechanical degradation and fracture of the electrode. The dark background is the secondary phase (CA+B). The white background is the $Li_zCu_xSn_y$ compounds. SEM images were obtained at 1 kX magnification. Scale bar is 100 μm.

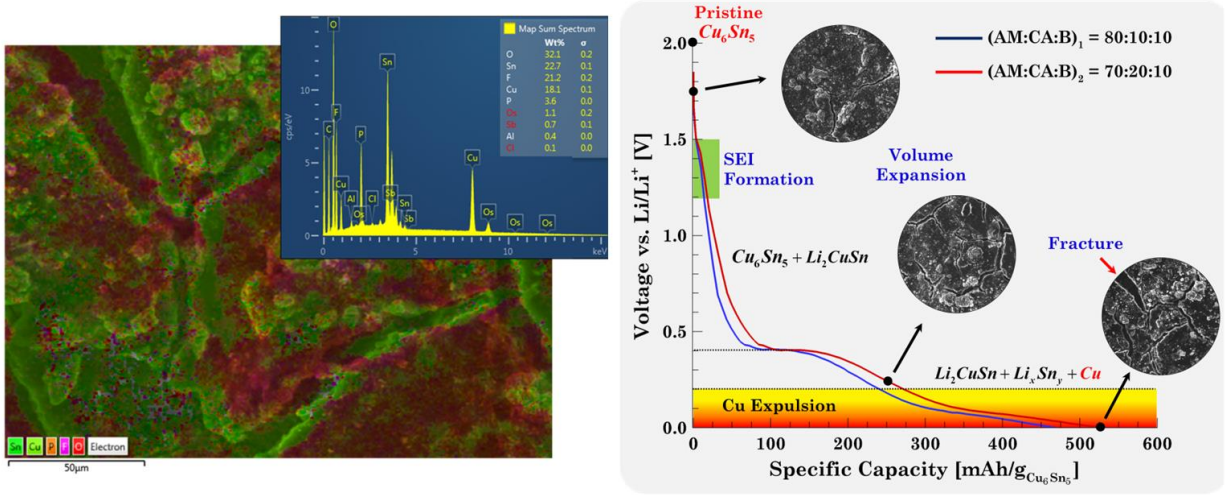

(a) (b)

Fig. 2.11 Electromechanical degradation regime of Cu_6Sn_5 electrodes. (a) EDS pattern analysis of the fully lithiated 70:20:10 electrode. Elements analysis: weight percentage quantification and identification by colors. Oxygen (red) can be associated to the Li-Sn alloys, While, copper (light green) is always found around the cracks. Bar scale is 50 μm. (b) Copper expulsion phenomenon aggravates when the electrode potential is pushed below 0.2 V vs. Li/Li^+ no matter the electrode processing condition (microstructural) or cycling rate (electrochemical).

The electrode composition was analyzed via a spectroscopy technique. Fig. 2.11 shows a representative Energy Dispersive Spectroscopy (EDS) result corresponding to the fully lithiated 70:20:10 Cu_6Sn_5 composite electrode. Even though the technique cannot detect small elements like lithium, its presence can be identified by recalling that lithium reacts with oxygen and water forming lithium oxides. The presence of oxygen is directly associated with the Li_xSn_y alloys. Copper is present from two sources, the electrode matrix and the one expelled from the matrix. Fluorine and phosphorous are residuals from binder and electrolyte. The weight percentage for carbon, see Fig. 2.11 (a), from the conductive additive, was purposely discarded as part of the element identification to have a more objective analysis of the rest of the components. Fig. 2.11 (a) also shows electrolyte residuals (F+P) only on the surface. Along with the electrolyte there is a large percentage of oxygen indicating that when the Li-Sn alloys appear, they accumulate at the surface. Interestingly, the largest amount of copper is found around the cracks. During the lithiation process, a through-plane volume expansion takes place, pushing the $Li_zCu_xSn_y$ to the surface and leaving an empty copper matrix behind. The copper expelled from the microstructure is then detected when the cracks exposed the inner layers.

Table 2.4 Electrodes composition extracted from the EDS test for the samples shown in Fig. 2.10. The values listed correspond to the *wt*% of each particular element found in the samples. Carbon percentage, associated with the conductive additive, was purposely excluded from the analysis.

	$(AM:CA:B)_1$ = 80:10:10						**$(AM:CA:B)_2$ = 70:20:10**					
Elements / Voltage	Cu	Sn	O	F	P	Al	Cu	Sn	O	F	P	Al
2.75	18.8	**39.3**	**8.5**	30.2	2.2	0.8	17.7	**30.0**	**9.6**	33.1	7.3	0.8
1.75	18.9	**32.7**	**14.5**	28.6	3.7	0.5	18.6	**23.9**	**19.6**	31.6	4.9	0.4
0.25	18.3	**28.0**	**22.3**	26.6	3.2	0.5	14.4	**25.3**	**27.2**	28.6	4.3	0.4
0.00	12.6	**22.0**	**41.4**	19.5	3.5	0.2	18.1	**22.7**	**32.1**	21.2	3.6	0.4

Finally, the EDS composition results for all 8 electrodes shown in Fig. 2.10 are listed in Table 2.4. As the amount of lithium content increases at the electrode, the formation of Li_xSn_y alloys increases as the oxygen levels shows. Consequently, the amount of tin available to alloy lithium decreases as Table 2.4 clearly shows. The presence of copper does not follow any particular trend since its

percentage depends, as explained before, on the cracks found on the test. The percentage of fluorine, associated with the binder, decreases since the electrode surface gets covered with the alloys formed during the lithiation.

The electrochemical results from Fig. 2.5 suggest the tin alloys start forming around 0.4 V vs. Li/Li^+ and a second reaction happens around 0.08 V vs. Li/Li^+, during the first lithiation at a low C-rate. The beginning of the alloying phase (0.4 V vs. Li/Li^+) is consistent for all the electrodes no matter the cycling rate. However, the second alloying phase strongly depends on the electrode processing conditions and the cycling rates. The micrographs obtained from the initial electrode lithiation show a minor volume expansion (*i.e.*, less number of protuberances across the electrode) above the 0.2 V, instead of 0.4 V vs. Li/Li^+. The drastic expansion and the electrode fracture actually become significant when the potential drops down below 0.2 V. At this potential, the EDS analysis shown in Fig. 2.11 (a) exhibited the presence of copper around the fractured areas. This indicates that the Cu expulsion phenomenon is aggravated when the electrode potential drops below 0.2 V vs. Li/Li^+, when the residual Cu_6Sn_5 and mostly the Li_2CuSn phases lead to pure tin alloys formation and expelled copper, as shown in Fig. 2.11 (b).

2.3.7 Microstructural Analysis

In order to have a comprehensive overview of the internal changes occurring on the composite electrode, a microstructural analysis of pristine and cycled electrodes was conducted. Representative reconstructed cross-sections from the imaged samples are shown in Fig. 2.2. For the μCT data particle fracture and likely segregation of Cu and Sn can be seen. The sample images show significant disintegration of particles in the 70:20:10 electrode, see Fig. 2.2 (a), and clear examples of particle fracture in other cycled electrodes as seen in the center right hand image of Fig. 2.2 (d) and in Fig. 2.2 (e). Furthermore, several particles with gray values within the same range to the Cu current collector are also clear in Fig. 2.2 (b), (c) and (d), suggesting expulsion of Cu or presence of intermediate products (Li_2CuSn). The grayscale variation in proximity to fractures seen on the right area on Fig. 2.2 (b) and (e) mirrors the behavior seen in nanoscale XANES data, where phase segregation of Cu_6Sn_5, Cu, and Li_2CuSn was observed near fractures [77].

Segmentation was performed to separate Cu, Cu_6Sn_5, and Sn from other solid phases (i.e., lithiated products with lower attenuation) and the pore/carbon/binder regions and the continuous phase size distributions of these regions were calculated using the methods of Münch and Holzer [83-85]. The results of this analysis are shown in Fig. 2.12. The composite electrodes with the 70:20:10 formulation show progressive size reduction in the active material when cycled to lower voltages, Fig. 2.12 (a). The lower performing 80:10:10 composition shows little change upon cycling when comparing the size distributions of particles.

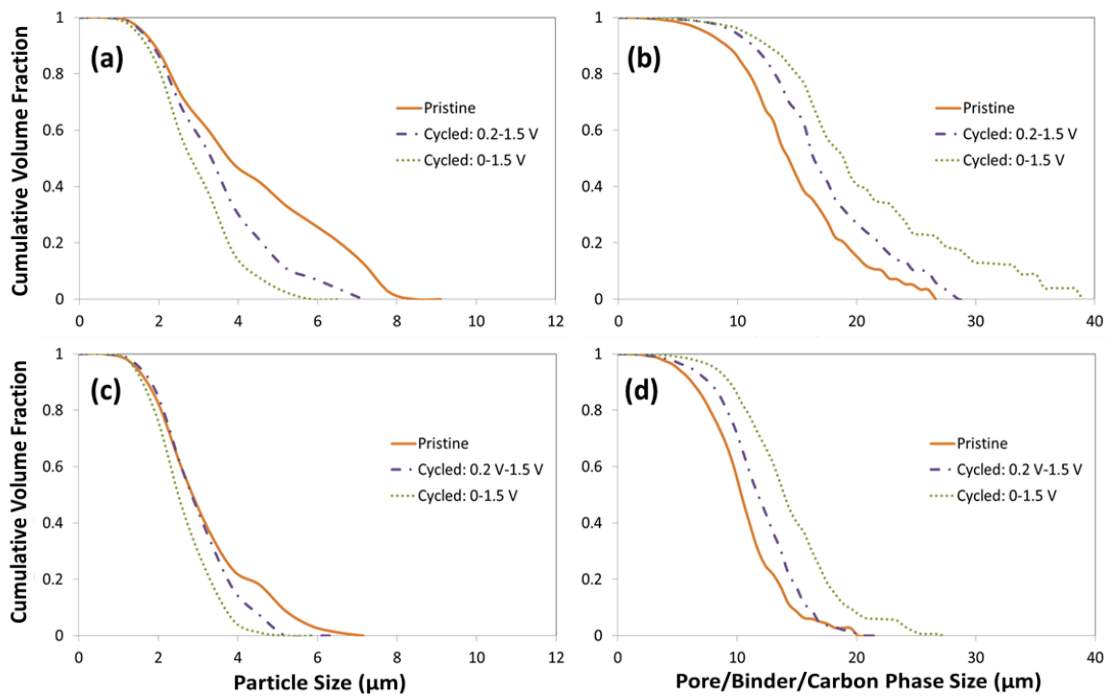

Fig. 2.12 (a) Normalized pore size distribution volume fraction for Cu_6Sn_5 and Cu particles in µm for the 70:20:10 composition. (b) Volume fraction for pore/carbon/binder phase size in µm for the 70:20:10 composition. (c) Normalized pore size distribution volume fraction for Cu_6Sn_5 and Cu particles in µm for the 80:10:10 composition. (d) Volume fraction for pore/carbon/binder phase size in µm for the 80:10:10 composition.

Analyzing the Cu, Cu_6Sn_5, and Sn solid phases from Fig. 2.12 (a) and (c), at the uncycled stage larger particles can be seen in the higher ranges of the size distribution. As the cycling process advances these particles appear to break up in the higher voltage window. Particles with sizes below 2 µm do not present any substantial change due to resolution limits. Higher resolution imaging would be needed to observe changes below this scale. Less change in particle size is seen

for the higher active material composition, with little shift in the PSD below 4 µm in the higher voltage window. As Cu_6Sn_5 converts to Li_2CuSn in the upper voltage window expansion and fracture begin to dissociate the larger particles, creating smaller ones which do not recover to the initial geometry shifting the overall PSD toward smaller sizes. Full lithiation of the tin to $Li_{4.4}Sn$ in the 0.0-1.5 V vs. Li/Li^+ acts to reduce the PSD of both formulations, with a slightly greater reduction for the 70:20:10 composition.

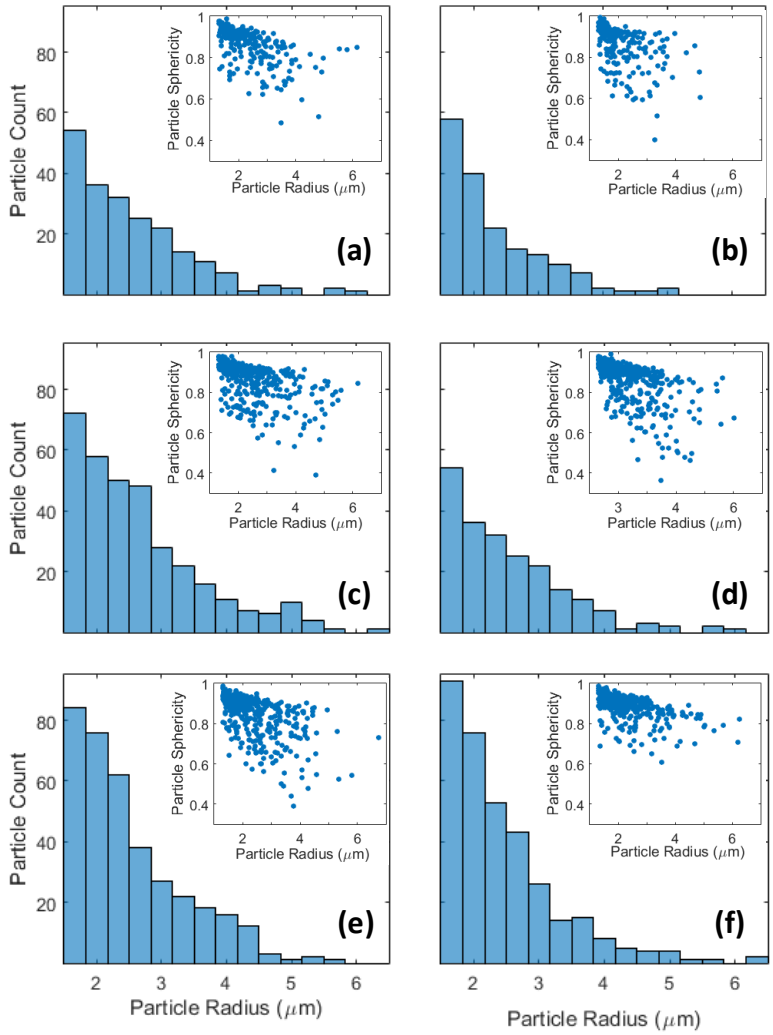

Fig. 2.13 Particle size histograms and sphericity (inset) for the Cu, Cu_6Sn_5, and Sn particle regions in (a) and (b) uncycled electrodes, (c) and (d) electrodes cycled between 0.2 – 1.5 V vs. Li/Li^+, and (e) and (f) electrodes cycled between 0.0 – 1.5 V vs. Li/Li^+. Data for the 70:20:10 composition is given in (a), (c), and (e). Data for the 80:10:10 composition is given in (b), (d), and (f).

A phenomenon that may relate the expansion and active material particle size reduction to the observed electrochemical behavior is the loss of accessible surface area. An increased variation in particle size for the 70:20:10 composition suggests that accessible electrode capacity is retained in those electrodes, Fig. 2.12 (a), permitting a greater change in the structure. Conversely, lack of variation in particle size for the 80:10:10 case suggests that microstructural changes due to expansion during lithiation/delithiation have reached a limited point with respect to accessible capacity of the electrode, Fig. 2.12 (c).

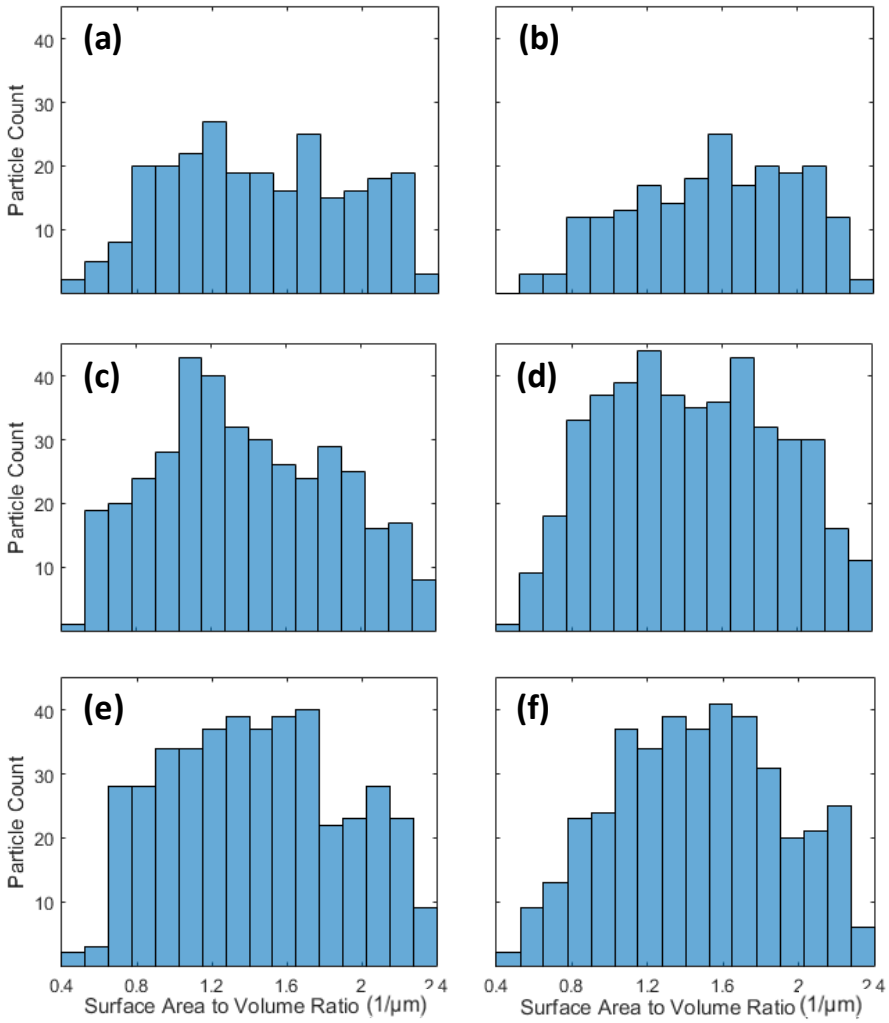

Fig. 2.14 Specific surface area for the Cu, Cu_6Sn_5, and Sn particle regions in (a) and (b) uncycled electrodes, (c) and (d) electrodes cycled between 0.2 – 1.5 V vs. Li/Li^+, and (e) and (f) electrodes cycled between 0.0 – 1.5 V vs. Li/Li^+. Data for the 70:20:10 composition is given in (a), (c), and (e). Data for the 80:10:10 composition is given in (b), (d), and (f).

For the pore/carbon/binder regions on both formulations, transport may be inhibited by the initial active material expansion and the matrix space available for material expansion, also contributing to performance degradation. This observation can be explained by considering that in the 80:10:10 formulation, the pore/carbon/binder regions exhibit a smaller change relative to the 70:20:10 formulation, likely due to the availability of more carbon in the supporting matrix allowing a greater degree of expansion for the 70:20:10 composition, Fig. 2.12 (b) and (d). It is also important to note that the open regions between the higher attenuating Cu, Cu_6Sn_5, and Sn particles in the cycled sample may contain lower attenuating phases such as reaction products that have not been dealloyed and active material pulverized below the 1.3 μm resolution of the measurement. This observation suggests that a reduced capability for strain accommodation and increased mechanical interaction between the active material particles reduces the 80:10:10 electrode performance, and extends the cycling lifetime.

The 70:20:10 composition is shown on the left Fig. 2.13 (a), (c), and (e), while the 80:10:10 data is shown in Fig. 2.13 (b), (d), and (f). Pristine sample data is shown at the top, Fig. 2.13 (a) and (b). Data for electrodes cycled down to 0.2 V vs. Li/Li^+ is shown in Fig. 2.13 (c) and (d). Data for electrodes cycled down to 0 V vs. Li/Li^+ is shown in Fig. 2.13 (e) and (f). Increased counts at smaller particle sizes suggests the pulverization of active materials for both compositions, but a more substantial loss of large particles with low sphericity is seen in 80:10:10 full lithiation. *In operando* cycling data of Sn electrodes suggests that highly convex regions serve as stress concentrators during lithiation and expansion [90-92]. Such regions may be associated with sharper, lower sphericity particles like those seen in the uncycled 80:10:10 cross-sections in Fig. 2.2 (f). The corresponding sphericity data in Fig. 2.13 (b) further demonstrates the presence of such particles. The absence of low sphericity particles in Fig. 2.13 (f) suggests an increased influence of mechanical degradation in the 80:10:10 structure. The evolution of specific surface area is shown in Fig. 2.14. Here a slight loss of specific surface area is seen in 70:20:10 case, with a consistent peak developing at a consistent center around 0.9 μm^{-1}. The higher active material samples 80:10:10 show more of a shift in the maximum specific surface area, with reduction starting with cycling in the 0.2 V vs. Li/Li^+ window. A further shift is seen when cycling to 0 V, suggesting a progressive loss of active surface area that could contribute to capacity fade.

3. ELECTRODE LEVEL DEGRADATION: ELECTRODE PROCESSING

Relevant Publications and/or Working Papers

1. (Joint first author) K. Rollag, D. Juarez-Robles, Z. Du, D.L.Wood, P.P. Mukherjee, 2019, *Drying Temperature and Capillarity-Driven Crack Formation in Aqueous Processing of Li-Ion Battery Electrodes*, ACS Appl. Energy Mater., 6, 7 , pp. 4464-4476 (doi: 10.1021/acsaem.9b00704)

Unlike conventional electrode processing for Li-ion batteries, which uses the expensive and highly toxic organic N-methyl-2-pyrrolidone (NMP) solvent, aqueous processing simply employs deionized water as the solvent. However, thick aqueous processed cathodes have been found to crack during drying. In this study, the influence of electrode drying temperature and thickness on cracking was investigated. $LiNi_{1/3}Mn_{1/3}Co_{1/3}O_2$ cathodes prepared with a hydrophilic binder, modified styrene-butadiene rubber (SBR), were coated at various thicknesses and dried at temperatures ranging from 20 °C to 70 °C. Experiments revealed cracking worsens with increased electrode thickness, and elevated drying temperatures. Cracks were formed during the capillarity driven phase during drying. Strong evaporation and weak diffusion played a critical role in the non-uniform distribution of the inactive phase. Images of electrode surfaces were processed to quantify crack dimensions and crack intensity factor (CIF). Average crack length and width, as well as CIF, increased with drying temperature and electrode thickness. Electrochemical performance revealed a strong and negative correlation between the crack density and performance in terms of specific capacity. Transport limitations associated with the presence of cracks adversely affect the advantage of high volume ratio of active materials in the thick electrodes.

3.1 Introduction

Widespread use of electric vehicles hinges on the advancement of energy storage technologies such as lithium-ion batteries (LIBs). Current research and development endeavors are focused on increasing the energy density of a battery while simultaneously reducing manufacturing costs [93]. Energy density can be improved, and cost can be reduced by optimizing the number of inactive components in a cell with the implementation of thicker electrodes. Furthermore, cost can be significantly reduced with aqueous electrode processing [94].

To meet high energy density demands, thick positive electrodes of 100~200 μm are required in LIBs. However, when a thick cathode is prepared via aqueous processing, the electrode coating cracks as it dries. Du et al. showed that the severity of such crack formations progressively worsens for increasingly thick electrodes [87], as shown in Fig. 3.1.

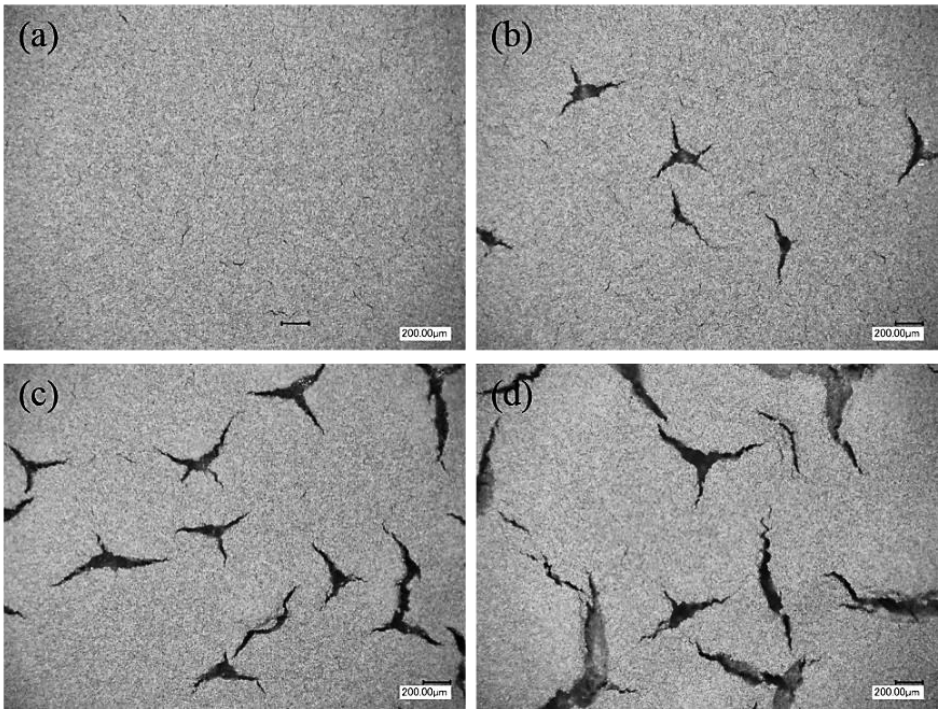

Fig. 3.1 Optical microscope images of aqueous processed NMC cathodes with areal mass loadings of (a) 15.0 mg/cm^2, (b) 17.5 mg/cm^2, (c) 20.0 mg/cm^2, and (d) 25.0 mg/cm^2 [87].

The electrode with 15.0 mg/cm^2 areal loading exhibited only subtle microcracks. However, the electrode with 17.5 mg/cm^2 loading had pronounced cracks with an average width and length of 50 μm and 300 μm, respectively. Cracks are seen to propagate further and increase in number as the mass loading was increased. In fact, the electrode with 25 mg/cm^2 loading had cracks which protruded all the way through to the aluminum foil current collector, resulting in weakened adhesion and delamination of the electrode from the current collector.

Consequently, aqueous processed cathodes are restricted to conservative thicknesses to avoid cracking. A standard aqueous processed positive electrode with areal loading of ~12.5 mg/cm^2 is

completely devoid of cracks. Cracks appear when electrode areal mass loadings exceed ~15 mg/cm^2.

Drying induced cracks have been widely studied in concrete [95-96], desiccated soils [97-98], ceramic films [99-100], colloidal dispersions [101-102], and latex films [103-104]. There is a general consensus that capillary pressure induced stress is the cause of cracking in drying particulate dispersions [104-107]. Initially, particles suspended in a solvent are coated on a rigid substrate. Evaporation drives the air-liquid interface towards the substrate. When the air-liquid interface encounters the subsequently close-packed particle network, capillary action forms liquid menisci among surface particles, giving rise to a negative capillary pressure.

Scaling inversely with pore radius, capillary pressure can be enormous. The pressure gradient across the air-liquid interface puts the entire film into compression, shrinking the film as it dries. Film shrinkage is constrained by the rigid substrate and stress is generated in the film. If this stress exceeds a critical value, the film will crack to alleviate it. Tirumkudulu and Russel [104] derived an expression for the critical stress required for the initiation of a single crack in a thin film:

$$\frac{\sigma_c R}{2\gamma} = 0.1804\left(\frac{2R}{h}\right)^{2/3}\left(\frac{GM\phi_{rcp}R}{2\gamma}\right)^{1/3} \qquad \text{Eq. 3.1}$$

where R is the particle radius, γ is the liquid-vapor surface tension of the solvent, h the thickness of the film at crack initiation, G is the shear modulus of particles, M is the coordination number, and ϕ_{rcp} is the particle volume fraction at random close packing. Based on this equation, thinner films will have a higher critical stress for crack initiation, making them less prone to cracking. This expression for the critical stress of cracking has been found to be in good agreement with other experimental results [104, 108].

For particles with higher shear moduli, particles deform only partially, or not at all, under compressive capillary forces until the maximum capillary pressure is reached and the air-liquid interface recedes into the particle network. Singh and Tirumkudulu [108] derived an expression for the maximum crack free film thickness by setting the capillary stress at the maximum capillary

pressure equal to the critical stress for cracking. The resultant critical crack-free film thickness is given as:

$$h_{\max} = 0.64\left(\frac{GM\phi_{rcp}R^3}{2\gamma}\right)^{1/2}\left(\frac{2\gamma}{P_{\max}R}\right)^{3/2} \quad \text{Eq. 3.2}$$

where, the dimensionless maximum capillary pressure for a collection of identical spheres is given by:

$$\frac{P_{\max}R}{2\gamma} = \frac{3\cos\theta}{2}\left(\frac{\phi_{rcp}}{1-\phi_{rcp}}\right) \quad \text{Eq. 3.3}$$

This stress-limited regime predicts $h_{\max} \sim (1/\gamma)^{1/2}$ and $h_{\max} \sim G^{1/2}$, indicating the crack-free thickness of a film can be increased by reducing the surface tension of the solvent and/or using particles with higher shear modulus.

The influence of evaporation rate on crack formation is less understood as capillary pressure is not a function of evaporation rate. Lee et al. [109] developed a scaling relationship for crack spacing relative to evaporation rate based on experimental observations of cracking in a number of dispersions ranging in particle volume fraction, evaporation rate, film height, and particle radius. The scaling relationship was derived from a proposed cracking mechanism in which negative capillary pressure drives the formation of cracks. Despite the range of parameters in their experimental dispersions, the authors found the data collapsed to one curve, and from it concluded the following proportional relationship:

$$\frac{y}{X} \propto \frac{{h_f}^{0.8}R^{0.2}}{E^{0.35}} \quad \text{Eq. 3.4}$$

where: y is the crack spacing, X is the hydrodynamic length scale, h_f is the dried film height, R is the particle radius, and E is the evaporation rate. According to this relationship, areal crack density is expected to increase for increasing evaporation rate as spacing between cracks narrows. It is hypothesized that cracking in thick, aqueous LIB cathode coatings will scale with evaporation rate in a similar manner as Eq. 3.4.

The effect of the evaporation rate on the conductive additive/binder/active material distribution in the electrode microstructure and the impact in the electrochemical performance was studied by Stein et al. [76]. Three mechanisms are present during the electrode drying: film evaporation, particle diffusion, and sedimentation. The final porous microstructure relies upon the evaporative and diffusion scales. Strong evaporation leads to particle's stratification from the electrode surface to the substrate, while, strong sedimentation leads to an inverse stratification from the substrate to the electrode surface. On the other hand, a strong diffusion allows uniform distribution of the slurry particles. The relative strength of evaporation to diffusion is quantified by the evaporation Peclet number, Eq. 3.5. Whereas, the sedimentation Peclet number, Eq. 3.6, relates [76]:

$$Pe_{evap} = \frac{\text{Evaporation rate}}{\text{Diffusion rate}} = \frac{Eh_0}{\left(\frac{kT}{6\pi\mu R}\right)} \ , \qquad \text{Eq. 3.5}$$

$$Pe_{sed} = \frac{\text{Sedimentation rate}}{\text{Diffusion rate}} = \frac{4\pi}{3}\frac{R^4 g\left(\rho_s - \rho_f\right)}{kT} \ , \qquad \text{Eq. 3.6}$$

where h_0 is the initial film height, k is the Boltzmann constant (k = 1.3806×10^{-23} *J/K*), ρ_s is the particles mass density, ρ_f is the slurry solvent density, T is the drying temperature, and μ is the viscosity of the solvent.

The evaporation Peclet number is directly proportional to the initial slurry height and particle size; and inversely proportional to the absolute drying temperature. According to the Peclet sedimentation number, there is a strong and direct dependence on the particle size and an inverse effect of the drying temperature. It is worth to notice how sedimentation is not affected by the initial height since it takes place from the substrate surface to the wet electrode surface.

In this study, an aqueous electrode processing procedure which utilizes a novel hydrophilic binder, modified styrene-butadiene rubber (SBR), was first developed to investigate the relationship between evaporation rate and crack formation. SBR is a ubiquitous binder in aqueous processing for anodes [110-113], but its complex interaction with cathode particles has prevented its standardized use in aqueous processed cathodes [114]. However, Targray [115] has claimed that by polymerizing SBR to form what they refer to as PSBR. They have created a polymeric binder applicable to both

anode and cathode chemistries that still preserve the positive aspects of SBR as an aqueous binder. A literature review indicated PSBR has yet to be introduced as a hydrophilic binder in LIB electrodes. Rather, its use in published studies has been limited to cathode ink for flexographically printed zinc battery cathodes [116], lithium-sulfur batteries [117], and electrodes for wearable technologies [118-119].

NMC electrodes prepared with PSBR ranging from standard thickness to double thickness were fabricated and dried at temperatures of 20 °C, 45 °C, and 70 °C. Electrodes dried at room temperature (20 °C) provided a baseline to which those dried at higher temperatures could be compared. Each electrode coating was analyzed via scanning electron microscopy (SEM). Image processing of SEM images was employed to quantify cracking in the form of crack severity, distribution of crack length, and distribution of average crack width. Half cells were fabricated and cycled at low and medium C-rates of C/10 and C/2 to investigate the electrochemical performance of each electrode.

3.2 Experimental Details

3.2.1 Cathode Preparation

Aqueous cathode slurry composed of the active material $LiNi_{1/3}Mn_{1/3}Co_{1/3}O_2$ (NMC333, Targray, 154.8 mA·h/g), carbon black (Super C45, Timcal), and binder was prepared with a 90:5:5 wt% ratio, respectively. Binder was a combination of sodium carboxymethyl cellulose (CMC, Aldrich) and modified styrene-butadiene copolymer (PSBR100, Targray) in a 1:4 wt% ratio. A solution of 2 wt% CMC dissolved in deionized (DI) water was prepared in advance via magnetic stirring for 24 hours. PSBR in the form of an aqueous emulsion with 15% solid content was added to the slurry as received.

To make the cathode slurry, DI water was first mixed with the premade CMC solution in a closed glass vial using a magnetic stirrer plate and a stirring bar placed within the glass. Dry mixing of NMC333 and carbon black was done with a mortar and pestle. The powders were then added to the glass vial and the slurry was mixed for 8 hours. PSBR was added to the slurry last, followed by 12 additional hours of mixing.

Electrodes of standard (initial wet thickness 200 μm; dry areal solid mass loading of ~11 mg/cm^2), intermediate (300 μm; ~15 mg/cm^2), and double thickness (400 μm; ~23 mg/cm^2) were coated via a doctor blade film applicator on an Elcometer film applicator. After the casting, the electrodes were allowed to dry at 20, 45, and 70 °C in a vacuum oven (MTI).

The mass of each electrode coating was measured every five minutes throughout the drying process (Ohaus analytical balance). The resultant water content profile was then fit to a curve by the least squares fitting method. The constant evaporation rate characteristic of the first drying regime was found by fitting the acquired water mass versus time data to a first degree polynomial function. In this case, the evaporation rate is reported in milligrams of water per minute. Since the volume of evaporated water is directly proportional to the reduction in film height during this first drying phase of constant evaporation, evaporation rate, *B*, is more conveniently reported in units of length per minute, *E*. Eq. 3.7 was used to convert the evaporation rate from milligrams of water per minute to microns per minute:

$$E = \frac{B}{\rho_f A} \ , \qquad \text{Eq. 3.7}$$

where A is the surface area of the electrode coating. The duration of the first drying phase was calculated from the known initial wet film height, h_0, and the average measured final dry film height, h_f, as follows $\Delta t_1 = \left(h_0 - h_f\right) / E$.

The remainder of the water content profiles corresponded to the second drying regime where evaporation rate is no longer constant. Based on the slow decay, the second drying regime was therefore fit to a negative exponential function, $m_w(t) = De^{-t/\tau}$, where τ is a characteristic time constant and D is the initial water mass content at the beginning of the second drying phase. The time constant provides an insight into the time scale of the second drying phase where the air-liquid interface has receded into the particle network. The duration of the second drying phase was calculated as the difference between the total time and the first drying phase time.

3.2.2 Electrode Imaging

After drying, a scanning electron microscope (SEM, Tescan Vega 3) was used to analyze crack formation in each electrode. Each SEM image was digitally analyzed to determine the crack severity, crack length distribution, and crack width distribution for each electrode thickness at each drying temperature. Crack severity, better known as crack intensity factor (CIF), is a common parameter used to quantify cracking in desiccating soils [120-122]. CIF can be simply defined as the ratio of the crack area to the total surface area of the sample. Both areas are calculated by image processing the micrographs in Matlab. The process began by first converting the original gray scale SEM image to binary by segmenting the image based on a predetermined threshold value of 100. This arbitrary value was kept constant for all images processed regardless of electrode thickness or drying temperature.

After morphologically filtering these images via the closing procedure, see Appendix A, the average area (in pixels) of the remaining connected objects was determined and set as the threshold value of 97 pixels in the final filtration step for all subsequent SEM image analysis. The procedure successfully eliminated the influence of processing errors on crack analysis as shown in Fig. 3.2. The end result was a clean binary image comprised of only the electrode crack formations caused by increased thickness and evaporation rate.

With image analysis complete on SEM images, the boundary of each crack was determined. The distance between boundary pixels was calculated to find the maximum distance. Once the two boundary pixels furthest from each other were identified, the boundary pixels connecting them were counted – providing the length of the crack. The area of each crack was determined by a built in Matlab function known as *regionprops*. The area was divided by the length to determine the average width of each crack. Furthermore, white pixels were summed and divided by the total number of pixels in the image to evaluate the CIF. The entire image analysis and crack quantification procedure were carried out for nine electrode samples (three thicknesses at three drying temperatures), with three SEM images taken from each of the nine samples. The probability density function of a normal distribution of crack length and crack width was plotted for each electrode based on the image analysis results to determine the effect of drying temperature on crack formation in thick aqueous processed electrodes.

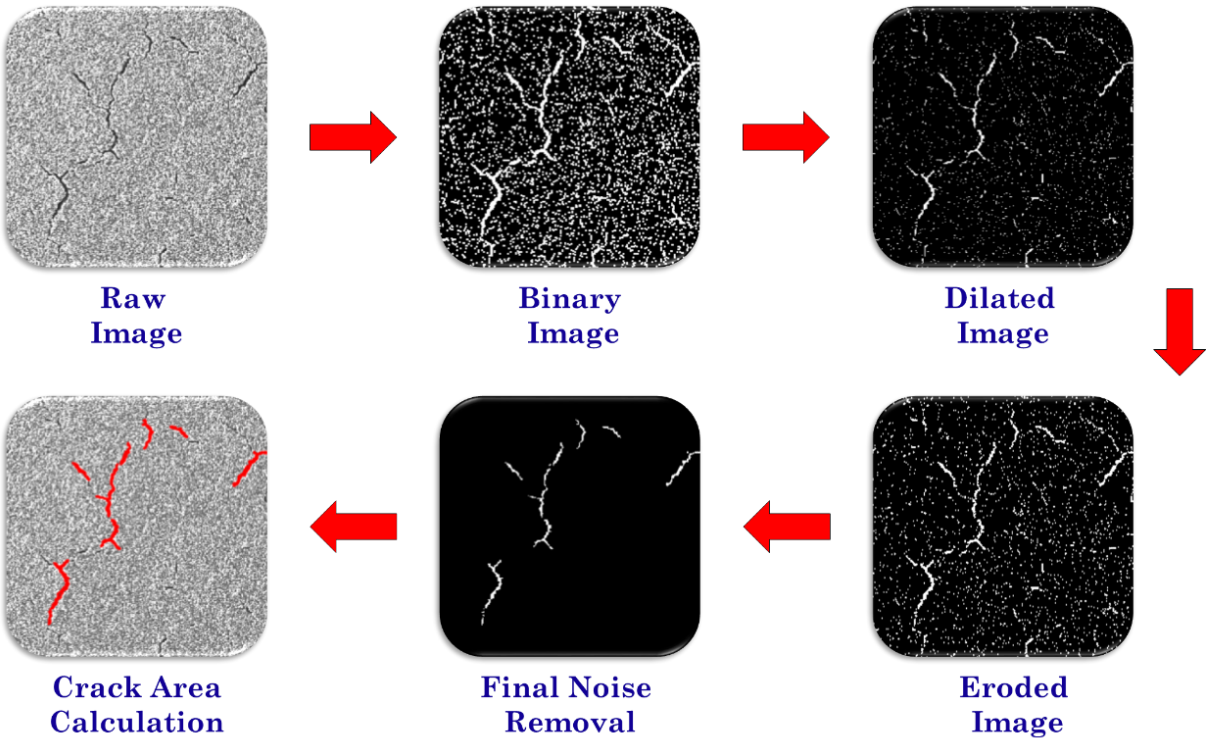

Fig. 3.2 Image processing used for crack's area quantification. The gray scale raw image was initially converted to a binary black-white scale. The resulting image is subjected to the morphological filtering technique known as closing (dilation + erosion). After this step, the image is processed one more time to remove the remaining noise. Final image is a binary matrix with white pixels delimiting the cracks.

3.2.3 Electrochemical Performance

Half cells made with lithium metal anode as the counter electrode were fabricated using a previously reported method [78] to analyze the electrochemical performance of the cathodes prepared with PSBR. A non-aqueous solution of 1.0 M $LiPF_6$ in ethylene carbonate (EC)/ diethyl carbonate (DEC) (1:1 by volume) was used as electrolyte. Cells were rested 24 hours after fabrication and cycled at a C-rate of C/10 and C/2 between [2.5, 4.2] V vs. Li/Li^+ for four cycles.

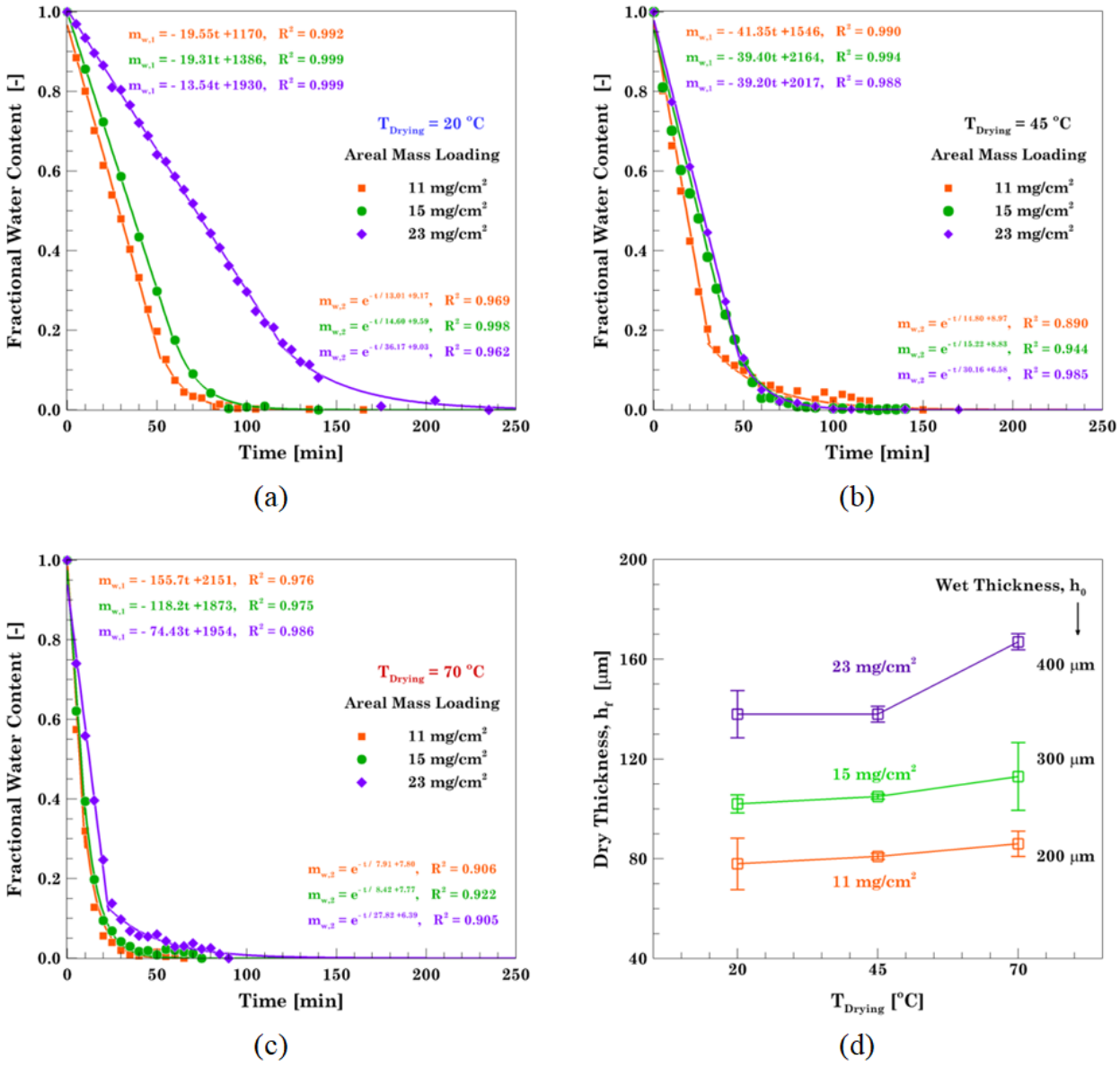

Fig. 3.3 Normalized water content profiles of drying electrodes of various thicknesses dried at (a) 20 °C, (b) 45 °C, and (c) 70 °C. Fitting functions for water content were normalized with their corresponding initial mass, for T_{Drying} = 20 °C: $m_{w,11}$ = 1209.8 mg, $m_{w,15}$ = 1387.8 mg, and $m_{w,23}$ = 1949.6 mg; for T_{Drying} = 45 °C, $m_{w,11}$ = 1591.9 mg, $m_{w,15}$ = 2209.0 mg, $m_{w,23}$ = 2109.9 mg; and for T_{Drying} = 70 °C, $m_{w,11}$ = 2153.5 mg, $m_{w,15}$ = 1921.1 mg, and $m_{w,23}$ = 2081.9 mg. Symbols and solid lines represent the actual mass measurements and the fitted curves, respectively. (d) Drying temperature effect on the final electrode thickness.

3.3 Results and Discussion

3.3.1 Evaporation Rate and Water Content Profiles of Drying Electrodes

The mass of each electrode was taken at regular time intervals (5 minutes) throughout the drying process. Mass measurements are shown in Fig. 3.3 (a-c), in the form of water content profiles, each of which had been normalized relative to the initial water mass of each electrode. Linear functions were fit to the evaporation phase of each water content profile, while exponential functions were fit to the capillary-driven phase. It should be noted that measurements inherently include some error – electrodes dried at room temperature were subject to temperature and air flow fluctuations. In addition, accurate mass data for electrodes dried at higher temperatures proved difficult due to rapidly changing coating mass. The electrode final thickness of the electrodes at the end of the drying process is shown in Fig. 3.3 (d). Formation of holes due to water vapor bubbling increases as the drying temperature increases. The presence of holes in the inner layers of the electrode makes the surface rough and increases its thickness.

During the drying process, water content quickly declined for electrodes dried at higher temperatures, and the rate of water loss was slower for thicker electrodes. Also, the first and second drying phases are observed in each water content profile. The first drying phase is characterized by a linear reduction of water mass as a constant evaporation rate drives the air-liquid interface and particles towards the substrate until vertical consolidation is no longer possible. Evaporation rates (E), averaged from the three electrodes, are shown in Fig. 3.4 (a) for each drying temperature. From the known initial and final film thicknesses, an estimation of the total time duration of the first drying phase (Δt_1) was calculated based on the evaporation rate obtained from curve fitting; results are shown in Fig. 3.4 (b). The time duration of the first drying phase agrees well with the experimental data in Fig. 3.3. Moreover, electrode thickness and drying time (during the period of constant evaporation) strongly correlate; doubling electrode thickness from 11 mg/cm^2 to 23 mg/cm^2 doubles the drying time, for all the electrodes.

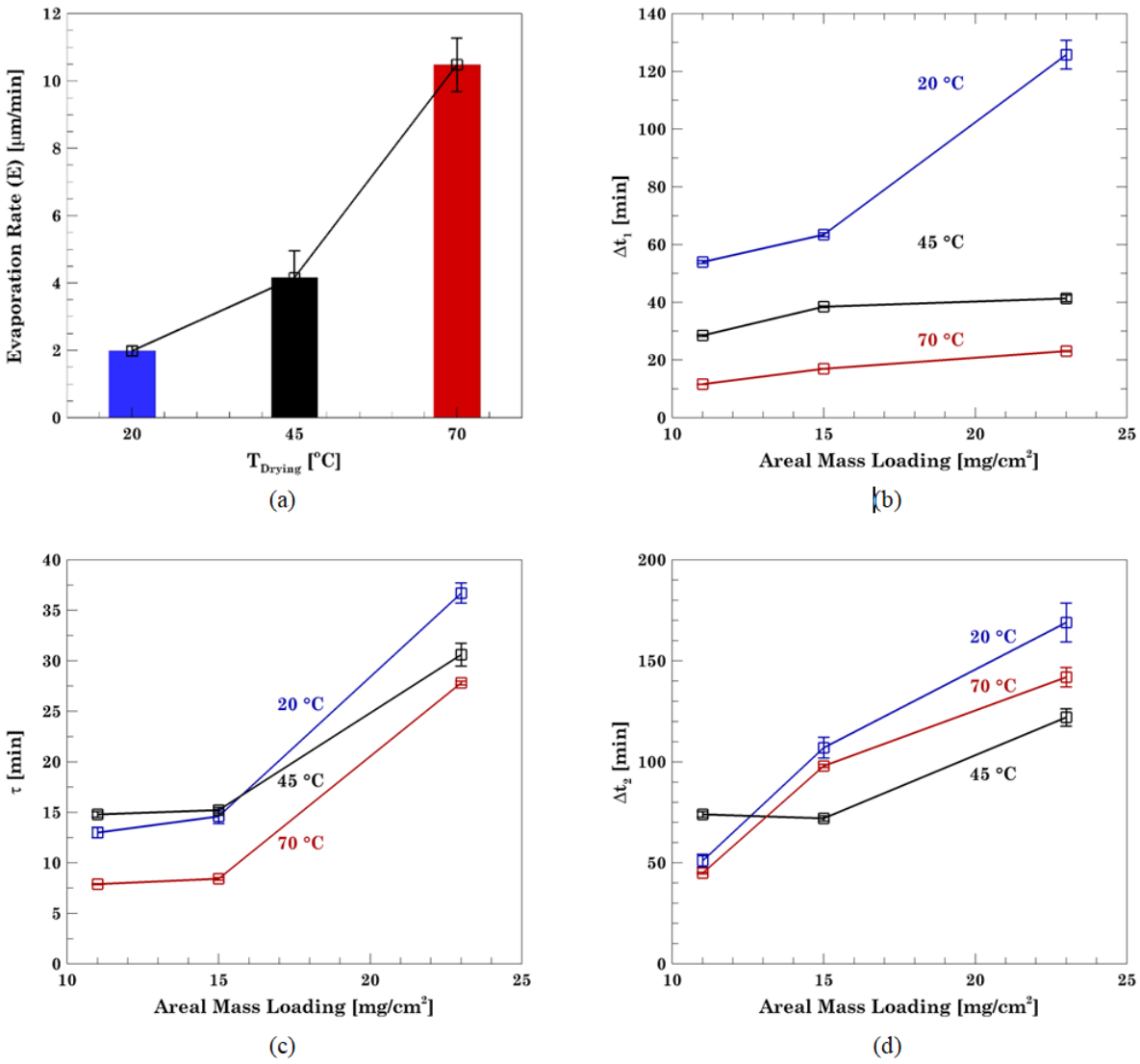

Fig. 3.4 (a) Average evaporation rate obtained from the linear functions fit to water content profiles. (b) Total time duration of the evaporation drying phase. (c) Time constants associated to capillary driven drying. (d) Total time duration of the capillarity drying driven phase.

The transition from the linear to the negative exponential decay indicates the point where the air-solvent interface reaches the packed slurry network. The transition time is shown in Fig. 3.4 (b). From hereafter the negative capillary pressure dominates the final powder packing and, hence, the cracks that form in the electrode. The time constant associated with the capillary-driven phase was derived from the exponential curve fitting and the results are shown in Fig. 3.4 (c). This parameter represents the drying time the electrode takes to reduce 36.8% of the initial water mass at the end of the evaporation phase. In an ideal case, the duration of the second drying phase will be at least

three times its corresponding time constant, $\Delta t_2 \approx 3\tau$. Fig. 3.4 (d) shows the actual duration of the second phase. The electrode was considered as dried when the mass measurements no longer exhibited any variation. At low temperature, the electrodes take a longer time to dry. The results for all the electrodes show a similar increasing trend as the mass loading increased; i.e., the thicker the electrode, the larger the remaining amount of water to be dried in the second phase. The slightly different trend exhibited by the electrodes dried at 45 ºC (see Fig. 3.4 (d)) arose from the fuzzy transition from the evaporation to the capillary-driven phase. The effect of the drying regimes on the final microstructures is subsequently analyzed in Fig. 3.5 and Fig. 3.6.

Table 3.1 Dimensions of electrode coatings used in image processing for crack quantification. Evaporation and sedimentation Peclet number characterizing the particles settlement during electrode processing drying

T_{Drying} [°C]	Wet Thickness (Solids+Solvent) h_0 [µm]	Dry Thickness (Solids) h_f [µm]	Dry Areal Mass Loading (Solids) [mg_{NMC}/cm^2]	Pe_{evap}		Pe_{sed}	
				NMC	CA + PSBR	NMC	CA + PSBR
20	200	78 ± 10.3	10.3 ± 0.5	0.177×10^6	0.646×10^3	4.304×10^4	7.570×10^{-6}
	300	102 ± 3.6	15.6 ± 0.7	0.300×10^6	1.092×10^3		
	400	138 ± 9.5	23.3 ± 2.0	0.354×10^6	1.290×10^3		
45	200	81 ± 1.2	10.9 ± 0.1	0.347×10^6	1.266×10^3	3.966×10^4	6.975×10^{-6}
	300	105 ± 1.0	16.0 ± 0.3	0.440×10^6	1.604×10^3		
	400	138 ± 3.2	22.0 ± 1.3	0.859×10^6	3.129×10^3		
70	200	86 ± 5.1	11.2 ± 2.0	0.812×10^6	2.956×10^3	3.677×10^4	6.467×10^{-6}
	300	113 ± 13.6	15.8 ± 1.4	1.179×10^6	4.293×10^3		
	400	167 ± 3.2	23.0 ± 2.2	1.812×10^6	6.599×10^3		

The NMC333 and Super C65 properties used in the Peclet numbers calculation Table 3.1 were obtained from the manufacturers. Average radius and bulk density are $R_{NMC} = 6\ \mu m$, $\rho_{s,NMC} = 4750\ kg/m^3$, for NMC, and $R_{C65} = 6\ \mu m$, $\rho_{s,C65} = 1950\ kg/m^3$ for the conductive additive [76]. Viscosity values for the aqueous electrode slurry with CMC and SBR for different shear rates has been reported in the range of 0.1 to 10 Pa·s [123]. For a 2 *wt*% CMC dissolved DI at a shear rate of 100 s^{-1}, the average solvent viscosity is 1 Pa·s [110]. Average slurry solvent density was calculated

from the dry powders and binder mass and the final volume. For the 90:5:5 *wt*% composition, the average density value was $\rho_f = 1478.6\ kg/m^3$.

Two-folding the initial thickness (200 to 400 μm), at a fixed temperature, doubles the evaporation strength. In the other hand, increasing the drying temperature, from 20 to 70 ^{o}C, slightly increases the diffusion effect by a factor of 1.146 ($Pe_{evap,\ 70}$ = (293.15 K/343.15 K) $Pe_{evap,\ 20}$ = 0.854 $Pe_{evap,\ 20}$) and simultaneously the evaporation rate (E). Thence, the drying temperature has a larger impact than the electrode thickness on the slurry particles rearrangement. In terms of the Pe_{sed} number for the NMC and secondary phase particles, the density difference also dominates the diffusion phenomenon for NMC but has a week effect on the secondary phase. Sedimentation effect introduces a negative additional effect to the non-uniform network distribution. Whereas, strong diffusion on the secondary phase particles lead to a uniform distribution throughout the electrode. Thus, strong evaporation and sedimentation and mainly weak diffusion are the main mechanisms behind the crack formation on thick electrodes at high temperatures.

3.3.2 Electrode Imaging and Crack Analysis

Once the electrodes were dried, the dry slurry thickness was measured with a coating thickness gauge (Elcometer) at multiple points throughout the electrode. The dry casted area was measured by tessellating the electrode into small square partitions and adding up their individual areas. While, the dry slurry mass was calculated by subtracting the substrate mass, measured prior casting, to the total dry electrode mass. Table 3.1 shows the initial wet and average dry thicknesses, as well as the areal mass loading of each aqueous electrode coating. The areal mass loading (11, 15, and 23 mg/cm^2), reported in Fig. 3.3, corresponds to the average areal mass loading of all electrodes dried at the three different temperatures with the same initial wet thickness. From hereafter, the convention to denote each of the electrodes will be in terms of this average mass loading.

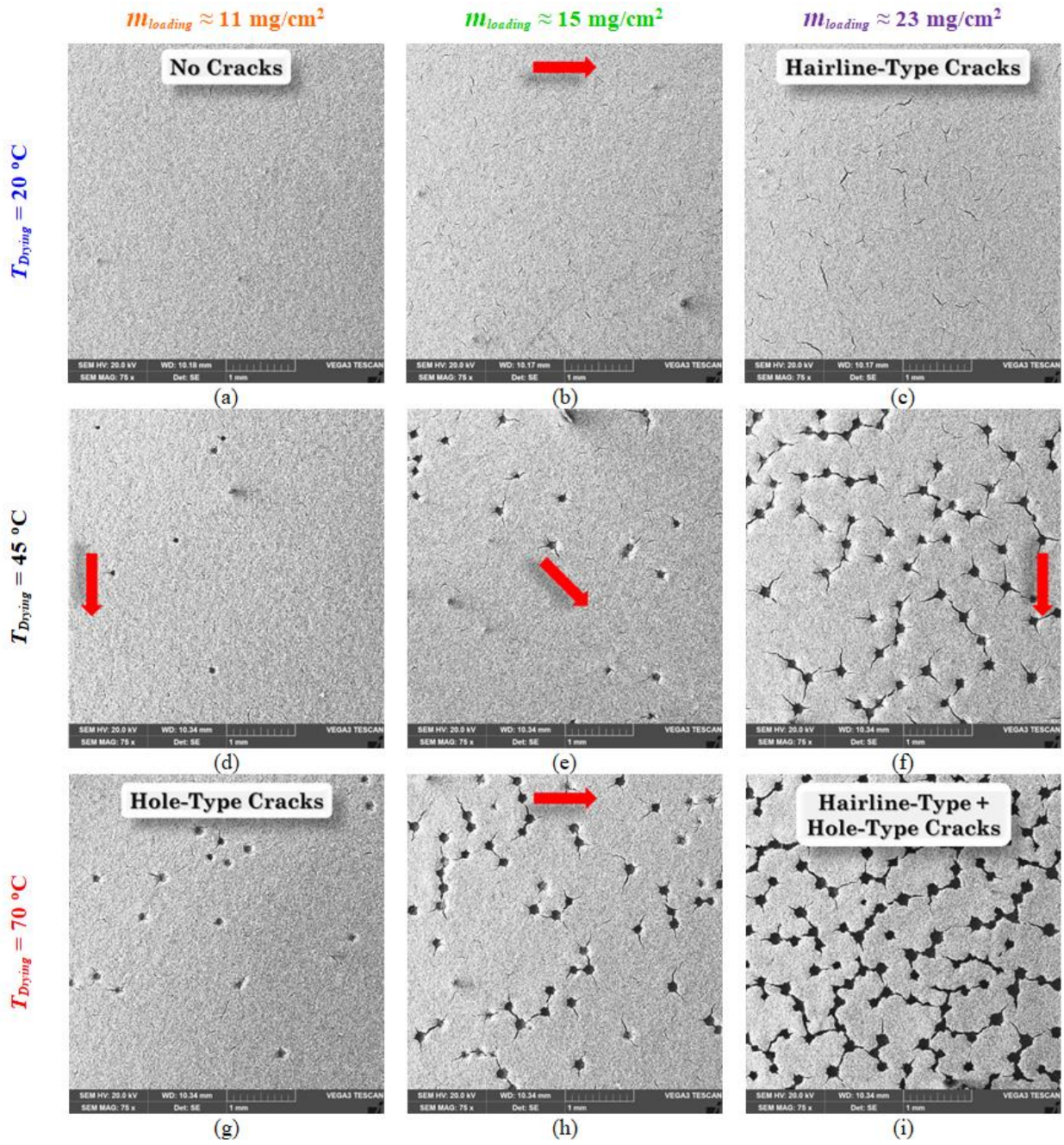

Fig. 3.5 Micrographs of pristine electrodes (75X magnification). Representative samples from electrodes dried at (a, b, c) 20 °C, (d, e, f) 45 °C; and (g, h, i) 70 °C, with areal mass loadings of 11, 15 and 23 mg/cm^2, respectively. The cracking effect increases as the drying temperature and the areal mass loading increases. Scale bar in all images is 1 mm.

The surface of each electrode, and subsequent crack formation analyzed by SEM at low magnification is shown in Fig. 3.5. The images provide clear qualitative evidence that the severity of cracking worsens with increasing areal mass loading, as well as increasing drying temperature.

The observed correlation between increasing mass loading and crack severity is in agreement with previous reports, though no such experimentally observed correlation with drying temperature has been reported in the literature [87]. Interestingly, holes are evident in electrodes dried at higher temperatures regardless of thickness, and the areal density of these holes increases with electrode thickness. On the contrary, electrodes dried at low temperature are free from any holes as shown in Fig. 3.5, suggesting an increase in drying temperature affects the evolution of the electrode microstructure in a detrimental way.

Even at this low magnification, the detailed crack pattern is easily observed. Hairline cracks can even be seen in the standard size electrode dried at 20 °C with a high mass loading. This observation disagrees with the well-established understanding that aqueous processed electrodes of standard thickness are crack-free [87, 124-126].

3.3.3 Image Processing

Image processing was performed on the SEM images shown in Fig. 3.5. The micrographs correspond to representative samples of each electrode. The final clean micrographs are used to quantify the crack severity, in terms of the crack length, the average crack width and the CIF. The crack length is the maximum distance between the boundary pixels from the crack. The average crack width is the total area to the crack length ratio, while, CIF is the ratio of white pixels to the total pixels in the image. For each loading mass and drying temperature, three different samples were analyzed and the average values for the CIF, the width and the length of the crack are shown in Fig. 3.6.

Except for Fig. 3.6 (b), the results reveal that a higher drying temperature leads to longer and wider cracks. Moreover, the distribution of crack lengths and widths widens as the drying temperature increases. In the case of the 23 mg/cm^2 electrode dried at 70 °C (see Fig. 3.6 (b)) only a subtle peak is evident in the crack distribution. The distribution of crack length and width likely widens for higher drying temperatures as a result of the holes observed in these electrodes. Holes were absent from electrode coatings dried at 20 °C; thus, the length and width of cracks were confined to a narrow distribution.

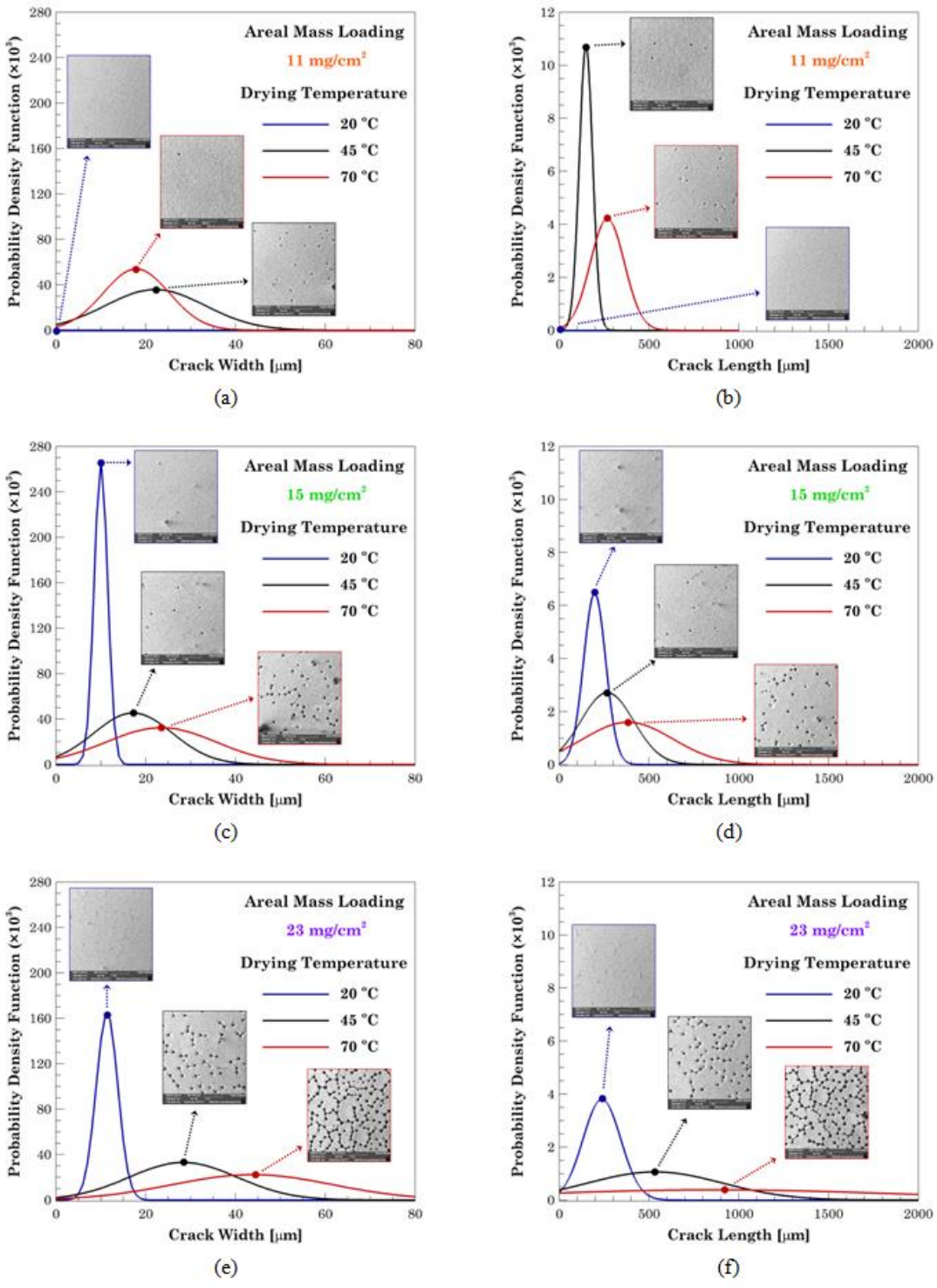

Fig. 3.6 Distribution of crack lengths and widths observed in aqueous electrode coatings with areal mass loadings of (a, b) 11 mg/cm^2, (c, d) 15 mg/cm^2, and (e, f) 23 mg/cm^2 dried at 20, 45, and 70 °C. All SEM images were taken at 75X magnification. Scale bar in all images is 1 mm.

Crack spacing, Fig. 3.7 (a), was calculated with the proportionality expression developed by Lee et al.[109] , $(y/X) \propto h_f^{0.8} R^{0.2} / E^{0.35}$ or $\lambda(y/X) = h_f^{0.8} R^{0.2} / E^{0.35}$, where λ is the proportionality constant. In this expression, there is a tradeoff between the physical aspects of the slurry and the thermodynamic properties from the solvent. If the mass loading increases, by thickening the electrodes, then the dried film height also increases and consequently, the crack spacing increases. The presence of no cracks on the 11 mg/cm^2 electrodes is reflected as an odd value at 20 ºC. On the other hand, as temperature increases, the evaporation rate also increases, see Fig. 3.4 (a), and the crack spacing, (y/X), decreases. The cracking spacing trend, Fig. 3.7 (a), along with the microscopic results, Fig. 3.5, support the initial hypothesis that cracking in thick aqueous electrodes becomes more severe when electrodes are dried at high temperatures.

One way to quantitatively prove the last statement is via the CIF of each electrode, Fig. 3.7 (b). There is a slight increase in the percentage of surface area covered by cracks for electrodes with areal mass loadings of 11 mg/cm^2 and 15 mg/cm^2, increasing from 0.00% to 0.62% and 0.31% to 3.30%, respectively. However, the CIF of thick electrodes (23 mg/cm^2) dramatically rises with increasing drying temperature – from 0.682% when dried at room temperature to 15.1% when dried at 70 °C.

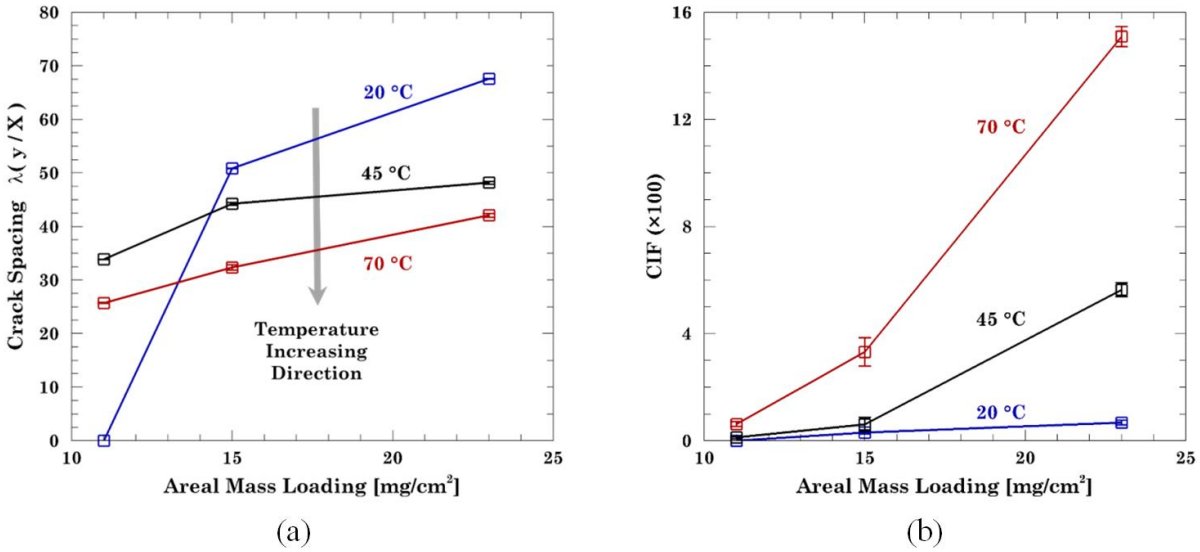

Fig. 3.7 (a) Crack spacing and (b) crack intensity factor for each electrode dried at various temperatures. CIF represents the fraction of the total surface area that is covered in cracks.

The worsening crack severity with increasing drying temperature can be attributed to the formation of holes, possible due to bubbling, during drying at high temperatures. Flaws, such as holes, are known to promote cracking and serve as nucleation sites for cracks in a thin film [127]. The process of crack formation initializes at the moment mounting capillary pressure overcomes the adhesion strength between the air-liquid interface and surface particles, and air invades the particle network. With air having penetrated the particle network, the film experiences in-plane capillary forces that propagate cracks. The adhesion strength between the air-liquid interface and surface particles is weakest at large pores, so cracks will nucleate at large pores first. Holes in the electrodes dried at elevated temperatures are extremely large pores relative to the close packed particle network, and thus serve as nucleation sites for cracking. Moreover, as the SEM images confirm in Fig. 3.5, the areal density of holes increases with increasing electrode thickness and drying temperature. As a result, holes promote severe crack formations that dominate the electrode surface area since cracks propagating from closely packed holes are more likely to intersect one another.

3.3.4 Electrochemical Performance

Fig. 3.8 shows the potential curves of each electrode cycled at a low (C/10) and medium (C/2) C-rates. As the mass loading increases (11 mg/cm^2 to 23 mg/cm^2), the maximum delivered reversible specific decreases regardless of drying temperature. Thus, the best electrochemical performance is obtained from the 11 mg/cm^2 electrode dried at 20 ^{o}C with a delivered specific capacity of 132 mA·h/g during the C/10 discharge, see Fig. 3.8 (a). Slow solvent evaporation and fast diffusion of the secondary phase leads to a uniform particle distribution, as shown in Fig. 3.5 (a-c), and increases the electronic conductivity of the porous electrode [86]. Performance for electrodes dried at 45 ^{o}C falls in between the ones for 20 ^{o}C and 70 ^{o}C with a C/10 discharge capacity in the range of 119~124 mA·h/g. At this drying temperature, the competition between the evaporation rate and the secondary phase diffusion initiates the development of small hairline- and hole-type cracks, Fig. 3.5 (d-e), worsening the electrochemical performance. The evaporation effect on the electrochemical performance becomes more evident on the 23 mg/cm^2 electrode dried at the same temperature, Fig. 3.5 (f). Conversely, for the same cycling rate, C/10, the worst electrochemical performance is obtained from the 23 g/cm^2 electrode dried at 70 ^{o}C with a delivered specific discharge capacity of 113 mA·h/g. The fast evaporation rate for the aqueous-based slurry induces an inhomogeneous distribution of the active particle and the secondary phase [86]. Thus, the active

material particle's agglomeration reduces the electrochemically active area. Whereas, the secondary phase agglomeration reduces the electronic conductivity of the porous electrode. Both effects hinder the utilization of the additional active material in thicker electrodes worsening their performance.

The two extreme performance conditions, for low and high drying temperatures, prove one significant aspect about high energy density Li-ion cells via electrodes thickening. Even if the active material capacity is high on thick electrodes, they also have low specific capacity because of the amount of inactive material. Thicker electrodes have longer diffusion paths for Li-ions in the electrolyte within the electrode [128], as well as longer migration pathways for electrons to reach the current collector. The mass transport limitation leads to underutilization of the NMC particles particularly near to the aluminum substrate. The appearance of cracks, associated with the aqueous electrode processing, increases the electrode reaction surface and the diffusion paths for Li-ions in the electrolyte; and reduces the kinetic overpotential. However, holes and hairline cracks also internally disconnect the secondary phase (SBR + Super C-65) microstructure and increase the charge transfer resistance transport in the solid phase.

Performance at low C-rates gives an insight into the ideal performance of the electrode. In a more realistic condition, faster charge/discharge rate (C/2) is necessary. Fig. 3.8 shows a comparison of the performance between the low and medium cycling rate. The discharge specific capacity for the 11 mg/cm^2 electrode dried at 20 ^{o}C dropped from 132 to 122 mA·h/g when the current was increased, i.e., there was a reduction of 7.5%, see Fig. 3.8 (a). Analogously for the 23 mg/cm^2 electrode dried at 70 ^{o}C, there is a drop on the delivered specific capacity from 106 to 77 mA·h/g, i.e., there was a reduction of 27.3%, see Fig. 3.8 (c). The performance decay analysis corresponds to a crack-free and crack-populated electrode. The rest of the drying-mass loading combinations lied in between the two extremes; see Fig. 3.8 (e-f). Presence of cracks, both hairline-type and hole-type, not only increase the bulk resistance due to a disrupted electronic flow between particles and current collector but also reduce the delivered capacity by the cell [129-132].

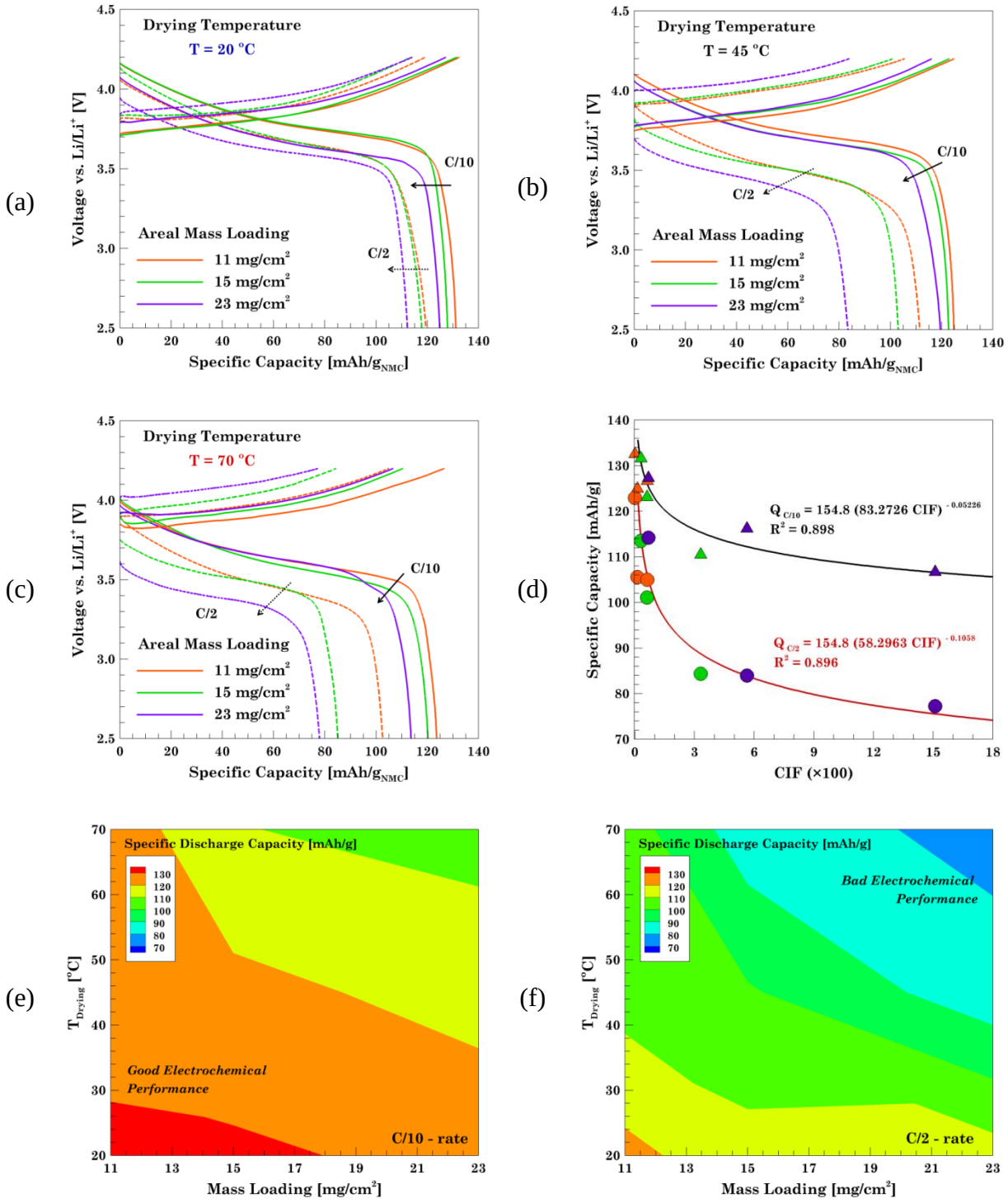

Fig. 3.8 Maximum reversible capacity as a function of the drying temperature: (a) T_{Drying} = 20 ^{o}C, (b) T_{Drying} = 45 ^{o}C, and (c) T_{Drying} = 70 ^{o}C. (d) Correlation between the electrochemical performance and electrode processing. Effect of mass loading and drying temperature on the maximum reversible capacity for (e) C10- and (f) C/2-rate. According to the electrochemical results, an increment on the electrodes thickness or the cycling rate will hinder the performance due to transport limitations on electrolyte and solid phase.

Finally, Fig. 3.8 (d) shows a strong correlation between the aqueous electrode processing of thick electrodes, represented by the CIF, and the electrochemical performance, represented by the specific discharge capacity. A power function, $Q = Q_0 \left(c_1 \cdot CIF \right)^{c_2}$, is used to correlate the maximum discharge capacity from Fig. 3.8 (a-c) and the corresponding CIF. In this expression, Q_0 represents the theoretical capacity of the NMC active material and c_1 and c_2 are two constants that depend on the mass loading and the cycling rate. For crack-free electrodes, i.e., CIF $\approx$ 0, the expected discharge capacity during the initial cycles will be close to the theoretical capacity. According to this relationship, an electrode with a high CIF number will not only have a large presence of cracks but it will also have a poor electrochemical performance even from the first cycles. Thus, the best electrochemical performance takes place at low mass loading (thin) electrodes dried at low temperature. The delivered specific capacity significantly decreases as the drying temperature and mass loading increases.

4. CELL LEVEL DEGRADATION: AGING TEST IN CYLINDRICAL CELLS

Relevant Publications and/or Working Papers

1. D. Juarez-Robles, J. Jeevarajan, P.P. Mukherjee, 2019, *Degradation-Safety Analytics (DSA) in Li-ion Cells. Part 1. Aging Effect*, working paper

Aging of Li-ion cell components occurs in a natural way due to continuous cycling. Improper handling and operation may lead the cell to failure and possibly going into thermal runaway. This condition represents a threat to safety not only for the cell integrity but also for the user health. Failure event can occur not only in brand new cells but also in aged cells. Current degradation studies focus either on the long-term aging degradation mechanisms or on fresh new cells' abuse test.

In this work, the interplay between aging and two abuse conditions, overcharge and externally short, is investigated in fresh and aged cylindrical cells at three different levels of degradation and two operating voltage windows, E_N = [2.7, 4.2] V and E_R = [2.9, 4.0] V. Experimental results will give insights on the potential hazards that an aged cell represents when it undergoes into a failure and how drastic it is in comparison with a fresh one. The aim is accomplished via a comprehensive and controlled lab test approach in order to get insights on the electrochemical, thermal and morphological behavior. Part I of the work investigates only the aging degradation and set a baseline for the combined degradation scenarios.

According to the aging results, cycle life can be two-folded by reducing 200 mV the voltage window at the expense of having a 20% reduction on capacity utilization. Differential voltage and differential temperature of the experimental data revealed a SOC dependence of the internal resistance and the heat generation, and their linkage with the graphite phase transition. Post-mortem analysis evidenced that Li-ion inventory reduction due to SEI formation; and electrochemical deactivation of cathode due to delamination and fracture, are the main aging degradation mechanisms behind the cell capacity loss.

4.1 Introduction

The success of portable electronics, wireless tools, and hybrid and electrical vehicles depends largely on their energy storage system [133]. Among all the electrochemical energy storage devices, lithium-ion batteries (LIBs) currently have the best properties to fulfill the wide range of requirements specific for these applications – high energy density, long lifetime, good power capabilities and also relatively low cost [1, 19]. The most beneficial combination of all these properties is the one which results in a cell with light weight, small volume, high voltage and high capacity [134]. Regardless of their superior performance over other energy storage systems, LIBs are still perceived as a threat mainly due to their reactive, flammable and volatile components [35, 135].

4.1.1 Safety

In recent years, safety issues associated with LIBs had been in the eye of the storm, mostly due to highly publicized events where Li-ion cells catching fire were involved [25]. One of the first incidents occurred in 1999 in the LAX airport where one pallet of Sanyo lithium-ion cells was mishandled by an employee. LIBs were dislodged from their packing and later caught fire [135]. As a result, the Federal Aviation Administration (FAA) prohibited the transportation of primary LIBs on commercial aircraft. In 2010, the Boeing 747 cargo plane, departing as UPS Airlines Flight 6, crashed due to the autoignition of a lithium-ion cells cargo pellet [26]. According to the FAA, up to date, there had been 206 airport incidents involving lithium batteries since March 1991 [136]. Safety concerns become more significant when they involved devices used in daily life. In September 2016, Samsung was forced to recall nearly 1 million Galaxy Note 7 phones after numerous reports of the devices going into thermal runaway during charging or use [27]. It was later revealed that the issue stemmed from two independent cell design flaws by the two different manufacturers, causing them to short circuit. In February 2017, a Dell Inspiron laptop powered by a LIB violently combusted while charging and proceeded to burst into flames three more times after being unplugged [28]. These examples illuminate the fragility of the Li-ion chemistry and demonstrate the necessity of understanding the response of Li-ion cells to abnormal conditions [30, 137].

4.1.2 LIBs and Degradation Mechanisms

Li-ion cells are a member of the secondary (rechargeable) battery type on which lithium ions have the ability to move from anode to cathode and vice versa depending on the discharge or charge

process, respectively. In order to obtain a reversible electrochemical system, intercalation reaction occurs. Intercalation reactions involve the reversible insertion and extraction of a Li-ion into a crystal lattice with minimal alterations to the host crystal [10]. While the electrolyte serves as the Li-ions transportation medium. To preserve electrical neutrality, during the charging process, for every electron that moves through the external pathway from the cathode to anode, a Li-ion deintercalates from the cathode and internally travels in the same direction as the electron until it eventually intercalates in the anode. As a consequence of the electrochemical processes, slight changes (degradation) on the electrode microstructure and composition are induced in a progressive and unpredictable way. The capacity reduction of the cell associated to those changes is an intrinsic degradation mechanism that cannot be avoided but can be partially controlled based on the storage [138] (calendaring) and cycling (aging) conditions [139].

4.1.3 Calendaring Aging

Calendar life refers to all aging processes leading to degradation of Li-ion cells independently of the charge/discharge history [140-141]. In contrast to the cycling life, where mechanical strain in the electrode active materials [65] or lithium plating [59, 142] can cause severe degradation, the predominant mechanism of calendaring is the evolution of passivating layers at the electrode–electrolyte interfaces. The formation, growth, or reconstruction of passivation layers consumes cyclable lithium as a result of electrolyte decomposition, i.e., reduction at the anode and oxidation at the cathode interface [143]. Furthermore, the growth of the passivation layer at the anode, which is usually referred to as the Solid Electrolyte Interphase (SEI), is said to be additionally catalyzed by dissolved transition-metal ions from the cathode, which are in turn reduced again to metals at the anode [144-145]. State of Charge (SOC) [146], storage temperature, and the extent of the storing time are the main factors driven the calendar aging degradation. Grolleau et al. found that the storage temperature has a stronger impact on the degradation rate and it aggravates if cells are stored at higher SOC [147], favoring the passivating layer growth [143].

4.1.4 Cycling Aging

Aging or cycling life refers to all the degradation processes associated with the charge and discharge processes. Every time a Li-ion cell is cycled, its capacity reduces mostly in an imperceptible way. However, in the long-term cycling, the cell loses a significant amount of its initial capacity [138]. The rate of capacity loss depends upon multiple factors like operating

temperature [148-150], cycling protocol [151], C-rate [152], and the charge/discharge cut-off voltages [153-154]. Determining the actual state of health of the cells after cycling is essential for recycling or repurposing them in secondary-use applications [3, 155].

Waldmann et al. studied the aging behavior of graphite/NMC+LMO cells in the operating temperature range of -20 to 70 ºC. Cells exhibited a minimum degradation rate at 25 ºC and it aggravated for higher and lower operating temperatures [150]. At low temperatures, aging is dominated by lithium plating, whereas, at high temperatures aging is dominated by cathode active material degradation and a repeated passivating layer growth on the anode one [148, 156].
Keith et al. experimentally analyzed multiple charging protocols (e.g., constant current – constant voltage, multistage constant-current, pulse charging, and a voltage-based trajectory) and their impact on the cycle life [157]. An ideal charging protocol must provide good capacity utilization with a minimal charging time while still holding a long cycle life. Among all the tunable parameters (C-rates or currents, voltage limits, number of stages and length of the pulses) in the protocol, the charging current was found to be the most significant one. Low current increases not only the capacity utilization but also the charging time. Fast charging can be achieved at high currents but it deteriorates the cycle life mainly due to the presence of lithium plating.

4.1.5 Operating Voltage Window

LIBs have a limited range of stability in terms of voltage and temperature [31]. Every combination of anode, cathode, separator and electrolyte materials define a safe operating voltage window (VW). The optimal window represents the voltage range on which the cell delivers the maximum capacity without compromising its cycle life. Extending the voltage window, by overcharging [154] or overdischarging [153, 158] the cell increases the capacity delivered but reduces the cycle life. Although, there is an extensive analysis of these two abuse scenarios, there are few studies of the cycle life of Li-ion cells in a reduced voltage window.

4.1.6 Destructive Physical Analysis

Recent studies on Li-ion cells performance focus on predicting their capacity fade [159], state of health [160] and cycle life. From modeling [161] to experiments, multiple degradation mechanisms like SEI formation, lithium plating, anode, and cathode are associated to the poor cycle life and in some rare occasions, actual evidence of those phenomena are presented. A straightforward solution is to

physically open the cell and extract the components for further analysis. If this solution is not feasible, e.g., in a diagnostic test for secondary-use application, then a nondestructive technique is a better option. Electrochemical impedance spectroscopy (EIS) [162], X-ray computed tomography (XCT) [163], and neutron scattering [164] are noninvasive techniques that allow diagnosing, visualizing, and detecting, respectively, interior features from the cell without disrupting it. Even so, these noninvasive, heuristic and inferential techniques do not provide the actual degradation imposed on the cell components affecting the actual cell performance and their implications on the safety aspects.

The goal of this work is to investigate the interplay between aging, operating voltage window, and abuse tests (overcharge and external short) in Li-ion cells and their safety implications. Part I focuses only on the aging effects in cylindrical Li-ion commercial cells. The objective is to characterize the changes occurring to the cells electrochemical properties as well as its morphology as the cells aged. The aim is accomplished via charge/discharge cycling under two different voltage windows. The cells are aged up to 10, 15 and 20% capacity fade (CF). The morphological changes are studied by conducting a destructive physical analysis (DPA) of the cell components and analyzing them via a micrography (scanning electron microscopy, SEM) and spectroscopy (energy-dispersive X-ray spectroscopy, EDS) techniques. Part II analyses the interaction between aging and overcharge abuse test. Part III analyses the interaction between aging and external short abuse test. Cycling results for the aged cells used in Part II and III are presented in the current work.

4.2 Experimental

In this study, NCR18650B Panasonic cells, considered the state of art for cylindrical cells [165], are used to conduct this study. According to the Material Safety Data Sheet (MSDS), the cell nominal voltage is 3.6 V and the recommended safe operating voltage window is 2.7 to 4.2 V. The rated capacity is 3.4 Ah (minimum capacity of 3.2 Ah) when the cell is discharged to 2.7 V using a constant current (CC) protocol and then charged back to 4.2 V using a constant current – constant voltage (CCCV) protocol with a cutoff current of 65 mA [166].

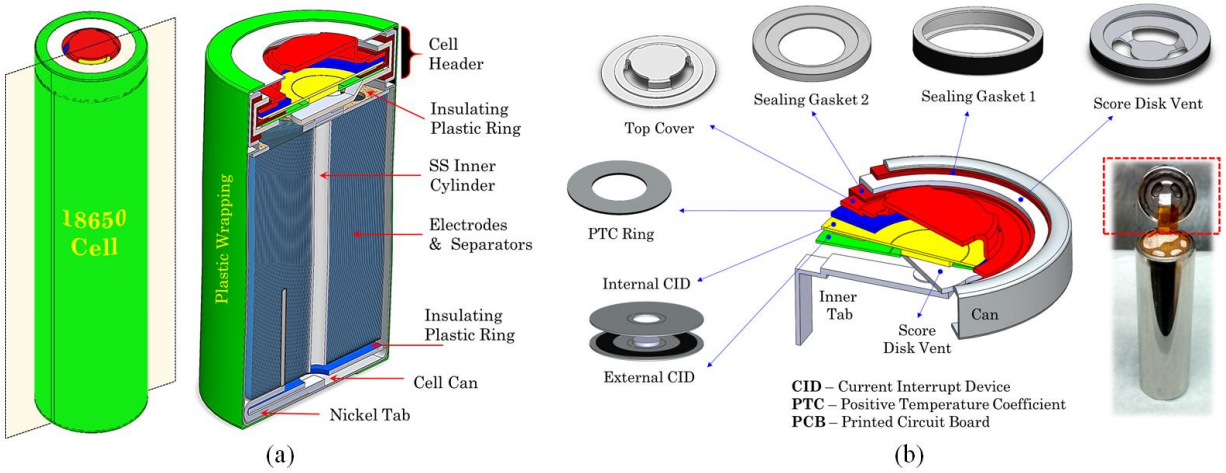

Fig. 4.1 Schematic of a conventional cylindrical 18650 Li-ion cell with single electrodes for anode and cathode. (a) Cross-section area of the cell along the axial direction. (b) Protections embedded in the cell header.

Prior to any aging or abuse test, it is necessary to discern the pristine condition of the cell components. Thus, the internal structure of a pristine cell is shown in Fig. 4.1 (a). The top terminal corresponds to the positive electrode (nickel cobalt aluminum oxide, $LiNi_{0.8}Co_{0.15}Al_{0.05}O_2$, NCA) and the bottom part to the negative one (graphite, C). The cathode terminal is next to the cell header. The anode terminal is connected internally to the electrodes by a nickel tab. Electrodes and separators are assembled in a jelly roll around the stainless steel mandrel. There are two plastic protectors at the top and bottom of the jelly roll. The blue one (bottom) prevents contact between the positive electrode and the can (negative electrode). While the brown one (top) prevents direct contact between the negative electrode and the internal nickel tab. In the cell header, there is a protection for high currents (PTC, positive temperature coefficient material) and high internal pressure (CID, current interrupt device). No PCB (protective circuit board) is included within the cell, Fig. 4.1 (b). The cell header is internally connected to the jelly roll via a nickel tab welded to the score disk vent.

4.2.1 Conditioning Test Protocol

The cell status is monitored using a conditioning test protocol. Cells are cycled 3 times between 2.7 and 4.2 V at 1 C-rate. The charging process is done with a CCCV protocol and a cutoff current of 50 mA. The discharging process is done using a CC protocol. The internal resistance is

calculated at 50% of the depth of discharge (DOD) by applying a 1.5 C (5.1 A) pulse during 100 ms during discharge. The typical response of the commercial Li-ion cell to the conditioning test is shown in Fig. 4.2 (a). It can be observed the current pulse excitation applied during the second cycle with its corresponding voltage response. By using the open-circuit voltage (OCV) from the resting process and the voltage response during the pulse period, see Fig. 4.2 (b), the internal resistance is calculated. The average internal resistance value at 50% SOC, of the fresh cells (25 or more) is ~44 mΩ.

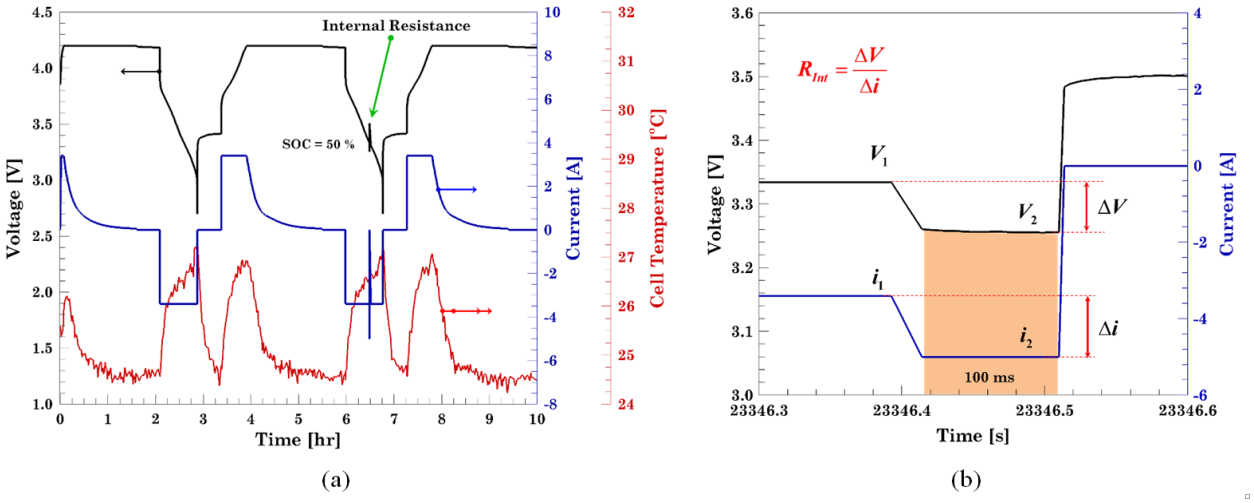

Fig. 4.2 Representative results obtained from the conditioning test conducted in a fresh cell. (a) Voltage and current response. (b) Internal resistance calculation by applying Ohm's law, $R = \Delta V / \Delta i$, during the current pulse response.

4.2.2 Cycling Protocol

Based on the recommended operating conditions given by the manufacturer two different voltage ranges are selected. The 'normal' operating window is defined in the range of [2.7, 4.2] V. This range is shortened 200 mV on each of the cutoff voltages. Thus, a 'reduced' operating window is defined in the range of [2.9, 4.0] V. Cells cycled in the normal and reduced voltage window are denoted from hereafter as 'N' and 'R', respectively. Cycling is done using a C/2 current for charging and discharging. Charge process to the corresponding upper voltage is done with a CCCV protocol and a 50 mA cutoff current. Discharge process to the corresponding lower voltage is done using a CC protocol. Cycling test is conducted at ambient temperature (~23 ^{o}C). The stopping criterion for cycling is based on the capacity fading. For each cell, the capacity fade is defined with respect to the capacity obtained during the first complete discharge. Prior to and after the cycling test, each cell is electrochemically characterized using the conditioning test early described.

Conditioning and cycling tests are conducted in a battery tester (Arbin system, BT2543-5V-5A-16). The skin cell temperature is measured, during the whole cycling test, by mean of a J-thermocouple (Omega, TJ72-CPSS-116U-6) tapped along to the axial direction.

4.3 Results and Discussion

A typical cell response to the conditioning test, also known as formation cycle, is shown in Fig. 4.2 (a). In a fresh new cell, lithium is stored in two main components, the electrolyte, and cathode. In the cathode material, intercalated lithium can be found in the lattice sites. While, lithium ions in the electrolyte are provided by the salts ($LiPF_6$, $LiBF_4$, $LiAsF_6$) dissolved in the solvent, usually carbonates. In a pristine condition, graphite stores no lithium. Aurbach et al. demonstrated that in the presence of organic solvents, lithium and graphite are thermodynamically unstable [167]. The side reactions between lithium, more specifically lithiated graphite and the electrolyte solution lead to the formation of the SEI passivating layer. The conditioning test has two purposes: (a) establishing the actual cell capacity, and (b) allowing the cell to form and steady chemical SEI layer. Even though cells are fabricated in a similar fashion, there still exists a cell to cell variation that must be taken into account to define the capacity fade in the cell during the aging process. Meanwhile, SEI formation is a necessary evil that prevents a continuous exfoliation of the active material and electrolyte decomposition [168].

4.3.1 Cycling

Representative voltage, current and skin temperature response for the cycling test during the first 40 hours is shown in Fig. 4.3 (a) and (c) for the normal and reduced voltage window, respectively. The percentage of capacity fade is defined in terms of the maximum discharge capacity during cycling that typically occurs during the second full cycle. The capacity values during the first cycle are typically discarded since the initial SOC at the beginning of the test may vary from cell to cell. The initial capacity for all the cells is listed in Table 4.1 and Table 4.2. Fig. 4.3 also shows one current pulse applied after the cell is being discharged to 50% of the discharge capacity obtained during the conditioning test. Fixing the discharge capacity percentage is the most objective way to compare the cells from both the normal and reduced voltage. Fig. 4.3 (a) and (c) shows that shrinking the voltage window not only reduces the charge and discharge time but also the capacity utilization from the cell. Meanwhile, Fig. 4.3 (b) and (d) shows the charge/discharge profiles at 5

different levels of capacity fade and the cycle number when they take place. Interestingly, the reduction of the delivered capacity from the cells cycled in the reduced VW comes along with an extension of the cycle life. In the end, it is a tradeoff between capacity utilization and cycle life. Reducing the voltage window 200 mV above and below the recommended cutoff voltages extends the cycle life almost twice. Another subtle detail shown in the voltage profiles, during the internal resistance measurement, is the voltage response.

The cell cycled under the normal VW exhibits a large voltage change in comparison to the reduced one. Since ΔV is proportional to the cell internal resistance, and internal resistance has a strong and direct relation with the cell degradation, this means that the cell cycled in the normal VW degrades faster than the reduced one. Cells degradation rates and internal resistance evolution is thoroughly discussed later.

Table 4.1 Cycle life summary for the cells aged in the normal voltage window, E_N = [2.7, 4.2] V.

Cell ID	Number of Cycles	Aging Test Time [Days]	Initial / Final Capacity [Ah]	Final / Goal Capacity Fade	Safety Test
$N_{10}NA_7$	**174**	36.83	3.032 / 2.710	**10.59** % / 10 %	No Abuse
$N_{15}NA_{10}$	**222**	54.18	3.228 / 2.728	**15.49** % / 15 %	No Abuse
$N_{20}NA_5$	**269**	56.60	3.243 / 2.590	**22.97** % / 20 %	No Abuse
$N_{10}OV_8$	**201**	47.22	3.129 / 2.765	**11.63** % / 10 %	Overcharge
$N_{15}OV_3$	**199**	48.21	3.192 / 2.700	**15.41** % / 15 %	Overcharge
$N_{20}OV_1$	**300**	89.94	3.138 / 2.499	**20.36** % / 20 %	Overcharge
$N_{10}EX_9$	**204**	47.22	3.137 / 2.803	**10.64** % / 10 %	External Short
$N_{15}EX_4$	**234**	56.08	3.204 / 2.724	**18.25** % / 15 %	External Short
$N_{20}EX_2$	**305**	89.94	3.227 / 2.469	**23.48** % / 20 %	External Short

Table 4.1 and Table 4.2 summarize the final status of all cells at the end of the cycling test. For each voltage window, three capacity fading percentages are selected: 10, 15, and 20%. For each of the CF percentages, one safety test: overcharge (OV) and external short (EX), is conducted. The cells labeled as NA are not subjected to any abuse test after being aged. Thus, a cell with a tagged as N_XOV_Y indicates that the cell Y was cycled under the normal voltage window until its capacity fade X%. After that, the cell was subjected to an overcharge test. Electrochemical results for all the 18 aged cells listed in Table 4.1 and Table 4.2 are presented in Part I of this article. However,

not all the DPA results are included here. Part I only accounts for the pure aging effect, thence, DPA results for only the 6 cells tagged as $N_X\,NA_Y$ and $R_X\,NA_Y$ are presented here. The DPA results for the overcharged (6 cells, $N_X\,OV_Y$ and $R_X\,OV_Y$) and externally shorted (6 cells, $N_X\,EX_Y$ and $R_X\,EX_Y$,) cells at the end of the cycle are presented in the Part II and Part III, respectively.

Table 4.2 Cycle life summary for the cells aged in the reduced voltage window, E_R = [2.9, 4.0] V.

Cell ID	Number of Cycles	Aging Test Time [Days]	Initial / Final Capacity [Ah]	% Capacity Fading [Ah]	Safety Test
$R_{10}\,NA_{11}$	**454**	78.76	2.522 / 2.218	**12.05 %** / 10 %	No Abuse
$R_{15}\,NA_{10}$	**616**	105.53	2.618 / 2.208	**15.65 %** / 15 %	No Abuse
$R_{20}\,NA_{7}$	**799**	142.37	2.570 / 2.055	**20.01 %** / 20 %	No Abuse
$R_{10}\,OV_{5}$	**267**	50.50	2.562 / 2.304	**10.07 %** / 10 %	Overcharge
$R_{15}\,OV_{3}$	**651**	115.95	2.567 / 2.175	**15.26 %** / 15 %	Overcharge
$R_{20}\,OV_{1}$	**787**	143.56	2.565 / 2.046	**20.22 %** / 20 %	Overcharge
$R_{10}\,EX_{6}$	**324**	60.04	2.553 / 2.291	**10.26 %** / 10 %	External Short
$R_{15}\,EX_{4}$	**647**	115.95	2.555 / 2.159	**15.50 %** / 15 %	External Short
$R_{20}\,EX_{2}$	**785**	143.05	2.567 / 2.049	**20.19 %** / 20 %	External short

The initial capacity of the cells reveals minor differences from one cell to another even when they come from the same batch. Cells are acquired from a reputable vendor, thus, arguments related to defective cells can be discarded. The fact that there are three cells destined to each of the CF percentages gives a broad spectrum in terms of the minimum and the maximum number of cycles that the cell can be used. Thus, for the normal VW, it takes at least 174 cycles until the cell capacity fades more than 10.59 %. The cell can be cycled almost 300 times until its discharge capacity drops below 20 % the initial capacity. On the other hand, for the reduced VW, it is necessary to cycle the cell 267 times to achieve 10.07 % of capacity fade. Whereas, it takes 785 cycles to get a 20% capacity fade. To put it in terms of real operating conditions, cells aged under the normal VW can be continuously cycled for almost ~90 days delivering ~3.2 Ah, at the beginning, and 2.4 Ah, at the end of its cycle life. Whereas, a cell aged under the reduced VW can be continuously cycled for almost ~143 days delivering ~2.5 Ah, at the beginning, and 2.0 Ah, at the end of its cycle life. This means the cycle life can be extended by 50 percent if the capacity utilization (associated with the VW reduction) is reduced by 20%.

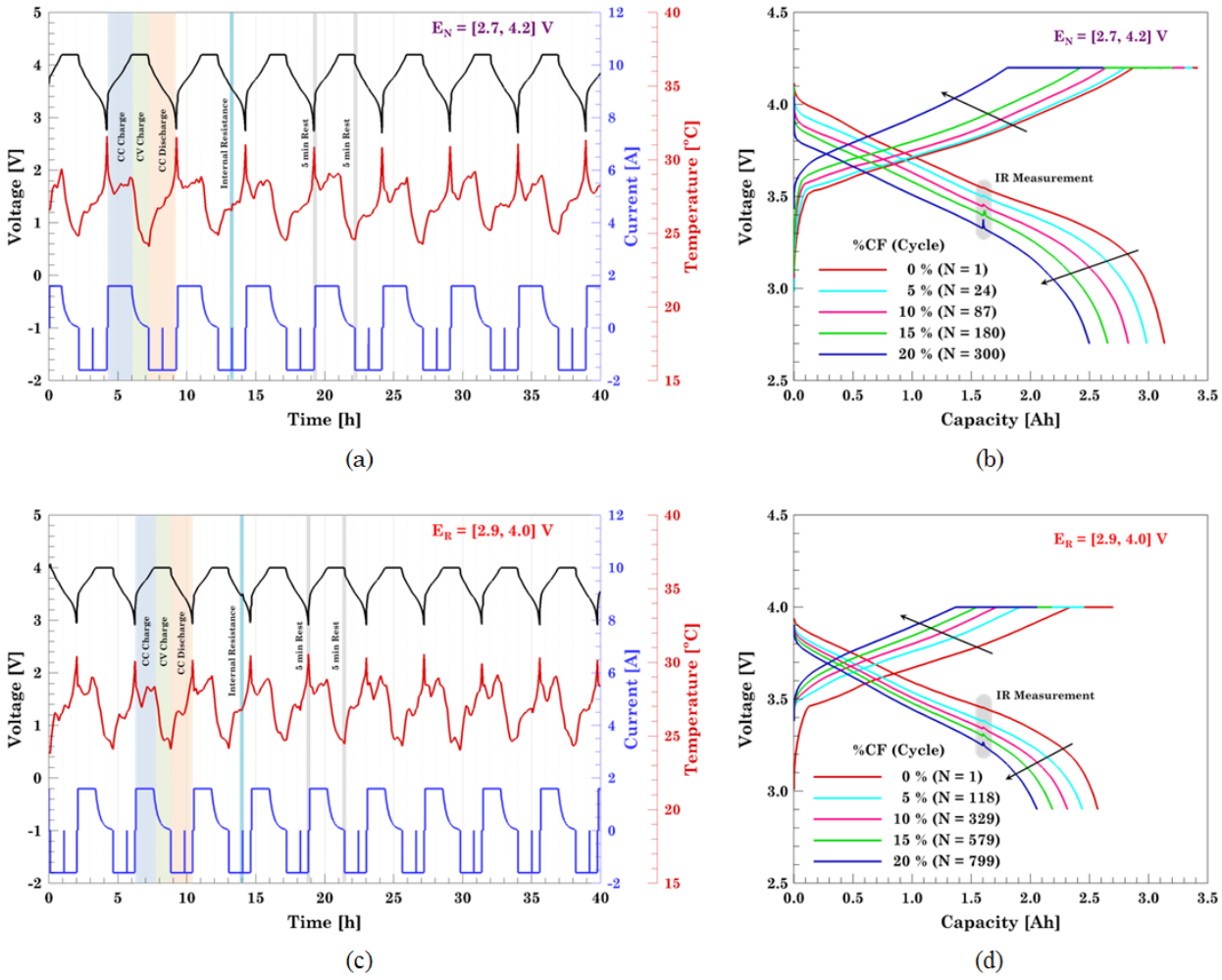

Fig. 4.3 Electrochemical performance results for the aging test under the two voltage windows. (a-b) Comparison of the first 40 hours for two representative cells cycled under the normal (cell $N_{20}OV_1$) and reduced ($R_{20}NA_1$) voltage window. (c-d) Charge/discharge voltage profile evolution as the cell cycling life diminishes 20% with respect to their corresponding initial discharge capacity.

Differential voltage plots, shown in Fig. 4.4, are derived from the CC charge/discharge profiles via a numerical differentiation. Data noise is removed by mathematical filtering to enhance the peaks from the dV/dQ plots. Multiple interpretations can be given to the differential voltage plots when combined with the respective differential analysis of the anode and cathode potentials. They can be used to detect the phase transitions [169] and the active mass evolution of the individual electrodes [170] with respect to the capacity. A different interpretation is given to the full cell differential voltage. Considering the constant current curves, $I = dQ/dt$, where I is the applied current, Q is the capacity, and t is the charge and discharge time. Also, the cell internal resistance

relates to the cell overpotential, η, by $\eta = IR_{Int}$. And, the full cell voltage can be expressed as $V = \eta + OCV$. Combining all the expressions, the differential voltage is deconvoluted in two contributions:

$$\frac{dV}{dQ} = \frac{d\left(OCV\right)}{dQ} + \frac{dR_{Int}}{dt} \qquad \text{Eq. 4.1}$$

The first term is inherent to the thermodynamic equilibrium of the cell and the second accounts for the change in the internal resistance. The first term mainly depends on the SOC and the operating temperature and it can be considered as constant. The second term is the relevant one for this work since it relates to cell degradation. The slippage voltage shown in Fig. 4.4, represented by the shift of the two main peaks, directly relates to the aging degradation. The two peaks represent mainly the phase transition for the graphite electrode [169]. Electrodes degradation induces an increment in the transport resistance in the solid phase. The large overpotential accelerates the phase transition at an early SOC, shifting the peaks (right to left) in the dV/dQ plots. During charge, no evident trend is found for the transition from Li_xC_{32} to Li_xC_{12} [171]. However, as the capacity and the SOC increases, the graphite phase transition from Li_xC_{12} to Li_xC_6 is more evident. The effect of the voltage window is reflected in the number of peaks, i.e., in the number of graphite phases and transitions among them. Shrinking the voltage window reduces the graphite phases present during cycling.

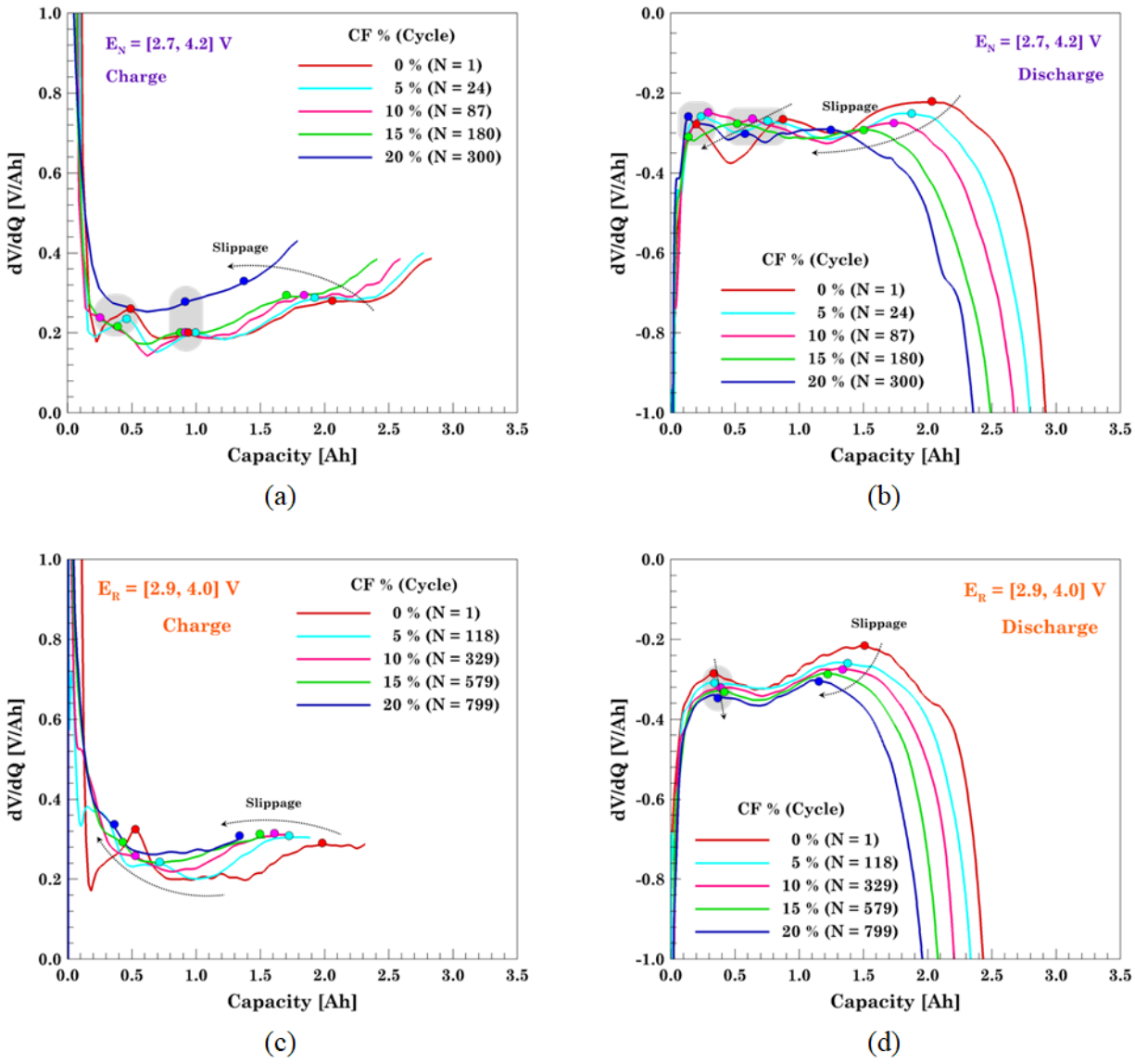

Fig. 4.4 (a-d) Differential voltage analysis of charge and discharge profiles for cells $N_{20}OV_1$ and $R_{20}NA_1$ cycled under the normal and reduced voltage window, respectively.

The effect on the cycle life of the voltage window is more evident in the capacity retention plot shown in Fig. 4.5. The discharge capacity for the 18 cells is shown in Fig. 4.5 (a). Cells cycled in the normal VW clearly provide a large capacity in comparison with the ones cycled in the reduced VW one. The discharge capacity gets a ~600 mAh reduction when the VW is shrank 200 mV above and below the cutoff voltages. The drawback of the increased capacity is the number of times that the cell can be cycled before its capacity fades more than 20% with respect to the initial capacity. The capacity retention plots, Fig. 4.5 (b), the normalized version of the discharge capacity

plots, give a more objective comparison of the cycle life. These plots reaffirm the fact that the cell cycle life can be considerably extended by reducing the capacity utilization from the cells. Thus, the mean number of cycles for the reduced VW two-folds the number for the normal one as shown in Fig. 4.5 (d).

Besides the capacity retention, the internal resistance is another way to estimate the state of health of the cells. There is a common consensus that the internal resistance increases as the cell starts degrading. The remaining question is how fast the cell degrades or equivalently, at which rate the internal resistance increases. Recent studies by Mandli et al. have proposed a linear increasing trend for this rate [172]. Present experimental results show a slightly different story, the internal resistance increases faster at the beginning of the aging test, then it slows down, and near to 80% of the capacity retention, it starts increasing again. At the beginning of the aging test, a continuous formation of the SEI dominates cell degradation. Once the passivating layer becomes quasi-stable on the graphite electrode, the non-uniform intercalation/deintercalation dominates the degradation phenomena. Non-uniform lithiation/delithiation process induces stress on both active materials, disrupts the electrode morphology, increases the transport resistance and consequently the cell internal resistance [64].

In order to determine the point at which the cell degrades at a faster rate, experimental data from all cells are used to fit an overall curve for each of the two SOH indicators (capacity fade and cell internal resistance). The individual CF and IR plots were the deciding factor to select the function that better fit the experimental results. Thus, a third-degree polynomial function is used to obtain the general curves for both voltage windows. The fitted equations for both, the normal and reduced VW cells, are included in Fig. 4.5 (e) with the corresponding curves. The faster degradation happening in the cells cycled under the normal VW becomes more evident with fast capacity decay and an accelerated increase on the cell internal resistance. The differential CF and IR curves, with respect to the number of cycles, provide an estimation of the moment when the cell begins to degrade at a faster rate. Two points are the main interest in these differential plots.

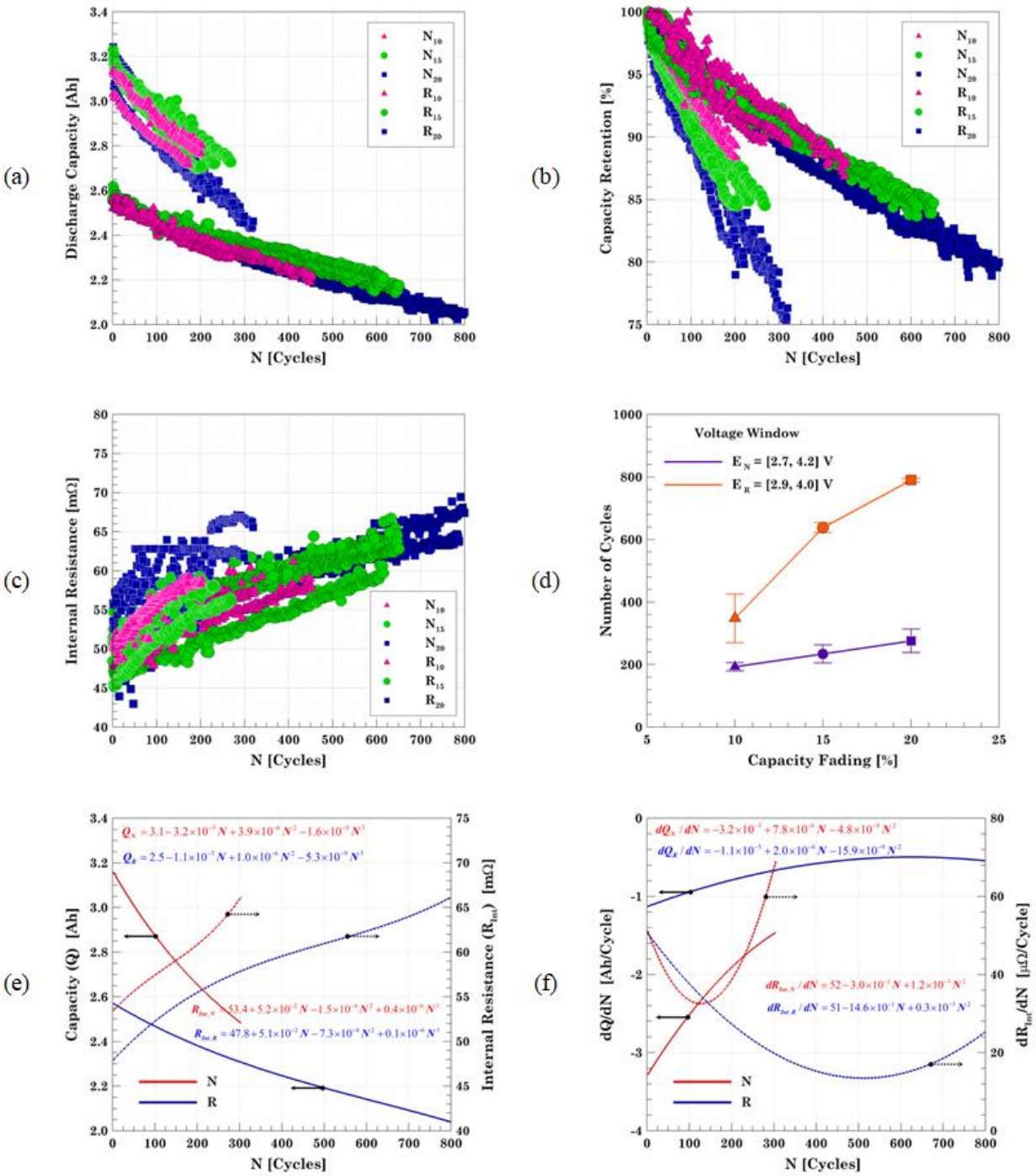

Fig. 4.5 (a) Discharge capacity, (b) capacity retention, and (c) internal resistance evolution through aging for all the cells from this study. (d) Average number of cycles required to achieve 10, 15 and 20% capacity fade as a function of the voltage window. Shrinking the VW extends the number of times the cell can be used but it reduces the delivered capacity. (e) Together, capacity fading and internal resistance measurement are good parameters to quantify the SOH of the cell. (f) Cell degradation can be quantified in terms of the rate of increment for the internal resistance and the rate of decrement for the discharge capacity.

In the differential internal resistance, the minimum point marks the departure for the aggravated degradation. For the cells aged under the normal VW, the minimum point occurs at cycle 127, when the discharge capacity has faded 11.2%. The large variation in the necessary number of cycles to achieve 10 or 20% CF can be explained by the fact that the 9 cells listed in Table 4.1 are already degrading at a faster rate. In the case of the cells aged under the reduced VW, the minimum point occurs at cycle 511, when the discharge capacity has faded 15.0%. For that reason, it takes roughly 150 cycles, to degrade the cell from 15 to 20% CF as shown in Table 4.2.

4.3.2 Thermal Response

There is a strong correlation between the internal resistance and the cell thermal response. Cells with high internal resistance are more prone to have a higher temperature during cycling. The morphological differences between the electrodes lead to an uneven temperature response during charge and discharge [173]. Thus, the maximum temperature rise happens during discharge and only these curves are analyzed. To put in on perspective, Fig. 4.6 (a) and (b) show the cell thermal response during discharge at different degradation levels ranging from 0 to 20% CF, for one representative cell aged on each VW. When the cells are fresh, the cell increases its temperature by 7 and 6 ^{o}C, for the normal and reduced VW, respectively. As the cell degrades, the temperature increment raises to 9.5 and 8.5 ^{o}C, respectively. The temperature rise is a consequence of the heat generated by the cell due to the electrochemical reactions and the charge transfer taking place during the charge and discharge process. As the cell degrades, irreversible chemical and electrochemical reactions, e.g., SEI growth and electrolyte decomposition, as well as the morphological changes, e.g., active particles fracture, hinder the charge transfer between the electrodes. The degradation phenomenon affects the transport processes, increases the cell internal resistance and alters the heat generated by the cell.

Heat generation has two main components, Joule heating (irreversible) and entropic heat (reversible) [174]. At low C-rates, the irreversible heat is negligible and the reversible heat is the predominant one. As the C-rate increases, the irreversible heat dominates and the reversible one becomes negligible. The aging test is done at a high C-rate (C/2), thence, it is reasonable to assume the heat generated is mainly due to irreversible heat. Joule heating can be calculated in terms of the electrical current and the average internal resistance ($\overset{g}{Q}_{irrev} = I^2 R_{Int}$). Instead, the inverse heat

transfer method proposed Mistry et al. is used to estimate the cell heat generation using the temperature profile [174]. The energy balance for the cell includes the energy stored by the cell, the heat generated and the energy dissipated by the convection mode and it can be expressed as:

$$mc\frac{dT}{dt} = \overset{g}{Q} - hA\left(T - T_{\infty}\right) \qquad \text{Eq. 4.2}$$

where m is the mass of the cell (m = 0.044 kg), c is the heat capacity (c = 837 J/(kg K)) [174], A is the cell surface area (A = 4.184×10^{-3} m^2), T is cell temperature in (^oC), T_∞ is the environmental temperature, h is the convective heat transfer coefficient ($W/(m^2K)$), and $\overset{g}{Q}$ is the heat generated by the cell (W). No temperature variation in the radial direction is considered since $Bi = 0.014 < 0.1$. From all the properties in Eq. 4.2, only T, $\overset{g}{Q}$, h, and T_∞ varies with time. To account for this variation, the cell temperature is fitted by the analytical expression in Eq. 4.3.

$$T = c_0 + \sum_{i=1}^{N} c_i e^{-t/\tau_i} \qquad \text{Eq. 4.3}$$

The time constants (τ_i) in the exponential function are geometrically distributed between the Nyquist frequency and the convection time constant, i.e., $\tau_i \in [\tau_{\min}, \tau_{\max}] = [2/f_s,\ mc/hA]$. The number of terms, N, is estimated via a sensitivity test. The coefficient of determination, R^2, between the experimental and the fitted values is the decision parameter to select N.

Ambient temperature cannot be assumed as constant since the cell is exposed to the environment. Thus, the ambient temperature is collected along with the cell temperature. During the rest period, after the discharge process, there is no heat generation, i.e., $\overset{g}{Q} = 0$. Hence, the convective heat transfer coefficient, h, for a specific degradation level, can be calculated from Eq. 4.2, using the corresponding temperature profile decay. The estimated h values vary as $\bar{h} \approx 9 \sim 20\ \ W/\left(m^2K\right)$.

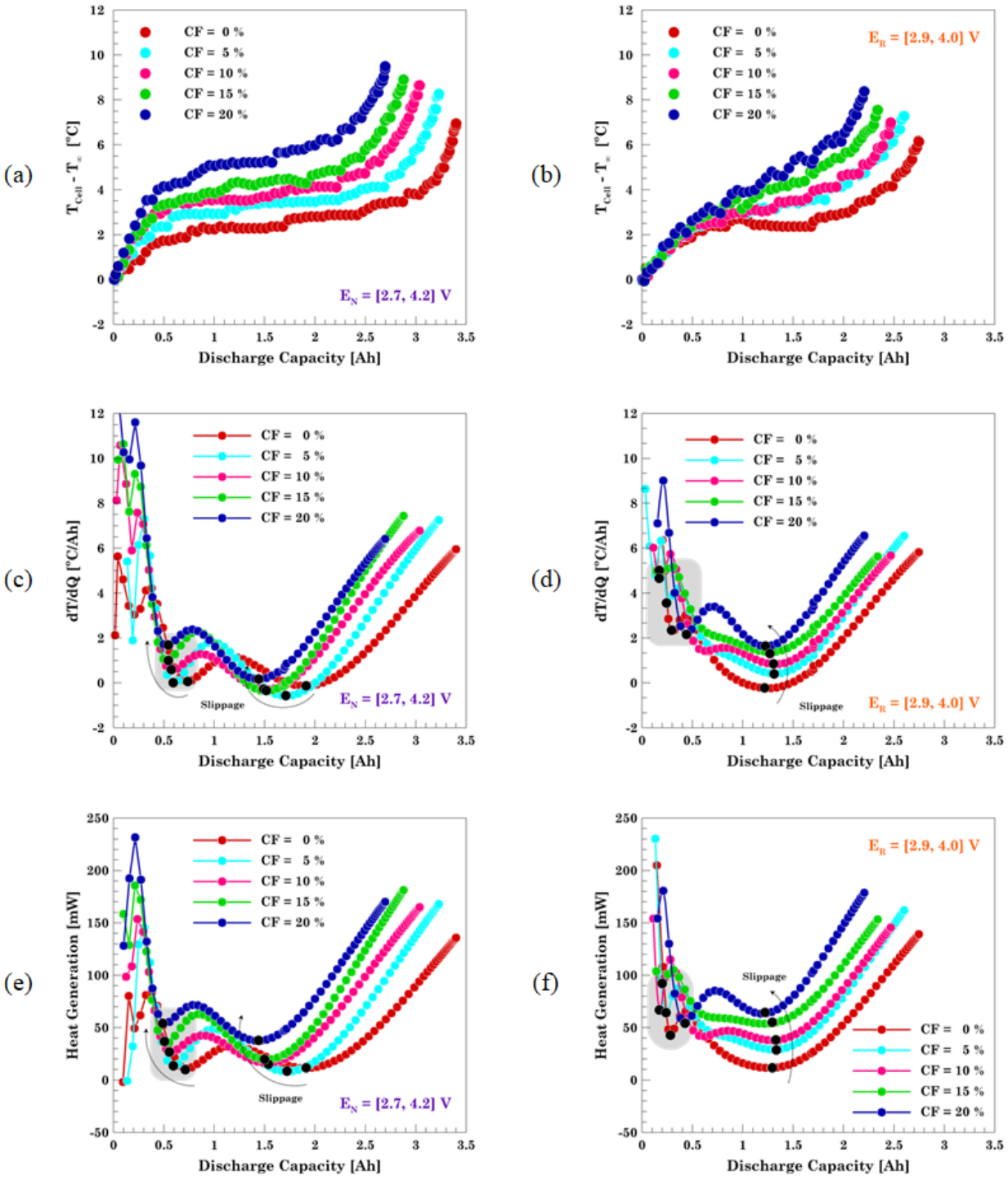

Fig. 4.6 Experimental thermal response of the cells as a function of the capacity fade percentage and the voltage window for the discharge process. (a-b) Cell skin temperature increment with respect to the environmental temperature. (c-d) Rate of temperature change with respect to capacity. (e-f) Heat generation estimated via an inverse problem calculation using the temperature profile during discharge.

At this point, the unknown heat generation for the T curves shown in Fig. 4.6 (a) and (b) is calculated and the results are shown in Fig. 4.6 (e) and (f). The differential temperature, dT/dQ, is a good estimator for the energy stored scaled by a $1/(mcI)$ factor. As dT/dQ follows a similar trend than the heat generated indicates the convective heat loss come to be quasi-constant and it only exacerbates at the end of the discharge. The rate of energy loss is much less than the heat generation rate leading the cell to self-heat.

Heat generation exhibits a SOC dependence, as shown in Fig. 4.6 (e) and (f), contrary to the idea of having a constant value ($\overset{g}{Q}_{Irrev} = I^2 \overline{R}_{Int}$, where $\overline{R}_{Int}$ is the mean internal resistance value) throughout the whole SOC range. The heat generated increases when the cell reaches the fully charged and fully discharged condition. This is consistent with the internal resistance change (dV/dQ), Fig. 4.4 (c) and (d), and its effect on the Joule heating effect. At these two extreme conditions, the internal resistance is maximized as well as the heat generated by the cell due to an increase in the cathode charge transfer resistance [175]. In the intermediate SOC range, the two local minima highlighted in Fig. 4.6 (e) and (f) correlates with the graphite phase transitions. A maximum point in the dV/dQ curve, Fig. 4.4 (c) and (d), corresponds to a minimum cell internal resistance and consequently the cell generates a minimum heat. As the cell ages and the electrodes degrade, there is a slippage of the HG points and the corresponding heat generated. As the cell ages, the extreme HG points occur at an early SOC and the heat generation increases. In terms of safety, an aged cell not only delivers less capacity but it also becomes more prone to fail due to thermal issues.

4.3.3 Post Mortem Analysis

At the end of the cycle life, cells are subjected to a destructive physical analysis aiming to determine any abnormality of the cell. Electrodes (NCA and graphite) and polypropylene (PP) separators are extracted from the aged cells, at the fully charged condition, using the procedure described on the Appendix B. In order to have a baseline for the morphological/physical changes, a fresh cell is subjected to a DPA establishing the pristine condition of the cell components. In Fig. 4.7 and Fig. 4.8, the orientation and position of the electrode with respect to the center is highlighted since degradation is anisotropic.

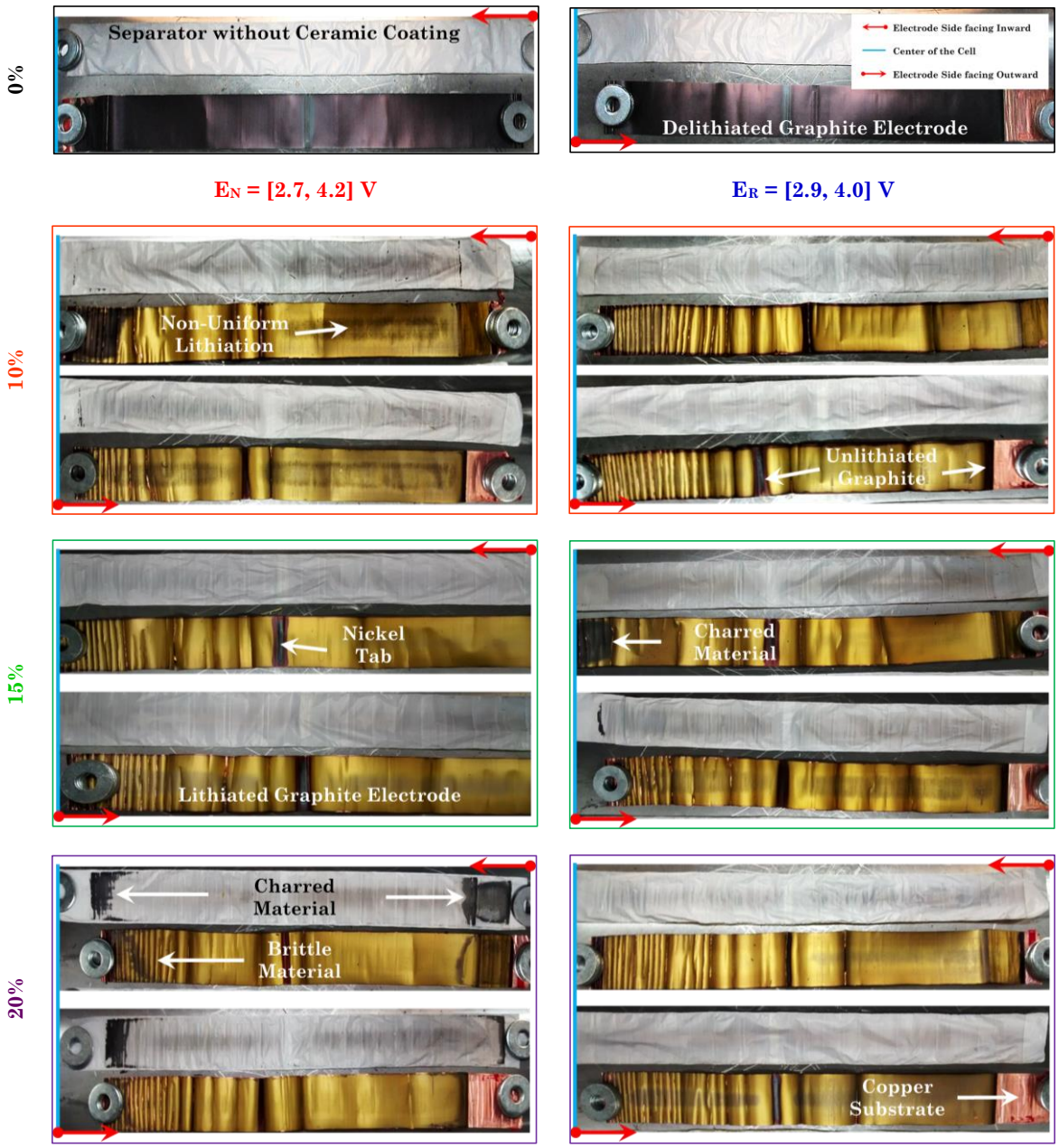

Fig. 4.7 Graphite electrode's degradation with cycling for both studied voltage windows. Left column: Normal voltage window; right column: reduced voltage window. Percentage of capacity fade is shown on the left side. Each side of the electrode is identified according to their orientation with respect to the cell center and the side of the electrode facing it.

The electrodes from the fresh cell (0% CF) are extracted as they come from the vendor. Cells are typically shipped at 30% SOC. Since the cell is never been cycled, either charged or discharged, its graphite electrode exhibits the characteristic purple-darkish color of the unlithiated graphite [176], see the 0% CF electrodes from Fig. 4.7. For this particular cell, NCA and graphite electrode are

double-side coated. However, the graphite electrode is not mirrored, i.e., the amount of material cast on the side facing the center of the electrode is larger than the one cast on the side facing outward. Similarly, there is an asymmetry on both separators present within the cell; the side of the separator facing cathode possesses an additional ceramic coating made of aluminum oxide (Al_2O_3) and cross-linked ethylene-oxide chains, see separators from Fig. 4.8. The solid separator membrane blocks dendrites from the alkali-ion anode and soluble redox species in the cathode side from crossing over to the cathode [177]. This ceramic coating spans only the area covered by the NCA electrode. The yellow stripe on the positive electrode is the nickel tab that connects the NCA electrode and the bottom of the cell can. The yellow color comes from the insulating tape preventing any possible internal short.

Graphite electrodes extracted from aged cells (10, 15, 20% CF) exhibit the characteristic golden color of the fully lithiated state, see Fig. 4.7. Non-uniform lithiation is the leading factor behind graphite degradation. The dark-ish color in the central area of the electrode is a characteristic feature of the non-uniformities. The degradation happening in the edge of the graphite electrode is less visible but it plays a key role in the safety aspects. The active material on the edge becomes electrochemically inactive due to a phenomenon denominated as ‘anode seclusion effect’. The slow lithium diffusion from the central active area to the edge of the electrode creates a concentration gradient between both areas. The lithium concentration gradient induced by charging/discharging the cell can be alleviated if the cell is allowed to be rest for long time periods (days) [88]. The 30-minutes rest left in between the charge and discharge process is not enough to reduce the concentration gradient and consequently there is a cumulative effect with cycling. The anode seclusion effect is also present in the electrode region near to both, the center of the cell and metallic housing. Thus, the graphite electrode contributes to the cell capacity fade not only because of the SEI formation but also due to the electrochemical seclusion of its outer areas, as shown in the graphite electrodes cycled in the normal VW. In the case of the cell cycled in the reduced VW, the amount of lithium intercalated/deintercalated is much less; hence, the effect is less visible even for the cell aged until 20% CF. It is important to remark that no lithium plating evidence was found on any of the electrodes.

Fig. 4.8 NCA electrode's degradation with cycling for both studied voltage windows. Left column: Normal voltage window; right column: reduced voltage window. Percentage of capacity fade is shown on the left side. Each side of the electrode is identified according to their orientation with respect to the cell center and the side of the electrode facing it.

The decaying electrochemical performance of the cell cannot be only attributed to the anodic electrode. The cross-talk between the graphite and the NCA electrode is also reflected in morphological degradation [173]. Non-uniformly lithiated areas in the graphite electrodes can be

explained by looking at the counterpart regions in the NCA electrode. Cathode electrode does not have a colorimetric spectrum as anode; still, it is still possible to distinguish the normal electrode and the degraded one. Pristine NCA electrode (0% CF) from Fig. 4.8, displays a shiny dark color under the light mainly due to calendaring. As the electrode ages and degrades, delamination of the outer layers near to the separator takes place exposing the inner layers of the electrode with the characteristic dull black color, see electrodes for the 10, 15, 20% CF from Fig. 4.8. Cathode delamination happens due to stresses induced by the non-uniform intercalation/deintercalation of lithium ions. The stress creates microcracks on the active particles in the short-term cycling. Propagation of the microcracks compromises the mechanical stability of the active material in the long-term cycling and eventually leads to the NCA electrode delamination [131]. Non-lithiated areas in the central region of the graphite electrode are the consequence of the mechanical degradation of the cathode. As mention early, the cathode degradation is anisotropic, i.e., the electrode side facing outward the center is the one with the largest amount of delaminated NCA active material and it aggravates if the electrode is near to the center. Along with the mechanical degradation of the cathode, the Al_2O_3 ceramic coating from separator interacts with the NCA electrodes by locally adhering each other. Thus, when the jelly roll is disassembled, the ceramic coating detaches from the PP separator, particularly for the electrode side facing inward the center near to the metallic housing. The electrochemically inactive ceramic coating shuts down the covered NCA active material. Both, delamination of cathode and separator shutdown are the leading contributors to the transport and kinetic resistance rise in an aged cell.

4.3.4 SEM

Microstructural disruption associated with the aging process is investigated via microscopy and spectroscopy. So far, Fig. 4.7 and Fig. 4.8 have shown the macroscopic evidence of the electrode degradation. More insights about the real mechanisms behind the cells decay performance can be found at the microscopically level. Lithiated graphite may look alike at the macroscopic level but they may differ at the microscopic level. Pristine samples (0% CF) harvest from the graphite and NCA electrodes are shown in Fig. 4.9 at low and high magnification. This will provide a wide vision of the whole electrode as well as the individual particles.

Pristine graphite has an amorphous platelet shape. The anode particle is conformed of graphene layers where lithium can intercalate in between. In the pristine condition, it is possible to

distinguish the particle layers boundary. As the cell ages (10% CF) and the electrode gets lithiated, intercalated lithium and SEI formation fulfill those gaps and the particle boundary disappears. Thickening of the SEI film becomes more evident in the cells aged until 15% of its capacity has faded. The graphite active particles get covered with a thicker passivating layer and consume the lithium inventory reducing the available energy during discharge. When the cells reach the 20% CF, the differences between the cycling VW emerge. The electrode harvested from the cell cycled with the normal VW exhibits large deposits on its outer surface. Even more, the graphite particles break down due to the expansion/contraction during the intercalation and deintercalation of lithium ions. The non-uniform lithiation leads the localized deposition of lithium plating only visible at the microscope. The localized plated material with a thickness in the micrometer order should not be confused with the SEI layer. On the other hand, the electrodes from the cell cycled in the reduced VW, exhibit a finger-like shape formation on top of the SEI passivating layer. This would indicate an early stage for the lithium deposition. The main difference between both conditions lies upon the fact that the cells cycled in the reduced VW never reach the fully charged condition, at most 90% SOC, whereas the ones cycled in the normal VW, they do.

The pristine NCA active particles are spherical agglomerates (mean diameter of 12 μm) of small particles. Its surface is flat indicating the electrode was calendered prior to the jelly roll assembly. Degradation on the cathode electrode can be chemical (electrolyte decomposition and reaction with NCA) and mechanical (fracture and agglomerate crumbling). Stress-induced by the non-uniform intercalation/deintercalation of lithium ions is the driven mechanism behind aging degradation. The fatigue effect can be interpreted in terms of the number of cycles as well as the voltage window. In the normal VW, the cycling loading represented by the amount of lithium intercalated/deintercalated is large, which means more particles participates in the electrochemical reaction. As the cell ages, the inner layers of the electrode become more prone to fracture and eventually lead to the NCA material delamination. Delaminated material for practical purposes is electrochemically inactive and reduces the cell capacity utilization, the cycle life and turns the counterpart graphite region into a secluded area. In the reduced VW, the cycling loading is smaller and it only affects the adjacent layers to the separator. The stress-induced, in this case, is reflected as a crumbling of the agglomerates from the surface.

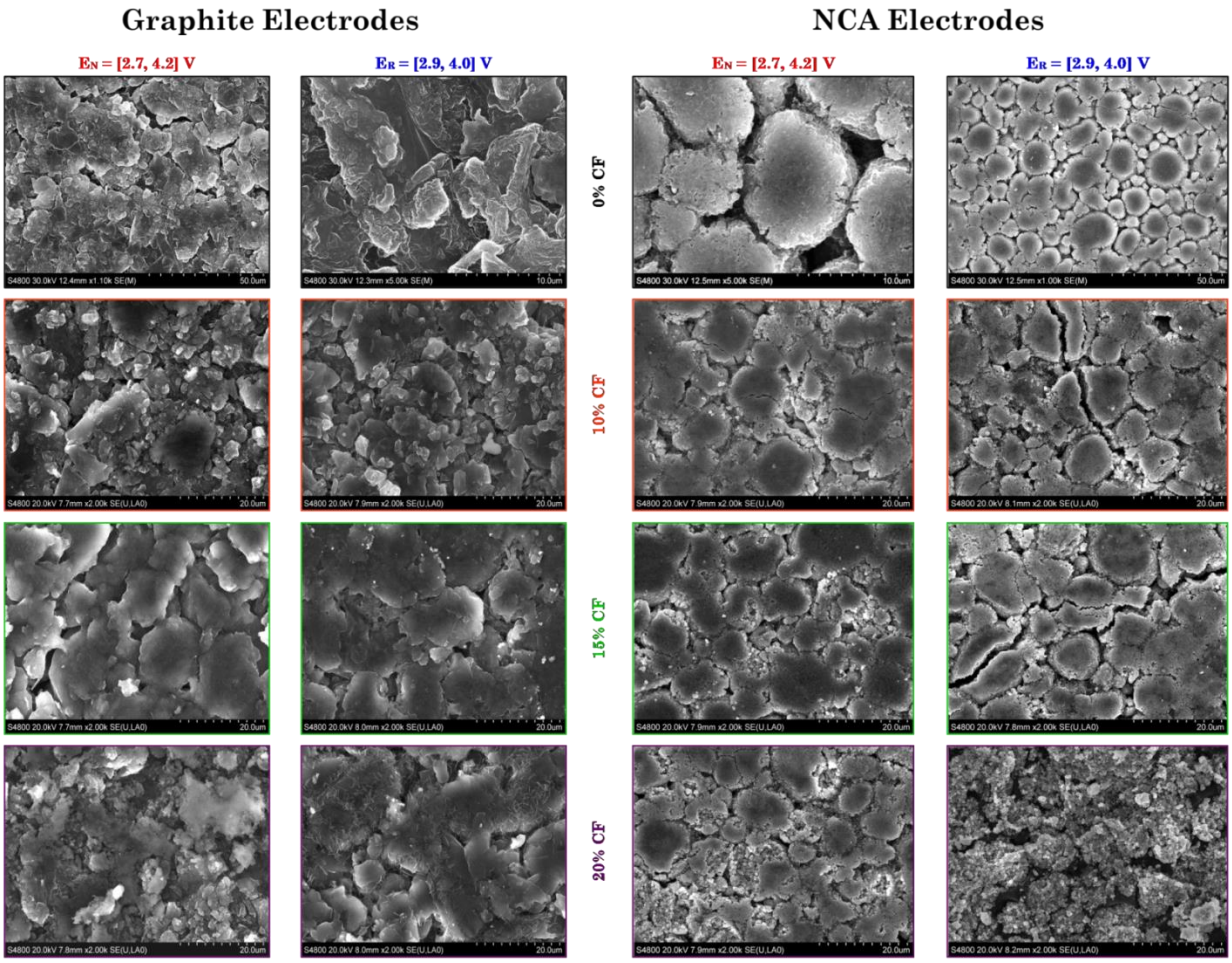

Fig. 4.9 Micrographs of graphite (columns 1 and 2) and NCA (columns 3 and 4) representative samples harvested from the fresh and aged electrodes. For the fresh cell electrodes (0% CF), a 1 kX and 5kX magnification images are shown. For the aged electrodes, only a 2 kX magnification is shown.

4.3.5 EDS

Chemical change on the electrode samples shown in Fig. 4.9 is done via EDS. The composition of the pristine graphite electrode is carbon from the active material and the conductive additive and fluorine from the binder. The presence of copper comes from the current collector and the rest of the elements are from the electrolyte residuals. As the graphite electrode ages, the SEI keeps growing. The main compounds on the SEI layer are lithium carbonate (Li_2CO_3), lithium hydroxide (LiOH), lithium fluoride (LiF), lithium oxide (Li_2O), lithium alkyl carbonate ($ROCO_2Li$, RCOLi) [178], where R is an alkyl group made of carbon and hydrogen. Thus, in the cells aged with the reduced VW, the increment on the oxygen and fluorine percentage is due to the SEI formation. The passivating layer hinders the exposed graphite for intercalation and reduces the carbon content

detected in the sample. Similar behavior is found in the cells aged under the normal VW, with 10 and 15% CF. The sudden reduction on the carbon content and large increment on the oxygen level, in the cell with 20% CF, indicates the presence of lithium plating. The connection between the oxygen level and lithium plating arises from the reaction of Li metal with air, when the sample is exposed to the environment, forming lithium hydroxide.

The chemical composition of the pristine NCA electrode confirms the presence of nickel (Ni), cobalt (Co), aluminum (Al) and oxygen (O). As the cathode electrode ages, the percentage of Ni and Co decreases due to the byproducts of the reaction of cathode oxygen with the carbonate solvents from the electrolyte. This explains the reduction of the oxygen percentage and the rise of the carbon percentage. The interaction between the NCA electrode and the ceramic coating from the separator is reflected as an increment of the Al percentage.

5. CELL LEVEL DEGRADATION: EXTERNAL SHORT TEST IN CYLINDRICAL CELLS

Relevant Publications and/or Working Papers

1. D. Juarez-Robles, J. Jeevarajan, P.P. Mukherjee, 2019, *Degradation-Safety Analytics (DSA) in Li-ion Cells. Part 2. External Short Test on Fresh and Aged Cells*, working paper

5.1 External Short

A common abuse condition experienced by Li-ion cells is an external short circuit, which occurs when the positive and negative terminals of a battery come into contact with minimal electrical resistance [179]. This causes the cell to discharge at a high rate, thus producing large amounts of current and rapidly generating heat within the cell as well as in the external circuit. If the cell temperature is not properly controlled, very high internal temperatures (~180°C) can spur undesired exothermic reactions in the cell, known as thermal runaway, which can even lead to fire or explosion [27, 180-181]. While the dangers of internal shorting in Li-ion cells have been well-documented, few studies have focused on the response of Li-ion cells to external shorting, which can easily occur due to faulty packaging or careless handling of cells[182-183]. This work seeks to explain the response of LIBs to an external short and to determine under what conditions this shorting could lead to damage or failure in cells[181, 184].

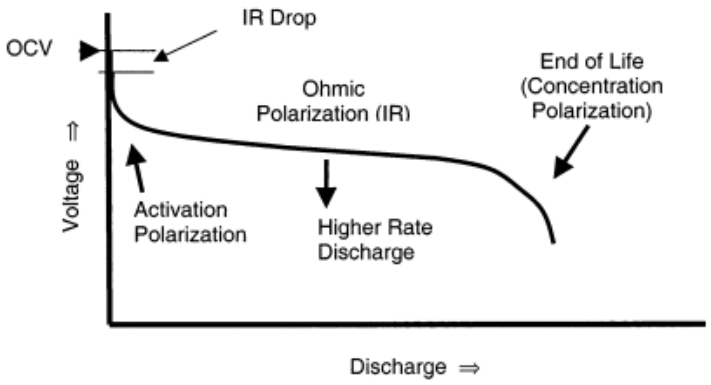

Fig. 5.1 Battery discharge curve, showing the influence of various types of polarization [9].

When the battery terminals are connected to an external circuit, the voltage drops to the closed-circuit voltage due to several types of losses (polarization), Fig. 5.1. The difference between the open and closed circuit voltages for a cell is known as the overpotential, η, and is defined as $\eta = E_{OCV} - E_T$, where E_{OCV} is the Open Circuit Voltage (OCV) and E_T is the terminal cell voltage with current flowing [9]. Activation polarization is the voltage drop related to the kinetics of the charge-transfer reactions taking place at the electrode/electrolyte interfaces [9]. Ohmic polarization is the voltage drop due to the internal resistance of a cell, dictated by Ohm's law ($E=iR$). This includes both resistances to electron and ion transfer in the cell, such as the resistance of the electrolyte to ion transfer and poor contact of conductive pathways between the reaction sites and the current collector in the electrode. Concentration polarization is caused by the unavailability of the active species at the electrode/electrolyte interface to continue with the reaction. As the reaction proceeds, active species particles must diffuse to the electrode surface to replace the previously reacted materials. The buildup of a gradient between the electrode surface and bulk concentrations causes a voltage drop. In constant resistance discharge, even for low resistor value, the current decreases during the discharge proportionally to the decrease in the battery voltage [185-186]. Therefore, drops in voltage will result in proportional current drops throughout our external short tests.

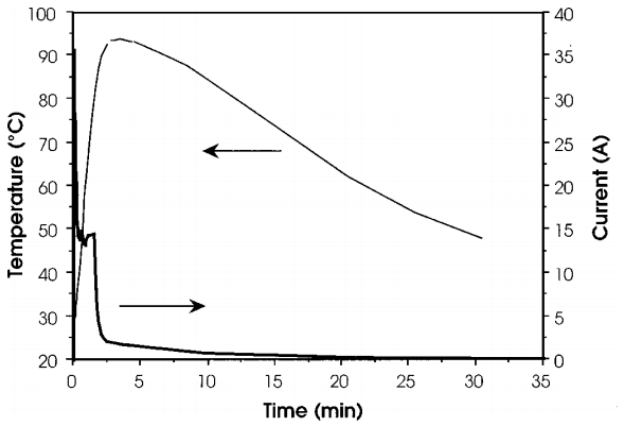

Fig. 5.2 Temperature and current for prismatic Li-ion cell in external short circuit test [187].

An external short circuit abuse test on prismatic $LiCoO_2/LiC_6$ batteries was performed by Leising et al. using a resistance of 6 mΩ [188]. In this test, cells were fully charged to +4.1 V and externally shorted. Within 0.2 s of starting the test, the current peaked and the voltage dropped severely to less than 0.25 V. For the next 1.5 minutes, the current held at about 14-15 A and the temperature

began to rise. At this point, the current fell to less than 2 A, but the temperature continued to steadily rise. After 3.5 min, the temperature peaked and the current began to decay to 0.0 A. The maximum surface temperature measured by the thermocouple was 109 °C. The temperature and current profiles for this test are shown in Fig. 5.2.

Wu et al. achieved similar results in an external short-circuit on prismatic cells with a capacity of 750 mAh [187]. This test was performed on both fresh cells (10 cycles) and cells that had already suffered some abuse (200 cycles). It also considered the influence of separator material, testing cells with polyethylene (PE), polypropylene (PP), and PP/PE/PP separators. The current and temperature behavior during the test are shown in Fig. 5.3. When the cells were shorted with an external resistance of 30 mΩ, the current peaked instantaneously at 25 A, stayed around 11 A for 70 s, and finally drops to less than 1 A. The temperature steadily rose for 70 s to a maximum of 110 °C. It is reported that results were identical for all three separators and that cycle number had a negligible effect on the behavior.

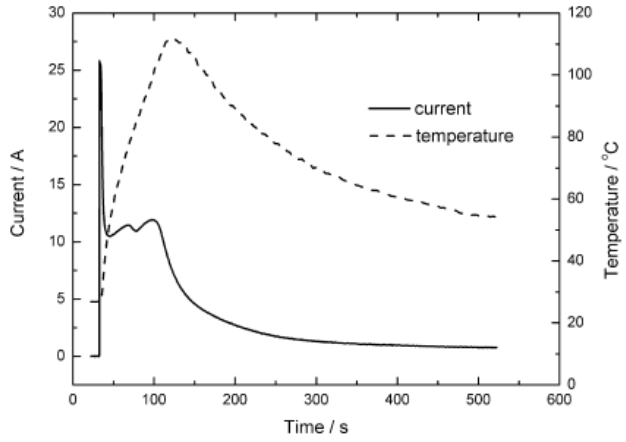

Fig. 5.3 Current and temperature behavior of battery in external short-circuit test after more than 200 cycles [187].

Previous studies of external shorting have not considered the impact of external circuit resistance during shorting. The impact of utilizing an 18650 cell rather than a prismatic cell will also be a key component in this study, as different cell geometries may have varying ability to dissipate heat. Additionally, the cylindrical cells used in this study have higher capacities than the prismatic cells of previous studies, which could cause more heat generation during a short. By discharging 18650

cells under low resistance conditions will allow to determine if the external short circuit represents dangerous conditions in the cell.

5.2 Experimental

Short circuit happens when there is an 'unintended' contact of the cell electrodes (internal or external) resulting in an excessive electrical current. In this study, an external short will be induced in fully charged commercial cells.

The external short test has been implemented with the circuit shown in, with 50 mΩ external resistance. Due to the large electrical current flowing through the circuit, it was necessary to use a high power ceramic resistor. A normal carbon resistor will burn if used in this test.

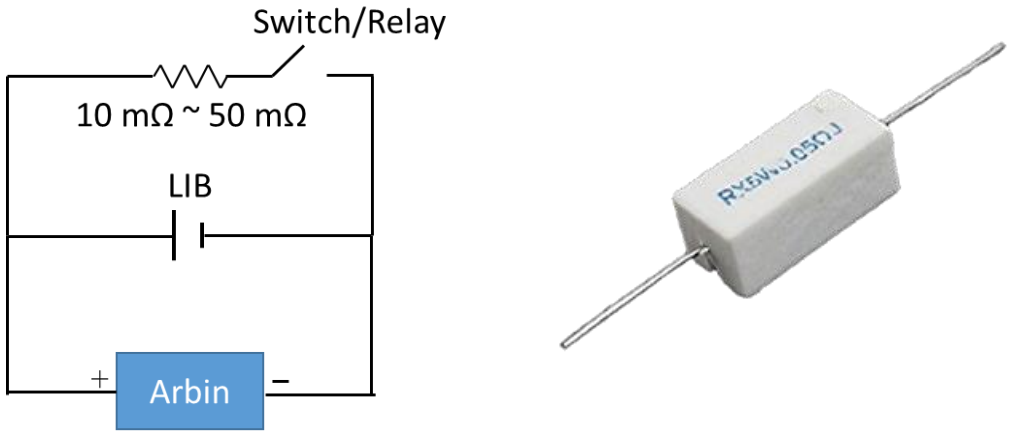

(a) (b)

Fig. 5.4 (a) Schematic connection used in the external short test. (b) High power ceramic resistor – 50 mΩ.

Cycling Protocol Prior the External Short Test

1. *Preparation:* CCCV charging, at 1C, up to 4.2 V with a cutoff current of 50 mA.
2. Rest 30 minutes.
3. *External Short:* Externally short the cell using a 50 mΩ resistor for 3 hours or until an event stop the test.
4. Rest 30 minutes.
5. *Conditioning Test:* Determine the new capacity and internal resistance.

The recorded voltage and temperature, during the 3 hours test, are shown in Fig. 5.5 (a). During a normal discharge, an electrical current flow through the external circuit while the voltage decreases at a low rate. During an external short test, the same phenomenon happens but the discharge rate is extremely fast. This translates into a large electrical current flowing to the external circuit and a fast voltage drop. In order to accomplish the externally demanded current, the rate of the reactions within the cell also increases causing a raise in the cell temperature.

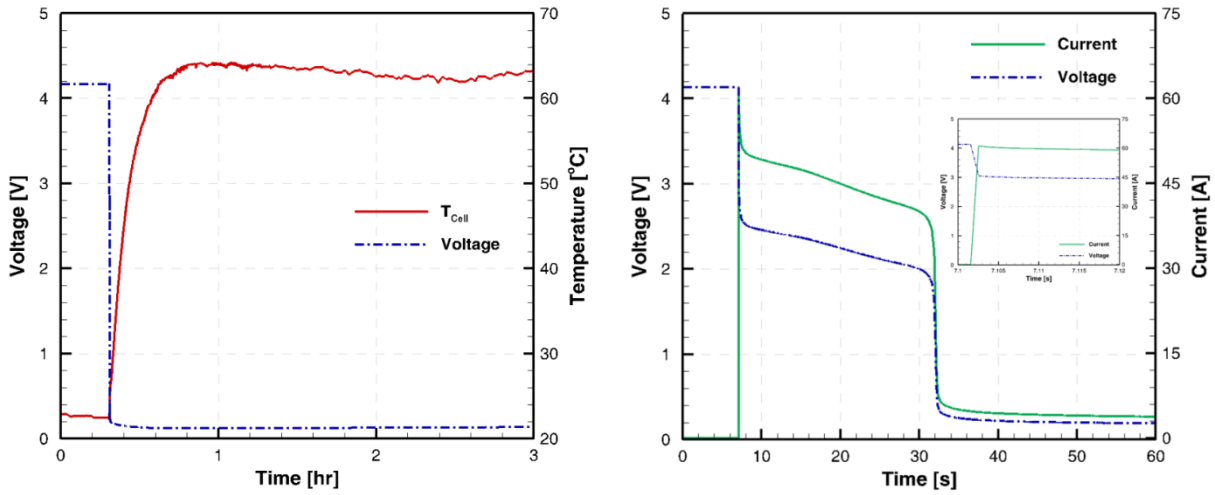

(a) (b)

Fig. 5.5 Voltage and temperature variation before and after the external short of cell.

The baseline for this test corresponds to the results obtained from a fully uncycled fresh cell. Even when the test lasted three hours, the main changes happen during the first seconds as it can be seen in Fig. 5.5 (b). An initial short plateau voltage appears at a cell voltage of 3.0 V. At the same time, the external current went from 0 to 60 A (peak current). The large current is only hold for some seconds after that it drops to zero. The thermal response behaves in an interesting way, temperature starts rising time ahead that the external short happened reaching a maximum value and then remaining constant.

5.3 External Short Test of a Cycled Cells

Fresh cells, Fig. 5.5, developed larger currents in comparison with the cycled cells, see Fig. 5.6. In this figure, it is also included a magnification of the instant when the cell is shorted. From the

voltage point of view, it could not be found a distinctive effect neither on the initial voltage drop nor in the time required to fully discharge. In some sense, this test is controlled by the external load. That could be a reason why no monotonically trend could be found in the voltage profiles.

In the cells cycled under the Normal voltage window, the initial external current increases first and then decreases as the capacity fading increases. While, in the cells cycled under the Reduced voltage window, the initial external current seems to increase as the capacity fading increases. It is important to remark that the current flowing through the external circuit was not measured directly. Ohm's law was used to back calculate the external current since the cell voltage was recorded and the resistance of the ceramic resistor was known. The resistor used for the different test was the same, thus, it is possible that due to the higher currents the resistance have change between tests causing the differences in the results. To put it in perspective, if the cell voltage is 4.0 V and the external resistor changes its value from 50 mΩ to 51 mΩ, the calculated current will change from 80 to 78.43 A.

Fig. 5.7 shows the temperature profile during the test. Even when the voltage drops faster from 4.2 V to ~200 mV, temperature keeps increasing for 15 minutes, then in reaches a constant value. A comparison of the thermal response, of the cycled cells, indicates that the cells cycled for the Normal voltage window reach a similar maximum temperature (66-68 ^{o}C), no matter their capacity fading. In regards to the cells cycled in the Reduced voltage window, the maximum temperature first increases and the decreases as the capacity fading increases.

In some cases, such as the cell Reduced 2, initially temperature and voltage gradually decreased. Suddenly, one voltage peak appears after 2 hours, increasing again the cell temperature for a short time. At this point, the SEI starts decomposing because most of the lithium from anode had been deintercalated but the demand of current still holds.

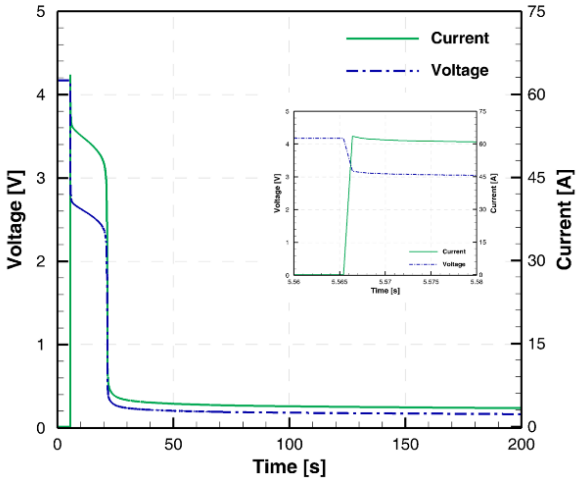

(a) Normal – CF = 10%

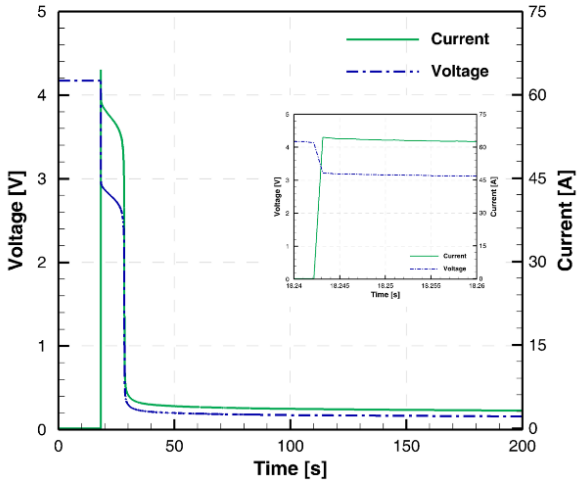

(b) Reduced – CF = 10%

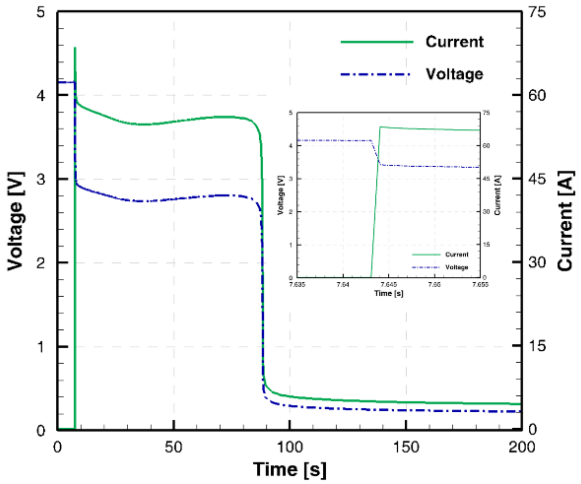

(c) Normal – CF = 15%

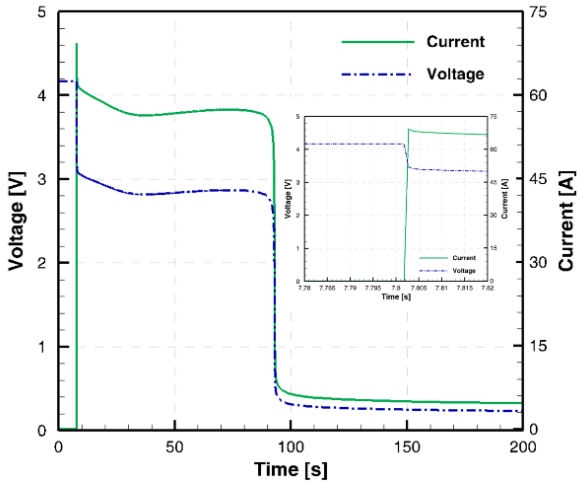

(d) Reduced – CF = 15%

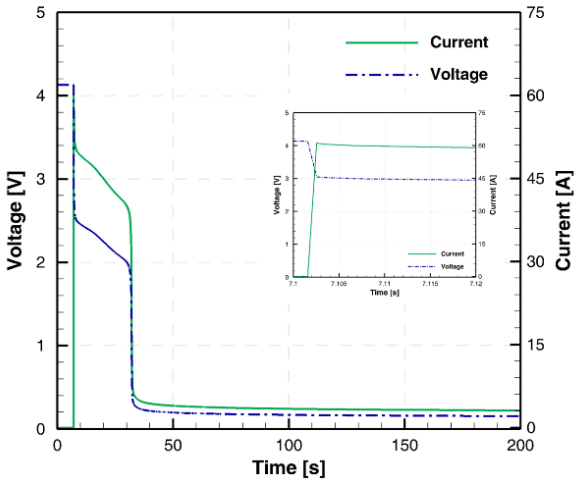

(e) Normal – CF = 20%

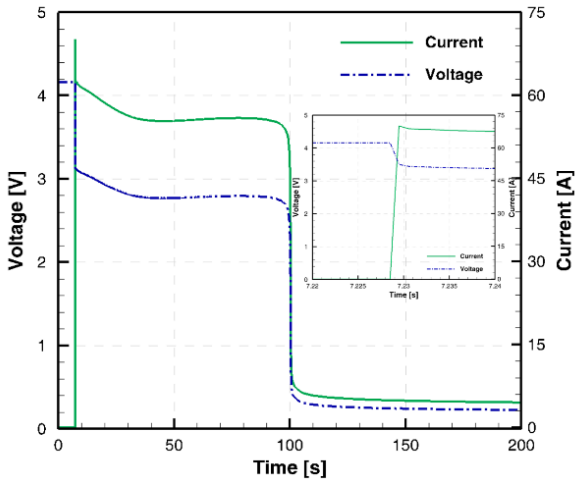

(f) Reduced – CF = 20%

Fig. 5.6 Current and voltage response from cells externally shorted after been cycled.

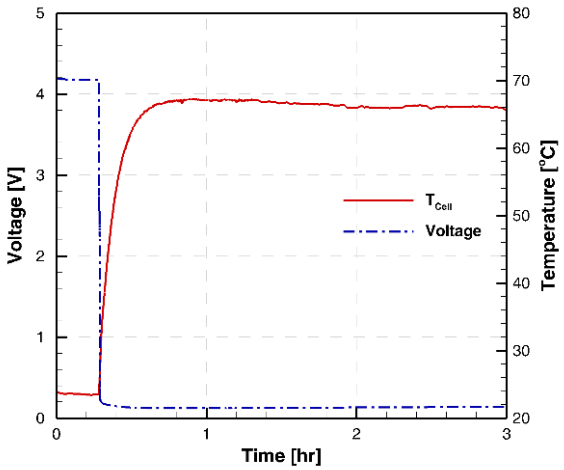

(a) Normal – CF = 10%

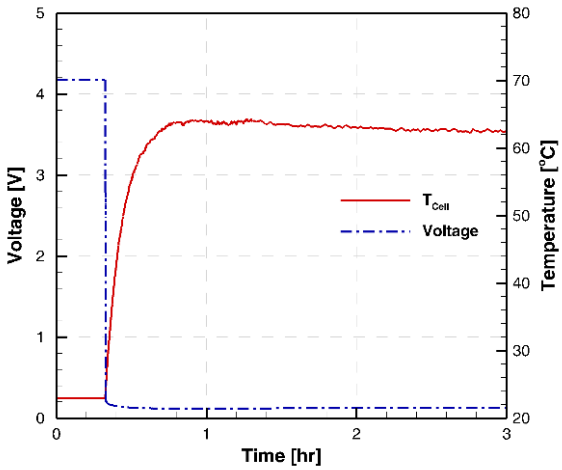

(b) Reduced – CF = 10%

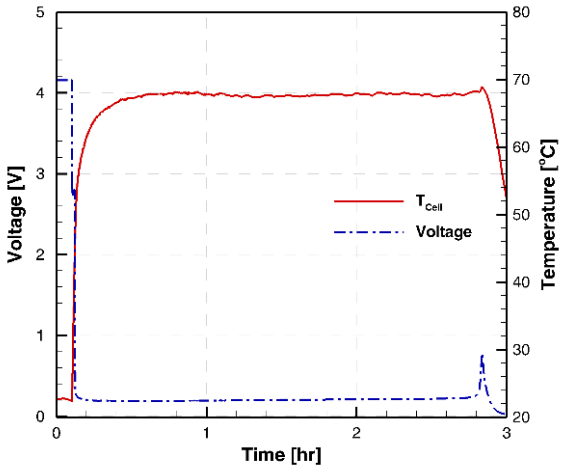

(c) Normal – CF = 15%

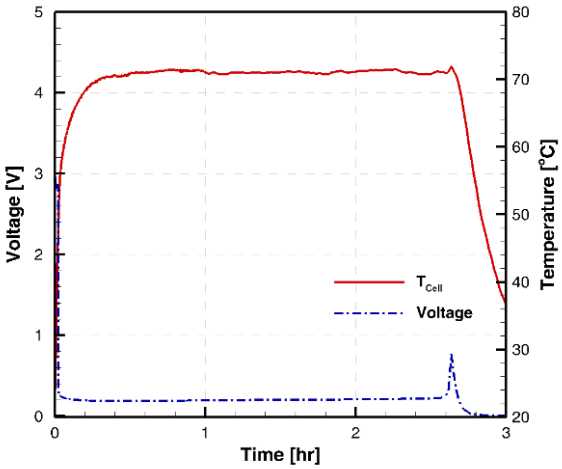

(d) Reduced – CF = 15%

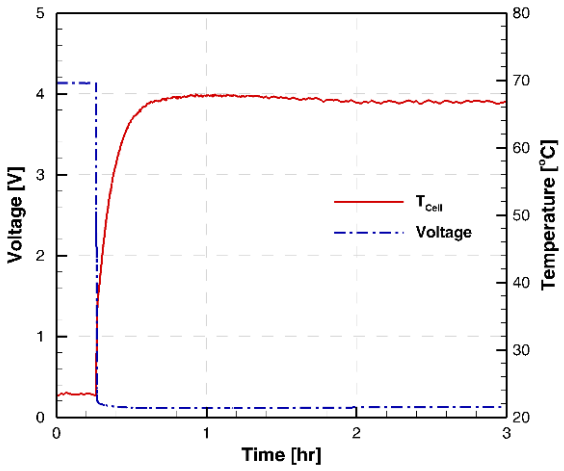

(e) Normal – CF = 20%

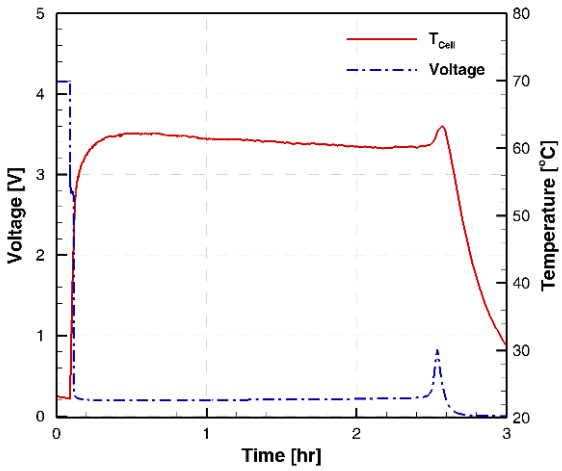

(f) Reduced – CF = 20%

Fig. 5.7 Current and voltage response from cells externally shorted after been cycled.

When no more lithium can be obtained from SEI, the voltage drops almost to zero, where it remains like that as long as the external load is connected. After the final peak voltage, the temperature will keep decreasing, since no more reactions are happening, until in reach ambient temperature. In none of the cases, the cells underwent to overdischarge (E < 0.0 V).

5.4 External Short Test – Comparison of All Cells

A comparison of the cell temperature and current for all the cells is shown in Fig. 5.8 to Fig. 5.10. All tests were shifted to share the same initial time and have a fair comparison. The profile for voltage and current have the same trend since current is obtained from Ohm's law with a constant resistance, $R_{Ext} = 50\ m\Omega$. The only difference appears before the test. Initially the cells were fully charged up to 4.2 V, and no current was flowing through the external circuit.

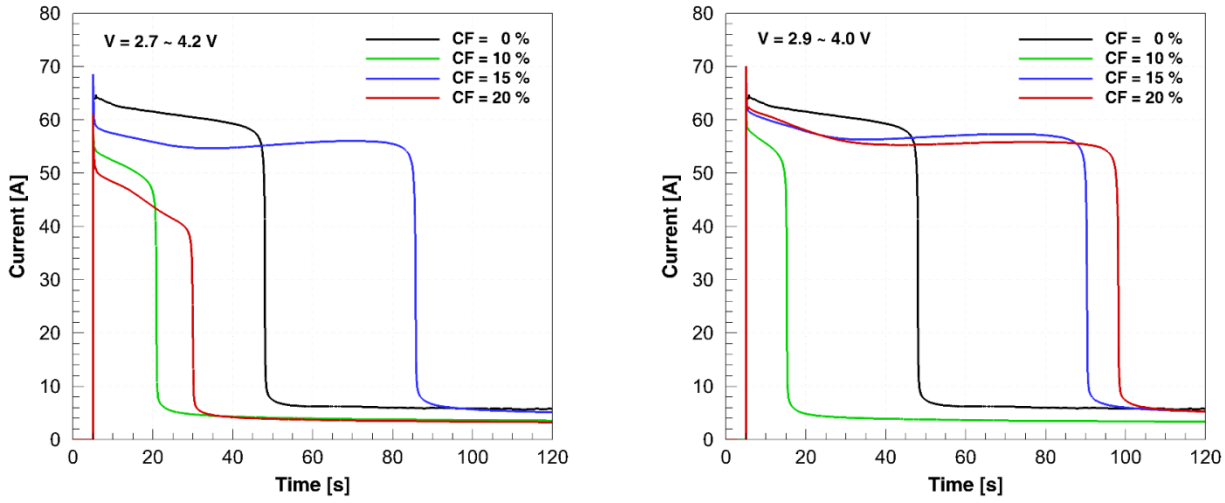

(a) (b)

Fig. 5.8 External short test comparison. Electrical current flowing through the external circuit for the cells cycled in the (a) Normal, and (b) Reduced voltage window.

The larger current developed by the fresh cells is all the material in them is available to intercalate lithium ions. While, in the cycled cells part of the electrode material (specially the anode) is already damaged and it does not participate in the electrochemical reaction, decreasing the amount of current and hence the temperature increment.

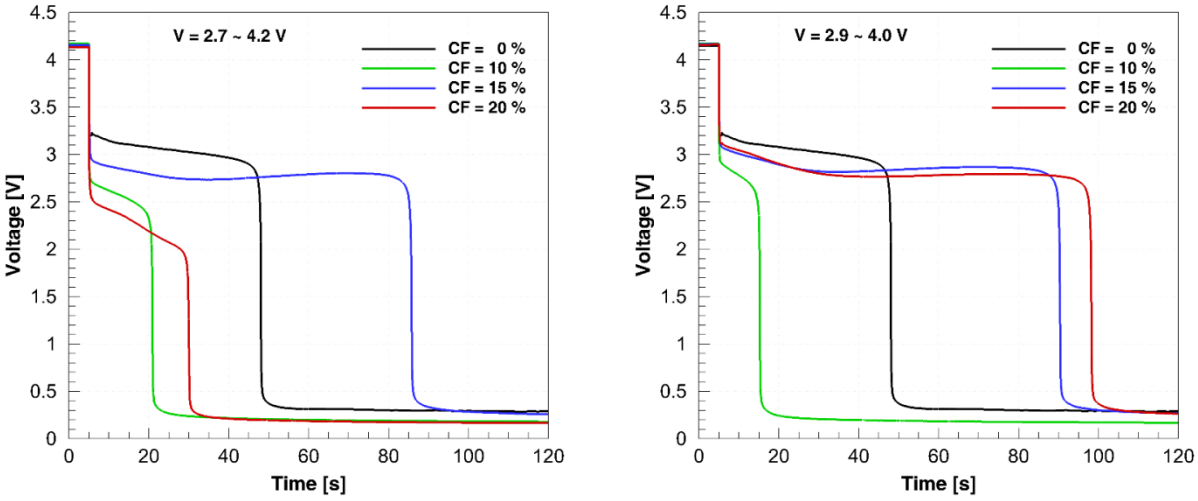

(a) (b)

Fig. 5.9 External short test comparison. Cell voltage during the safety test in the cells cycled in the (a) Normal, and (b) Reduced voltage window.

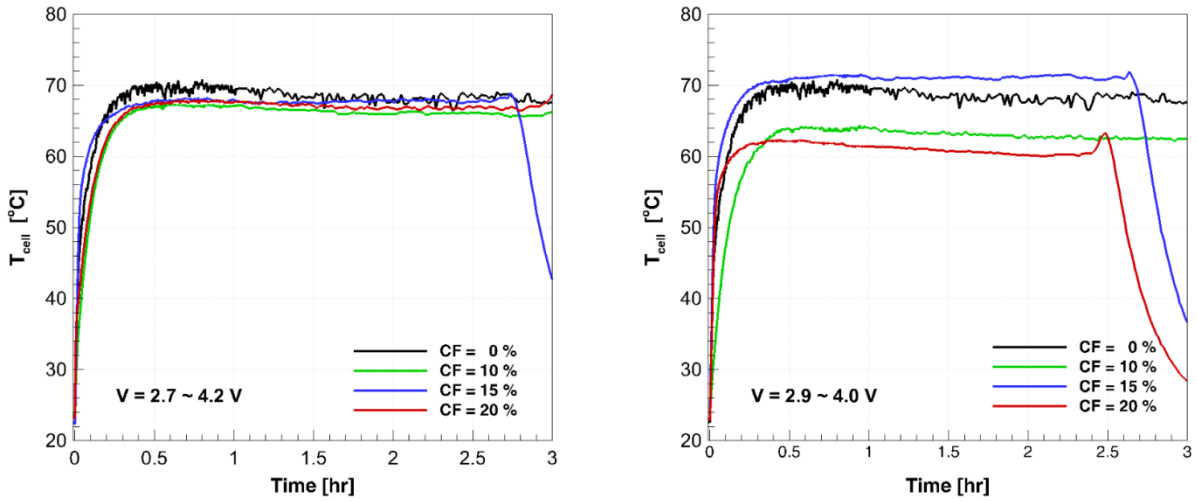

(a) (b)

Fig. 5.10 External short test comparison. Cell temperature during the safety test in the cells cycled in the (a) Normal, and (b) Reduced voltage window.

5.5 DPA of a Externally Shorted Fresh Cell

The DPA of a fresh uncycled cell externally shorted (XS Cell 0). Fig. 5.11 shows the anode and cathode electrodes from one of the externally shorted cells. No visual evidence of electrolyte decomposition was found. However, there were detected two main physical effects, drying and some charring especially in the cathode. The drying could be appreciated in both electrodes. While,

the burning only appear in a very small spots in the piece of the sheet closer to the center of the cell.

Fig. 5.11 Dried electrodes sheet after external short test.

5.6 DPA of a Externally Shorted Cells after Cycling

The results of the DPA for the external short test conducted in the cells with different capacity fading are shown in Fig. 5.12 to Fig. 5.15. It is important to remind that the electrodes shown have two different effects on them. First, is the damage cause by the long time cycling and second the effect due to the external short test. The effect of externally short the cell on the electrodes seems to be almost negligible. The results obtained from the cells externally shorted are quite similar to the ones obtained from the cells only cycles. The electrode with more damage is cathode in comparison with the anode.

The external short test definitely caused some damage in the cell (electrochemical test showed an increase of the internal resistance). However, degradation due to cycling is more dominant and does not allow seeing any significant difference. Previous results obtained from the SEM showed some melting of the ceramic coating cast on top of the cathode material. There are two possible reasons why the effect of the external short test is minimum. The first one is that during the test, the cells were not allowed to go to overdischarge, i.e., that the test was stopped when the voltage drops bellows 2.0 V. Also, the elapsed time of the test was very small. Even when the current developed was large, this only last for a short period of time.

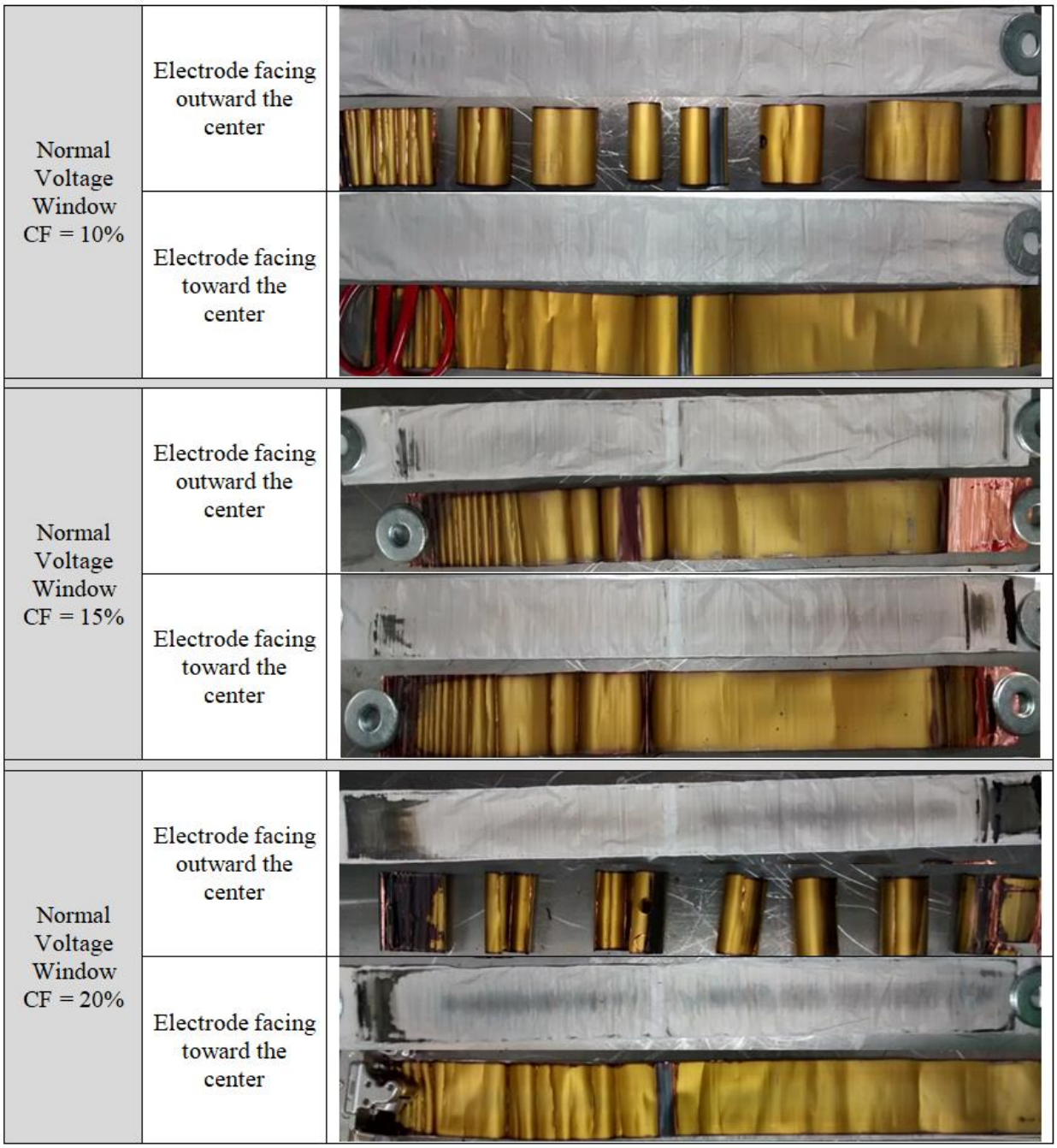

Fig. 5.12 Graphite electrodes and separators, without a ceramic coating, extracted from cells cycled in the Normal voltage window and then externally shorted.

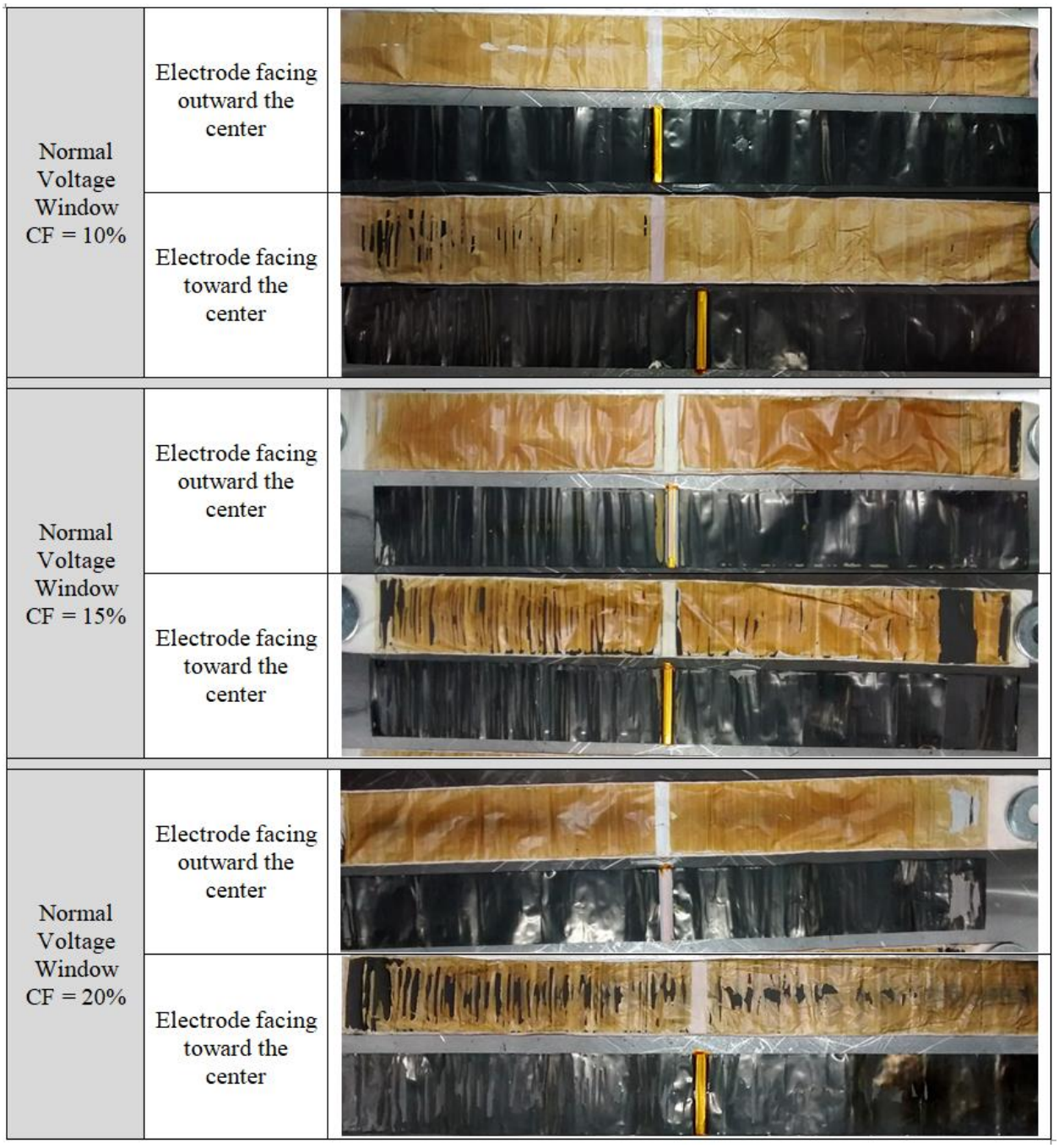

Fig. 5.13 NCAO electrodes and separators, with a ceramic coating, extracted from cells cycled in the Normal voltage window and then externally shorted.

Reduced Voltage Window CF = 10%	Electrode facing outward the center	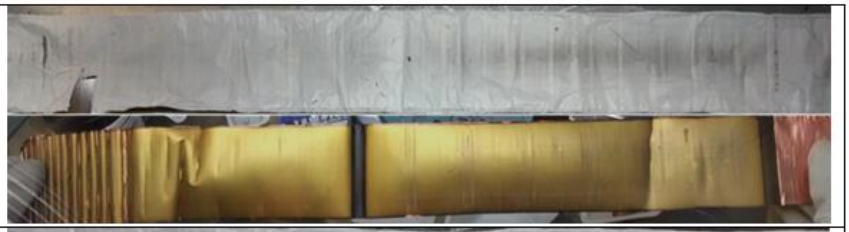
	Electrode facing toward the center	
Reduced Voltage Window CF = 15%	Electrode facing outward the center	
	Electrode facing toward the center	
Reduced Voltage Window CF = 20%	Electrode facing outward the center	
	Electrode facing toward the center	

Fig. 5.14 Graphite electrodes and separators, without a ceramic coating, extracted from cells cycled in the Reduced voltage window and then externally shorted.

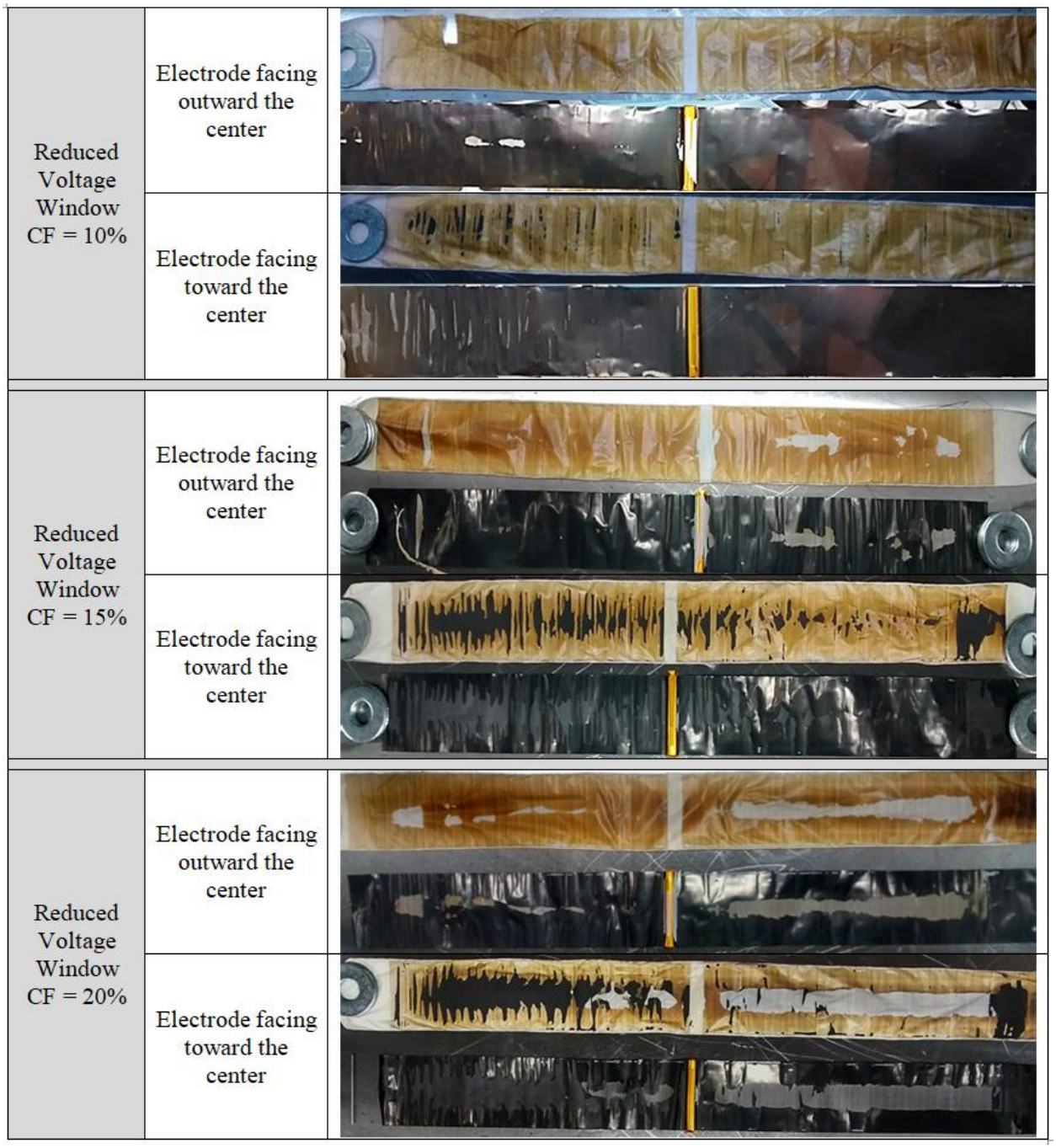

Fig. 5.15 NCAO electrodes and separators, with a ceramic coating, extracted from cells cycled in the Reduced voltage window and then externally shorted.

5.7 SEM/EDS

5.7.1 Fresh Cell

An uncycled fresh cell was fully charged and then externally shorted using a 50 mΩ ceramic resistor. A sample from each of the electrodes were punched out in the glovebox and taken to the SEM microscope.

A comparison between the SEM images of a fresh, see Fig. 5.16 and Fig. 5.17, and an external shorted cell showed some significant differences among the electrodes. The anode from the externally shorted cells exhibited some flat and melted material on top of the graphite. This could be due either to the binder or the separator. A similar comparison can be conducted between the images for the cathode at 1 kX and 10 kX. Again, a flat melted surface can be observed in the cathode microstructure for the externally shorted cell.

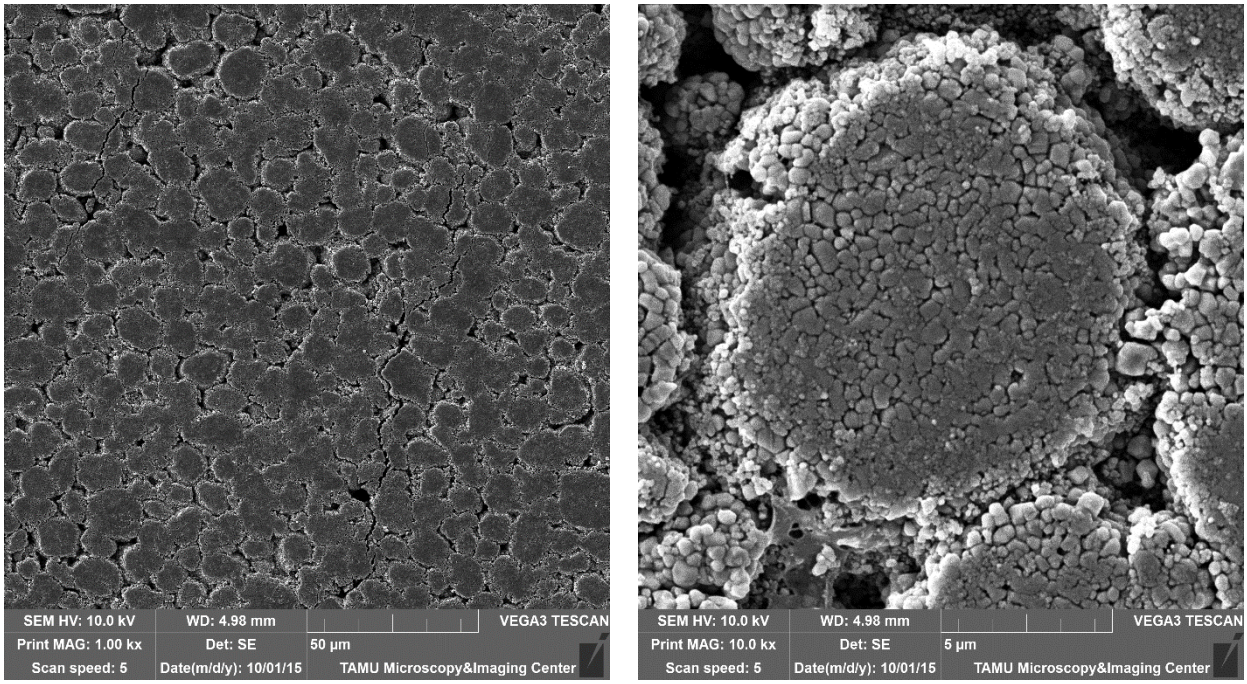

(a) (b)

Fig. 5.16 SEM image of the cathode from an externally shorted fresh cell with: (a) 1 kX (SE) magnification and (b) 10 kX (SE) magnification.

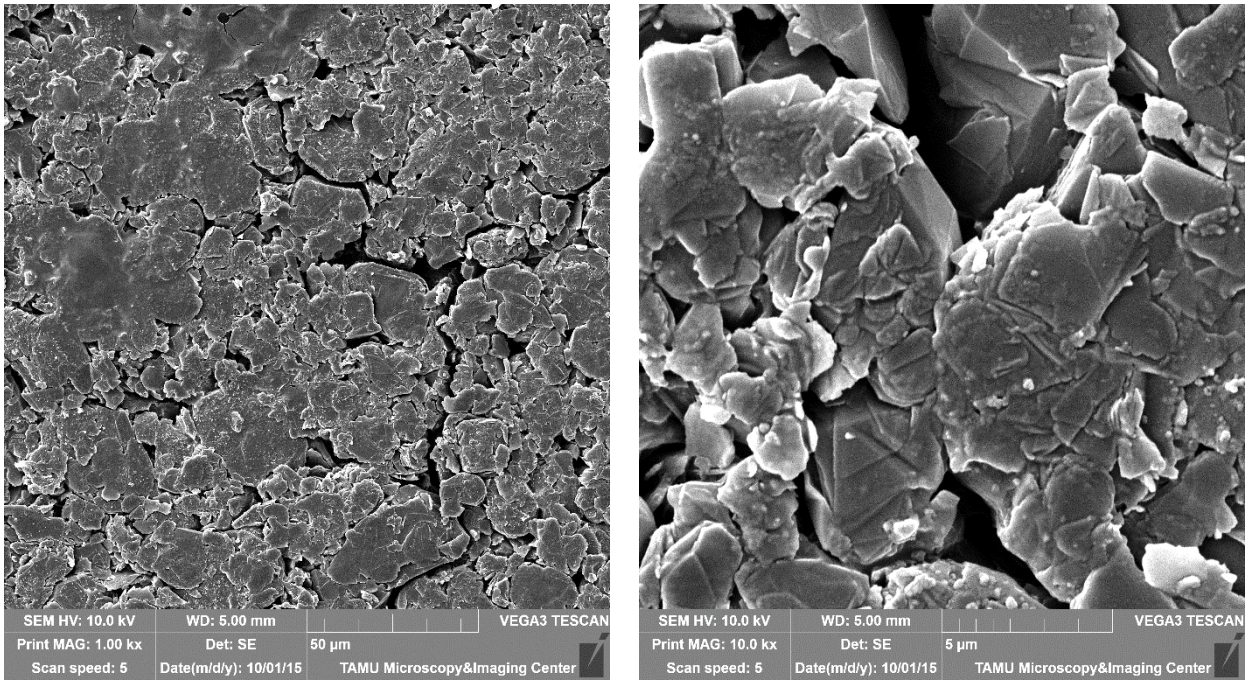

(a) (b)

Fig. 5.17 SEM image of the anode from an externally shorted fresh cell with: (a) 1 kX (SE) magnification and (b) 10 kX (SE) magnification.

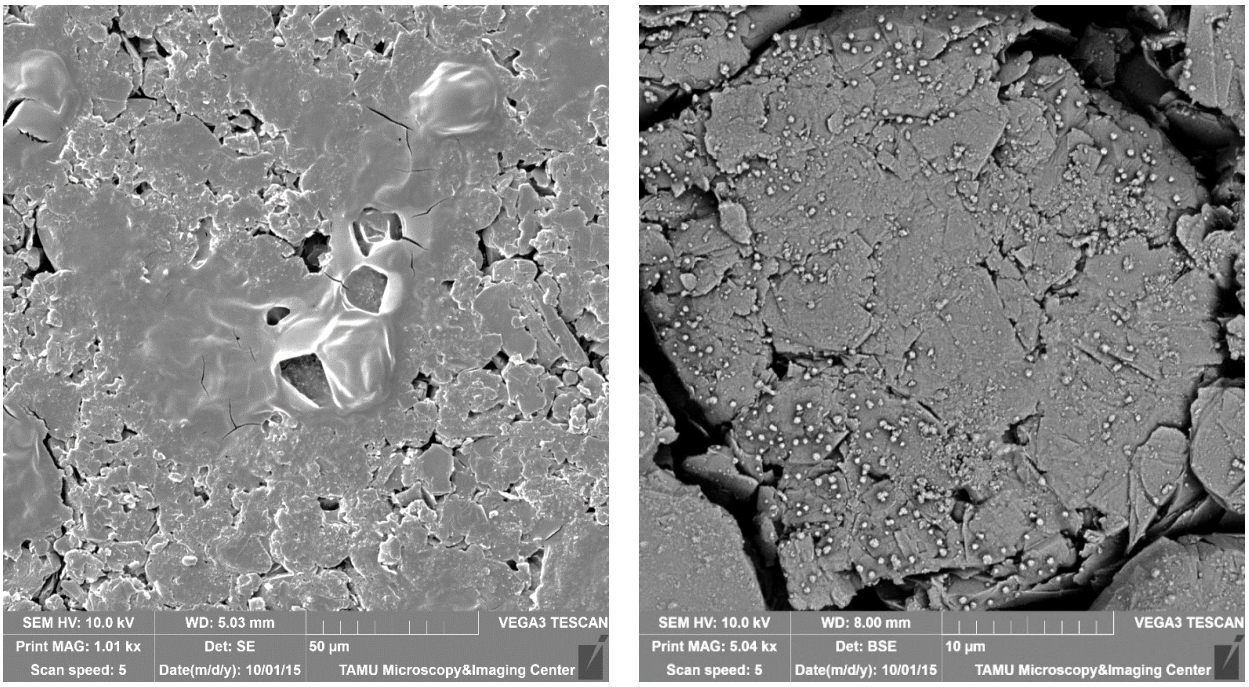

(a) (b)

Fig. 5.18 Degradation on the anode from an externally shorted fresh cell with: (a) Melted material, 1.01 kX (SE) and (b) cracking formation, 5.04 kX (BSE).

Two main effects are observed in anode due to the external shorting: melting, Fig. 5.18 (a), and microcrack formation, Fig. 5.18 (b). Melting can be caused either by the binder or the separator. Microcrack formation is due to the Diffusion Induced Stress (DIS) during the external short. The high deintercalation leads to high concentration gradient inside the active particle, which causing high stress accumulation and forms microcracks [65]. The small white dots in Fig. 5.18 (b) are the remaining salts from the electrolyte solution.

5.7.2 Normal Voltage Window - CF = 10 %

One of the cells with 10% of capacity fading, after been cycled in the Normal voltage window was subjected to an external short test. The SEM images taken from each of the electrodes are shown in Fig. 5.19.

In the graphite electrode, melted material was found on its surface, unlike the fresh cell which only has random distributed spots, the cycled cell exhibited large zones covered by this kind of material. In the NCAO electrode, degradation only on its surface was found; it seems like if the active particles crumbled. The material lost by the electrode, in most of the cases, was found stuck in the separator and the ceramic coating.

As a reference point, the melting point temperature of the materials surrounding the electrodes was investigated and listed in Table 5.1. This temperature is important because and the end this could be related with the melted material deposited on the abused electrodes.

Table 5.1 Melting point temperature of the cell components materials.

Name	Chemical Formula	Cell Component where it can be found	Melting Point Temperature [ºC]
Aluminum (III) Oxide	Al_2O_3	Ceramic coating	2072
Polyvinylidene Fluoride (PVDF)	$-(C_2H_2F_2)_n-$	Binder	177
Polypropylene (PP)	$-(C_3H_6)_n-$	Separator	160
Polyethylene (PE)	$-(C_2H_4)_n-$	Separator	115 - 135

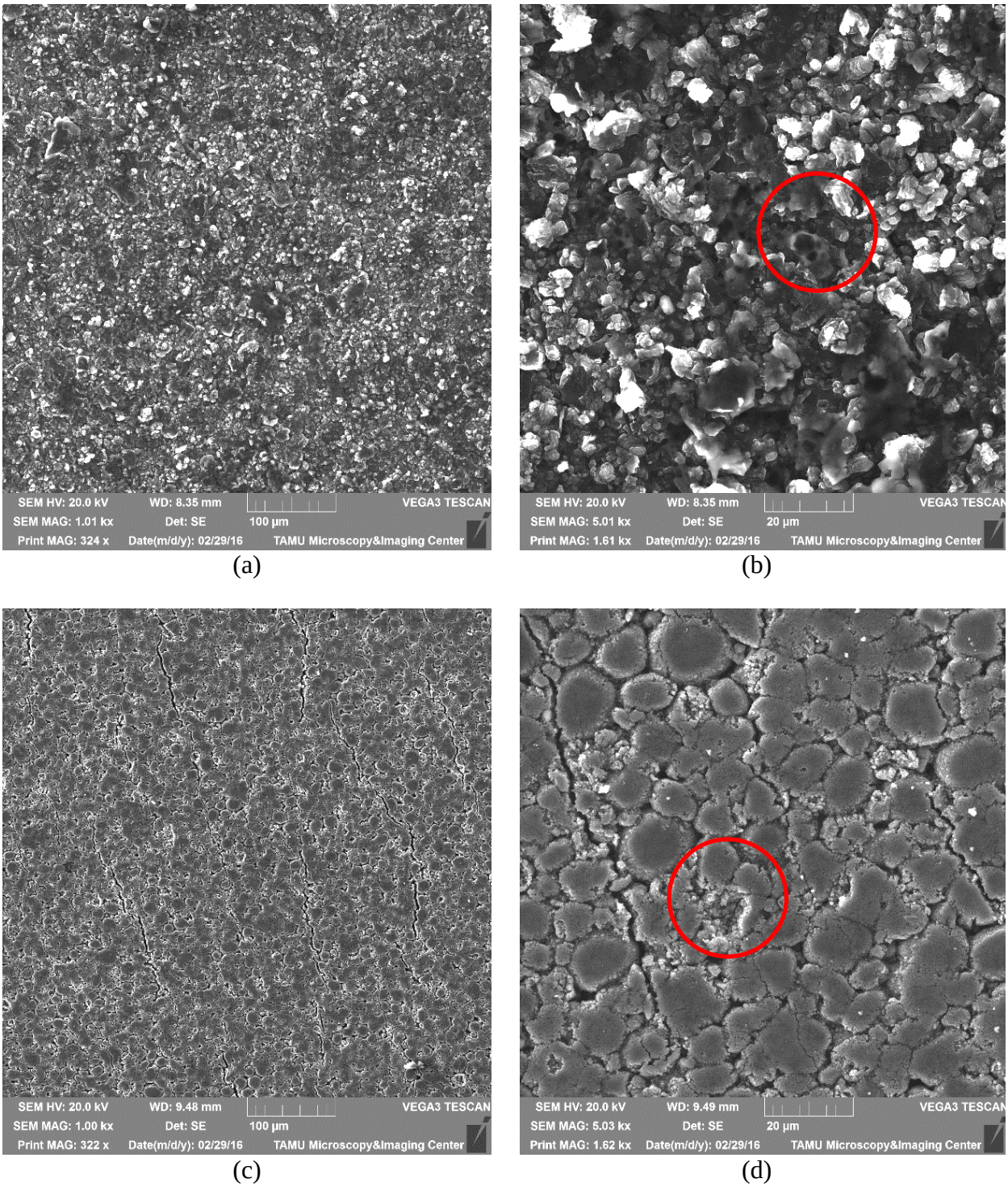

Fig. 5.19 SEM images of the electrodes from the externally shorted cell N10. Anode: (a) 1 kX (SE) magnification, and (b) 5 kX (SE) magnification. Cathode: (c) 1 kX (SE) magnification, and (d) 5 kX (SE) magnification.

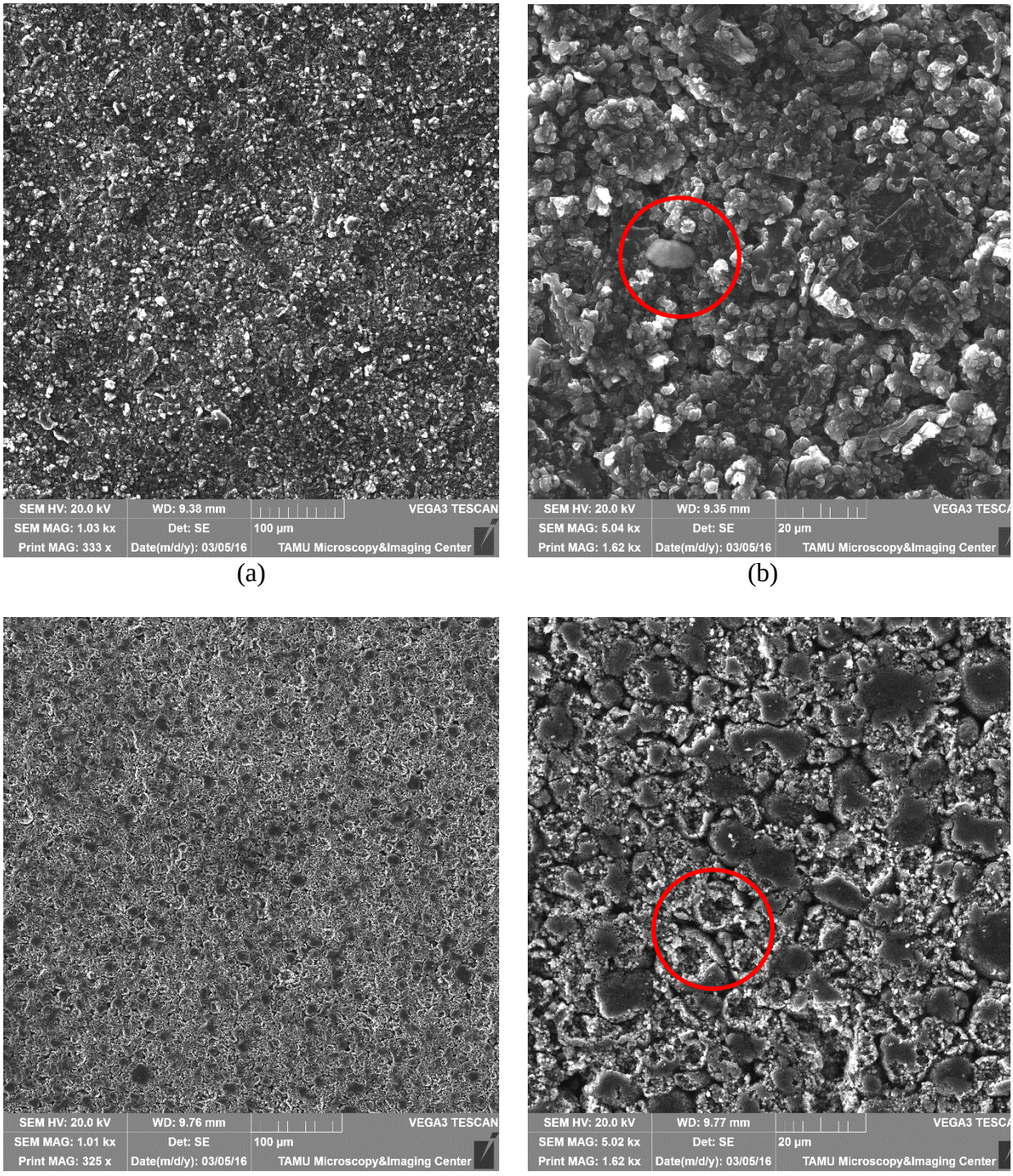

Fig. 5.20 SEM images of the electrodes from the externally shorted cell N20. Anode: (a) 1 kX (SE) magnification, and (b) 5 kX (SE) magnification. Cathode: (c) 1 kX (SE) magnification, and (d) 5 kX (SE) magnification.

5.7.3 Normal Voltage Window – CF = 20 %

One of the cells with 20% of capacity fading, after been cycled in the Normal voltage window was subjected to an external short test. The SEM images taken from each of the electrodes are shown in Fig. 5.20. It is important to remark that prior the safety test, the electrodes already have some degradation due to the cycling they had been subjected.

In the graphite electrode most of the surface and the laminated layers seems to be covered by the melted material. A new feature found is the presence of chunks stuck to the surface. Those chunks could be either material from the separator or binder. Even when the external cell temperature was small, inside of the cell the temperature could be higher and enough to melt either the binder or the separator.

In the NCAO electrode the crumbling of the electrode is more evident. This time, it happens not only in random spots but in a uniform way throughout the whole electrode. Information from the other cells will allow determining is this crumbling was due to the cycling or the external shorting.

5.7.4 Reduced Voltage Window – CF = 10 %

One of the cells with 20% of capacity fading, after been cycled in the Normal voltage window was subjected to an external short test. The SEM images taken from each of the electrodes are shown in Fig. 5.21. In this case the voltage window was reduced which cause that a large number of cycles were needed to achieve the desired capacity fading.

In the anode, there was a presence of melted material deposited on the electrode surface. The white spots in Fig. 5.21 (b) correspond to a non-conductor material. The spots are white due to a charging effect because the material cannot conduct the incident electrons. That material could be pieces of the separator.

In the cathode, no visible damage could be appreciated. In the cells from Section Ba, this electrode showed some crumbling but in this cell it doesn’t. The differences may arise due to the cycling effect and from the external short test.

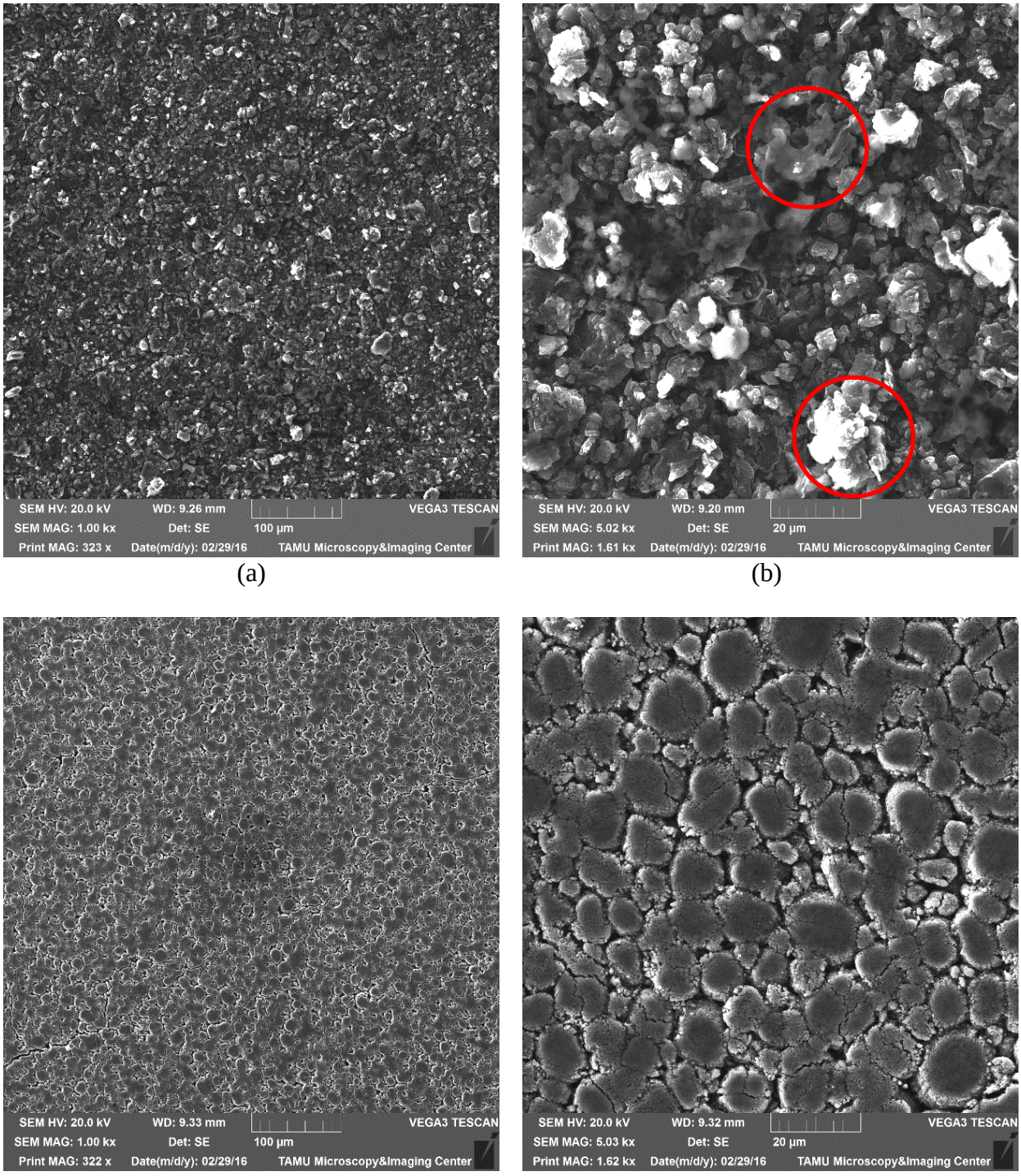

Fig. 5.21 SEM images of electrodes extracted from the externally shorted cell R10. Anode: (a) 1 kX (SE) magnification, and (b) 5 kX (SE) magnification. Cathode: (c) 1 kX (SE) magnification, and (d) 4.88 kX (SE) magnification.

5.7.5 Reduced Voltage Window – CF = 20 %

From the DPA it was found that the negative electrode showed some charring on the edge of the electrode as well in the zones where the tab was connected to the copper current collector. Fig. 5.22 (a) and (b) show a close up to this electrode. Four different zones can be identified in this electrode. Zone 1 (golden color) corresponds to the lithiated graphite. Zone 2 (gray/silver color) could either be some lithiated graphite at different SOC or some degraded graphite. Zone 3 corresponds to unlithiated graphite. While, there seems to be some charring in Zone 4.

(a) (b)

Fig. 5.22 DPA of Cell R20. Close up to the graphite electrode. (a) Electrode near to the center of the cell. (b) Different zones found in the electrode.

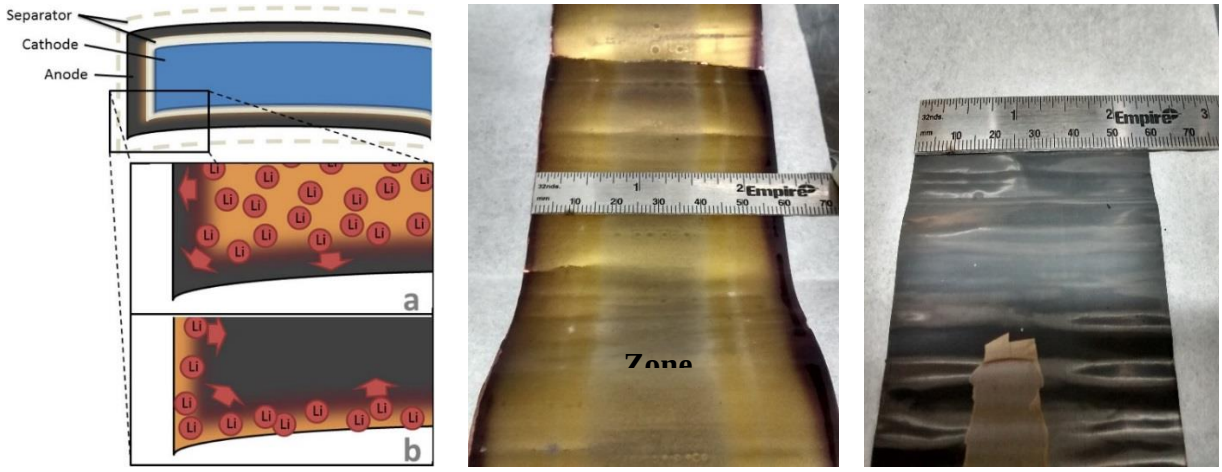

(a) and (b) (c) (d)

Fig. 5.23 DPA of Cell R20. (a) and (b) Schematic diagram of lithium diffusion between anode active region and overhang region[2]. (c) Width of the negative electrode, and (d) width of the positive electrode.

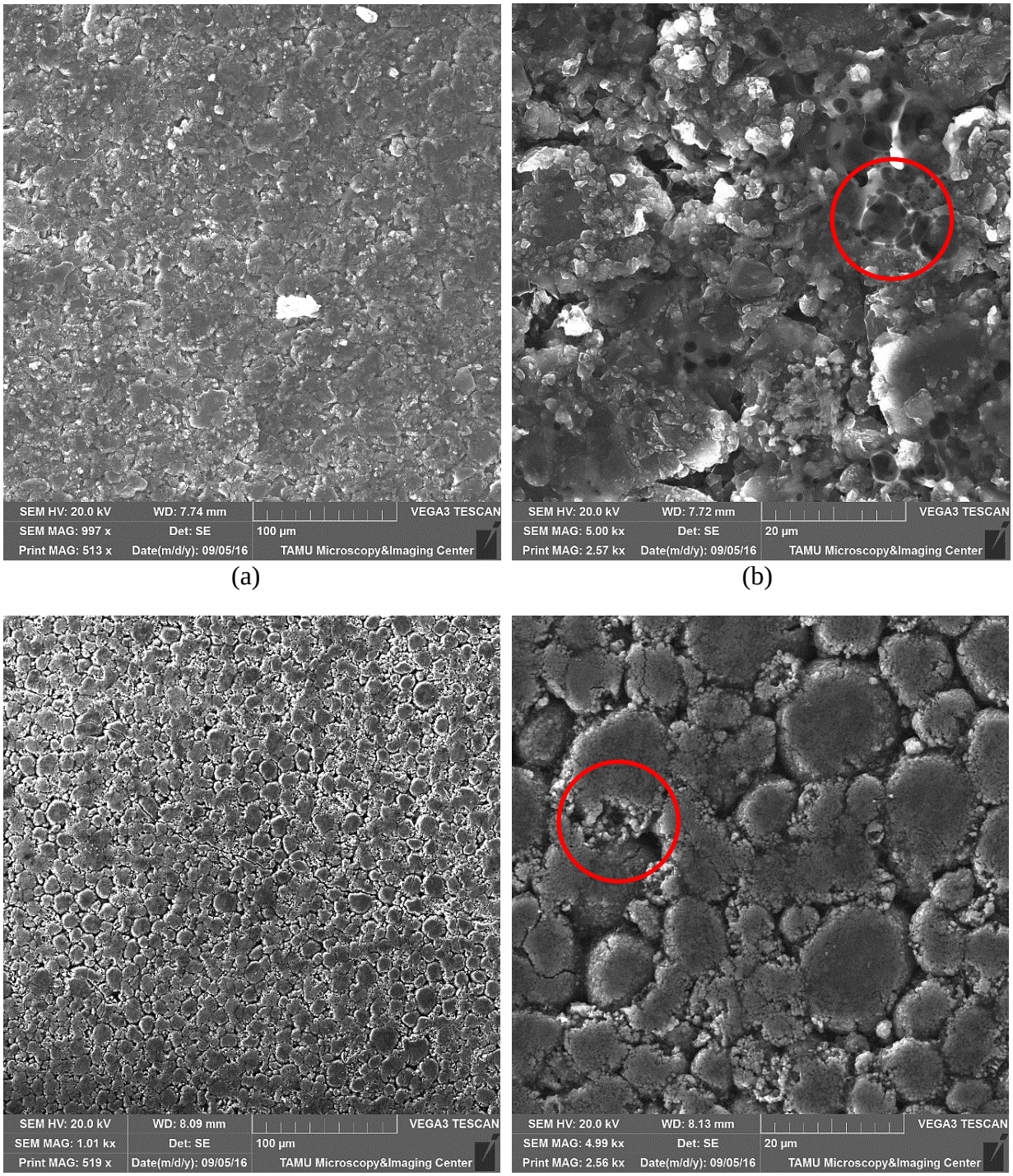

Fig. 5.24 SEM images of the electrodes extracted from Cell R20. Anode: (a) 1 kX (SE) magnification and (b) 5 kX (SE) magnification; Cathode: (c) 1 kX (SE) magnification and (d) 5 kX (SE) magnification.

According to Gyenes et al., the differences in color between Zone 1 and Zone 3 could be due to a difference in the size of the electrodes [88], particularly the width, see Fig. 5.23 (a) and (b). This difference will cause that the anode electrode overhang, the small portion of the electrode that extends past the positive electrode. The difference in coloring is due to a difference in the SOC on the different zones caused by the relatively slow diffusion.

To probe if there was an anode electrode overhang, the width of both electrodes was measured. However no difference in width was found, see Fig. 5.23 (c) and (d). The width of both electrodes was 6 cm. Another possible explanation for this difference in the SOC could be a misalignment of the electrodes.

The electrodes from this cell were studied via SEM. First, it was obtained low magnification images, from anode and cathode, to identify the most representative zones from them. In general, cathode, Fig. 5.24 (c) and (d), did not exhibit any damage on its microstructure. There was no found also any presence of melting of the separator. However, in the graphite electrode, there was found some material from the separator, see Fig. 5.24 (a). Even more, a presence of separator melting coated on top of the electrode was found, Fig. 5.24 (b).

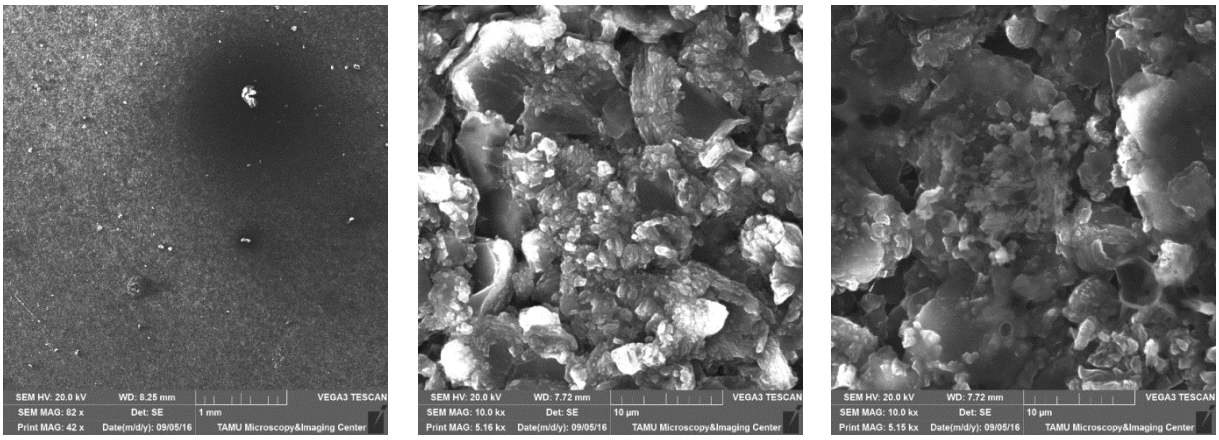

(a) (b) (c)

Fig. 5.25 SEM images of the graphite electrode. (a) Different zones found in the electrode, bright and dark zones, 82 X (SE) magnification. (b) Zone 1 (bright), 10 kX (SE) magnification. (c) Zone 3 (dark), 10 kX (SE) magnification.

To investigate if there was a difference between the Zones described in Fig. 5.25. The sample tested contained material from Zone 1 (Golden color, lithiated graphite) and Zone 3 (Black color,

unlithiated graphite). In Fig. 5.25 (a), it can be seen that the difference between the two zones is also evident from the SEM images. A close up to each of these zones reveals a meaningful difference between them. Fig. 5.25 (b) and (c) show that the Zone 1, which contains lithiated graphite, exhibits few zones covered with the melted separator. While, Zone 3, which contains unlithiated graphite, seems to be covered everywhere by this melting. This coating may cause some blockage of the active material and impede that it could be lithiated.

6. CELL LEVEL DEGRADATION: OVERCHARGE TEST IN CYLINDRICAL CELLS

Relevant Publications and/or Working Papers

1. D. Juarez-Robles, J. Jeevarajan, P.P. Mukherjee, 2019, *Degradation-Safety Analytics (DSA) in Li-ion Cells. Part 3. Overcharge Test on Fresh and Aged Cells,* working paper

6.1 Overcharge

Although overcharge for a single cell may not be a significant problem, when the entire battery pack gets damaged due to thermal runaway even in a single cell, the results can be catastrophic. As early mentioned, every commercial battery comes with a certain set of specifications as recommended by the manufacturer for safe operation of the battery. In the case of Panasonic Li-ion NCR18650B [189] cells used in the study, the voltage window of safe operation is prescribed to be from 2.7 V to 4.2 V. With that description in mind, overcharge of the cells is thus said to occur when the cell is charged beyond the upper limit of 4.2 V.

6.2 Cell Protections

Commercial Lithium-ion cells have several protective measures built into them to protect them from abusive conditions. These conditions can lead to a current and temperature surge in the cells leading to potentially hazardous consequences. Hence the need for in-built cell protections has been realized. Some of these measures are shutdown separators, positive temperature coefficient resistors (PTC), current interruption device (CID), printed circuit boards (PCB), pressure sensitive rupture disks and vents [190-191]. The most basic safety device in a battery is a fuse that opens on high current. Some fuses open permanently and render the battery useless; others are more forgiving and reset. In order to find better solutions, manufacturers have included various other safety measures within the cell as discussed below [192].

6.2.1 Shutdown Separators

Shutdown type separators have also been implemented in commercial batteries as one of the primary ways for abuse protection. A shutdown separator inhibits ion-flow by melting process

when exceeding a certain temperature threshold. However, there can be some drawbacks associated with it. Firstly, separator shutdown is an irreversible phenomenon. Secondly, even if a separator meltdown occurs, there is some current that is able to pass through micro pores in the separator which are formed due to high temperatures. Thus, this can pose a safety hazard if the battery is not disposed of immediately after separator malfunction. Early versions of Li-ion cylindrical cells primarily used polypropylene single layer separators. However, most of the prismatic Li-ion cells manufactured today either contain a PE single layer or a PP/PE/PP tri-layer separator. Since polyethylene has a lower melting temperature than polypropylene-, polyethylene-based separators offer lower shutdown temperatures [192]. There have been several studies in which various separator materials have been tested in regards to the improvement in overall thermal stability of cells. In the work done by Roth et al., separator response as a function of temperature and high voltage was measured for Li-ion 18650 cells. The separators used for their study were the Celgard Trilayer shutdown separator and SEPARION non-shutdown separator. The Celgard material is a shutdown separator consisting of three layers of polypropylene (PP) and polyethylene (PE) in a PP/PE/PP configuration while the Degussa SEPARION® material is a single layer of polyethylene terephthalate (PET) impregnated with alumina/silica [36]. Shutdown separators were found to delay the thermal runaway, yet it is important to realize that these separators only offer a delay – not complete protection from thermal runaway.

Fig. 6.1 A positive temperature coefficient device retrieved after disassembly from an overcharged 18650 Li-ion cell.

6.2.2 Positive Temperature Coefficient (PTC)

The resistance of a PTC device increases with an increase in temperature turning into a current limiting device. The active component in a PTC is a highly filled composite of conductive filler and polymer binder. When the temperature increases, the binder starts to expand thereby leading to an increase in the resistance of the composite. PTC is ideally supposed to be reversible and it is especially useful for damage caused due to external shorting. It protects against current surges. The current limiting capability and activation temperature can be modified by tailoring the active material used.

- Built-in to almost all 18650's
- Inhibits high current surges
- Protects against high-pressure, over temperature
- Resets and does not permanently disable the battery when triggered.
- May not work when module included multi-cell series and/or parallel configurations

Fig. 6.1 is a picture of the PTC device taken after disassembly of a Panasonic 18650 Li-ion cell. The two metallic disks are separated by a thin layer of conductive polymer. Conductive-polymers are phase change materials. The two plates sandiwich a blackish phase change material which transforms into an amorphous material upon activation. The expansion from this phase change inhibits current flow and increases the resistance of the cell thereby effectively bringing the current down to an acceptable level [190].

6.2.3 Current Interrupting Device (CID)

A CID can be indirectly activated by high temperature. Increase in the temperature inside the cell causes an increase in the vapor pressure of the non-aqueous electrolyte solvent, which triggers a break in the contact between the jelly-roll and header assembly. CIDs are built-in to almost all 1865 cylindrical Li-ion cells.

- They are not visible without opening the battery
- Incorporated together with the PTC
- May not work when module includes multi-cells series and/or parallel configurations

Because overcharge leads to thermal runaway in lithium-ion cells, many cell designs include built-in mechanisms to prevent overcharge. Overcharge can lead to significant gas generation within a cell prior to the cell entering a thermal runaway condition. In prismatic form factors, and particularly in cells with thin cases or with soft-pouch cells, gas generation within the cell will result in cell swelling and may force electrodes apart, effectively limiting the transfer of ions and interrupting charging. This process can prevent thermal runaway of the cells, but is not always effective. The geometry of cylindrical cells prevents separation of electrodes if gas generation occurs. Cell designers have developed mechanical charge interrupt devices (CIDs) for cylindrical cells used in consumer electronic devices. On activation, CIDs physically and irreversibly disconnect the cell from the circuit. Although CIDs are usually described as overcharge protection devices, they will activate if anything causes cell internal pressure to exceed the activation limit. This could include overcharge, cell overheating, significant lithium plating followed by electrolyte breakdown, mild internal shorting, and/or significant cell over-discharge. CIDs must also be appropriately matched to cell chemistry so that overcharge conditions result in sufficient gas generation prior to thermal runaway to activate the CID. If a CID is not properly matched to cell chemistry, low current overcharge or very high over currents may not activate a CID sufficiently early to prevent cell thermal runaway.

6.2.4 Safety Vents

With many cell chemistries, the electrochemical process can give rise to the generation of gases, particularly during conditions of overcharge. This is called gassing. If the gases are allowed to escape, the active mass of chemicals in the cell will be diminished, permanently reducing its capacity and its cycle life. Furthermore the release of chemicals into the atmosphere could be dangerous. Manufacturers have therefore developed sealed cells to prevent this happening. Sealing the cells however gives rise to a different problem. If gassing does occur, pressure within the cell will build up, this will usually be accompanied by a rise in temperature which will make matters worse, until the cell ruptures or ignites. To overcome this second problem sealed cells normally incorporate some form of vent to release the pressure in a controlled way if it becomes excessive. This is the last line of defense for an abused cell if all the other protection measures fail. Cells are not meant to vent under normal operating conditions. Usually during abuse, other devices described such as the PTC and CID override the vent.

While these measures may be sufficient in some applications, the scaling up of Lithium-ion batteries for use in automotive requires a more stringent approach to safety and protective measures. There are several complex processes that occur during the overcharge of Lithium-ion batteries. These may include but are not limited to:

1) An increase in cell temperature
2) Decomposition of the electrolyte
3) Lithium plating
4) Decomposition of electrodes
5) Gas evolution
6) Melting of separator

In order to address these issues, one or more of these approaches can be implemented:

- Increasing the exposed surface area of the cell will allow proper dissipation of the heat energy to the ambient
- Minimizing or eliminating the side reactions occurring during overcharge [193].

However, almost all the applications today require the batteries to be compact in size which eliminates solution 1. Thus, as it stands now, most research in Li-ion cells safety is geared toward finding a solution for the prevention of unwanted side reactions.

According to literature, there are several avenues towards which overcharge research is geared. Some of these may be aimed at characterizing better and thermally more stable electrode materials. Cui et al. found that when two cells with an LFP cathode but with differing anode materials were tested, significantly varied results were observed. The two anode materials compared were $Li_4Ti_5O_{12}$ and graphite [194]. It was found that the cell with the $Li_4Ti_5O_{12}$ showed better thermal runaway performance than its graphite counterpart. Similarly, another study done compared different cathode materials and their behaviour during overcharge. Two types of commercial 18650 Li-ion cells with different cathode materials were used in this work. The LCO-Graphite cells exhibited a thermal runaway behavior from 50% to 120% SOC, while LMO/Graphite cells exhibited a thermal runaway behavior from 75% to 120% SOC. In the case of 120% SOC,

overcharge, both cells presented a thermal runaway behavior, but there was a significant difference between the onset temperatures of thermal runaway. The onset temperatures of thermal runaway behavior at 120% SOC of the LCO/Graphite and LMO/Graphite cells were 176.4 °C and 189.8 °C, respectively. The cell using LCO as cathode material was found to be more thermally unstable than the cell using LMO [195]. Larsson and Mellander showed that Li-ion cells which were LFP based showed better thermal stability than their cobalt based counterparts [24]. Thus, it is widely published in literature that cobalt based cathodes are inherently more unstable than other chemistries. Some other works are geared toward finding ways to use electrolyte additives to improve cell performance and these have already been discussed in a previous section.

Other works aim to trace the step by step process of overcharge and perhaps the charging rate dependence of Lithium-ion cells [196-197].The research by Finegan et al. aim to probe the degradation mechanisms leading up to the overcharge-induced thermal runaway of a lithium-ion pouch cell [198]. A combination of high-speed operando tomography, thermal imaging and electrochemical measurements were used. Fig. 6.2 lays out a sequence of events related to the evolution of voltage, temperature and chemistry of cell leading up to thermal runaway.

- *Region 1*: Caused is alleged to be the irreversible heat generation mechanisms such as ohmic losses which are most prevalent at high C-rates.
- *Region 2*: Initiation and progression of the decomposition/formation of the SEI.
- *Region 3*: Rise in voltage is caused by the resistance increase associated with the gas pockets forming between the active layers and the subsequent fall in voltage is due to decrease in resistance by the bursting of the pouch and the gases are channeled away.
- *Region 4*: The sharp maximum voltage is due to the shutdown of the separator and damage to the internal circuit caused by rupture of cell.

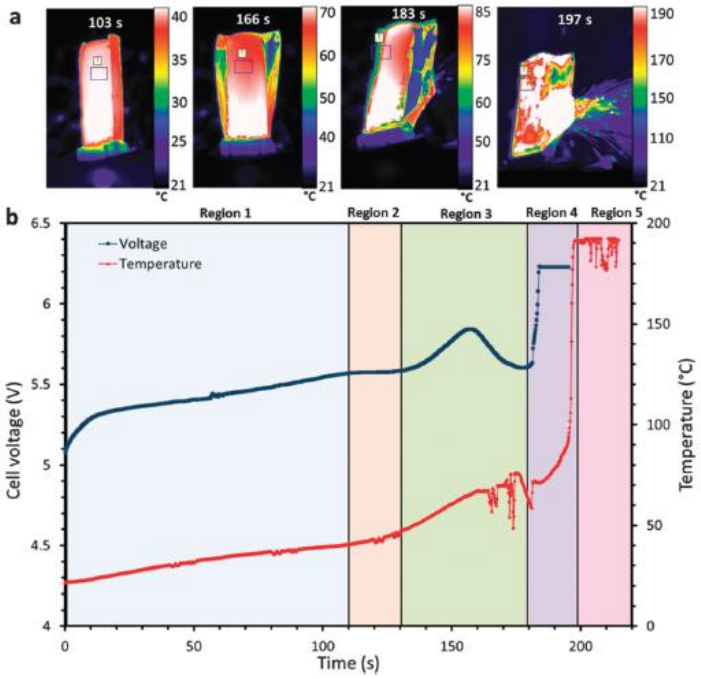

Fig. 6.2 Degradation mechanisms leading up to the overcharge-induced thermal runaway of a lithium-ion pouch cell.

Batteries are constructed in a variety of shapes and sizes. Some common cell designs are cylindrical or prismatic cells. To form higher voltage batteries, the cylindrical cells are stacked in series and sealed together. Higher current can be obtained by increasing the electrode area, resulting in a larger diameter or longer length cell. A single cell that is wrapped by heavy outer plastic layers may create situations where ventilation is a concern. This condition worsens in large battery packs since the batteries are installed very close to each other in these packs. As one of the main degradation factors, overcharge occurs not only in a single cell, but also in battery packs where the cells are connected in series and there is a mismatch in their capacity. When these cells are used by the thousands such as in the case of a Tesla Model S vehicle, the large number of cells with even minor inconsistencies can easily accumulate significant heat.

As previously mentioned, every commercial battery comes with a certain set of specifications as recommended by the manufacturer for safe operation of the battery. According to the instructions of most battery manufacturers, the reliable operating temperatures required by a majority of current automotive lithium-ion batteries (C/LMO, C/NCM, C/LFP, C/NCA) are: discharging at -20 to

55 °C and charging at 0 to 45 °C and for lithium-ion battery with LTO negative electrode, the minimum charge temperature can be -30 °C. Usually, the operating voltage of lithium-ion batteries is between 1.5 V and 4.2 V (C/LCO, C/NCA, C/NCM and C/LMO about 2.5-4.2 V, LTO/LMO about 1.5-2.7 V and C/LFP about 2.0-3.7 V) [195].

At this point, it is prudent to highlight an important fact. Batteries are constructed in a variety of shapes and sizes and their overcharge behavior is heavily dependent on the cell design and manufacturing processes. The varied electrode materials, cell manufacturers, solvent/electrolyte chemistries and basic cell type/design are all parameters that significantly affect the obtained results. Hence, despite the widely available literature on overcharge behavior of Li-ion cells, very little commonality is to be found.

6.3 Experimental

Overcharge (also called high voltage) in a lithium ion battery happens when it is charged up far away from the safe operating voltage window. Cell manufacturers specify a voltage window of operation to ensure continuous and safe operation. This voltage window describes the lowest discharge voltage and highest charge voltage. Usually when a cell is charged beyond this upper voltage cutoff, it is said to be in an overcharge state. The upper limit is set to ensure that the cathode material is not deintercalated beyond its cyclable lithium amount, electrolyte is stable and anode does not experience deteriorating effects such as lithium plating, dendrite formation and extreme growth of Solid Electrolyte Interphase (SEI).

Cycling Protocol Prior the Overcharge Test

1. *Preparation*: CCCV charging, at 1C, up to 4.2 V with a cutoff current of 50 mA.
2. Rest 30 minutes.
3. *Overcharging*: CC charging the cell up to 12 V or until an event stop the test.
4. Rest 30 minutes.

Two cells were tested under this protocol and their results are shown in Fig. 6.3. In these plots, it is shown only the profile for the overcharge. When a cell is charge or discharge in the

recommended voltage window, the cell temperature raises due to the electrochemical reactions and the processes happening in the cell. In the overcharge test, it was also found a raise in temperature due to the electrochemical reactions happening during the lithium intercalation in the anode. However this temperature raising will be accompanied of an extra term due to the side reactions caused by the abuse. In fact, it can be appreciated that the temperature increment is not monotonically but rather multiple trends can be appreciated. These different trends had been associated in the technical literature to dendrite formation, electrolyte decomposition, internal short circuit, and degradation not only from both electrodes but also from the separator and its ceramic coating.

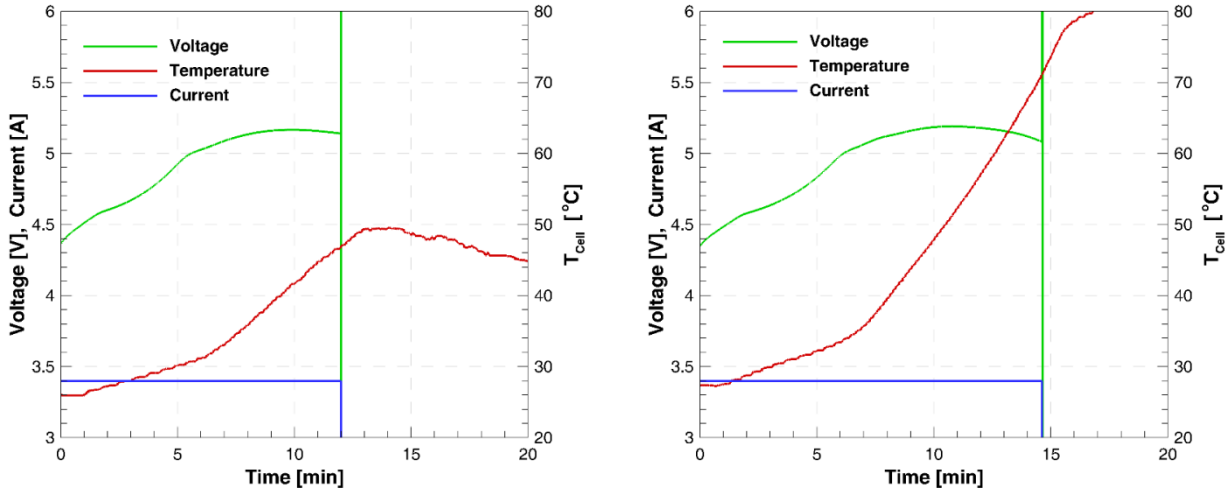

(a) (b)

Fig. 6.3 Variation of voltage, current and temperature during the overcharge of (a) fresh cell 1, and (b) fresh cell 2.

In both cells the Current Interrupt Device (CID) got activated before reaching the set upper bound voltage. The maximum temperature reached by the fresh cell 1 was 49.5 ºC, and 80.3 ºC for the fresh cell 2. The difference in temperature can be due to the thermocouple position. In the first cell, the tip of the thermocouple got exposed to the ambient temperature. While for the second cell it was completely insulated and attached to the cell. One important fact about the thermal response is that even when the cell already failed, its temperature still keep increasing as can be appreciated in Fig. 6.3.

During the test, the cell got internally disconnected. In order to check the internal connection, the cell resistance was measured with a multimeter obtaining an average value of ~300 kΩ for the cell 1 and ~15 kΩ for the cell 2. The higher resistance is a clear signal that the cells are internally disconnected. Moreover, the maximum voltage achieved by the cells did not overpass the 5.3 V. During the failure, the voltage measurements exhibited voltages larger than 50 V and then lower than 0 V (this part correspond to the green vertical line from Fig. 6.3 at the end of the test). These extreme values could either represent the moment where the CID kicked in or that the voltage measurement was simply out of the range of the battery tester.

It is important to remark that the test can be done only once since the cell cannot be cycled after the test is done. For that reason, only one conditioning test was conducted prior the overcharge test after that the cell was only subjected to a DPA. This step is suggested to be done carefully. Opening an overcharged cell is dangerous even when is done in a glovebox.

6.4 Overcharge Test of a Cycled Cells

Voltage, current and temperature profiles during the test are shown in Fig. 6.4. The temperature reported in this Figure corresponds to the cell temperature. A type - J thermocouple was tape along the axial direction on the cell surface. The overcharge test strongly depends on the C-rate used to keep charging the cell. At 1C-rate the average test time is 8 minutes.

In all tests, the electrical current has a constant value, since the cell is overcharged using a CC protocol. Meanwhile, voltage increases until one of the cells protections get activated. After the cell gets disconnected, voltage suddenly increases to a large voltage and one instant later drop to zero or below. One point of interest is the maximum voltage achieved by the cells during the test. In all the cases, this value was ~5.2 V. This maximum voltage has a strong dependence on the C-rate used to overcharge the cell.

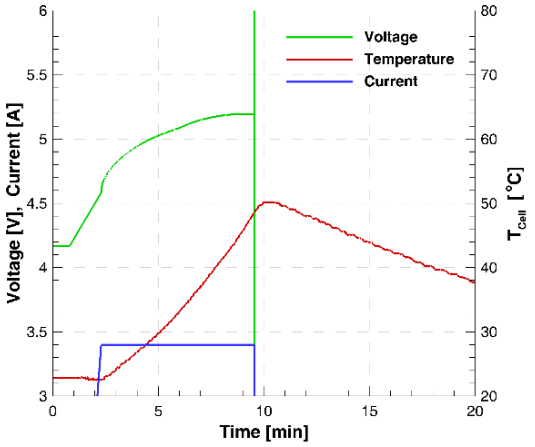

(a) Normal Voltage Window – CF = 10%

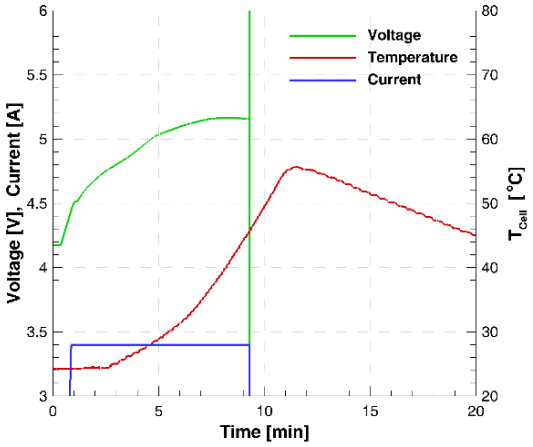

(b) Reduced Voltage Window – CF = 10%

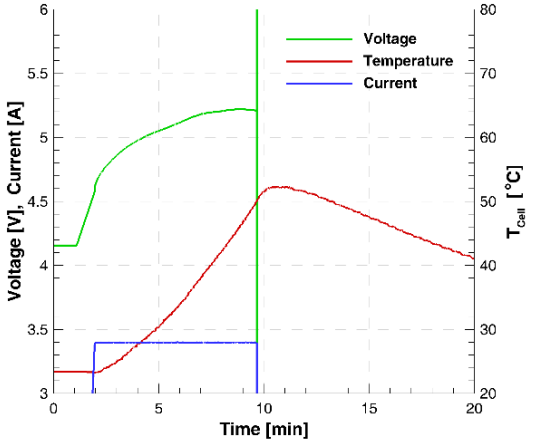

(c) Normal Voltage Window – CF = 15%

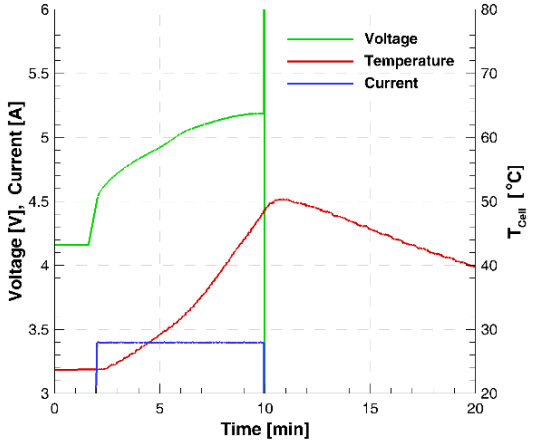

(d) Reduced Voltage Window – CF = 15%

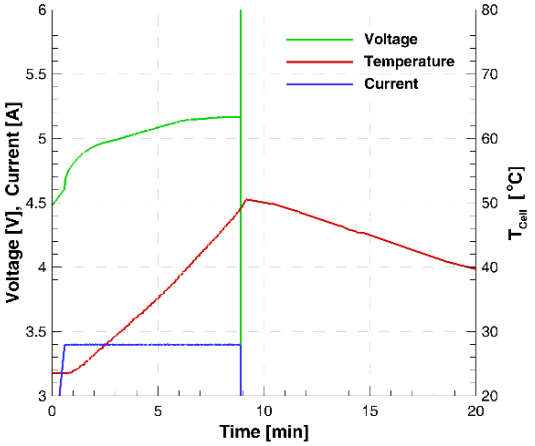

(e) Normal Voltage Window – CF = 20%

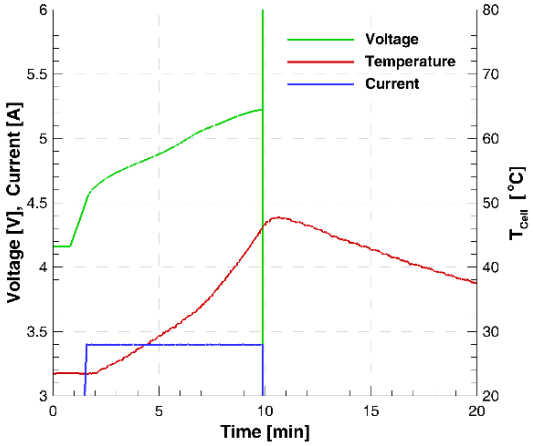

(f) Reduced Voltage Window – CF = 20%

Fig. 6.4 Current, voltage and cell temperature response from overcharged cells after been cycled.

The voltage profile has multiple subtle characteristics but also meaningful. One way to appreciate this, it is by taking a look at how the voltage increases with time. First of all the rate of growth is not monotonically. Near to the failing point, the cells with low capacity fading exhibit a maximum voltage, after which the voltage decays and leads to failure. As the capacity fading increases, this increase-decrease-trend in voltage disappears and the cell simply reaches its maximum voltage and immediately fails.

During the charging process, temperature starts increasing. And, it keeps increasing after the cell gets internally open. The main difference between the Fresh cells and the cycled cells is the elapsed time after the test while the cell still keeps increasing its temperature. For the cells cycled in the normal voltage window the maximum temperature achieved is the same for the three cycled cells no matter their capacity fading. For the cells cycled in the reduced voltage window, there is a clear trend for the thermal response. The maximum temperature of the cell decreases as the capacity fading of the cell increases. Based on the range where the cell where operating during this safety test, it can be ensured that the PTC protection did not got activated.

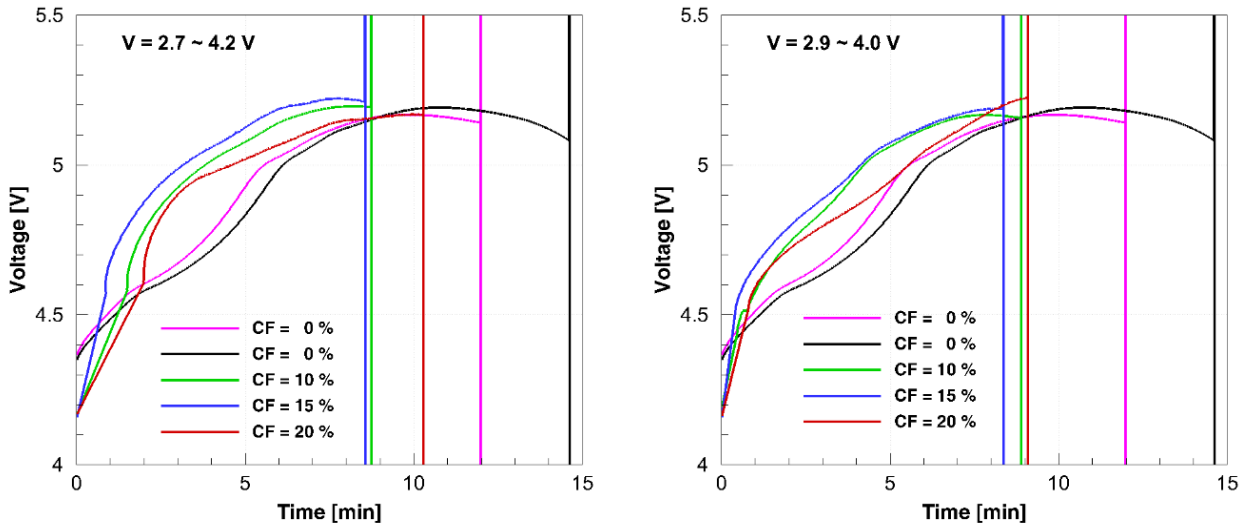

(a) (b)

Fig. 6.5 Overcharge test comparison. Overcharge voltage profile of the cells cycled in the (a) Normal, and (b) Reduced voltage window.

6.5 Overcharge Test – Comparison of All Cells

A comparison of all the experimental results is shown in Fig. 6.5 and Fig. 6.6. In general terms, there is not a clear trend neither in the voltage nor the temperature profiles. Only the fresh cells can hold this abuse test for a longer time. The same cell is the one that exhibited the highest temperature of the cell.

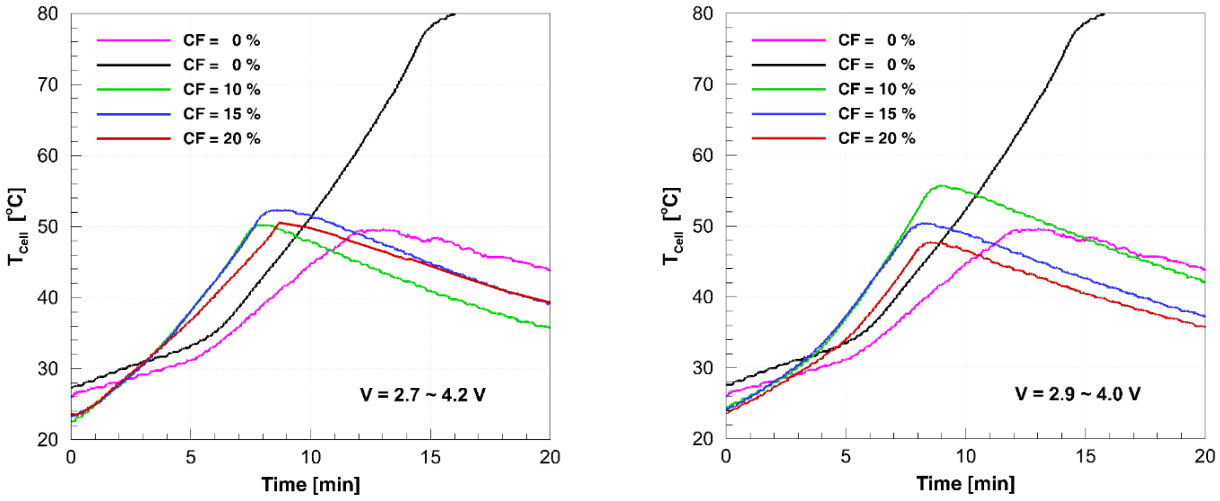

(a) (b)

Fig. 6.6 Overcharge test comparison. Temperature of the cells cycled in the (a) Normal, and (b) Reduced voltage window.

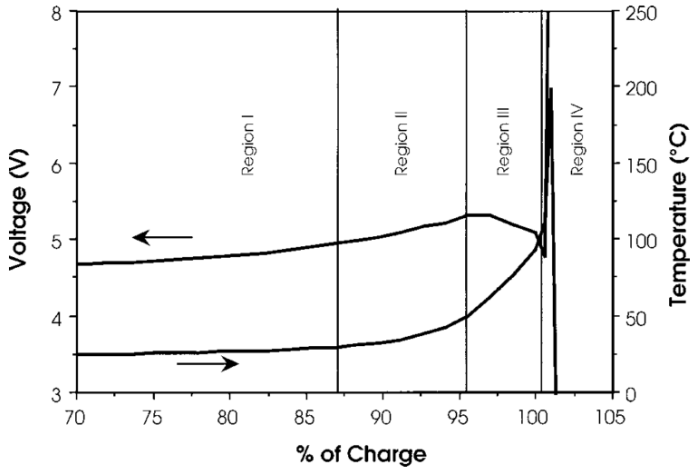

Fig. 6.7 Temperature and voltage overlay plot for 1.5 Ah prismatic Li-ion cell overcharged at 1.5 A with a 12 V power supply. Temperature was measured in the internal cell stack. 100% of charge is equivalent to full removal of Li from $LiCoO_2$ in the cathode [199].

6.1 Overcharge Test - Regions

So far, the results for overcharge test have been analyzed only based on the maximum temperature and voltage achieved. One interesting result was found in the literature in regards to the processes happening during the overcharge test. Leising et al. conducted an overcharge test in a $LiCoO_2$/Graphite cell (1.5 Ah) [199]. Their analysis not only focused on the maximum temperature but also how temperature raises. They identify four different stages/regions during the test, see Fig. 6.7.

Region I

1. Voltage increases at a mostly steady rate during overcharge from the increase of the cathode potential with increasing delithiation of Li_xCoO_2. At greater than 60% charge, lithium metal would be deposited on the graphite anode.
2. Cell swelling was measured during this region of the test, and is likely due to electrolyte oxidation at the high voltage cathode.
3. Temperature is stable and shows little increase during this portion of the test.

Region II

1. Temperature begins to rise at a slow rate.
2. An increase in cell R_{dc} is measured in the 80 to 95% charge range which is associated with increased resistance at the cathode, but returns to a lower value at >95% charge.
3. The cell voltage peaks at >5V.

Region III

1. The cell temperature begins to rise more rapidly, with an inflection point at >95% of charge.
2. The cell voltage begins to drop slightly from about 95% charge to just before 100% charge.
3. When the internal temperature of the cell reaches >100°C the voltage of the cell sharply falls for a brief period, most likely due to a decrease in the internal resistance of the cell due to the elevated temperature.

Region IV

1. Above an internal temperature of 135°C, the polyethylene separator begins to melt and greatly increases the internal resistance of the cell. The cell voltage spikes to the limit of the power supply (~12 V), and the current drops to a lower value.

2. The voltage of the cell becomes unstable, in the 10-12 V range. The current also fluctuates.
3. The internal cell temperature increases rapidly and is recorded in the 190-220 °C range just before the cell ruptures.
4. The cell ruptures.

Similar regions can be observed in the cells overcharged in this project. Temperatures and voltages may not be the equal since the materials are not the same. But similar trends and regions can be found in the voltage – temperature profiles, see Fig. 6.8.

An analysis of the limits of these regions in the entire overcharged cell may help to define how far it can extend the safety voltage operating window for this particular brand/cell. The properties and processes happening on each region must be corroborated experimentally and by conducting a post-mortem analysis of the different components within the cell.

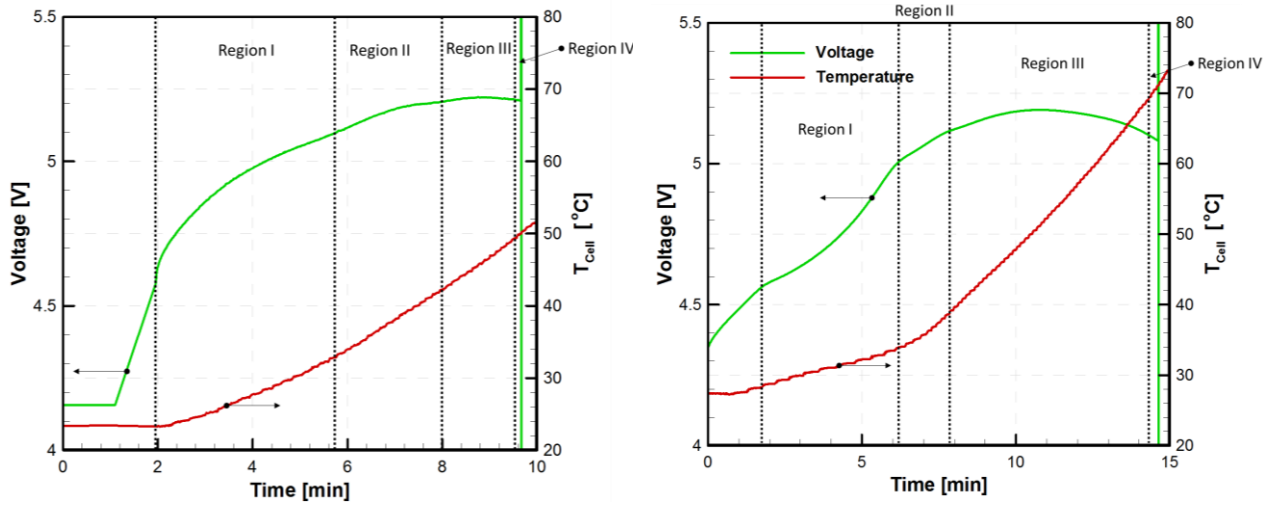

Fig. 6.8 Temperature and voltage profiles during overcharge test for Cell N20 (15% CF) and Fresh cell 2.

6.2 Destructive Physical Analysis

6.2.1 DPA of an Overcharged Fresh Cell

Two fresh cells were subjected to an overcharge test. In both cases, the cell protection got activated during the test disconnecting the cell internally. The CID is one of the protections included in this kind of cells. If the pressure within the cell significantly increases, it pops up and disconnects the

cathode from the jelly roll electrodes. One of the overcharged cells (OC Cell 0) was opened and the electrodes were extracted to be studied. The electrolyte was collected and stored in the glovebox to be tested later.

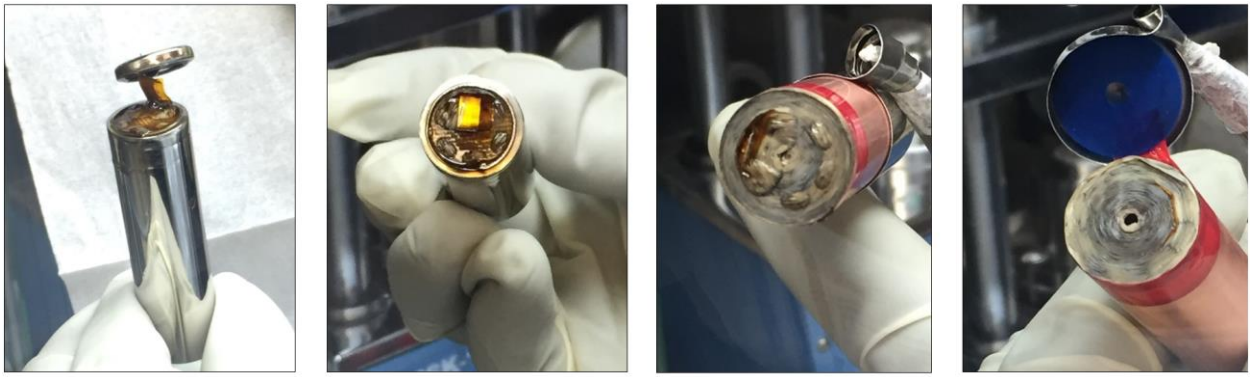

Fig. 6.9 DPA of the cell subjected to the overcharge test. (a) Bubbling in the cell, (b) electrolyte decomposition, (c) cathode connection, and (d) anode connection.

After opening the cell in the glovebox, some internal damage could be seen. At the beginning, there was some bubbling within the cell, which can be caused due to some internal reaction, see Fig. 6.9 (a). This side reaction it is most likely be due to lithium plating since the lithium film would start reacting, with the few amount of oxygen contain in the glovebox, once the electrodes got exposed. The electrolyte showed some decomposition turning into a brown color (typically translucent), see Fig. 6.9 (b). Electrolyte was collected in an IKA tube and stored in the glovebox. Fig. 6.9 (c) and (d) show the exposed electrodes to the cathode and the anode connection, respectively. It can be visualized that there is a black strip in the center of the anode electrode. That area corresponds to the zone where the nickel tab is connected and it appears even a fresh cell.

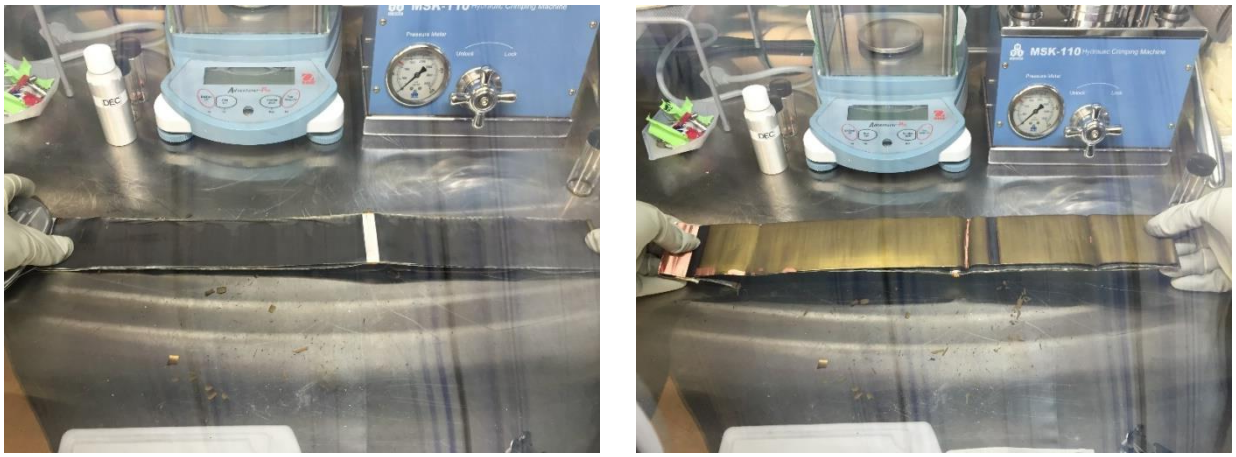

(a) (b)

Fig. 6.10 Electrodes from a fresh cell subjected to the Overcharge test. (a) Cathode, and (b) anode.

The cathode electrode did not show any visual damage, Fig. 6.10 (a). While, the anode electrode showed a golden color due to the intercalated lithium in the graphite, see Fig. 6.10 (b). Graphite was completely dry and it flaked off just by handling it, especially in the zone near to the center of the cell. The main damage happened in the separator. The ceramic coating came out from the separator and got stuck to the cathode electrode; see Fig. 6.12 (b).

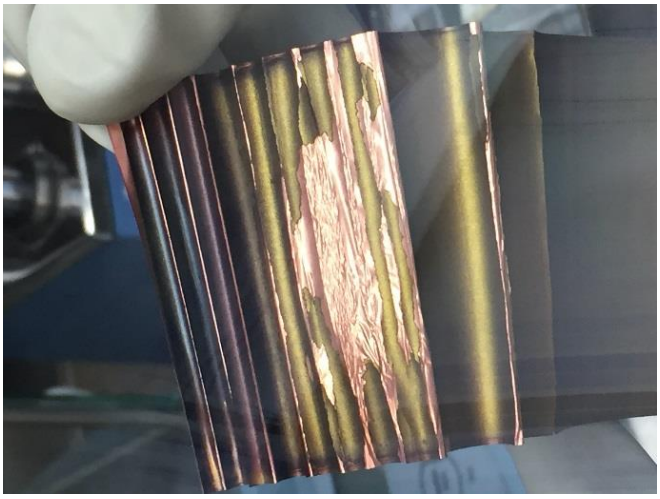

Fig. 6.11 Burning of the anode electrode in the zone near to the center of the cell.

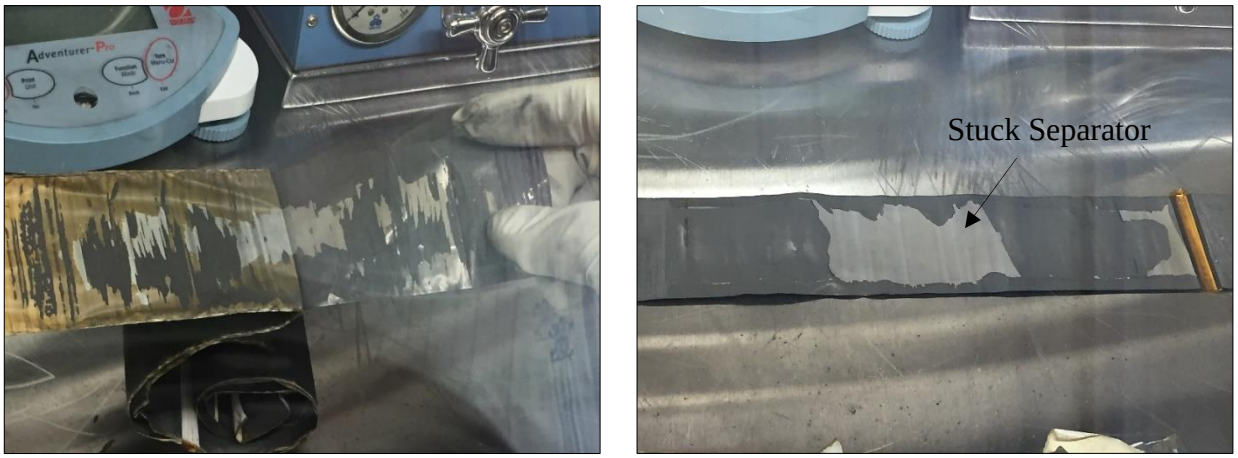

(a) (b)

Fig. 6.12 (a) Cathode material coming out of the electrode and getting stuck on the separator. (b) Melted separator stuck on the cathode material.

6.3 DPA of an Overcharged Cells after Cycling

The overcharged test consists on charging the cell beyond the recommended upper limit voltage provided by the manufacturer. The commercial cells (NCR18650B) used in this study have an upper voltage of 4.2 V. The cells are first fully charged up to 4.2 V using a CCCV protocol. Then, they are charged up to 12 V or until cell failure occurs.

The electrodes extracted from the overcharged cells are shown in Fig. 6.13 and Fig. 6.16. In some cases the electrodes may appear to fell apart like in the anode electrode side, facing toward the center. In that case, only pictures of one of the sides of the electrode were initially collected. In order to reduce the occupied space the electrode was cut in multiple times. In some cases, a sample disk was punched from the electrode to be analyzed in the electron microscope.

Normal Voltage Window CF = 10%	Electrode facing outward the center	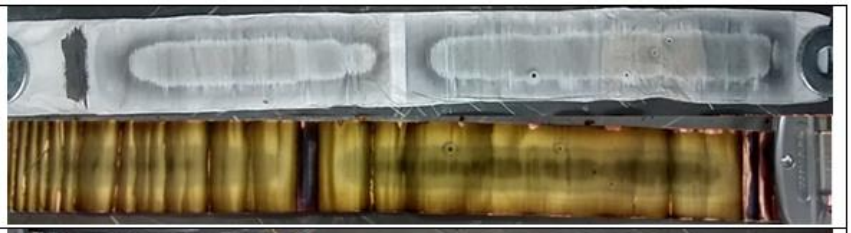
	Electrode facing toward the center	
Normal Voltage Window CF = 15%	Electrode facing outward the center	
	Electrode facing toward the center	
Normal Voltage Window CF = 20%	Electrode facing outward the center	
	Electrode facing toward the center	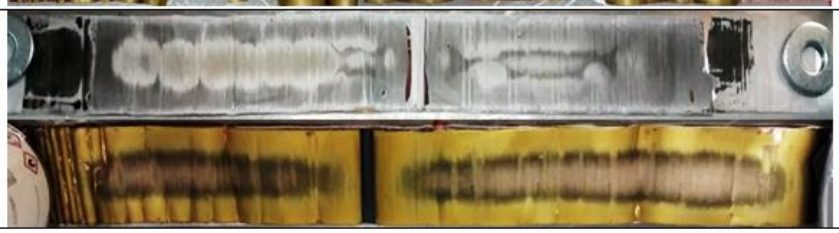

Fig. 6.13 Graphite electrodes and separators, without a ceramic coating, extracted from cells cycled in the Normal voltage window and then overcharged.

Normal Voltage Window CF = 10%	Electrode facing outward the center	
	Electrode facing toward the center	
Normal Voltage Window CF = 15%	Electrode facing outward the center	
	Electrode facing toward the center	
Normal Voltage Window CF = 20%	Electrode facing outward the center	
	Electrode facing toward the center	

Fig. 6.14 NCAO electrodes and separators, with a ceramic coating, extracted from cells cycled in the Normal voltage window and then overcharged.

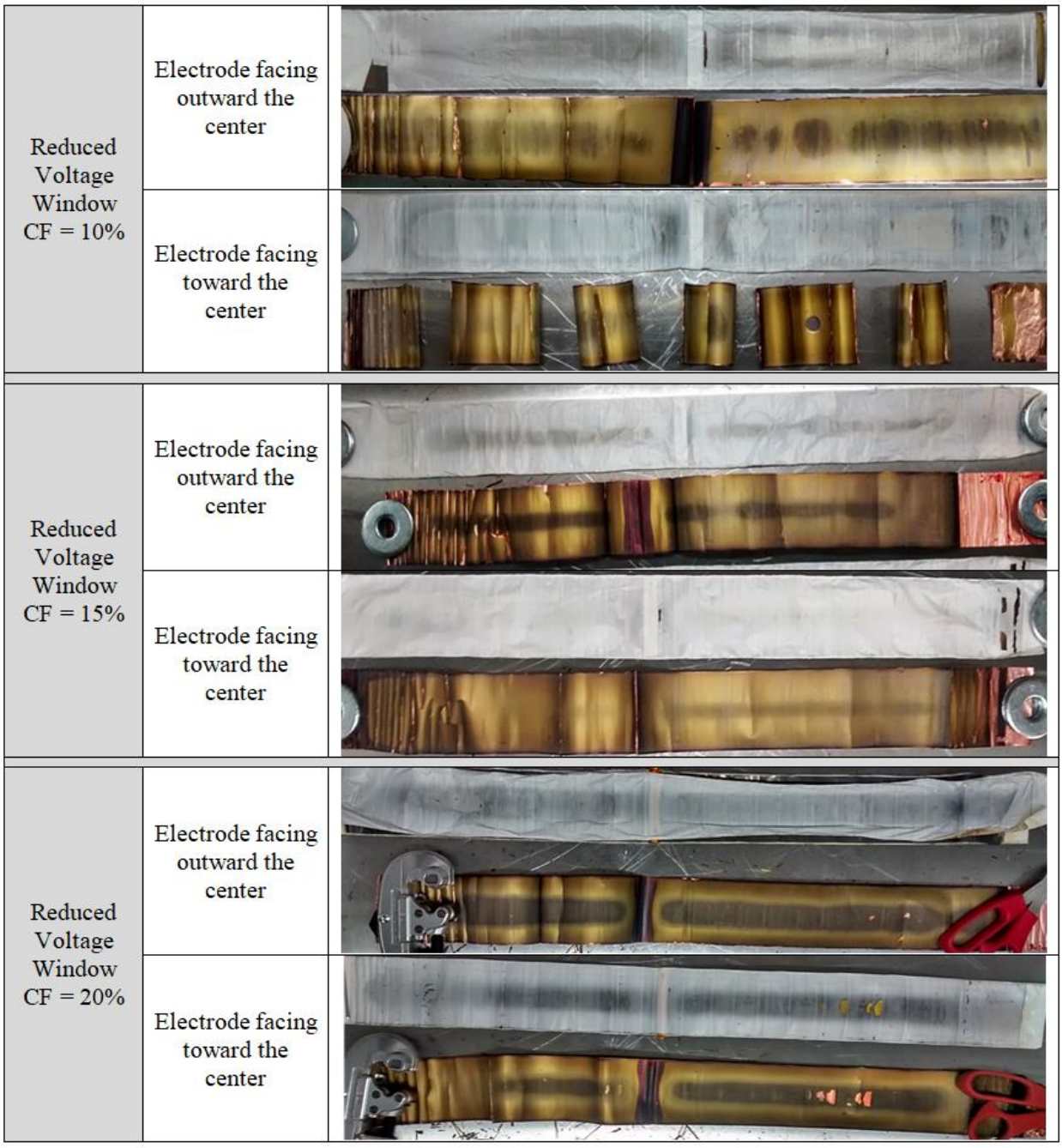

Fig. 6.15 Graphite electrodes and separators, without a ceramic coating, extracted from cells cycled in the Reduced voltage window and then overcharged.

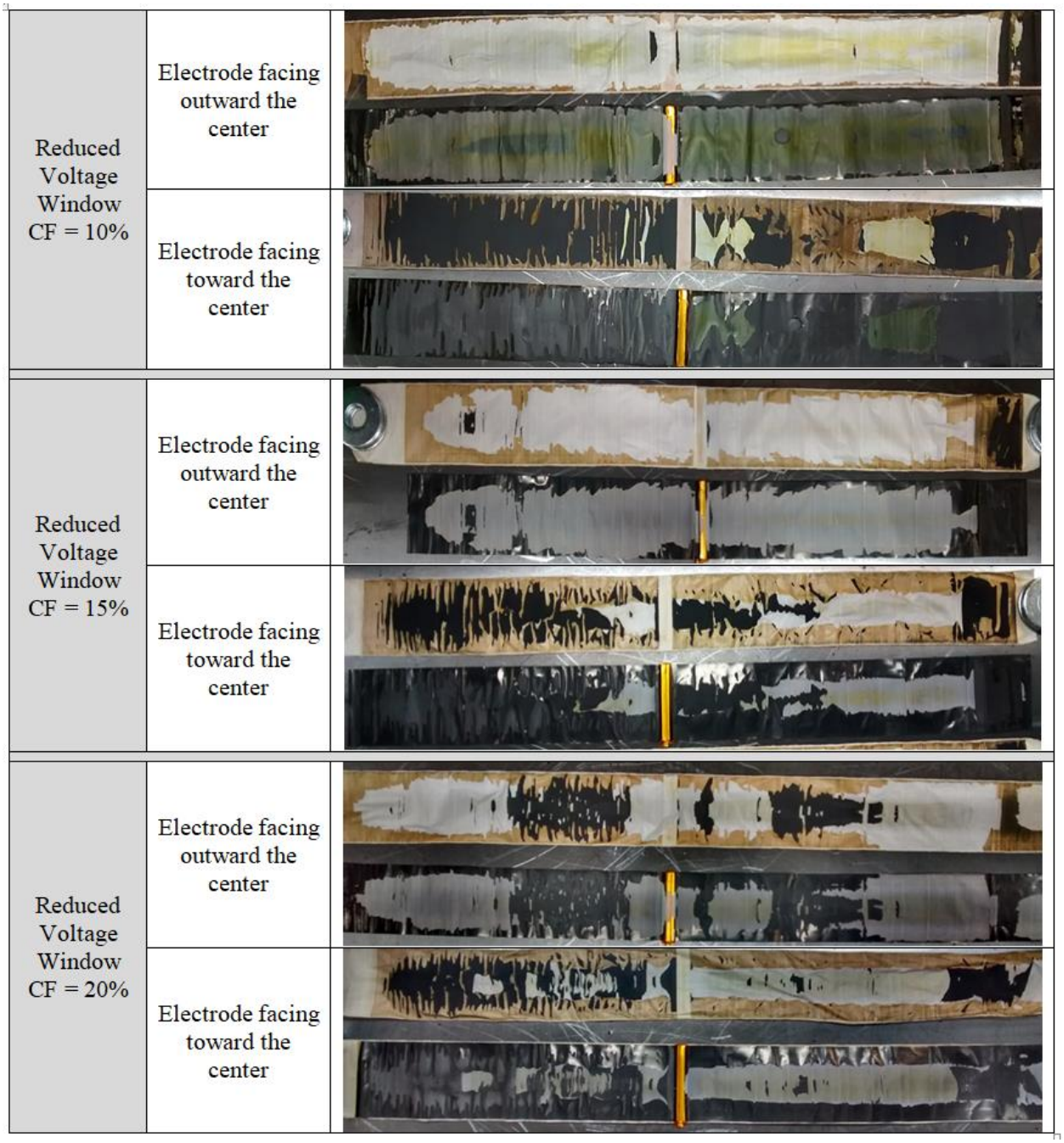

Fig. 6.16 NCAO electrodes and separators, with a ceramic coating, extracted from cells cycled in the Reduced voltage window and then overcharged.

The effect of overcharging the cell showed this time some effect in the graphite electrode. Anode material from the center of the electrode appears stuck in the separator. One hypothesis for this effect is due to dendrite formation and penetration of the separator. Degradation in the cathode electrode can be correlated with the colorimetric state of charge of the cell. The zones in anode

fully lithiated zones (golden color) in anode corresponds to the zones with larger damage in the cathode. These particular zones seem to provide more lithium during the overcharge causing mechanical stability problems and leading the cathode material to come out of the electrode.

6.4 SEM/EDS

6.4.1 Fresh Cell

An uncycled fresh cell was charged beyond the voltage specifications provided by the manufacturer. Initially the cell was aimed to be charged up to 10 V at 1C-rate. However, the cell got internally disconnected before it reached the set upper voltage. Cathode electrode did not present any significant damage on its microstructure, see Fig. 6.17 (a). However, some parts of the cathode electrode got stuck in the separator and the material come out exhibiting the inner layers of the electrode as shown in Fig. 6.17 (b). A higher magnification of the sample showed some deposition on the electrode, see Fig. 6.17 (b). The presence of phosphorus on the EDS test, Fig. 6.18, indicates the presence of dry electrolyte.

The SEM and EDS results conducted on the anode electrode are shown in Fig. 6.19 and Fig. 6.20. In comparison with the fresh cell, the anode material presented some kind of coating on its surface. Initially it was thought that it was due to the melted separator. However, based on the cell temperature it does not seen to be likely that neither the separator nor its ceramic coating can get melt at that temperature.

The EDS test conducted on the anode indicated the presence of electrolyte and a large concentration of oxygen. It is important to remark that the electrode samples were stored in a closed glass vial filled with Argon. The samples were exposed to air only when they were placed onto the microscope platform. This exposition could cause some reaction between the oxygen in the environment and the intercalated lithium ions on graphite. The reaction between these two elements was reflected during the EDS, Fig. 6.20, where an oxygenated species was detected.

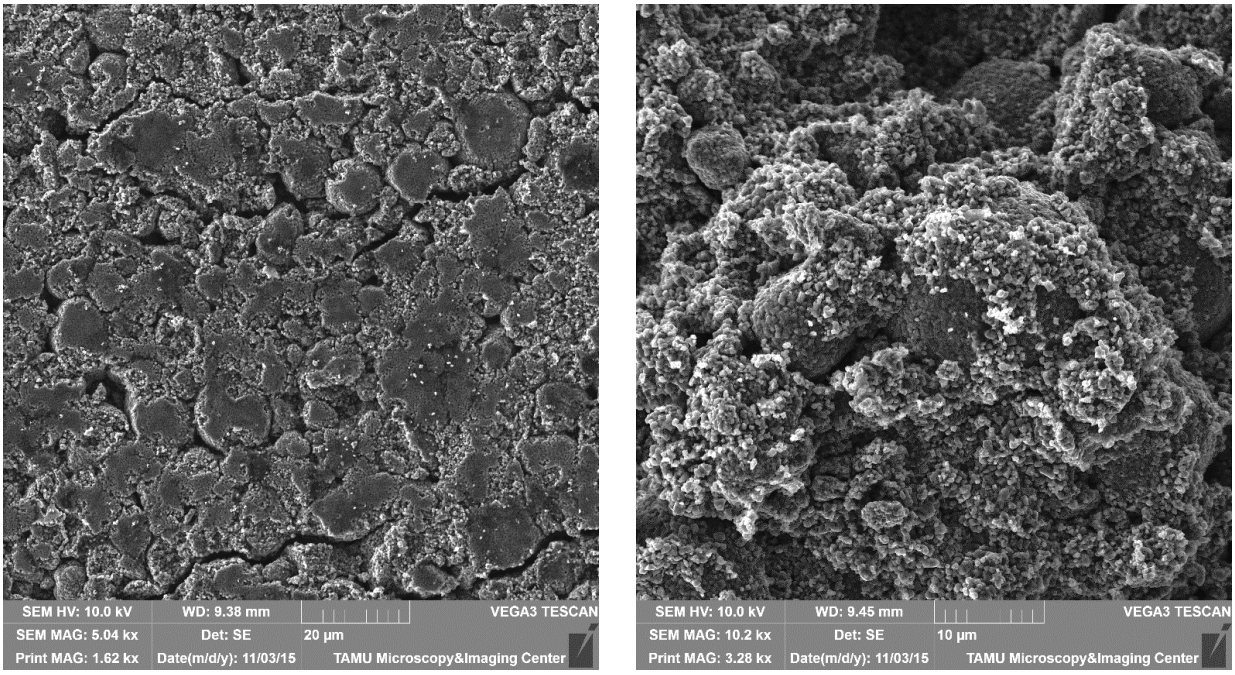

(a) (b)

Fig. 6.17 SEM images of cathode extracted from an overcharged fresh cell at (a) 5 kX (SE) magnification, and (b) 10 kX (SE) magnification.

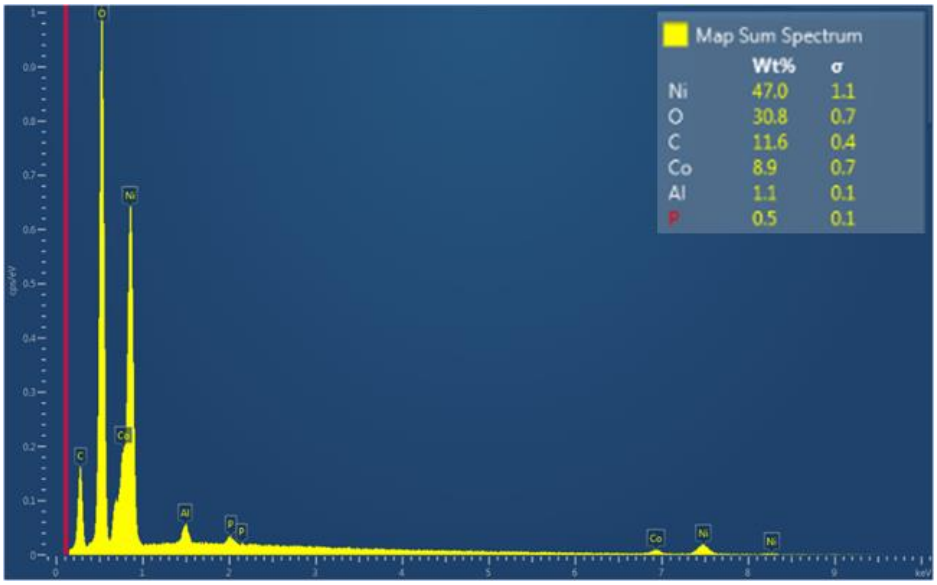

Fig. 6.18 EDS results for the cathode electrode extracted from an overcharged fresh cell.

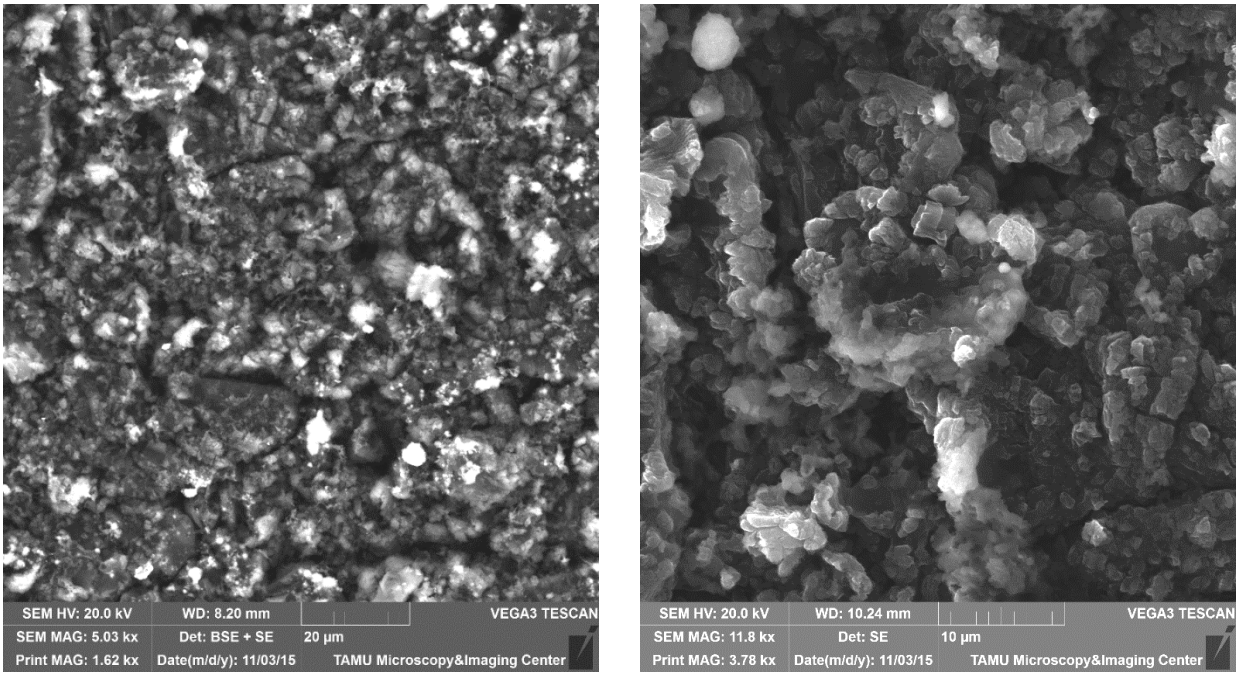

(a) (b)

Fig. 6.19 SEM images of anode extracted from an overcharged fresh cell at (a) 5.03 kX (BSE+SE) magnification, and (b) 11.8 kX (SE) magnification.

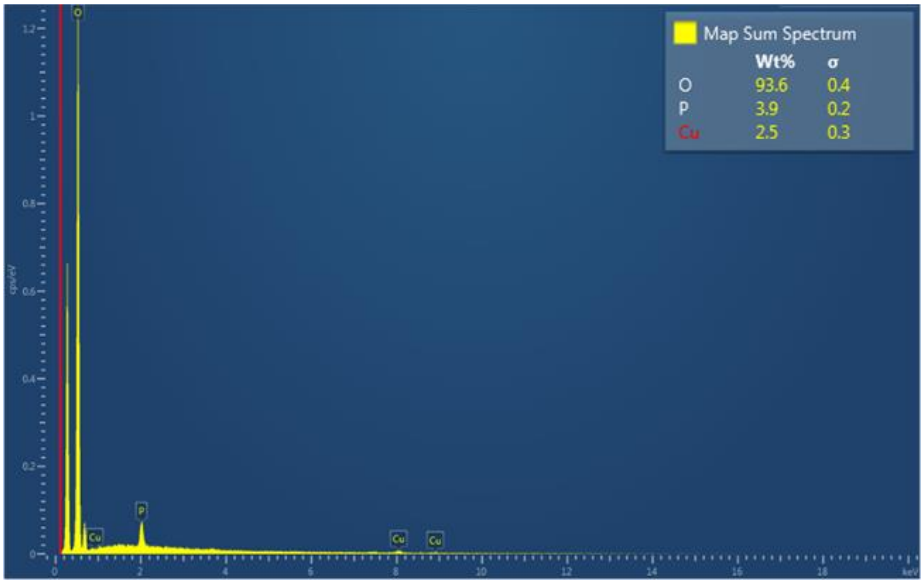

Fig. 6.20 EDS results for the anode electrode extracted from an overcharged fresh cell.

In order to investigate the nature and structure of the coating on the anode electrode, a new sample was taken following a similar procedure conducted by Kramer [200]. In their work, they investigated the presence of lithium plating on the anode electrode. They chemically modified the lithium

plating by making it react with Isopropanol (IPA). The chemical composition may change however its microstructure would not.

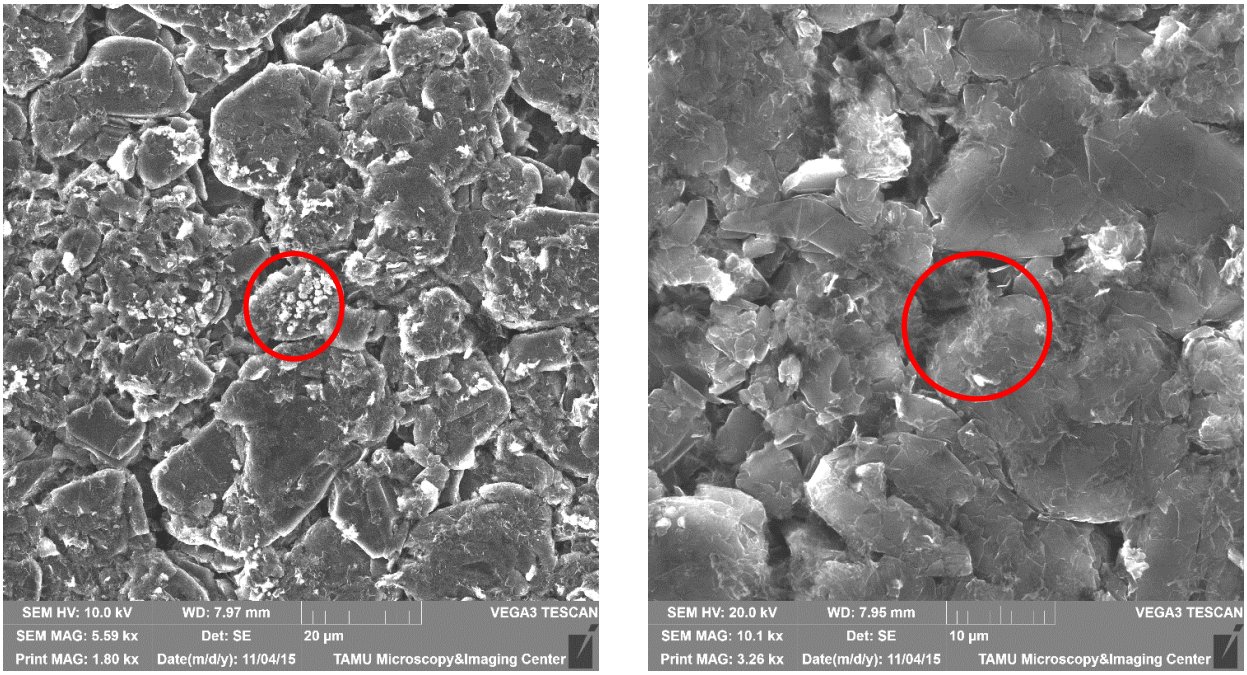

(a) (b)

Fig. 6.21 SEM images of anode, extracted from an overcharged fresh cell and rinsed with IPA at (a) 5.59 kX (SE) magnification, and (b) 10.1 kX (SE) magnification.

The anode electrode was rinsed with IPA within the glovebox. Then, it was kept in a glass vial filled with Argon. Then, the samples were taken to the MIC to obtain their respective SEM images. The presence of spider web – like shape (red circles in Fig. 6.21) on top of the graphite layers is a possible indication of the presence of lithium plating in the anode electrode.

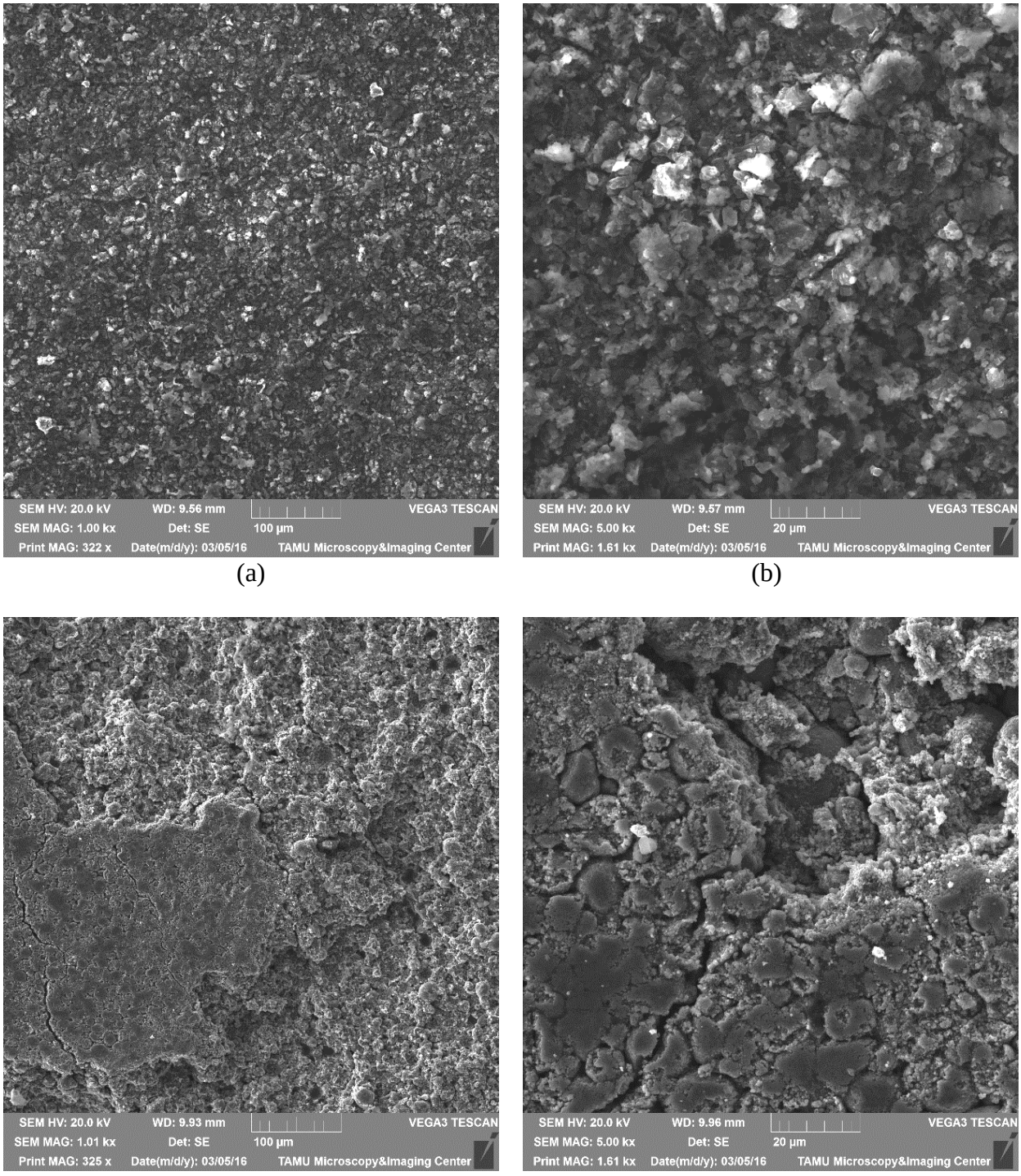

Fig. 6.22 SEM images of extracted electrodes from the externally shorted cell Ba 8. Anode: (a) 1 kX (SE) magnification, and (b) 5 kX (SE) magnification. Cathode: (c) 1 kX (SE) magnification, and (d) 5 kX (SE) magnification.

6.4.2 Normal Voltage Window – CF = 10 %

SEM images from the electrodes extracted from the overcharged cell are shown in Fig. 6.22. The graphite electrode does not show any significant damage. Due to the overcharge, lithium plating could be form. However, since the sample was exposed to the air in order to get these images, the lithium metal reacted with the oxygen and could not be captured in the images. In the case of the cathode, the material not only crumbled but big pieces of it came out of the electrode, as it can be seen Fig. 6.22 (c). Those pieces appeared stuck in the separator.

6.4.3 Normal Voltage Window – CF = 15 %

The electrodes, anode and cathode, from two overcharged cells were extracted and analyzed in the Electronical Microscope. The samples were obtained from N01 (CF = 20.22%) and N03 (CF = 15.41%). Since the samples were prepared within the glovebox and then translated inside of a sealed bag, they did not react with the oxygen and water from air. However, in order to get the images is necessary to expose them to the environment. The cathode electrodes did not exhibited any reaction, but the anode did, see Fig. 6.23.

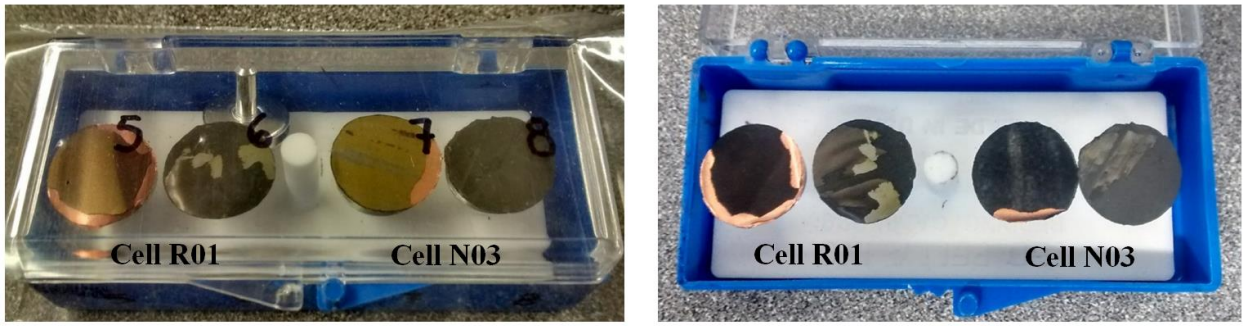

(a) (b)

Fig. 6.23 Electrodes extracted from two overcharged cells: Cell R01 (20%), Cell N03 (15%). (a) Samples just removed from the glovebox. (b) Samples after taking the SEM images.

The samples were taken from some representative zones of each of the electrodes. For the Cell N03, the anode sample once again includes a golden zone (lithiated) and a silver zone (possible lithium plating); the cathode sample includes one zone where the active material came out from the electrode.

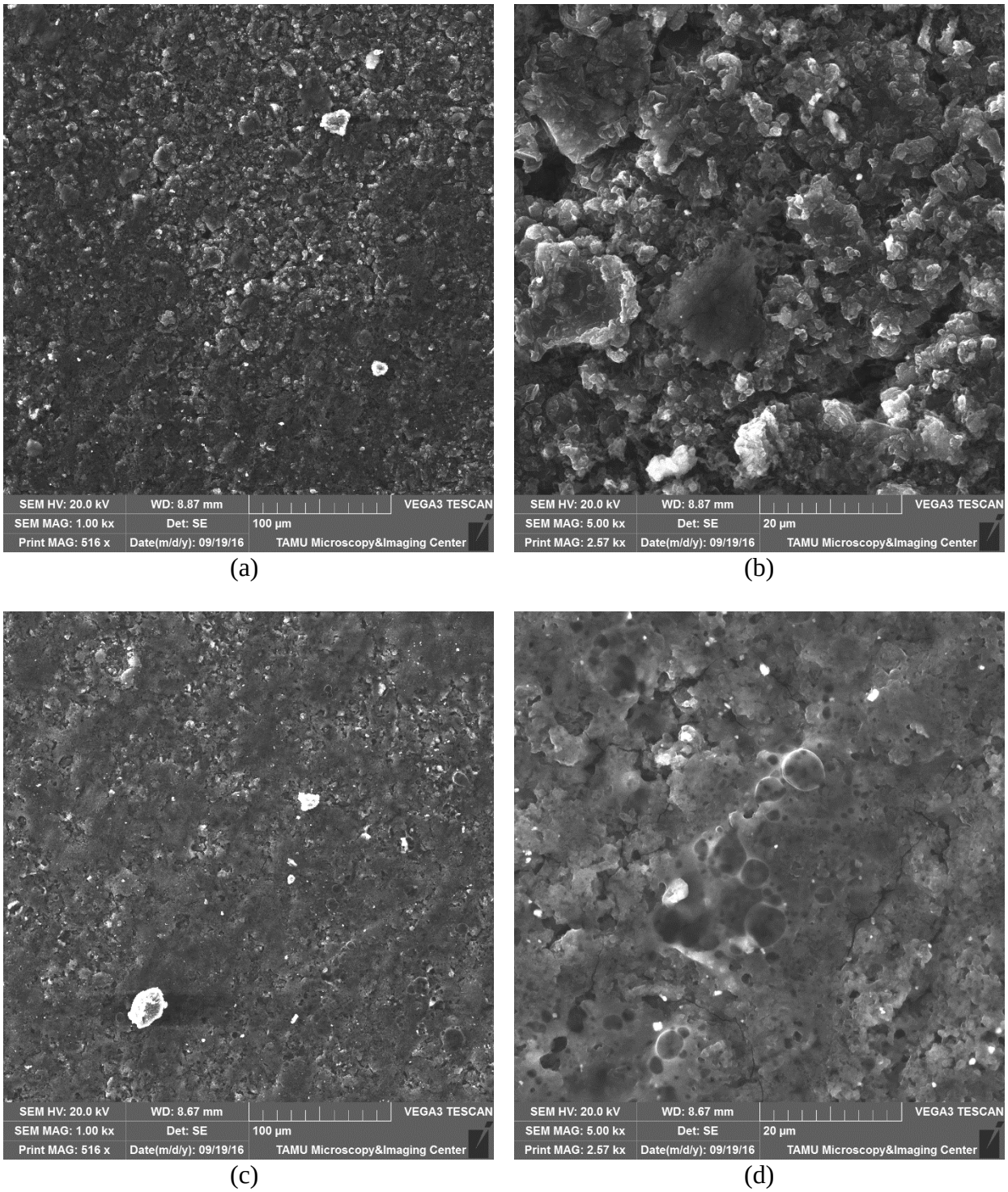

Fig. 6.24 SEM images of the anode extracted from the overcharged N03. Golden zone: (a) 1 kX (SE) magnification, and (b) 5 kX (SE) magnification. Silver zone: (c) 1 kX (SE) magnification, and (d) 5 kX (SE) magnification.

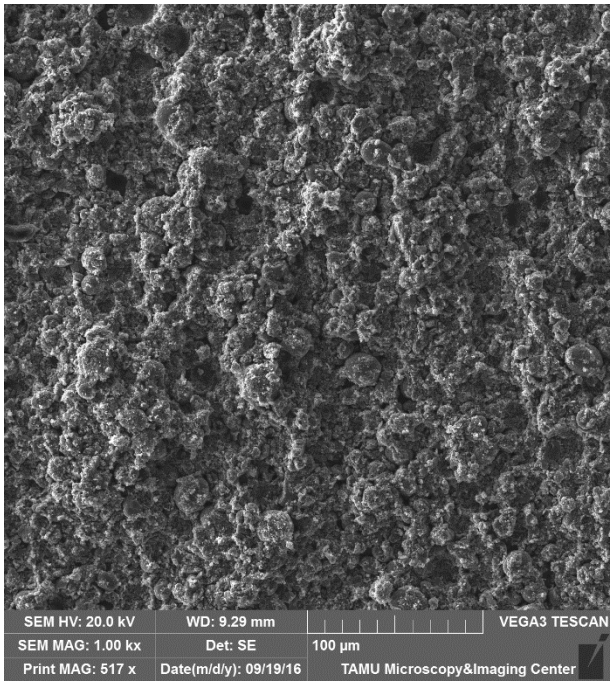

(a)

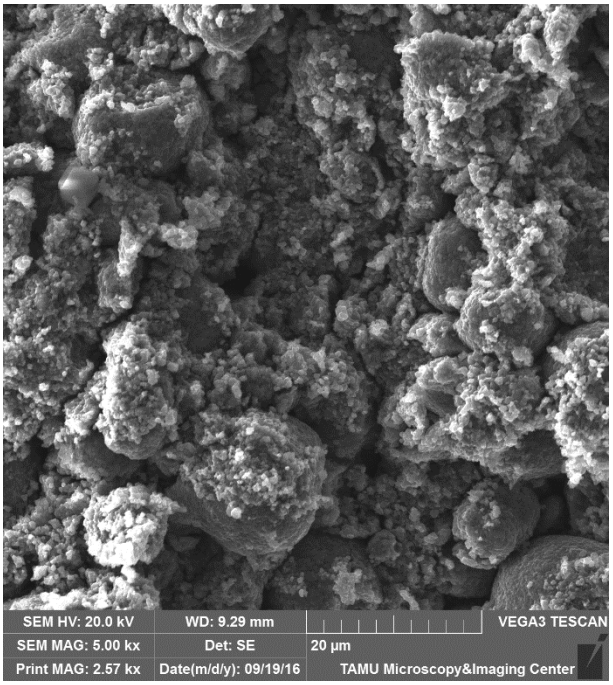

(b)

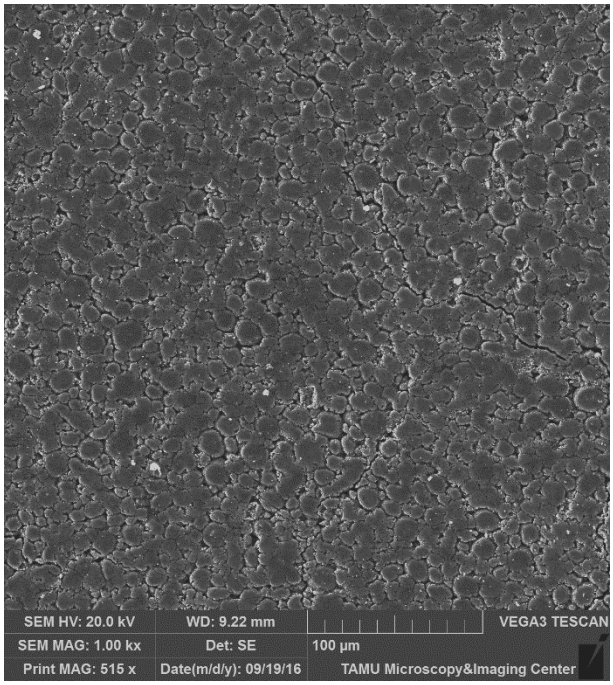

(c)

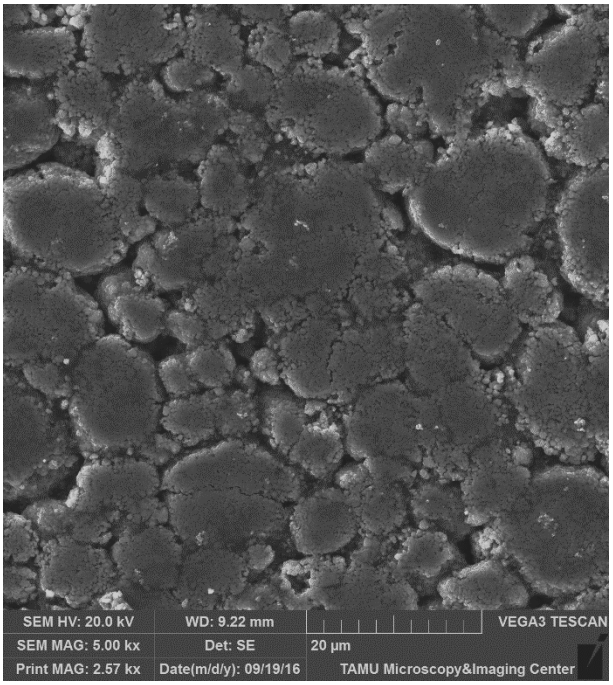

(d)

Fig. 6.25 SEM images of the cathode from Cell N03. Zone where the active material came out from the electrode: (a) 1 kX (SE) magnification, and (b) 5 kX (SE) magnification. Electrode surface: (c) 1 kX (SE) magnification, and (d) 5 kX (SE) magnification.

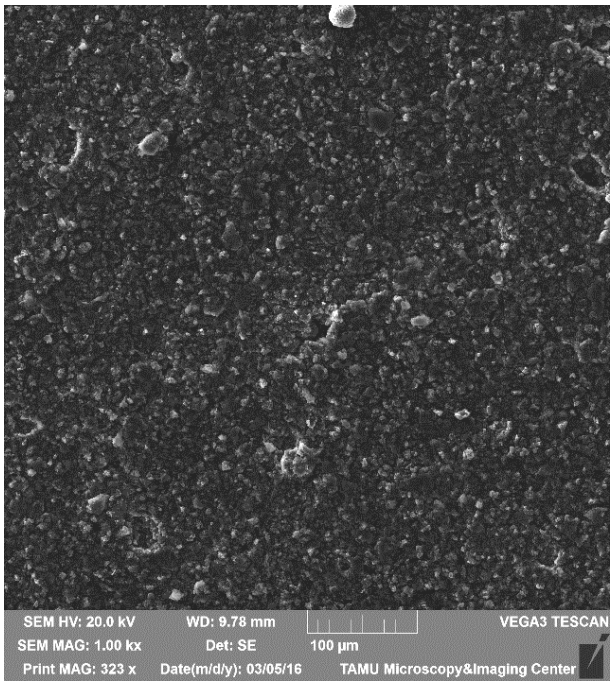

(a)

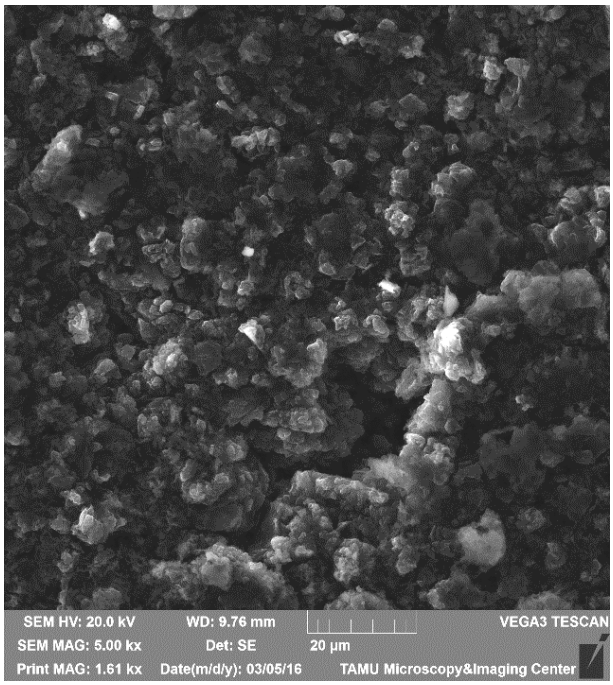

(b)

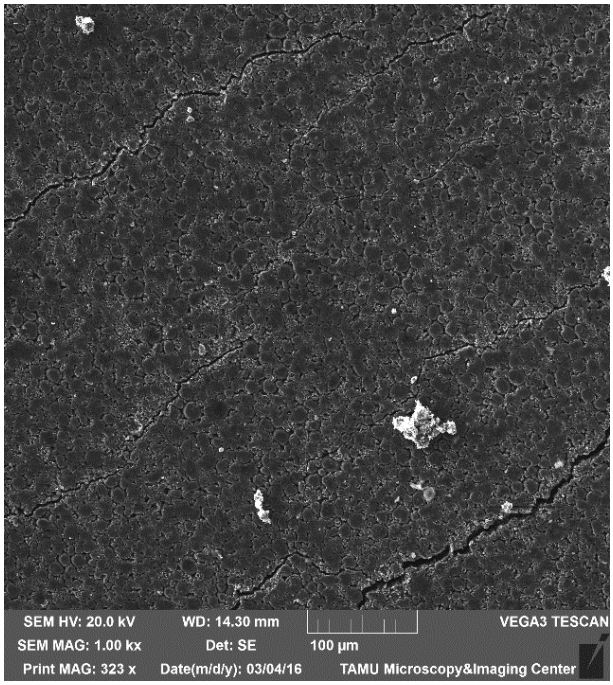

(c)

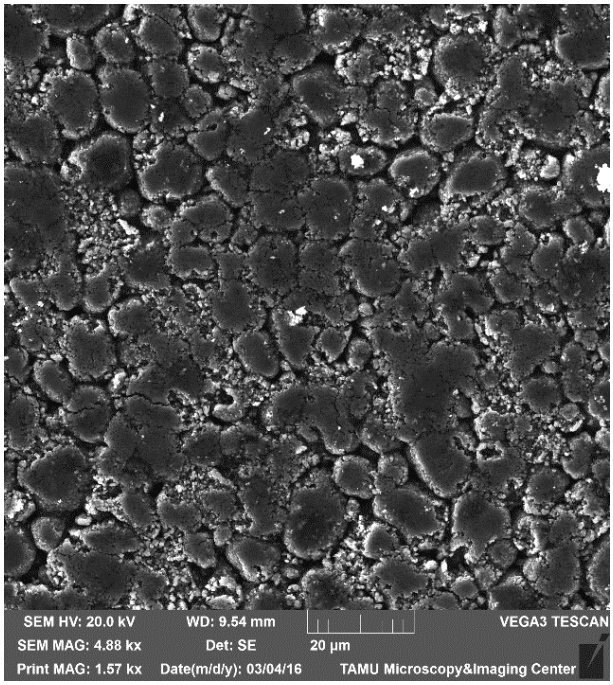

(d)

Fig. 6.26 SEM images of the electrodes from the externally shorted cell N01. Anode: (a) 1 kX (SE) magnification, and (b) 5 kX (SE) magnification. Cathode: (c) 1 kX (SE) magnification, and (d) 4.88 kX (SE) magnification.

6.4.4 Normal Voltage Window – CF = 20 %

The SEM images of the electrodes extracted from Cell N01, see Fig. 6.25, showed similar results than the ones found for Cell N08 (CF=10%) and Cell N03 (CF=15%). No visible damage was found in the graphite electrode. The layer structure is well preserved and only small sites with spider web-like material, that could be associated with lithium plating and dendrite formation, were found.

In the case of the cathode electrode, degradation is more significant and evident. Large pieces of material appear stuck in the separator. Also, the material of the ceramic coating was found stuck in the surface of the electrode. Fig. 6.27 shows one of the zones from the cathode. The surface of the electrode is the first reference. The black layer on top of it corresponds most likely to the ceramic coating. In the left side, the surface filled with wholes corresponds to the internal layers of the electrode. The holes are the places where the active material used to be. This image is significant because it represents not only one small site of the electrode but all of it since the damage was uniform.

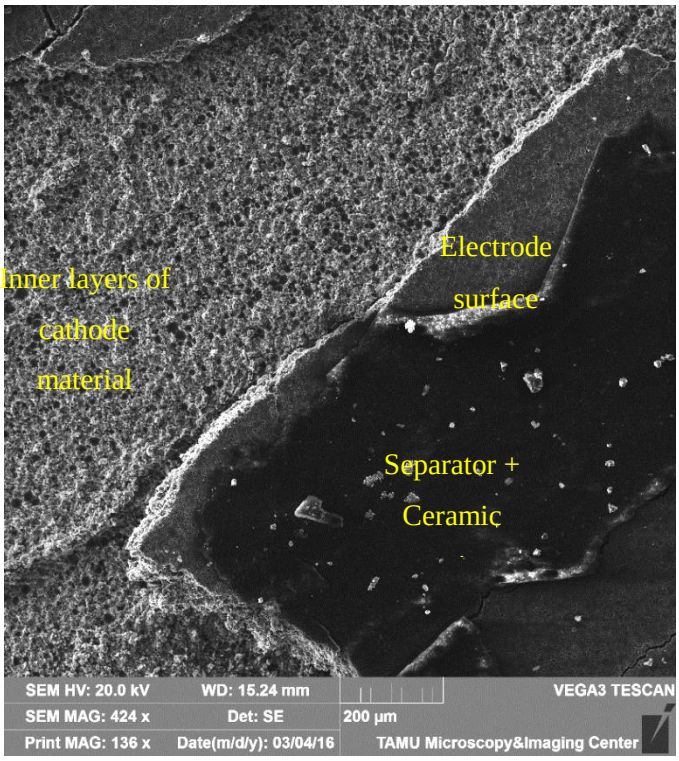

Fig. 6.27 SEM images of the cathode electrode from the externally shorted cell N01. Evidence of the material detached from the electrode.

6.4.5 Reduced Voltage Window – CF = 10 %

The SEM images obtained for the electrodes of the overcharged cell cycled under the Reduced voltage window are shown in Fig. 6.28. Unlike the results found for the cells cycled in the Normal voltage window, this time the graphite electrode exhibited a layer of melted material. There are only two possibilities for this, it could be either the binder or the separator (the ceramic coating only faces the cathode electrode). For the NCAO electrode, the active material showed some minor degradation. It is important to remark that this sample was obtained far away from the center of the cell. This point is important since most of the cells exhibited large degradation near to their center. Also, it was found some pieces of separator on the surface, see Fig. 6.28 (d).

6.4.6 Reduced Voltage Window – CF = 20 %

Samples were taken from some representative zones of each of the electrodes extracted from cell R01, see Fig. 6.29 and Fig. 6.30. Sample from anode includes two zones, one golden (lithiated) and one black (unlithiated) zone; the cathode sample includes one zone with some separator stuck on top of it. The SEM images from the black zone of anode seem to be covered with more melted material than the one from the golden zones. The material deposited on top of the electrode does not allow lithium to intercalate properly. This could be the reason why in the same electrode there is fully lithiated graphite (golden color) and at the same time, there is some graphite that has not been lithiated (dark-ish color).

For cathode, it was found large zones of the electrode where all the material near to the surface came out. Images of zones, the normal one and the one with the material removed are shown in Fig. 6.30. Just because the material did not come out, it does not mean it did not have any degradation. As well as the rest of the electrode from the cycled and overcharged cells, the surface of the cathode showed some crumbling. One possible reason for this degradation could be that its microstructure becomes unstable once that most of the lithium is deintercalated from it.

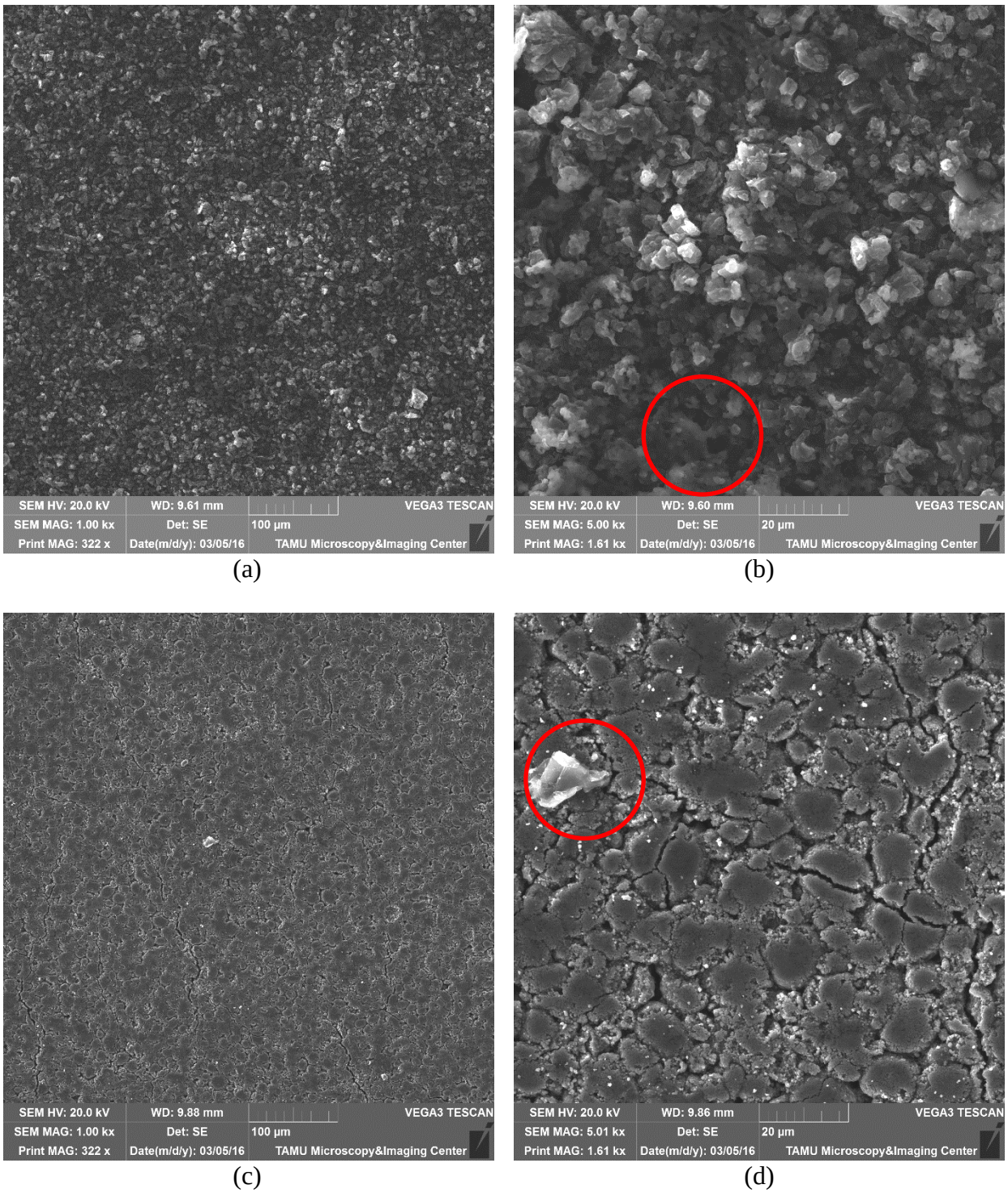

Fig. 6.28 SEM images of the electrodes extracted from the overcharged cell R05. Anode: (a) 1 kX (SE) magnification, and (b) 5 kX (SE) magnification. Cathode: (c) 1 kX (SE) magnification, and (d) 5 kX (SE) magnification.

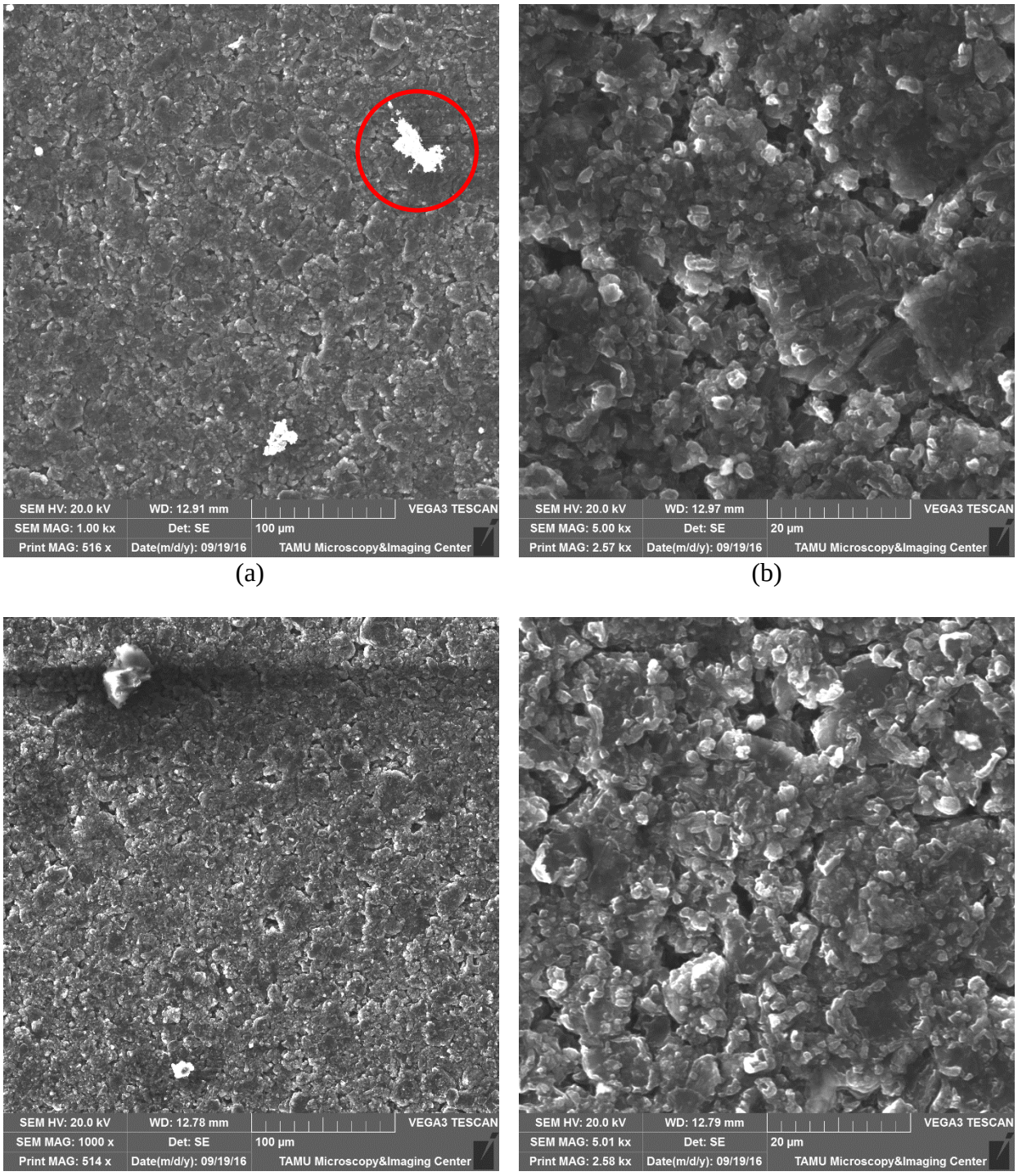

Fig. 6.29 SEM images of the anode (graphite) from cell R01. Golden zone: (a) 1 kX (SE) magnification, and (b) 5 kX (SE) magnification. Black zone: (c) 1 kX (SE) magnification, and (d) 5 kX (SE) magnification.

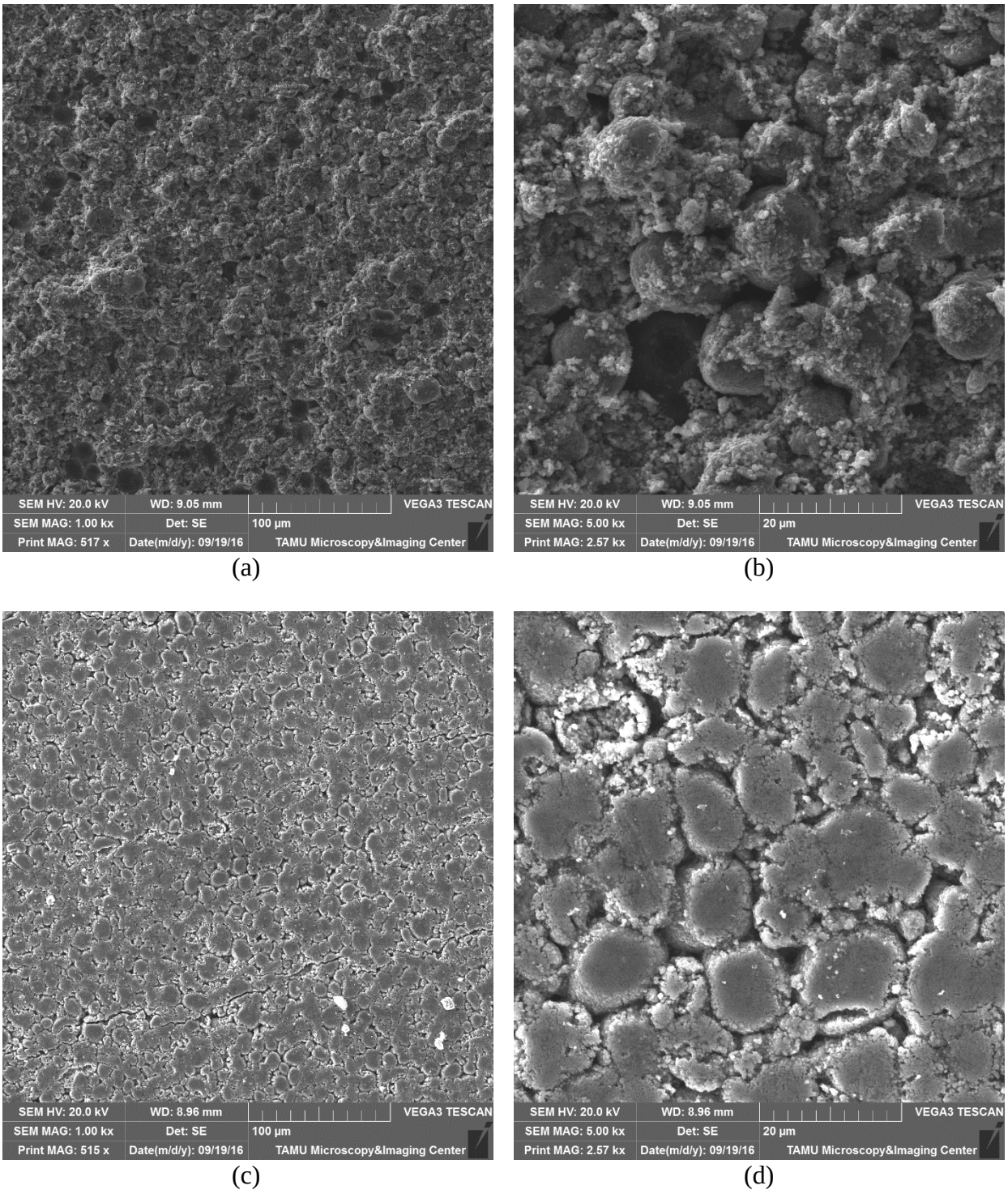

Fig. 6.30 SEM images of the cathode from cell R01. Zone where the active material came out of the electrode: (a) 1 kX (SE) magnification, and (b) 5 kX (SE) magnification. Electrode surface: (c) 1 kX (SE) magnification, and (d) 5 kX (SE) magnification.

In Fig. 6.31 , a different zone of the cathode electrode is shown. This area clearly shows a deposition of the separator/ceramic coating in the surface of the electrode. The covering material exhibited a fibrous structure very common in the separator material. In the previous results it was also found some melt material, however it could not get any details about its topology.

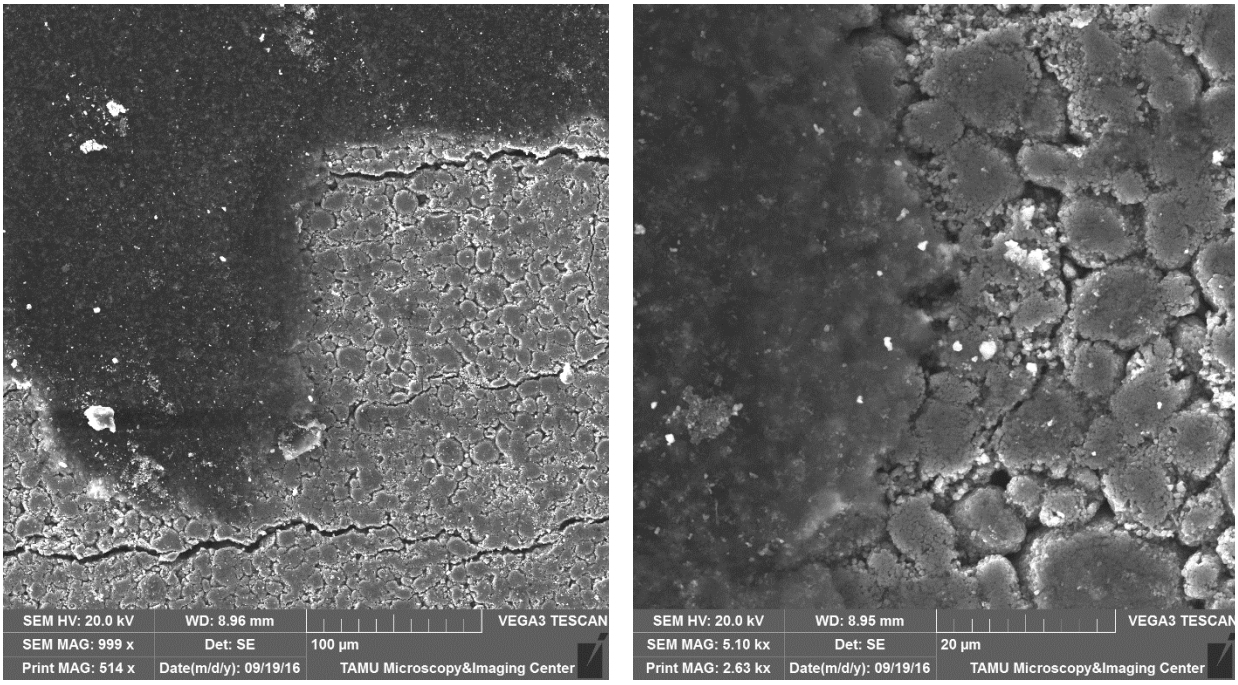

(a) (b)

Fig. 6.31 SEM images of the cathode from Cell R01. Zone where the electrode was covered with melted separator: (a) 1 kX (SE) magnification, and (b) 5 kX (SE) magnification.

In the next section, it will be shown the results obtained for the separator and its ceramic coating. These two materials have been mention in the previous section but so far, no evidence or details of these had been given.

6.5 SEM Images of the Separator

Two membrane separators extracted from a fresh cell and an overcharged cell (Cell N01, 20% of capacity fading) were selected for this analysis. The material of the membranes is not an electronically conductor material. This causes a charging effect when the samples are placed under the electron beam in the microscope, leading to a bright image which doesn't allow observing its morphology.

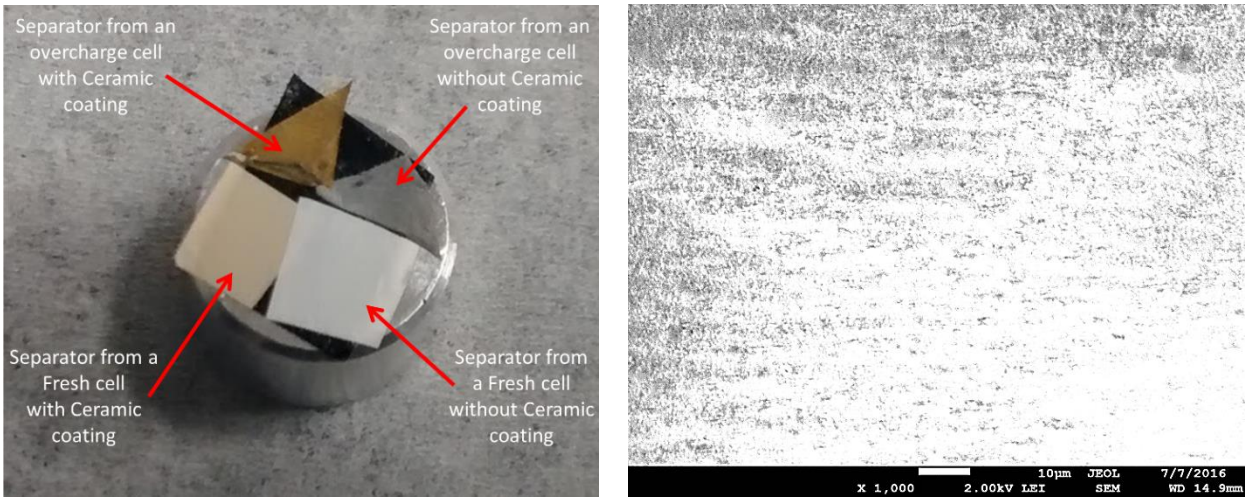

Fig. 6.32 Separators extracted from a fresh cell and an overcharged cell. Charging effect exhibited by the membrane at the microscopy.

In order to get the images is necessary to reduce the emission current and the accelerating voltage. This condition reduces the amount of electrons reaching the separator and hence reducing the charging effect. The usual emission current and accelerating voltage are 12 µA and 10 kV, respectively. At this condition is very easy to obtain SEM images of the electrodes but not from the separator.

The SEM images shown in Fig. 6.33 were taken using a 2 kV accelerating voltage and 12 µA emission current in a JEOL microscope. Unfortunately, it was not possible to obtain a clear image for the fresh cell separator with the ceramic coating. The separator from the overcharge cell without the ceramic coating exhibit some melting and some incrustations of the anode material. In the side with the ceramic coating, small particles of binder and conductive additive were found.

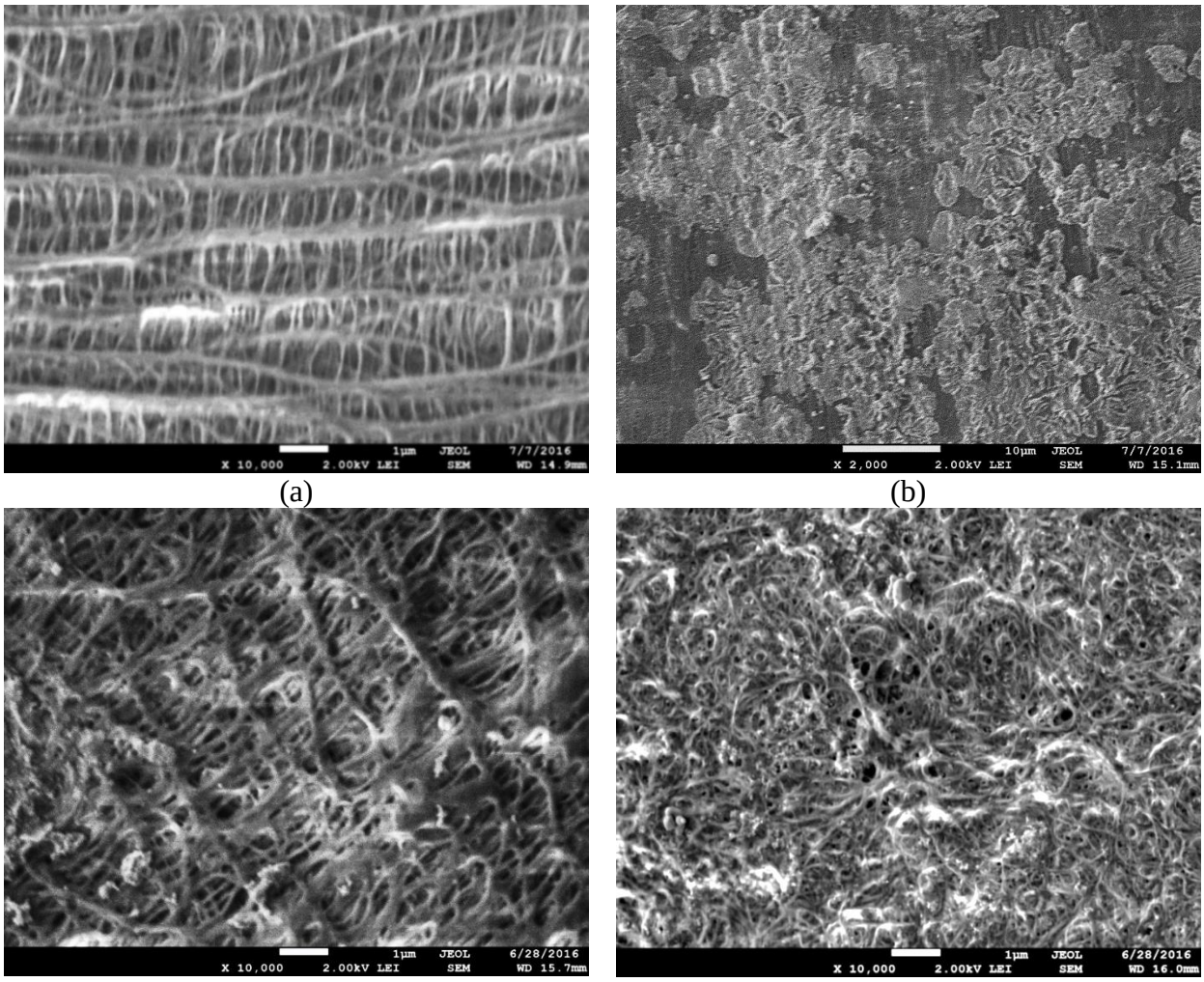

(a) (b)

(c) (d)

Fig. 6.33 SEM images for the membranes from a fresh cell: (a) without ceramic coating, 10 kX (SE), and (b) with ceramic coating, 1 kX (SE). And from an overcharged cell: (c) without ceramic coating, 10 kX (SE), and (d) with ceramic coating, 10 kX (SE).

7. CELL LEVEL DEGRADATION: OVERDISCHARGE TEST IN CYLINDRICAL CELLS

Relevant Publications and/or Working Papers

1. (Joint first author) C. Fear, D. Juarez-Robles, J. Jeevarajan, P.P. Mukherjee, *Elucidating Copper Dissolution Phenomenon in Li-Ion Cells under Overdischarge Extremes*, J. Electrochem. Soc., 2018, 165, 9, A1639-A1647, doi: 10.1149/2.0671809jes

The mechanisms driving the thermo-electrochemical response of commercial lithium-ion cells under extreme overdischarge conditions (< 0.0 V) are investigated in the context of copper dissolution from the anodic current collector. A constant current discharge with no lower cutoff voltage was used to emulate the effects of forced overdischarge, as commonly experienced by serially connected cells in an unbalanced module. Cells were overdischarged to 200% DOD (depth of discharge) at C/10 and 1C rates to develop an understanding of the overdischarge extremes. Copper dissolution began when a cell reached its minimum voltage level (between −1.3 V and −1.5 V), where the anode potential reached a maximum value of ~4.8 V vs. Li/Li^+. Deposition of copper on the cathode, anode, and separator surfaces was observed in all overdischarged cells, verified with EDS/SEM results, which further suggests the formation of internal shorts, although the cell failures proved to be relatively benign. The maximum cell surface temperature during overdischarge was found to be highly rate-dependent, with the 1C-rate cell experiencing temperatures as high as 79 °C. Concentration polarization and solid electrolyte interphase (SEI) layer breakdown prior to the initiation of copper dissolution are proposed to be the main sources of heat generation during overdischarge.

7.1 Overdischarge

Commercial Li-ion cell manufacturers typically specify a voltage window for safe operation in order to prevent undesirable side reactions from occurring in the cell. A condition known as overdischarge occurs when a cell is discharged below the manufacturer's recommended lower voltage limit. Overdischarge is becoming an increasingly common issue as greater numbers of

cells are being connected in parallel-series configuration, as is the case in systems requiring high voltages, such as electric vehicles (EVs) [158]. When placed in a battery arrangement, the voltage of individual cells should be monitored in order to keep them in balance and within the manufacturer's specification. Slight differences in the manufacturing of the cells can cause some cells to have less capacity than others in the series[180]. Nevertheless, when the module is discharging, the cells with lower capacity are demanded to deliver the same amount of energy as other cells. When lower capacity cells in an unbalanced module discharge beyond their recommended lower voltage limit, overdischarge occurs and permanent capacity fade or failure can be caused [52]. Additionally, overdischarge below the manufacturer specified low voltage limit will result in the dissolution of the copper anodic current collector, which can deposit on internal cell components and induce an internal short [180, 201]. Typically, internal shorts due to an overdischarge condition are benign, leading to a dead cell in a fail-safe mode. However, the dissolution of copper from the anode current collector causes additional issues such as delamination of the anode and the deposition of copper on the surfaces of the cathode, separator and anode, which hinders the flow and intercalation/deintercalation of lithium-ions during charge and discharge [202]. This causes lithium ions to deposit as lithium metal rather than intercalating into the anode electrode, as the surface of the anode is covered with copper.

7.2 Previous Analysis

While many studies have investigated the effects of overdischarge in LIBs below the manufacturer's recommended lower cutoff voltage [203], few prior studies have focused on overdischarged below 0.0 V. Kishiyama et al. studied the effects of 0.0 V overdischarge on Li-ion cells whose anodes used current collectors made of either titanium or copper [204]. They demonstrated that the dissolution of copper is the main cause of capacity loss in cells under this condition. It was also shown that the Solid Electrolyte Interphase (SEI) layer could break down if the anode potential exceeds 3.5 V vs. Li/Li^+. Mao demonstrated that anode potential can reach as high as 3.8 V when overdischarging a Li-ion cell to 0.0 V [205]. Therefore, it is possible that both copper dissolution and breakdown of the SEI layer are causes of capacity loss during the overdischarge process. A study performed by Li et al. observed swelling in a $LiCoO_2$ - based pouch cell that was overdischarged to 0.0 V, using gas chromatography to detect and quantify the gases that caused the swelling [203]. Carbon dioxide, carbon monoxide, and methane were found to be the

most abundant gases in the overdischarged cells. The authors proposed that the carbon dioxide and carbon monoxide were produced from the decomposition of the SEI.

Guo et al. proposed using extreme overdischarge as a method to consistently induce internal shorting in lithium-ion cells, caused by the dissolution of copper and the creation of electrical shunts when it was redeposited on electrode surfaces [180]. Cells were subjected to extreme overdischarge of varying degrees before recharge was attempted. It was found that for cells in which the discharge was terminated before 112% DOD, full recharge could be achieved with only minor side effects, while cells that were terminated beyond 114.5% DOD could not be recharged back to full. The authors of this study also note that increasing the capacity ratio of the anode to the cathode can delay the DOD at which copper dissolution begins.

A study by He et al. investigated the failure mode of commercial 18650 $LiFePO_4$ cells subjected to repeated overdischarge to DODs from 105% to 120% [158]. The proposed failure mode from this study is the gradual formation of copper bridges through repeated cycling, which cause micro-shorting and self-discharge. They also performed cyclic voltammetry tests on copper electrodes in $LiPF_6$ electrolyte to determine precise oxidation and reduction potentials for copper. The oxidation and reduction potentials of the Cu to Cu^+ reaction were measured at 3.92 and 3.28 V, respectively, while the potentials of the Cu^+ to Cu^{2+} reaction were measured at 4.17 and 3.19 V [158]. Because these tests were performed ex-situ, the measured potentials cannot directly predict the in-situ oxidation and reduction potentials of copper at graphite anodes and lithium metal oxide cathodes. To track the potential evolution of each electrode throughout a 1C-rate overdischarge to 120% DOD, a modified three-electrode 18650 cell, using lithium metal as the reference electrode, was employed. The anode potential increased from -0.5 to 4.5 V vs. Li/Li^+ during the test, while the cathode potential decreased from 3.80 to 3.18 V vs. Li/Li^+ [158].

Kasnatscheew et al. analyzed the potential development and interactions between electrodes in a three-electrode Swagelok® cell with an NMC cathode, graphite anode, and Li metal reference electrode throughout a deep overdischarge phase [206]. A characteristic potential plateau at ~3.56 V was detected at the graphite electrode due to the copper oxidation process at the current collector. The constant anode potential following the onset of copper oxidation indicates that the process

continued throughout the remaining discharge phase. The time shifted potential plateau observed at the positive electrode, was attributed to the competitive reaction between the conventional lithiation reaction and the parasitic Cu plating reaction.

Overdischarge of 18650 cells in a parallel arrangement was studied by Nemanick et al. in a test to simulate an electronic control failure [202]. Cells were overdischarged via successive cycling in which 60% of the nominal capacity was discharged and only 90% of the removed charge was returned during recharge in each cycle. All cells appeared to develop shorts after 9 cycles. Even so, cell temperatures peaked at around 40 °C during cycle 9 and returned to near-ambient temperatures for the cycles following the shorting, showing the fail-safety of this form of cell abuse. Cross-sectional SEM confirmed that dendrites had formed on the cathode surface and penetrated through the separator, often visibly connecting through to the anode [202].

In this study, the response of commercial 18650 LIBs to a single deep overdischarge is examined in order to elucidate the mechanisms that lead to cell failure under this condition. A constant current discharge phase with no lower cutoff voltage is used to overdischarge the cell to 200% DOD so that a thorough electrochemical analysis of the entire overdischarge condition could be performed. Differential voltage analysis is used to study the copper dissolution reactions as a function of DOD. Destructive physical analysis (DPA) was employed to visually inspect damage in the cell, and the morphological changes on the electrodes were studied by analyzing cell components using micrographic (SEM) and spectroscopic (EDS) techniques.

In order to decouple the behaviors of the anode and cathode and to examine the interactions between the electrodes during extreme overdischarge, a series of half-cell tests were performed. Electrodes harvested from the commercial 18650 cells are used to construct coin-type half cells with graphite and NCA. Half-cell tests can provide useful information on the electrochemical behavior of an electrode, as they place the electrode under study opposite an electrode of known potential. Although the half-cell analysis cannot account for any interactions that occur between electrodes in the full cell overdischarge, it enables an in-depth analysis of the reactions that occur at each electrode at different potentials and DODs. Since no copper current collector is present in the NCA/Li half cells, the deposition of copper on the NCA surface cannot be studied with this

test, but other effects of overdischarge on the cathode can be examined without interference. The results of the half-cell tests and the commercial full cell test will provide a complete picture of the reactions occurring during extreme overdischarge of Li-ion cells, which will permit the elucidation of the mechanisms causing cell failure in this way.

7.3 Experimental

Commercial Panasonic NCR18650B cylindrical cells, obtained from a reputable vendor, were used in this study. The rated capacity of these cells is 3350 mAh at 25°C when discharged at a C/5 rate. The manufacturer-recommended voltage window is 2.5-4.2 V. The cathode active material is $LiNi_{0.8}Co_{0.15}Al_{0.05}O_2$ (NCA, nickel cobalt aluminum oxide) and the anode active material is graphite (C), with aluminum and copper foil as current collectors, respectively. The separator is composed of polypropylene (PP) and polyethylene (PE) with an oxide-polymer composite layer of alumina (Al_2O_3) [177]. Cell voltage and electrical current were controlled and recorded by an Arbin-BT2000 battery cycler. Temperature measurements were recorded from a K-type thermocouple (Omega) attached to the exterior surface of the cell.

The cell was conditioned by charging and discharging two times, measuring the full cell capacity and internal resistance on the second cycle at 50% of the Depth of Discharge (DOD). Charging was performed under a constant current (CC) mode at a C/20-rate up to 4.2 V, followed by a constant voltage (CV) charge at 4.2 V until current fell below 0.05 A. Discharging was performed under CC conditions at a C/20 rate to a cutoff voltage of 2.5 V. Internal resistance was measured during the discharge phase at 50% SOC by applying a short current pulse at 1.5C for 100 ms. The cell was then fully charged to 4.2 V and allowed to rest.

To perform the overdischarge test, the cell was once again charged, discharged, and charged, this time at C/10 (335 mA), in order to ensure a 0% DOD at the beginning of the test. The cell was then subjected to a constant current discharge phase with no lower cutoff voltage, inducing extreme overdischarge. The discharge was allowed to continue until a 200% DOD was reached. Overdischarge was performed at rates of C/10 (335 mA) as well as 1C (3350 mA) to determine the possible effect of discharge rate on cell response during the process. The voltage and surface temperature of the cell were monitored and recorded throughout the test via the battery cycler.

Electrodes were harvested from a fresh Panasonic NCR18650B cell and used to construct 2300-type coin cells. Because the electrodes from the cylindrical cell are double-sided coated, the active material on one side had to be removed to expose the foil current collector. This was achieved by applying drops of isopropyl alcohol to the electrode surfaces and carefully scraping off the active material with a scalpel. Two graphite half cells were created using the anode from the fresh 18650 cell and the procedure described in reference [78]. These cells were conditioned by cycling at C/10 rate between 0.1-2.5 V vs. Li/Li^+. After the second discharge to 0.1 V, one cell was overcharged at C/10 and the second half cell at 1C-rate with no upper cutoff voltage to 200% DOD, emulating the overdischarge of the anode in a full cell. Two NCA half cells were created from the cathode material and were conditioned by cycling at C/10-rate between 3.5-4.2 V. After the second charge to 4.2 V vs. Li/Li^+, the cells were overdischarged independently at C/10 and 1C-rate with no lower cutoff voltage to 200% DOD.

Destructive physical analysis (DPA) was performed on the overdischarged cell to determine what damage had been caused to cell components. Cells were disassembled within a sealed argon glovebox (MBraun) for safety and to prevent reactions with the environment from affecting interior components. After performing DPA, scanning electron microscopy (SEM) and energy-dispersive X-ray spectroscopy (EDS) were performed on representative anode and cathode samples to examine the electrode surfaces after overdischarge abuse and to verify that the material deposited on the cathode surface is copper, dissolved from the anodic current collector.

7.4 Results and Discussion

Most off-the-shelf commercial cells are shipped at lower states of charge, typically at 30% DOD. The cells may be in storage for an indefinite time before they are sold and hence at least two conditioning cycles were performed on all the cells before other tests were conducted. The discharge capacity obtained in the first full cycle was 3330 mAh, which was slightly smaller than the rated capacity of the cell (3350 mAh). The 0% DOD was defined as the charge capacity obtained at the end of the CCCV charging from the conditioning test. The average internal resistance of the cells was 45 mΩ.

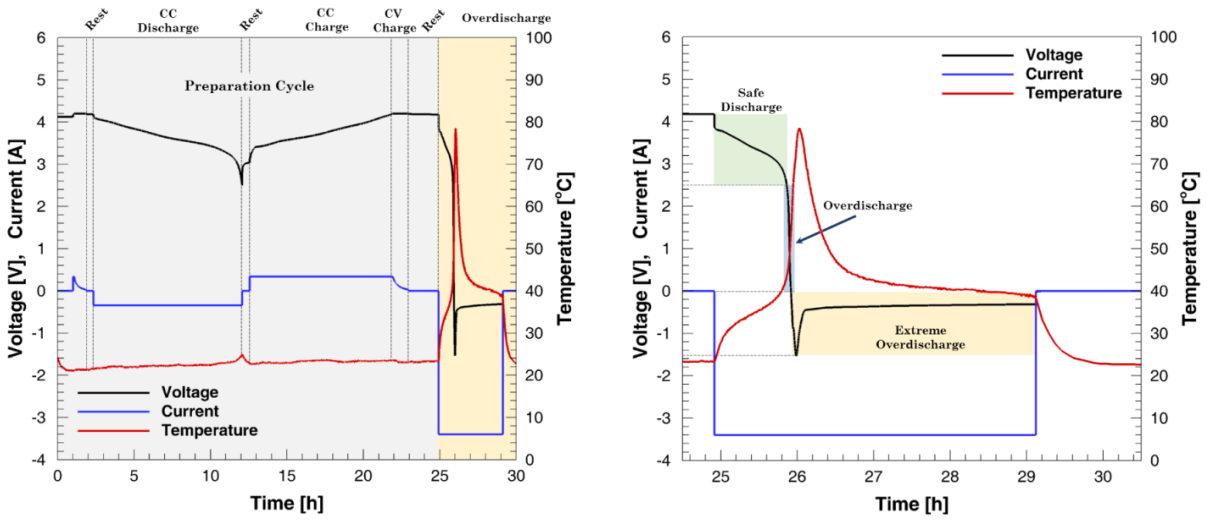

(a) (b)

Fig. 7.1 Experimental protocol for the overdischarge test at 1C discharge rate. The test consists of two steps: a preparation (CC discharge and CCCV charge at C/10 rate) and then the overdischarge process (CC discharge at 1C-rate). The preparation test ensures the cell to be fully charged prior the final overdischarge process, which is held for more than 3 hours.

The protocol used in the experimental test for the 1C overdischarge is shown in Fig. 7.1. The protocol ensures the cell to be fully charged prior the overdischarge test. At 2.5 V, which is the manufacturer-recommended lower cutoff voltage, the discharge capacity at a 1C-rate is 3214 mAh. This voltage range is considered a safe voltage window where the cell can be cycled with a long lifespan. If the cell is discharged below 2.5 V without going below 0.0 V, the cell is overdischarged, leading to electrolyte degradation and SEI decomposition [203]. For the 1C test to 0.0 V, a discharge capacity of 3401 mAh was obtained. After that, the cell was driven to an extreme overdischarge condition (below 0.0 V) until the cell reached a 200% DOD.

The voltage profile for the overdischarge test can be roughly divided into four stages as shown in the differential voltage plot for the C/10 overdischarge test in Fig. 7.2 (a). In Stage I, the voltage dropped rapidly from an inflection point in the voltage curve around 1.8 V to a distinct platform at about -1.0 V. In Stage II, the voltage continued to fall to its minimum value of -1.3 V. Stage III showed an increase in voltage with significant fluctuations, while in Stage IV, the voltage increased asymptotically to -0.23 V with very little fluctuation. An analogous examination of the 1C rate overdischarge test showed that Stage I, II, III, and IV started at 1.2 V, -0.9 V, -1.5 V, and

-1.3 V, respectively. At the end of the extreme overdischarge, the asymptotic voltage reached for the 1C trial was -0.3 V. Note that while the voltage levels of these points vary with the discharge rate, the characteristic trend of the voltage profile is consistent for all tests performed on this type of cell. In order to facilitate the stage limits identification, the voltage vs. DOD plot were contrasted with its corresponding first and second order differential voltage curves (see Fig. 7.2). The peak maximum voltage values were identified as the zeros of the first order differential voltage plot. The plateau voltages with changes in concavity were identified using the zeros of the second order differential voltage plot.

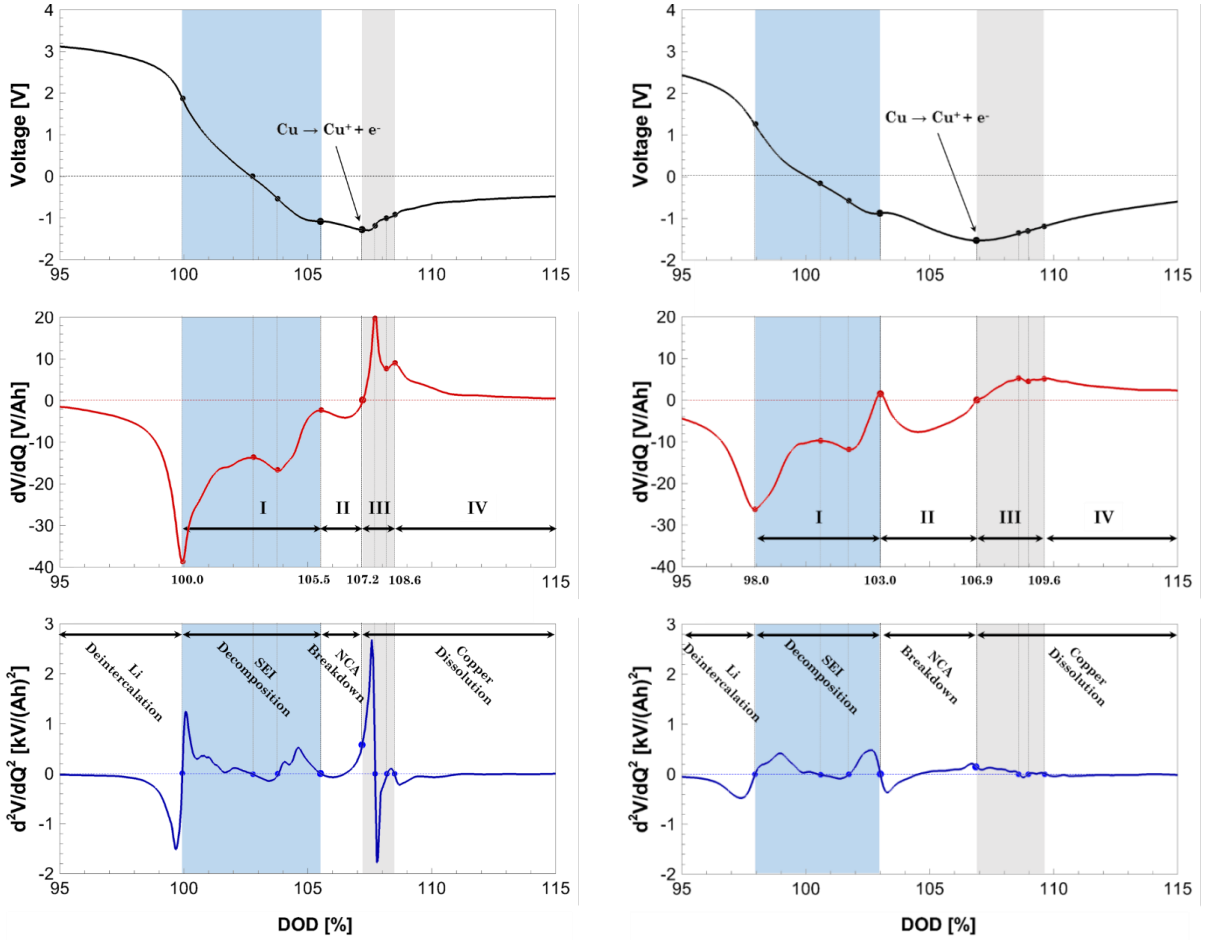

(a) C/10 - rate (b) 1C - rate

Fig. 7.2 Zero (V vs. DOD), first (dV/dQ vs. DOD) and second (d^2V/dQ^2 vs. DOD) order differential voltage as a function of DOD. In the voltage plot, it is highlighted the DOD at which copper dissolution dominates the performance of the cell. Zeros for the first and second differential voltage allow tracking the electrochemical changes – concavity shifts – within the cell. The side reactions, indicated in the differential voltage plot, can be identified by the four (I, II, III, IV) overdischarge stages.

The voltage decline in Stage I, from Fig. 7.2 (a), is driven primarily by the increasing potential of the anode, as the overall capacity of the cathode is always designed to be lower than that of the anode in commercial cells in order to avoid possible lithium plating and dendrite formation on the anode during charging[158]. Deintercalation of the remaining Li^+ ions from the anode and their introduction back into the cathode rapidly increase the anode potential throughout Stage I and gradually decrease the cathode potential. Stage I begins at an inflection point in the voltage curve around 1.8 V, which signifies the initiation of SEI decomposition. This inflection point is also evident in the graphite half-cell voltage curve, shown in alignment with the full cell curve in Fig. 7.3. According to Kishiyama et al., SEI breakdown can occur when the anode voltage reaches ~3.5 V or higher and can generate gases and heat within the cell[204]. This process, which occurs throughout Stages I and II, exposes the chemically reactive surface of graphite to the electrolyte, further increasing the anode voltage and decreasing the voltage of the cell. As Stage I continues, another inflection point at ~0.0 V indicates the point at which the cathode potential begins to fall rapidly due to a lack of interstitial site availability and the buildup of a concentration gradient of Li in the NCA. The falling cathode potential and rising anode potential cause the full cell voltage to decrease until a plateau is reached at the end of Stage I. This brief plateau was also observed in the NCA half-cell tests (see Fig. 7.3), and indicates the introduction of new Li-rich phases in the cathode structure to accommodate the excess Li being forced into it. The volumetric expansion of NCA to incorporate these phases can cause cracking and permanently damage the cathode microstructure.

During Stage II, the rising potential of the anode dominates the full cell voltage behavior, as the cathode potential remains relatively constant. The anode potential continues to rise until it is high enough to overcome the overpotential required for copper dissolution. The oxidation potential of Cu to Cu^+ was measured ex-situ by He et al. using cyclic voltammetry to be 3.92 V *vs.* Li/Li^+ in $LiPF_6$ electrolyte [158]. In this work, the Cu to Cu^+ oxidation potential was measured in-situ using Cu/Li half cells to be 3.54 V at C/10 (3.60 V at 1C) and almost no initial peak for reaction overpotential was present. The difference between the in-situ and ex-situ measurements can be accounted for by the closer proximity of electrodes to each other in the in-situ tests, leading to a reduced effect of electrolyte resistance. In the case of the graphite/Li half cells, shown in Fig. 7.3, the anode potential consistently reached a peak around 4.8 V, indicating the requirement of a large

overpotential to initiate copper dissolution when a graphite coating is present. This is possibly due to charge transfer resistance of the Cu^+ ions, as they are too large to travel directly through the graphite and must travel primarily around the edges of the electrodes. In the full cell analysis, copper oxidation begins when it reaches its minimum value at the end of Stage II, identified by a zero in the differential voltage curve (see Fig. 7.2).

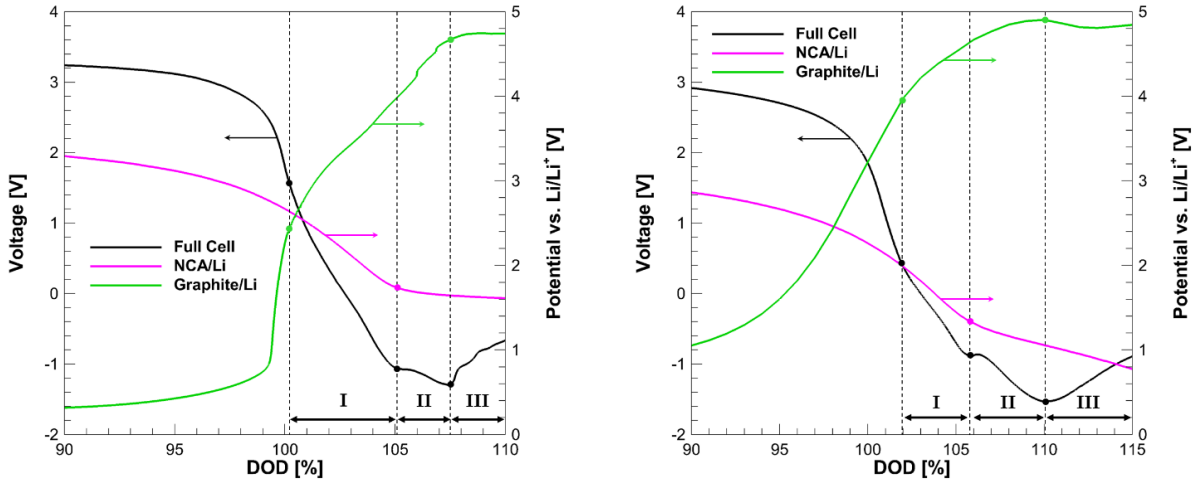

Fig. 7.3 Half-cell overdischarge voltage curves for (a) C/10-rate and (b) 1C-rate, aligned with experimental voltage curves from full cells. The processes driving the full cell behavior are decoupled, showing the respective contributions of the cathode and anode to the full cell voltage and to the definitions of Stages I, II, and III.

Following the onset of the copper dissolution reaction, the anode potential falls as the overpotential for the reaction is relieved. The anode potential decreases rapidly throughout Stage III, while the cathode potential gradually decreases at a slower rate, resulting in an increase in the full cell voltage. According to the ex-situ measurements of He et al., Cu^+ ions dissolved in the electrolyte will reduce to metallic copper at around 3.19 V [158]. In these tests, the cathode potential fell below this value prior to the onset of dissolution, so the large time-shift between the start of copper oxidation at the anode and copper reduction at the cathode reported by Kasnatscheew et al. is not observed. Although the NCA/Li half-cell results in Fig. 7.3 show a continuous decrease in potential with increasing DOD, this result does not account for the presence of copper ions in the electrolyte. Therefore, the NCA/Li half-cell voltage curve does not accurately represent the full cell cathode behavior after the start of Stage III. When the reduction and intercalation of Li at the NCA surface

is competed by the reduction and deposition of Cu, the intended Li reaction is kinetically hindered and the cathode potential slightly increases [206]. Therefore, the start of copper deposition at the cathode can be associated with the minimum cathode potential in the full cell. Stage III ends at an inflection point, where the cathode reaches its minimum potential and copper deposition begins to occur.

Stage IV is characterized by a plateau in the anode potential at ~3.54 V for the remainder of the overdischarge, indicating the continuing dissolution of copper from the current collector (9, 18). The voltage rise in Stage IV is driven by the increasing potential of the cathode, as the overpotential for copper reduction is relieved and copper ions compete with lithium ions to be reduced at the electrode surface. The gradual rise in voltage can be attributed to inhomogeneous blockage of the cathode's reactive surface by copper deposits, as well as the formation of micro-shorts as copper deposits begin to penetrate the separator. As copper bridges grow, the internal short resistance gradually decreases and a lower magnitude of voltage is required to pass a constant current through the device (in accordance with Ohm's Law)[180]. As the cell reaches Stage IV of the overdischarge, the electrochemical reactions within the cell stabilize and the voltage curve asymptotically approaches a plateau around -0.23 V. At this point, the copper bridges across the cell have grown sufficiently to cause the cell to behave as a resistor in the circuit rather than an electrochemical system, as electrical current is able to pass directly through the cell.

The temperature responses, measured by K-type thermocouples on the cell surfaces, are shown alongside their corresponding voltage curves in Fig. 7.4. As expected, surface temperature was found to be highly rate-dependent for the overdischarge process, as the 1C cell reached a maximum temperature of 79.2 ºC while the C/10 cell only reached a maximum temperature of 36.9 ºC. Temperature begins to increase rapidly around 100% DOD as ionic concentration gradients begin to build in both electrodes near the end of normal discharge. An inflection point in the temperature curve aligns with the initiation of SEI breakdown, showing that this process further increases the heat generation rate. The cell temperature reaches a maximum shortly after the onset of copper dissolution and gradually declined afterwards. This thermal response at both low and high C-rate points out that once the copper substrate starts dissolving, the thermal behavior of the cell is dominated by convection and not by the side copper dissolution reaction. This response also

indicates that no threatening thermal condition arises from the formation of the internal short, showing the relative fail-safe behavior of extreme overdischarge.

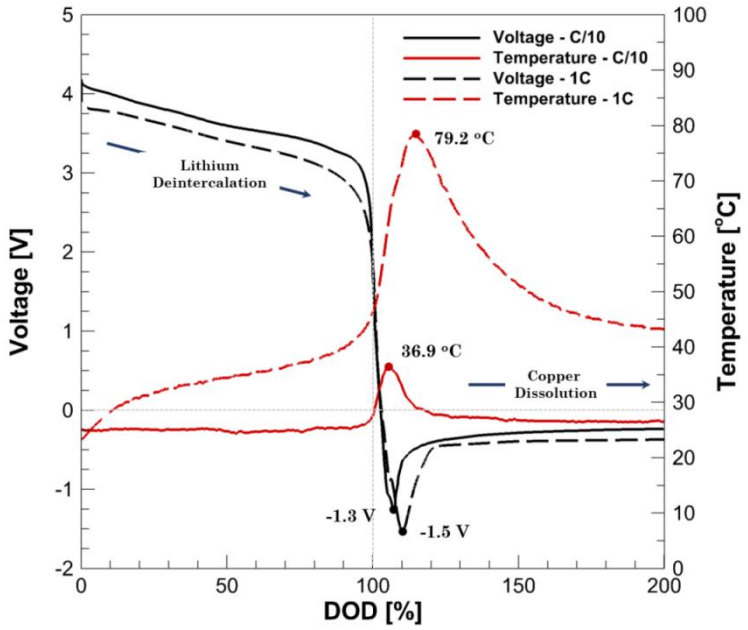

Fig. 7.4 Extreme overdischarge at low (C/10) and high (1C) rate. Electrochemical and thermal response of the cell during the overdischarge test.

Destructive physical analysis was performed on cells that experienced extreme overdischarge so that internal damage to cell components could be analyzed. A depiction of the process used to deconstruct the cells is shown in Fig. 7.5. In order to acquire a baseline for comparing the DPA results, a fresh cell was opened first. The unraveled cathode, anode, and separator surfaces of the fresh cell are shown in Fig. 7.6 (a) and (b). Both electrodes are double-sided, appearing smooth and black in the discharged state, although anode color varies with state of charge [176]. The separator material is white on the anode-facing sides and tan on the cathode-facing sides due to the Al_2O_3 ceramic coating facing the cathode. This coating is intended to improve the thermal stability of the separator and mitigate the consequences of lithium dendrite formation in the cell by preventing internal shorts from penetrating the separator [207].

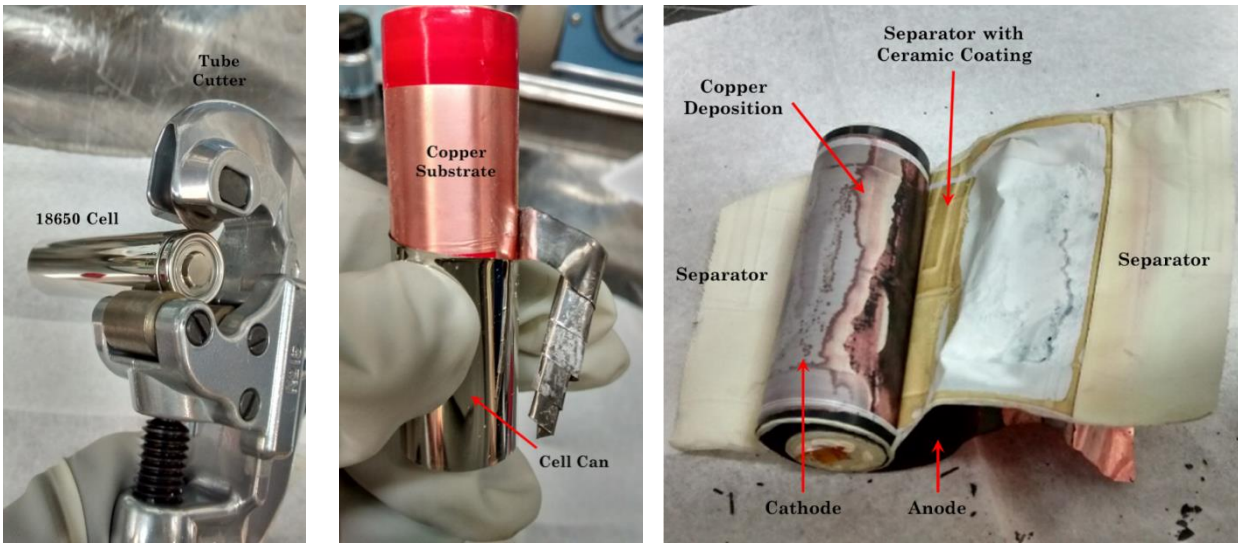

(a) (b) (c)

Fig. 7.5 Destruction physical analysis of the overdischarged cell. Process of the disassembly of cells: (a) cell header is removed using a tube cutter, (b) casing is peeled away with needle pliers, and (c) electrodes and separators are unrolled. Externally, the jelly roll did not show any visual damage to the naked eye. However, during the electrodes unrolling the negative electrode showed some brittleness and it felled apart by simply touching it.

The anode of the overdischarged cell suffered visible damage; see Fig. 7.6 (c). Before it was unraveled, the graphite material surface appeared mostly undamaged, but several deep cracks were found in the roll after it was unraveled. The dissolution of the copper current collector greatly reduces the mechanical stability of the anode while subsequently increasing the charge transfer resistance of the cell. Cracking also results in capacity loss and, in extreme cases, loss of electrical connection between the anode and the external circuit. As the anode was unraveled, it was revealed that the remaining copper current collector was extremely thin and unstable. Much of the anode material crumbled under light stress as it was unraveled, leaving large gaps in the roll, as shown in Fig. 7.6 (c). Meanwhile, the anode-facing separator faces showed essentially no damage or discoloration.

The cathode of the overdischarged cells also showed a visible degradation, Fig. 7.6 (d). Unlike the anode, the positive electrode did not exhibit any cracks or brittleness. On the contrary, the mechanical stability of the electrode seems to be reinforced due to the presence of the copper on its surface. The cathode active material from the electrode and the ceramic coating from the separator were the elements with the largest instability.

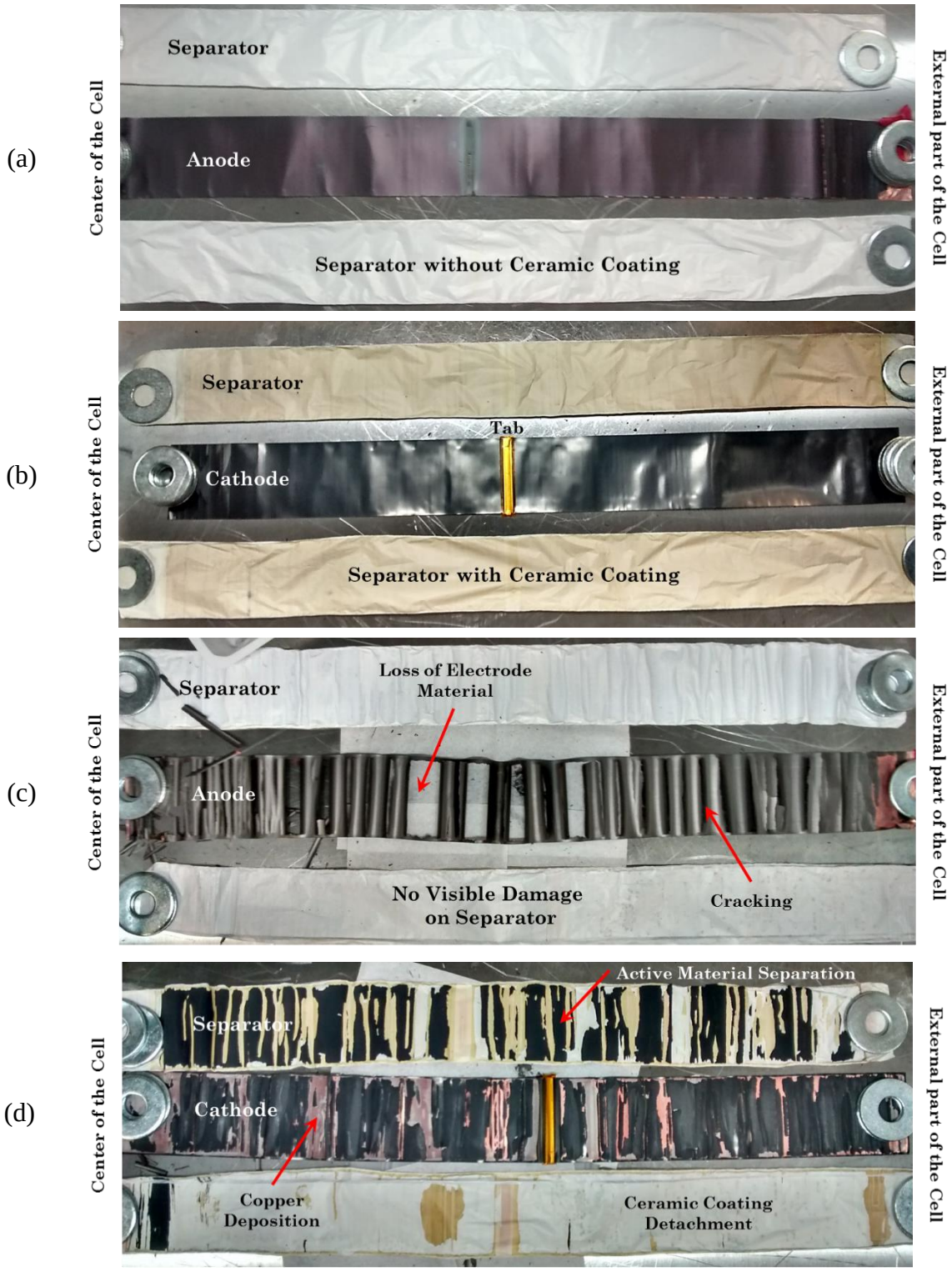

Fig. 7.6 Destructive physical analysis test. Electrodes harvested from a fresh cell (not cycled) and separators facing them: (a) anode, and (b) cathode. Electrodes harvested from the overdischarged cell at 1C-rate. (c) anode, and (d) cathode.

Cathode active material showed some detachment from the electrode, while the ceramic coating was detached from the separator. In all cells, the cathode-facing separators facing the exterior of the cell exhibited a predominant detachment of the ceramic coating while the separator facing the center of the cell exhibited a detachment of the cathode active material.

The center-facing side of the fully unraveled cathode roll and the corresponding separator faces are shown in Fig. 7.7. Extensive damage to both the cathode and separator surfaces is evident due to the non-uniformity and discoloration of the components. The degraded cathode can be divided into three zones, as labeled in the close-up image of Fig. 7.7. In Zone A, the ceramic coating on the separator detached and stuck to the cathode. The coloring of Zone A suggests that a layer of copper below the ceramic is providing the adhesion. In Zone B, a layer of cathode material adhered to the separator, tearing away from the electrode. Zone C represents a region where no material was ripped from either the electrode or separator surface, but a layer of copper deposition is visible. Samples from each of the three zones were taken for SEM and EDS post-mortem analysis to prove the presence of copper.

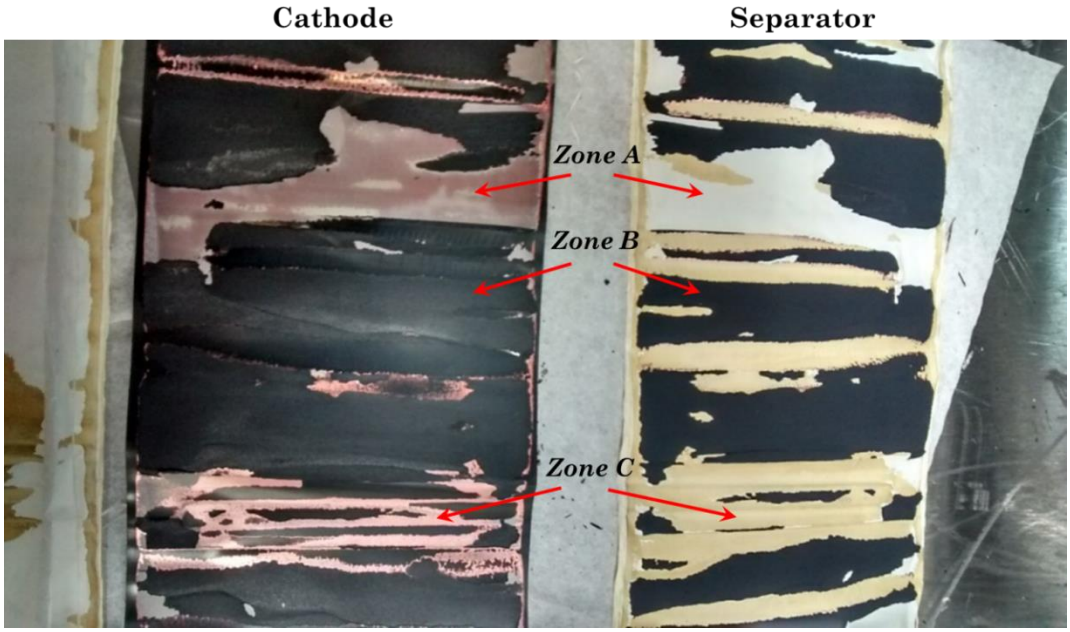

Fig. 7.7 Characteristic electrode degradation zones found close-up center-facing cathode surface, aligned with the corresponding separator. *Zone A*: detachment of ceramic coating from separator. *Zone B*: detachment of cathode active material. *Zone C*: copper deposition on cathode surface without material detachment from either electrode or separator.

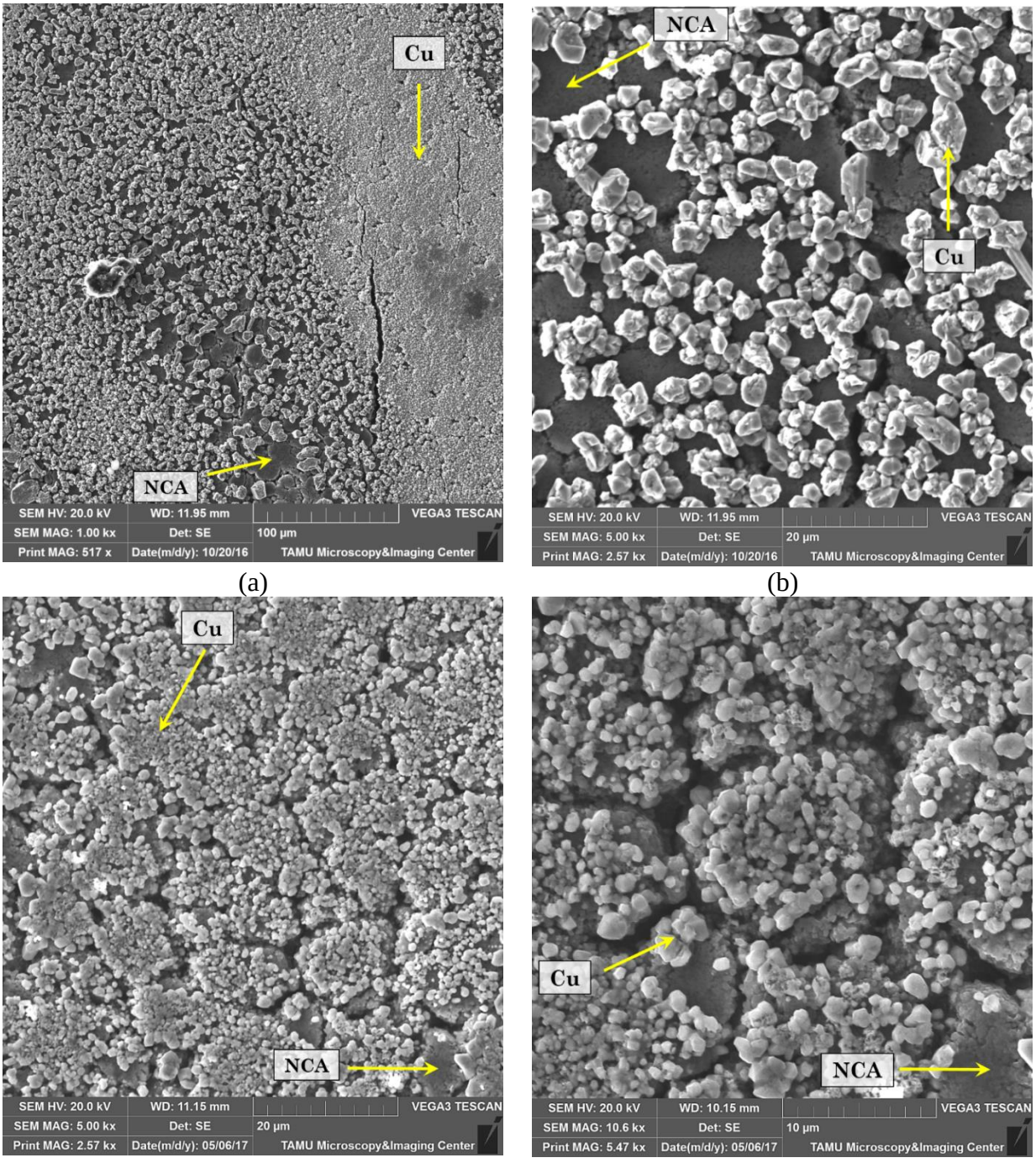

Fig. 7.8 SEM images of cathode surface of overdischarged cells. (a) C/10-rate at 1 kX magnification, (b) C/10-rate at 5 kX magnification, (c) 1C-rate at 5 kX magnification, (d) 1C-rate at 10 kX magnification. Copper deposits appear as light-colored particles on the surface.

The cathode surfaces of two overdischarged cells were examined via SEM imaging following the DPA. One cell, shown in Fig. 7.8 (a) and (b), was overdischarged at a C/10-rate, while the other,

shown in Fig. 7.8 (c) and Fig. 7.9 (d), was overdischarged at a 1C-rate. The most notable difference between these cells is the size of the grains formed by the copper deposits. In comparing Fig. 7.8 (b) and (c), each using a magnification of 5 kX, the grains formed in the 1C cell are significantly smaller and appear to be distributed more uniformly across the surface. This result can be explained by nucleation kinetics, as more nuclei tend to form and propagate during high-rate phase formation, resulting in finer grains [208].

Table 7.1 Elemental composition of samples extracted from the C/10 overdischarged cells obtained via EDS.

Sample			**Composition (*wt %*)**							
Electrode	*Zone*	*Description*	*Cu*	*C*	*O*	*Ni*	*Co*	*Al*	*F*	*P*
Cathode	A	Separator adhesion	**22.6**	23.5	22.0	4.6	1.4	16.4	6.9	2.6
Cathode	B	Removed cathode material	**0.0**	42.4	13.7	31.8	6.4	2.4	0.0	0.0
Cathode	C	Exposed copper	**47.9**	0.0	14.0	27.8	5.8	0.8	2.8	0.0
Anode	-	Graphite surface	**3.5**	95.7	0.0	0.0	0.0	0.0	0.0	0.8

The cathode sample from Zone A, see Fig. 7.9 (a) and (b), represents a region where the separator coating adhered to the cathode surface as the cathode and separator were peeled apart during DPA. This sample contained large amounts of copper, carbon, oxygen, and aluminum. The high concentration of aluminum and oxygen indicate that the ceramic coating of the separator was present on this surface. Fluorine and phosphorus are both present in the cell's electrolyte in the form of $LiPF_6$, and thus both elements should be embedded in the separator material. The presence of 22.6% copper by weight confirms that copper deposition occurs in the separator material as well as on the cathode surface. Zone B represents a region where the surface of the cathode material was torn away and the bulk active material was exposed, as seen in Fig. 7.9 (c) and (d). In this region, neither copper nor the elements of the electrolyte were present, indicating that copper was deposited primarily on the cathode surface rather than intercalating into the matrix. In Zone C, the cathode surface was left intact, but was coated with a layer of copper, as seen in Fig. 7.9 (e) and (f). EDS results indicate that this region contained 47.9% copper by weight, confirming that the cathode surface was the preferred location for copper deposition.

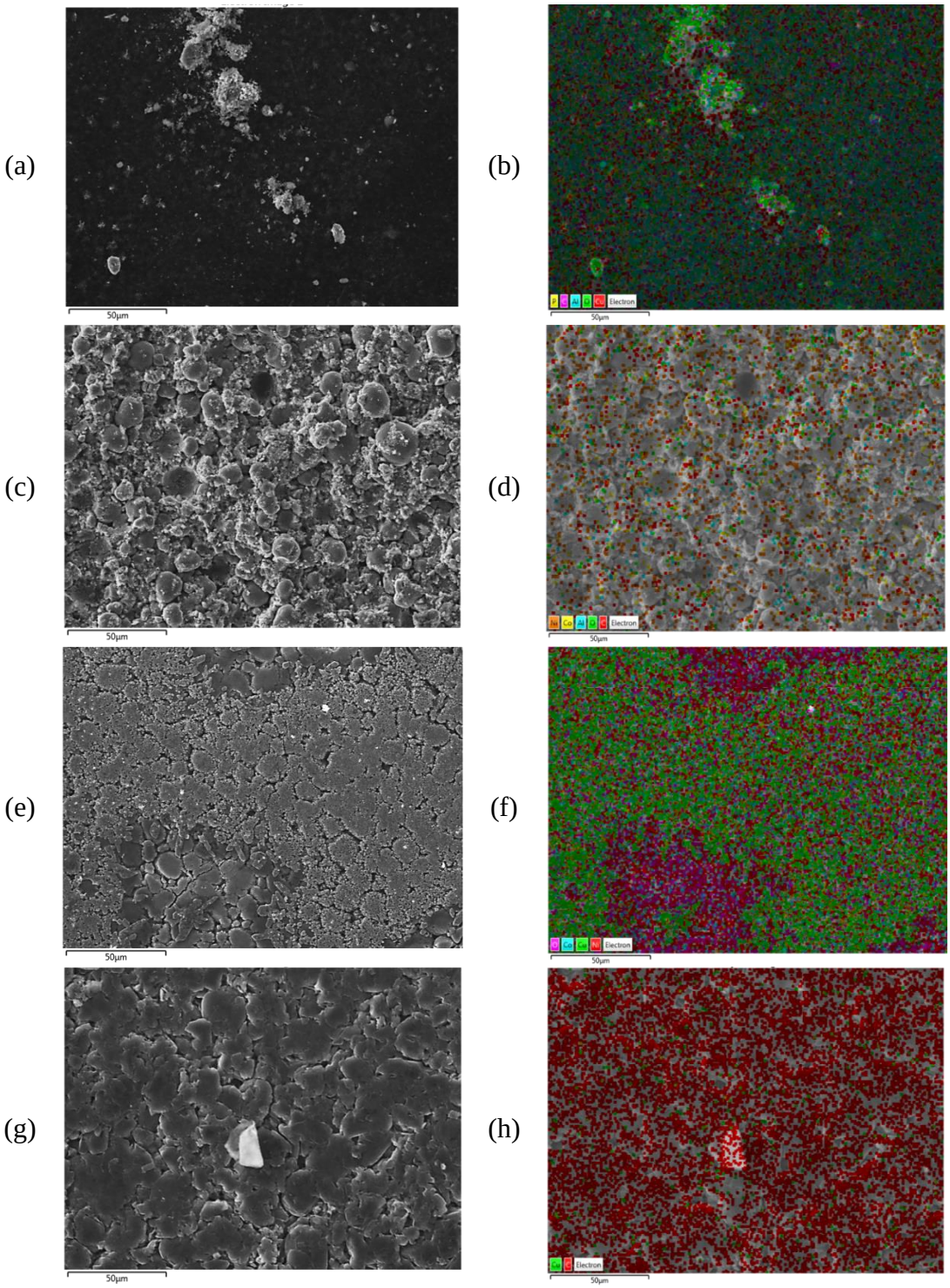

Fig. 7.9 EDS images of the samples extracted from the C/10 extremely overdischarged cells. (a) SEM (1.0 kX) and (b) EDS test of a cathode sample from Zone A: separator ceramic coating adhered to cathode surface. (c) SEM (1.0 kX) and (d) EDS of a cathode sample from Zone B: cathode bulk active material exposed. (e) SEM (1.0 kX) and (f) EDS of a cathode sample from Zone C: cathode surface with a deposited layer of copper. (g) SEM (1.0 kX) and (h) EDS of an anode sample. Percentages of identified elements are listed in Table 1.

A sample from the anode surface was also tested, see Fig. 7.9 (g) and (h), and it was discovered that this surface contained 3.5% copper by weight. The presence of copper deposits on both electrode surfaces, as well as within the separator, indicates that an internal short was formed in the cell. Although internal shorting can be consistently induced through deep overdischarge, as suggested by Guo et al., this method does not realistically simulate the dangers of internal shorting during cell operation because the stored energy in a cell at the end of a deep overdischarge phase is minimal. Since the magnitude of the final voltage plateau is small for both discharge rates, the power through the short remains low ($P = iV$) and the heat produced is safely dissipated in the cell. Although localized heating and evaporation of the electrolyte can be a concern when passing current directly through an internal short, no swelling or venting was observed in these tests.

8. CELL LEVEL DEGRADATION: AGING AND OVERCHARGE INTERPLAY IN POUCH CELLS

Relevant Publications and/or Working Papers

1. D. Juarez-Robles, A. Arun-Vyas, J. Jeevarajan, P.P. Mukherjee, 2019, *Degradation Mechanisms on Cycling at Different Overcharge Levels*, working paper

Overcharge is a serious concern for single cells and becomes extremely severe for large scale applications of Li-ion batteries. Despite the availability of several studies of aging-induced and overcharge-induced degradation, there still exists a knowledge gap of what would happen if both degradation mechanisms simultaneously occur.

In this work, commercial graphite/LCO pouch cells (5Ah) are continuously cycled at different upper cutoff voltages, 4.2 through 4.8 V, to elucidate the cumulative effect of the overcharge process on the long-term cycling. The extent of overcharge is an important parameter for the electrochemical performance and cell integrity. As the upper cutoff voltage is extended, the cell gains a higher initial capacity but the cycle life diminishes significantly. Cells overcharged beyond 4.5 V had a significant volume expansion and a large capacity fade rate. The cell starts to swell at this stage and a considerable increase in the temperature and internal resistance of the cells is observed. Lithium plating and electrolyte decomposition were observed in cells charged beyond 4.5 V, with SEM-EDS verifying their presence. Electrochemical evidence of both degradation modes appears as a voltage undershoot in the discharge curves. A comparative study of various State of Health (SoH) estimation parameters is presented with the introduction of a new dimensionless SoH indicator, Φ_R, based on internal resistance measurement. The proposed degradation number was found to be a good indicator of aggravated degradation in cells.

Introduction

8.1 Degradation-Safety Phenomena and Battery Management

Humanity faces the challenge of satiating the ever-increasing energy demand. This has led to rapid growth in the adaptation of renewable sources of energy. Although they produce the cleanest form

of energy, the fluctuations in electricity generation from these sources possess a great challenge to integrate it into the grid. Energy storage would compensate for the fluctuations and address the deficit in the supply and demand of electricity. Electrochemical systems are one of the most common techniques to store energy because they can produce electricity without any harmful emissions and minimal maintenance requirement. Lithium-ion batteries (LIBs) are one those electrochemical devices that convert the chemical energy of a substance to produce current. LIBs come as a boon to facilitate the use of renewable energy sources; however, safety-related incidents remain a concern. The safety issues in a LIB mainly arise under abuse and abnormal conditions. Although stringent battery safety standards are being followed in the industry, accidents involving LIBs are still witnessed. To prevent these accidents from occurring, it is important to understand the various abuse conditions leading to catastrophic events.

8.2 Aging

Lithium-ion batteries have found applications at all levels with portable devices at a small scale; electric vehicles at a medium scale; and grid energy storage at large scale. The widely use of LIBs in transport and portable applications is due to their high energy density, high efficiency, and long cycle life. Fulfilling the demand for such markets require more energy and better battery life from Li-ion batteries. To enhance battery life, understanding of the battery aging mechanism becomes essential. The capability of LIBs to store energy depletes over time and this phenomenon is defined as capacity fading (CF). Capacity loss may be a consequence of long cycling, i.e., using the batteries for a large number of charge and discharge cycles, unsuitable storage conditions, or an uncalled abuse condition.

Battery aging can be broadly classified in two ways: calendar aging and cycle aging. Calendar aging refers to the capacity loss that occurs when the cell is on the shelf and not in use.[138] Cycling aging refers to capacity fade and degradation of a cell being used continuously. Cycling rate,[157] operating temperature,[209] and voltage range[201] are the major parameters that affect the battery life and the extent of degradation. Charge-discharge protocol is also a major factor which impacts battery life and the extent of degradation.[157]

Aging mechanism provokes degradation of the LIB's components namely the electrodes, the electrolyte, the separator, and the current collectors. The degradation of the components is attributed to several chemical reactions that occur along with long-term cycling.[210] The reasons can be classified as loss of active material on the positive and the negative electrode, as well as the loss of the lithium inventory.[211-212] The reaction between the anode, usually graphite, and the electrolyte forms a passivating layer commonly known as solid electrolyte interphase (SEI). SEI layer growth due to cycling results in a reduction of the lithium inventory, consumption of the anode active material, electrolyte decomposition and increases the cell internal resistance.[178, 213] Under extreme conditions, such as very low temperature[214-215] or high charge rates,[216] lithium plating may occur. Charging the battery under these conditions can lead the anode potential to fall below 0.0 vs. Li/Li^+, thus, not allowing the lithium to intercalate and instead of depositing on the graphite active material surface. This phenomenon is known as lithium plating results in loss of lithium inventory and consequently in the cell capacity fade.[150, 217-218] The plated lithium can again react with the electrolyte to form a new layer of SEI or can detach from the surface becoming dead lithium.[219]

The capacity loss that occurs in the initial cycles is dominated by the SEI growth and the capacity under load is observed to have a linear dependence on the charge throughput.[220-221] Schuster et al. report an aberration from the linear dependence and have observed the appearance of nonlinear aging after prolonged cycling for NMC/graphite cell at moderate temperature and charging rates. The transition point from linear to nonlinear degradation is believed to be the point where lithium plating becomes the dominant degradation process. The deterioration in ionic kinetics of anode due to SEI growth and loss of graphite active material are considered as the primary reason for the occurrence of lithium plating.[212]

Yang et al. conducted a study of long-term aging behavior for NMC/graphite pouch cells. An anomalous voltage undershoot is reported in their study at high discharge rates of 3C. This is a typical indicator of poor electrolyte performance and has been reported in the study of cells at freezing temperatures.[214] The subsequent occurrence of SEI growth along with lithium plating clogs the pores near anode-separator interface and reduces the anode porosity. The reduction in the anode porosity leads to the rise in the transport resistance in the electrolyte resulting in the

voltage undershoots.[222] The plated lithium layer may grow further and form dendrites like structure, which in the worst-case scenario can pierce through the separator causing an internal short circuit resulting in a catastrophic situation. This event would not only lead to capacity loss instead could result in cell failure. Cell failure accompanied by a hazardous situation is often a consequence of an abuse scenario, such as overcharge.

8.2.1 Overcharge

Overcharge is often caused due to a faulty charger in portable electronics. The failure of a Battery Management System (BMS) to stop charging beyond the upper cutoff voltage is the primary cause for overcharging a battery.[223] Zhang et al. define overcharge as a state when electricity is forced through even after it has gained full capacity.[224] One important manufacturer specification is the voltage range under which the battery must be operated to get the best performance, i.e., optimal capacity and extended lifetime. If the cell is charged beyond the recommended upper cutoff voltage, then the phenomenon is known as overcharge. Overcharging a battery leads to degradation of cell components depending on the extent of overcharge and can result in a thermal runaway in extreme cases. Thermal runaway induced by overcharge is considered harsher than the other abuse conditions as while overcharging the cells gain excessive energy.

Over the years several efforts have been made by the researchers to understand the behavior of LIBs under overcharge abuse condition. Some of these studies have been purely experimental,[188, 225-228] some purely model-based,[229-230] and few are a combination of both. Gas and heat generation attributed to the occurrence of various side reactions are the most commonly reported characteristics observed during overcharge.[230] Ohmic heat accounts for the initial part of the heat generation. In overcharge, the intercalation sites in anode start filling up and as the anode is completely lithiated, Li-ions start plating the active material surface. The ohmic heat generated increases the cell temperature and facilitates the exothermic reaction of the plated lithium with the electrolyte. The heat released due to the anodic reactions and cathode over-delithiation lead to an unstable chemical condition. The electrolyte also reacts with cathode when its potential goes beyond the safe electrochemical window. The reaction between the electrolyte and both electrodes produces gases and increases the cell internal pressure. The gas generated can be vented out from a cylindrical cell. However, in a pouch cell, severe swelling is observed and in extreme cases, the

cell will rupture.[188] The cell rupture exposes lithium to the atmosphere further resulting in an exothermic reaction with moisture present in the air. The excessive amount of heat generation accelerates the rise in cell temperature. Along with this, the growth of lithium dendrites may pierce through the separator causing an internal short circuit increasing even more, the cell temperature. The heat generated through the side reactions and the internal short circuit can lead to thermal runaway. This becomes a serious issue when the cell is embedded in a module or stored close to other cells. The cell to cell propagation of thermal runaway can even be more catastrophic.[231]

The extent of degradation in overcharge depends on various factors such as C-rate, operating temperature, size, architecture, and chemistry of the cell. Ouyang et al. conducted a study on the overcharge induced capacity fading in an NMC+LMO/graphite pouch cell. Capacity fade occurred till 120% SOC with an increase in the internal resistance. At 140% SOC, the cell started swelling and loss of active material took place.[232] Leising et al. studied the effect of C-rates for an overcharge of prismatic LCO/graphite cells. They observed that at low C-rates swelling, temperature and internal resistance increased at a lower rate as compared to the cells overcharged at higher C-rates.[40] The cathode was found to be the major source of heat generation thus confirming that overcharge is cathode dominated process which was consistent with DSC studies conducted by Zhang et al..[188, 233]

Electrolyte decomposition during overcharge is another key aspect to better understand the gas evolution and cell degradation. If the electrode voltage exceeds the stable voltage limit, the electrolyte starts decomposing and forms gases initiating an aggravated degradation of the cell.[234-235] Gas generation is believed to displace the electrolyte and block the ionic path for transport of Li-ions thus making a region of electrode inactive and resulting in the capacity fade.[228] Carbon dioxide (CO_2), carbon monoxide (CO), hydrogen (H_2), methane (CH_4), ethylene (C_2H_4), and ethane (C_2H_6) were found to be the major components of gas evolution during the overcharge test of LIBs. To find out which gases are released from each electrode, Metzger et al. isolated the cathode and anode in two separate cells. The study concluded that CO_2 and CO are produced at cathode whereas, H_2, CH_4, C_2H_4 are formed at the anode.[236] The flammable nature of the carbonates poses a safety concern in the wake of thermal runaway.

8.2.2 Current Work

Despite the availability of several studies of aging-induced degradation and overcharge-induced degradation, there still exists a knowledge gap of what would happen if a LIB is continuously cycled under overcharge condition. It is important to understand how the increase in the voltage window affects the capacity retention, cycle life, and degradation of the cell components. The objective of this work is to understand the degradation behavior of Li-ion pouch cells when cycling under overcharge extremes. This study aims to provide an in-depth understanding of such degradation mechanisms and be a guide in safety developments of battery systems.

8.3 Experimental Details

In this study, a 5 Ah commercial pouch cell (Wanma) obtained from a reputable vendor is used as the working cell for the electrochemical test. The pouch cell has graphite (C) and lithium cobalt oxide (LCO) as its anode and cathode, respectively. The electrochemical tests are carried out at ambient temperature using a battery tester (Arbin, BT-2000). Voltage, current, resistance, temperature, and capacity are recorded for each cycle and further used to analyze the results. The sampling rate for all tests and parameters is 1 Hz.

8.3.1 Conditioning Test

Prior to any test, a formation cycle is conducted on every cell under the recommended voltage window, E_{safe} = [2.7, 4.2] V, given by the manufacturer. The conditioning test helps to evaluate the charge/discharge capacity accounting for the cell-to-cell variation and to form the electrochemically stable SEI. The conditioning test consists of three cycles using a Constant Current – Constant Voltage (CCCV) charge and a Constant Current (CC) discharge at a C/10-rate with a cutoff current of C/50 (100 mA). A 30-minutes rest is left in between the charge and discharge process.

8.3.2 Long-Term Cycling

After performing the conditioning test, the cells are subjected to long-term cycling at different overcharge levels. The cells are charged up to the upper cutoff voltage, E_{upper}, at 1C-rate using a CCCV protocol with a C/50 (100 mA) cutoff current. The E_{upper} values selection is done in such way that the cell has to be overcharged while still is cyclable, i.e., the cell must not be driven to a

no-return point where the cell cannot be longer be discharged. Thus, a fully discharged fresh pouch cell is overcharged at C/5-rate until failure to characterize the overcharge behavior of the working cell. The electrochemical result is used to select the E_{upper} values to be used for cycling under the continuous overcharge condition. Fig. 8.1a shows that the cell starts to fail as the voltage rises to 5.0 V. In order to avoid failure of the cell in the initial cycles, the upper cutoff voltages up to 4.8 V are chosen for this study. The cells are discharged to a common lower cutoff voltage, 2.7 V, at 1C-rate using a CC protocol.

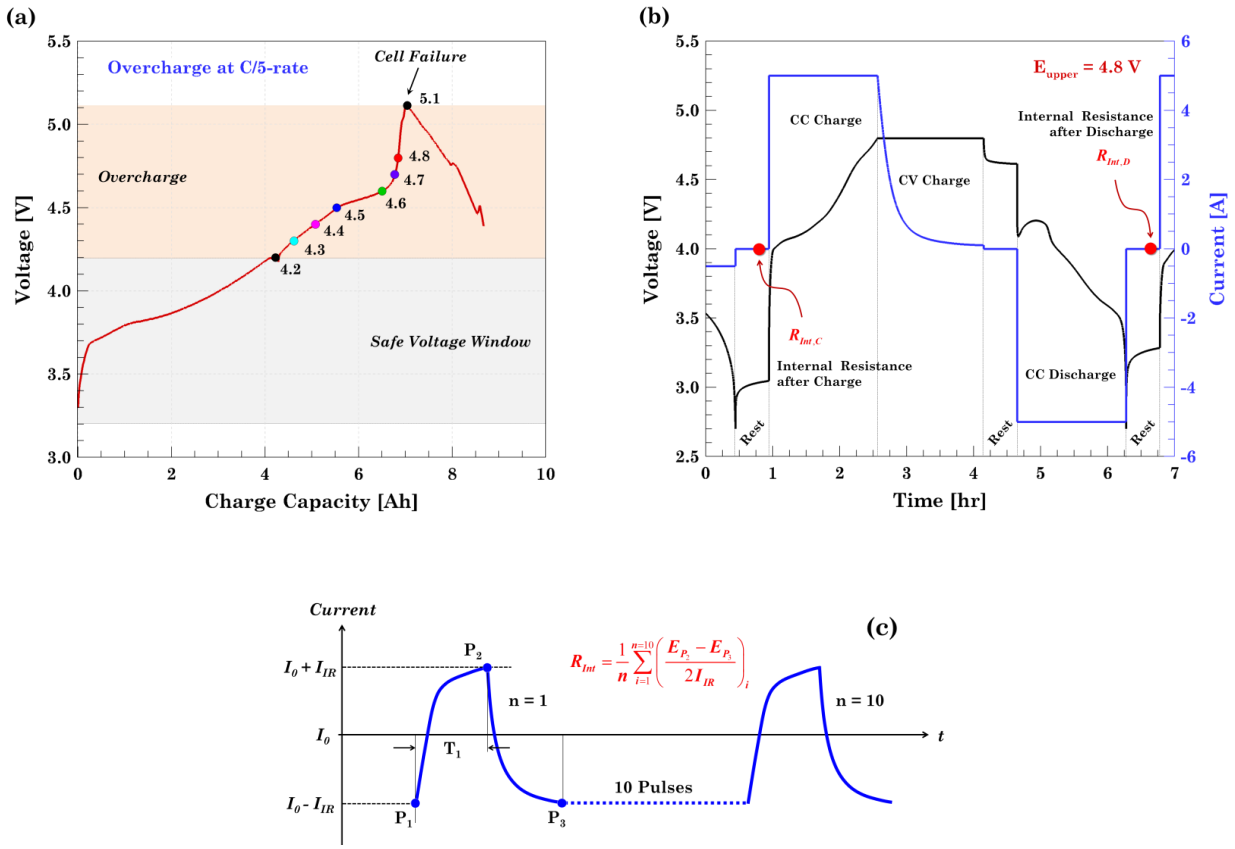

Fig. 8.1 Design of the long-term cycling protocol. (a) Selection of the cutoff voltages selection based on the voltage response from an extreme overcharge. The onset of failure takes place when the cell reaches 5.1 V. (b) Internal resistance measurement during cycling after charge and discharge process. (c) In-built function method to estimate the average internal resistance.

In between every charge and discharge process, the cell is rest for 30 minutes with an internal resistance (IR) measurement using the in-built function from the battery cycler, as shown in Fig. 8.1b. The initial 25-minutes rest allows the cell to reach thermal and electrochemical equilibrium. At this point, a current pulse train is passed through the cell and the average IR is calculated from

the Ohm's law, see Fig. 8.1c. Then, the cell is rest for another 5 minutes before moving to the next cycle. The in-built function uses a total of 10 pulses with a 1.0C current amplitude (5 A) for a period of 100 ms. For every cycle, two IR values are calculated one after the charge, $R_{Int,D}$, and one after the discharge, $R_{Int,C}$. Monitoring the IR provides valuable information on the SoH of the cell as the cell ages.

A 20% capacity loss with respect to the nominal capacity of the cell (5 Ah) is set as the stopping criteria for the aging + overcharge test. If the LIB is driven beyond this degradation level, it no longer fulfills the primary application requirements and it compromises the safe and useful operation in a secondary application.[3]

8.3.3 Heat Generation

All abuse conditions finally lead to thermal abuse and in extreme conditions, it may translate into a thermal runaway condition. Hence it is important to investigate the temperature evolution of the cell, as a function of the SOC, SOH and the upper cutoff voltage, for cycling under continuous overcharge conditions. The cell skin and ambient temperature are recorded using a T-type thermocouple (Omega) attached on the surface of the battery. Heat generation is back-calculated using the inverse heat transfer method proposed by Mistry et al.[174] using the thermal response of the cell. The method is applied to the CC discharge and the CC charge. CV charge is not analyzed because heat generation starts decreasing as a consequence of the current decrement and that convection becomes more predominant than the heat generated. An analysis of the energy balance involves the heat generated during the charge/discharge process, heat dissipated to the environment by convection and energy stored by the cell, as shown in Eq. 8.1,

$$mc\frac{dT}{dt} = \overset{g}{Q} - hA\left(T - T_{\infty}\right) \qquad \text{Eq. 8.1}$$

where m is the mass of the cell ($m = 0.097\ kg$), c is the heat capacity ($c = 837\ J/(kg{\cdot}K)$) [174], A is the surface area ($A = 12.344{\times}10^{-3}\ m^2$), T is cell skin temperature (^oC), T_∞ is the ambient temperature, h is the convective heat transfer coefficient (W/(m^2·K)), and $\overset{g}{Q}$ is the heat generation (W). No spatial variation in temperature is considered since $Bi = 0.012 < 0.1$. From all the

properties in Eq. 8.1, T, $\overset{g}{Q}$, h, and T_∞ varies with time. To account for the temporal variation, the cell temperature is fitted by the analytical expression in Eq. 8.2.

$$T = c_0 + \sum_{i=1}^{N} c_i e^{-t/\tau_i} \qquad \text{Eq. 8.2}$$

The time constants (τ_i) in the exponential function are logarithmically distributed between the Nyquist frequency and the convection time constant, i.e., $\tau_i \in [\tau_{\min}, \tau_{\max}] = [2/f_s,\ mc/hA]$. The number of terms, N, is estimated via a sensitivity test using the coefficient of determination, R^2, as the decision criteria.

The convective heat transfer coefficient is assumed to vary with time and it is back-calculated from the resting period, after the discharge process, when the heat is no generated and convection is the only heat transfer mode. The estimated h value varies as $\bar{h} \approx 10 \sim 20\ \ W/\left(m^2 \cdot K\right)$. Once h is known, the heat generation profile can be calculated. This method has the advantage of showing the variation of the heat generation as a function of the SOC rather than estimating a single value with the applied current and the internal resistance, $\overset{g}{Q} = I^2 \overline{R}_{Int}$.

8.3.4 Destructive Physical Analysis

At the end of the cycling test, the aged cells are subjected to a destructive physical analysis (DPA) to complement the electrochemical results. Overcharged cells have more energy stored than fresh cells and hence opening them poses a threat to safety. For that reason, the cell autopsy is carried out in an argon filled glove-box (H_2O and O_2 content < 0.1 ppm, MBraun) at a fully discharge condition to minimize the risk of a hazard.

An effort has been made to measure the volume expansion in the cells by quantifying the increase in cell thickness taking a fresh cell as the reference for comparison. The fixture has two parallel acrylic plates fastened at the ends with 4 sets of nuts and bolts. The cell was placed between the two plates and was tightened using the screws until the cell stopped moving and remained fixed in that position. A Vernier caliper was used to measure 12 readings (3 on each side) the inner distance between the plates.

Electrodes taken out after dismantling the aged cells are studied via Scanning Electron Microscopy (SEM) (Hitachi S4800) and Energy Dispersive X-Ray Spectroscopy (EDS) techniques. More details of the procedure used to disassemble the cell can be found in the Appendix C reported by Juarez et al.. Representative samples are extracted by cutting small pieces of electrodes inside of the glovebox and then transferred to the microscope. A 30 kV acceleration voltage and 10 μA current are used to get the SEM images at different magnifications. EDS analysis is also done on the same samples to get the chemical composition of the electrodes.

8.3.5 Gas Chromatography/Mass Spectroscopy (GC/MS)

The electrolyte collected while conducting the cell DPA is analyzed with the Agilent 5975C MSD equipment. The chromatographic separation is performed using a DB-5MS column (30 M x 0.250 mm x 0.25μm film). Helium is used as the gas carrier with a constant flow rate of 0.8 ml/min. Electron impact and chemical ionization are obtained in the mass range of 45-500 atomic mass unit (amu). The injector temperature is 250 ^{o}C and the split ratio of 1:20 is used with 1 μl of the sample being injected.

8.4 Results and Discussion

8.4.1 Cycling Performance

The typical protocol used for cycling the cell under continuous overcharge is exemplified with the cycling profile for the cell cycled in the voltage range of [2.7, 4.8] V, see Fig. 8.2a. In agreement with previous results, as the cell degrades, capacity decreases, temperature increases, CC charge time decreases, and the CV charge time extends. And, the temperature during discharge is greater than the charge one due to morphological differences between the electrodes and the asymmetrical intercalation/deintercalation rates.[173]

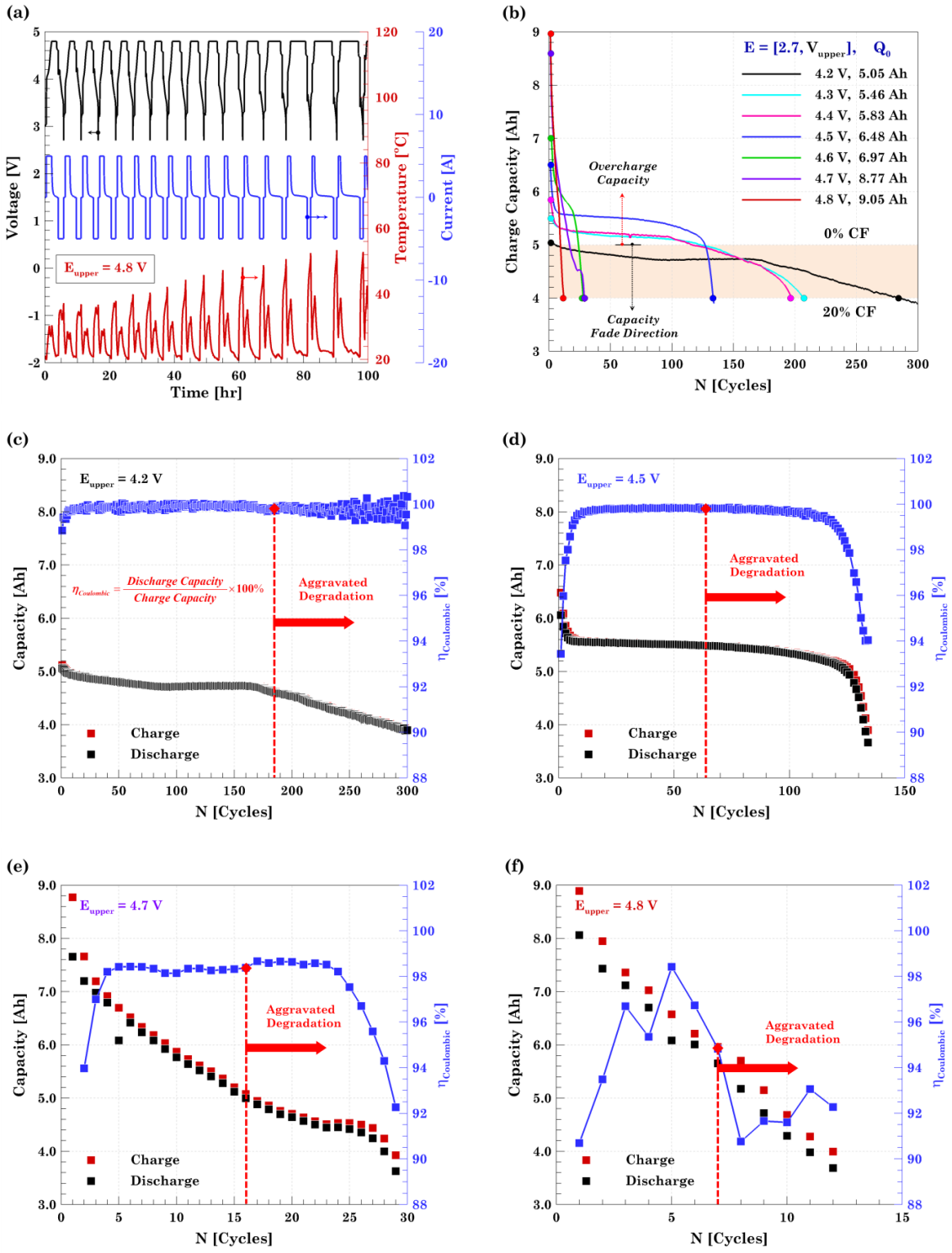

Fig. 8.2 Long-term cycling and cycle life. (a) Representative cycling protocol corresponding to the 4.8 V cell. (b) Capacity fading definition and cycle life comparison. Capacity fading and coulombic efficiency for (c) aging dominated regime, 4.2 V; (d) slight overcharge regime, 4.5 V; (e) overcharge dominated regime, 4.7 V; and (f) extreme overcharge regime, 4.8 V. The red dashed line represents the cycle at which degradation is exacerbated.

Capacity fade quantification is usually done by comparing the actual capacity of the cell with respect to its initial capacity measured during the first full cycle. This method is suitable when the cells are cycled under the same voltage window and it is necessary to account for the cell-to-cell variations. In this case, the voltage window is different with an increasing initial capacity as the upper voltage limit is also increased. Due to the different capacities observed for each cell in the first cycle, the initial capacity cannot be taken as a reference for capacity fade. Hence the nominal capacity of the cell (5 Ah) is taken as the reference to observe capacity fade. The charge capacity of 4 Ah represents 20% capacity loss with respect to the nominal capacity and is the stopping criteria for all the tests, Fig. 8.2b. The additional capacity obtained above 5 Ah is defined as the overcharge capacity.

An initial comparison of the long-term cycling at the different cutoff voltages is shown in Fig. 8.2b. The charge capacity for the first cycle, denoted by Q_0, demonstrates the root of the commonly misleading idea that more energy can be stored in the cell if the upper cutoff voltage is extended. The cell attains maximum capacity (9.05 Ah) when cycled from 2.7 - 4.8 V and least (5.11 Ah) when cycled from 2.7 – 4.2 V. It should also be noted that as the upper cutoff voltage increases, the cell decay increases rapidly, Fig. 8.2b. The cell cycled under the safe voltage window of 2.7 - 4.2 V faded to 80% capacity in 290 cycles whereas the cell cycled in the voltage window of 2.7 – 4.8 faded to 80% capacity in 15 cycles. So, there exists a trade-off between the initial capacity obtained and the cycle life of the cell. By expanding the voltage window, i.e., by increasing the extent of overcharge, a higher initial capacity can be obtained whereas the cell cycle life is compromised.

Depending on the overcharge level, two degradation mechanisms, aging and overcharging, compete in terms of the degradation dominance. Thus, the cell cycled up to 4.2 V is purely dominated by the normal aging processes, whereas, the long-term performance from the cell cycle up to 4.8 V, is fully dominated by the degradation mechanisms associated to overcharge. In between the two upper cutoff voltage extremes, there is a competition between aging and overcharging. The long-term cycling results allow elucidating that at 4.6 V, the overcharge effect becomes predominant and cycle life gets significantly reduced as shown in Fig. 8.2b. Based on the long-term cycling and the overall results, the results are grouped into four regimes associated with

the predominant degradation dominance. The results from the cells belonging to one group shared similar electrochemical, thermal characteristics. For that reason and from hereafter, only one representative result from each of the following groups is presented.

Aging Dominated Regime. This degradation scenario is represented by the cell cycle up to E_{upper} = 4.2 V, i.e., the safe voltage window. Capacity fade results from this cell are mainly due to conventional degradation mechanisms. This cell achieves an initial capacity of 5.05 Ah and it takes 285 to reduce to 80% of the nominal capacity. The capacity fading plot for this scenario is shown in Fig. 8.2c. Capacity fades faster during the first cycles due to SEI formation. Once the SEI layer becomes stable, capacity decreases at a slower rate until the non-uniform lithiation/delithiation and lithium plating takes place ($N_{Cycle} \approx 170$) and capacity fades at a faster rate.

Slight Overcharge Regime. This degradation scenario is represented by the cells charged up to E_{upper} = 4.3, 4.4, and 4.5 V. Aging still dominates the degradation phenomena with a slight contribution from overcharge. The 4.3, 4.4, and 4.5 V cells achieve an initial capacity of 5.46, 5.83, 6.48 Ah, and they take 209, 198, 135 cycles, respectively, to reduce their charge capacity to 4.0 Ah. The capacity fading plot for this scenario is shown in Fig. 8.2d. The initial overcharge capacity gained by extending the upper voltage window is quickly lost in less than 10 cycles. Then, the capacity plot exhibits the characteristic slow decay associated with the conventional aging. The degradation associated with SEI growth and most importantly, the presence of lithium plating leads to the transition from the linear to non-linear capacity fade trend ($N_{Cycle} \approx 120$).

Overcharge Dominated Regime. This degradation scenario is represented by the cells charged up to E_{upper} = 4.6 and 4.7 V. Degradation phenomena associated to overcharge becomes dominant with a minor degradation associated with aging. The 4.6 and 4.7 V cells achieved an initial capacity of 6.97, 8.77 Ah and both take 29 cycles, respectively, to reduce its capacity to 4.0 Ah. The capacity fading plot for this scenario is shown in Fig. 8.2e. The two cells under this condition exhibit a slight volume expansion. The large cutoff voltage at the end of the charging process promotes the electrolyte decomposition and its reaction with the LCO electrode. The fast capacity fade for the two cells not only depends on the exacerbated lithium plating presence but also the

electrolyte contribution, whereas, lithium inventory consumption by SEI growth becomes negligible.

Extreme Overcharge Regime. This degradation scenario is represented by the cell cycle up to E_{upper} = 4.8 V, the safe. Degradation imposed by overcharge hinders the cell cyclability and leads the cell to an early failure. This cell achieved an initial capacity of 9.05 Ah and it takes 15 cycles to reduce to reach the end of the cycle life. The capacity fading plot for this scenario is shown in Fig. 8.2f. The cell under this condition swelled to a size almost twice its initial volume. Lithium plating and electrolyte decomposition are the two degradation mechanisms behind the accelerated capacity fade. The electrolyte decomposed not only generates the gases but also reduces the pathways in the electrolyte to transport the Li-ions and secludes large portions of both electrodes.

Coulombic efficiency, η, is defined as the ratio of discharge to the charge capacity. It is an indicator of how much energy can be extracted from the LIB with respect to the energy stored. Low coulombic efficiency signifies that less discharge capacity is obtained as compared to the charge one, indicating that the cell is losing capacity as a consequence of energy lost due to the side reactions. Fig. 8.2c-f shows the evolution of the coulombic efficiency with its corresponding charge and discharge capacity. Coulombic efficiency is low at the beginning of the aging test due to the formation of the SEI passivating layer. As aging goes, η increases again since lithium inventory stops decreasing since SEI becomes stable. At the end of the cycle life, η decreases again as the chemical and electrochemical degradation takes over the cell performance. In extreme cases such as the cells charged up to 4.6, 4.7 and 4.8 V, the η starts decreasing a faster rate as the cells start failing and do not show up the characteristic parabolic trend.

Although the point at which the cell starts failing faster can be inferred from the capacity fade plot, an analytical way to predict the onset of rapid degradation needs to be explored. A differential analysis of capacity (dQ/dN) and coulombic efficiency (dη/dN) with respect to the number of cycles is shown in Fig. 8.3. Third-order and sixth-order polynomial are found to be the best fit for the charge capacity and coulombic efficiency data, respectively.

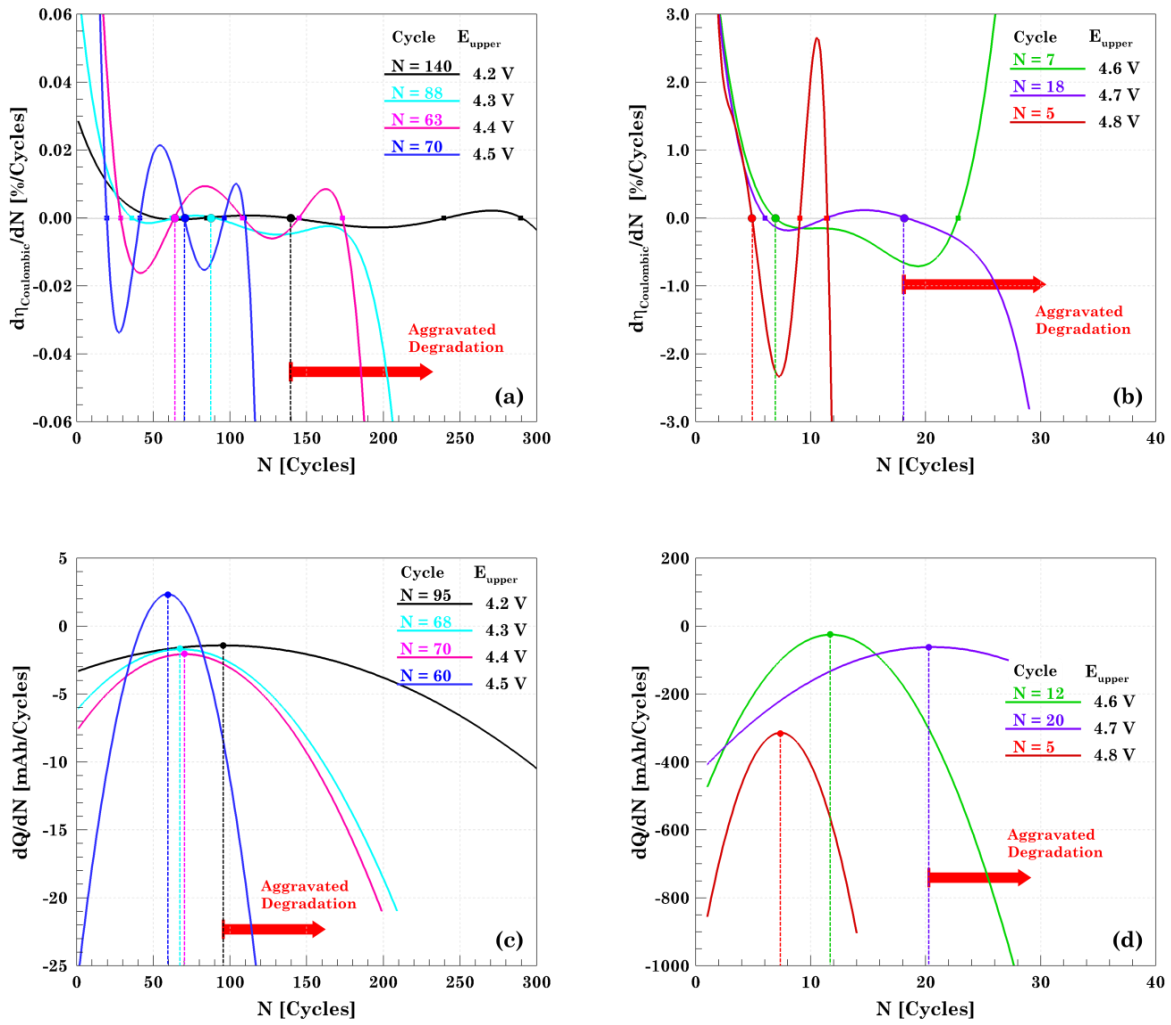

Fig. 8.3 State of health prediction based on the aggravated degradation onset. Differential coulombic efficiency for (a) the aging dominated and slight overcharge regimes, 4.2-4.5 V; and (b) overcharge dominated and extreme overcharge, 4.6-4.8 V. The onset of aggravated degradation is represented by the maximum coulombic efficiency. Differential capacity analysis for (c) the aging dominated and slight overcharge regimes, 4.2-4.5 V; and (d) overcharge dominated and extreme overcharge, 4.6-4.8 V. The peak of the parabola represents the capacity trend changes, in particular, the cycle where capacity starts fading faster.

The peaks obtain in the dQ/dN serves as an indicator for cell degradation and that a change has occurred in the cell. Similarly, the point at which the dη/dN crosses zero indicates the point where the coulombic efficiency reaches its maximum value. Usually, the coulombic efficiency increases in the first few cycles and remains constant until the cell starts to fail. There are several points in the dη/dN curve at which the curve crosses zero, see Fig. 8.3c-f. Although multiple zeros can be

found only a few of them represent the onset of faster degradation, the selection is done along with the capacity fade plot. A general trend visible in both the plots for dQ/dN and dη/dN is that as the upper cutoff voltage is increased the number of cycles for initiation of cell degradation decrease. For example, the prediction for the onset of failure for cell cycled up to 4.2 V is 95 cycles and 140 cycles as per the dQ/dN and dη/dN, respectively. Whereas, for the cell cycled up to 4.8 V the prediction for the onset of failure is 7 cycles and 5 cycles as per the dQ/dN and dη/dN, respectively. The discrepancies between the predictions made by the differential coulombic efficiency and the differential capacity do not allow elucidating the cycle where the cell starts fading fast. Internal resistance is another indicator for the prediction for SOH and consequently for the aggravated degradation.

Internal resistance has been explored as one of the parameters to monitor the SoH of the battery. It is important to have knowledge of SoH in order to predict the occurrence of any severe failure and avoid hazardous events.[237] Two major inferences can be made by observing the data presented in Fig. 8.4. Firstly, it can be observed that the cell internal resistance increases indicating that the cell has started degrading. Another notable inference is that as the upper cutoff voltage is increased, the IR magnitude increases at a faster rate. Moreover, the resistance of the cell charged up to a higher voltage increases in a lesser number of cycles. For example, both the charge and discharge resistance of the cell cycled from E_{upper} = 4.2 V goes from 28.7 to 35.8 mΩ after 285 cycles. However, for a cell cycled up to E_{upper} = 4.8 V, the resistance of the cell increases from 17.8 to 44.4 mΩ in just 13 cycles. The cell charged up to a higher cutoff voltage degrades faster and further strengths our understanding about the increase of resistance leading to capacity fade of cells. The rise in the internal resistance of the cell is mainly attributed to the growth of the SEI layer with cycling and the level of mechanical degradation of the electrodes.[238]

The magnitude of resistance at the end of the discharge is higher than the one at the end of the charge when the cells are fresh. The discharge resistance remains higher for the majority of the initial cycles but after a point, the charge resistance becomes larger than the discharge resistance. Owing to this characteristic trend a non-dimensional parameter Φ_R has been defined and proposed as an indicator of aggravated degradation. The proposed degradation number, Φ_R , is defined as the following ratio,

$$\Phi_{R} = \frac{R_{Int,C} - R_{Int,D}}{R_{Int,D}} \qquad \text{Eq. 8.3}$$

The proposed SoH indicator is negative when the cell is fresh since $R_{Int,C} > R_{Int,D}$. The cell is said to degrade faster when Φ_R crosses the zero mark. The cycle number where the crossing happens is indicated in Fig. 8.4a-e, e.g., for the cell cycle up to 4.5 V, $\Phi_R = 0$ at the 51 cycle. At this point, the resistance at the end of the charge surpasses the discharge one due to the degradation imposed by cycling and overcharging the cell. Thus, on every cycle, a small portion of the energy stored will be used to overcome the increase in the resistance and reduce the capacity utilization of the cell. From the predictions made, it is evident that the cell charged up to a higher voltage fails at a faster rate which is in agreement with the results presented for the capacity fade and the coulombic efficiency.

To compare the accuracy of all the SoH indicators analyzed in this study, a comparative study with the actual point at which the cell starts to fail faster has been presented in Fig. 8.4f. The actual point is obtained by directly analyzing the capacity fade results. It can be observed that Φ_R is a better predictor as compared to the other parameters. The incorrect predictions made by dQ/dN and dη/dN come from the fact that both the capacity fade and the Coulombic efficiency curves are relatively flat making it difficult to predict the onset of fast failure. For the cells cycled to higher voltages including 4.5 V to 4.8 V, all three parameters are very close to the actual point of failure. Thus, all the indicators discussed can at least alert about any possible future failures which can be taken as a measure to conduct a complete inspection of the battery. Moreover, Φ_R was found to be the best predictor of aggravated degradation and can be utilized for SoH monitoring in LIBs. Based on the cycle prediction done via the degradation number, voltage profiles are obtained at five cycles corresponding to: first cycle (0% CF), last cycle (20% CF), and the cycle where faster degradation starts ($\Phi_R = 0$), and two more cycles in between the last three points, see Fig. 8.5a-d.

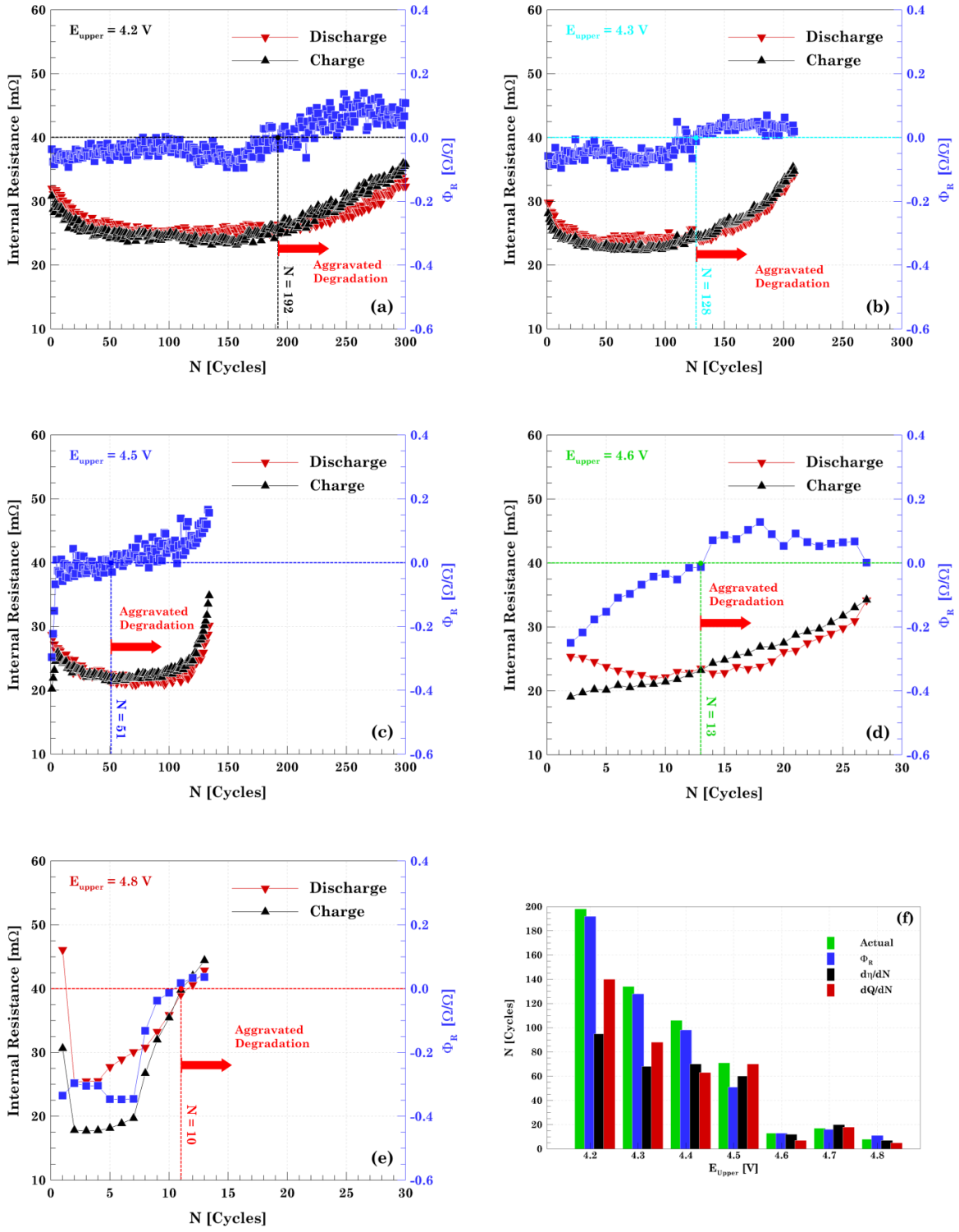

Fig. 8.4 Internal resistance evolution at the end of the charge/discharge process and proposed degradation number for the (a) aging dominated regime, 4.2 V; slight overcharge, (b) 4.3 and (c) 4.5 V; (d) overcharge dominated, 4.6 V; and (e) extreme overcharge, 4.8 V. (f) Cycle number predicted by each SoH parameter representing the onset of aggravated degradation.

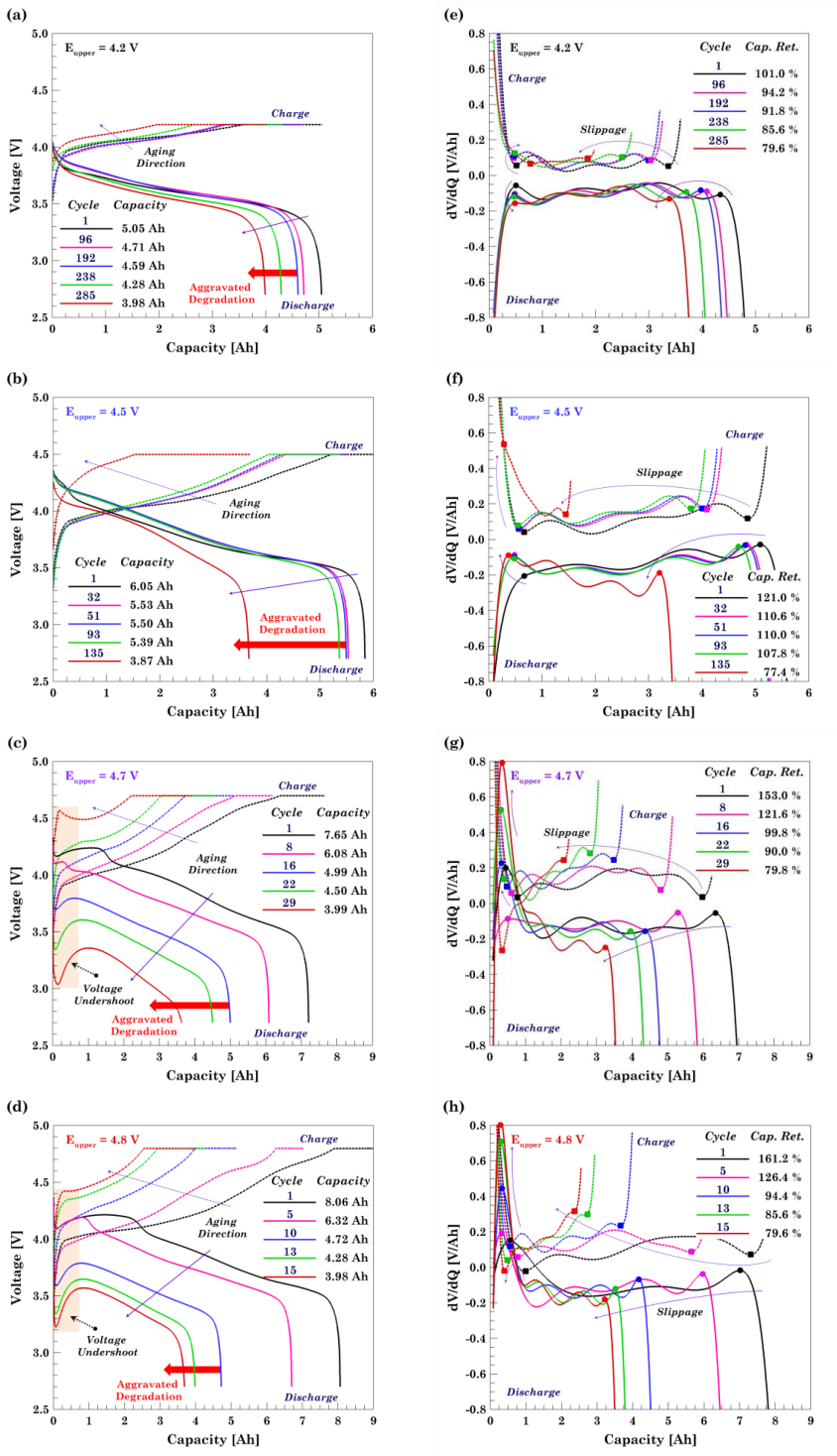

Fig. 8.5 Charge/discharge voltage profiles at different degradation levels for the (a) 4.2 V; (b) 4.5 V; (c) 4.7 V; and (d) 4.8 V. Differential voltage curves obtained by differentiating the 7th order polynomial fitting curves associated to the (e) 4.2, (f) 4.5, (g) 4.7, and (h) 4.8 voltage curves. Electrolyte degradation and pore clogging in graphite are the main causes behind the voltage undershoot on the cells charged beyond 4.6 V. Horizontal peaks slippage in the differential voltage curves indicates the capacity loss rate.

Long-term cycling results show that the number of cycles to retain capacity decreases with an increase in upper cutoff voltage. However, a sudden drop in the cycle life is observed when the cell is driven in the overcharge dominance, $E_{upper} \geq 4.6$ V. In order to further investigate the reason, voltage vs. capacity plots are shown in Fig. 8.5a-d. The four cells cycled up to 4.2, 4.3, 4.4, and 4.5 V are similar to a typical voltage capacity curve of lithium-ion. This confirms the hypothesis that overcharge have a reduced effect on the cell degradation in the voltage range of [2.7, 4.5] V. An aberration is observed when the upper cutoff voltage is increased beyond 4.5 V. A unique feature of "voltage undershoot" is observed for all the plots shown in Fig. 8.5c-d. In the discharge curve for cells charged up to 4.6, 4.7 and 4.8 V, the voltage decreases to a low value (local minima) and suddenly starts to increase. The occurrence of this voltage undershoot is considered a typical indicator of poor electrolyte performance and occurs when the cells transitions from linear to non-linear aging resulting in lithium plating. It is known that as the cell is cycled for a very long time the SEI growth leads to capacity fade. Hence, the subsequent occurrence of SEI growth along with lithium plating clogs the pores near anode-separator interface and decreases the anode porosity. This reduction in anode porosity leads to a rise in the transport resistance in the electrolyte resulting in a rapid drop of cell voltage and the voltage to undershoot.[214, 222] Voltage undershoots appears as a convex bump in the discharge curves and as a subtle concave bump in the CC charge curve. The voltage undershoots magnitude increase as the cell ages and it amplifies as the upper cutoff voltage is increased. Voltage undershoot is more evident at the beginning of the discharge because the pores are still clogged due to the SEI formed over the plated lithium during the last charge.

To elucidate the overcharge behavior of the cell and further investigate the changes occurring during the overcharge reaction, a differential voltage (dV/dQ) analysis is performed. Differential voltage plots shed light on how the cell resistance varies as a function of the SOC. Data for CC charge and discharge is acquired and a 7^{th} order polynomial is found to be the best fitting curve for the experimental data and from them, dV/dQ is calculated. The mirror trend between the charge and discharge dV/dQ curves arises from the numerical method. The vertical asymmetry between the two processes is an enhancement of the morphological difference between anode and cathode and their intercalation reaction rates.[173]

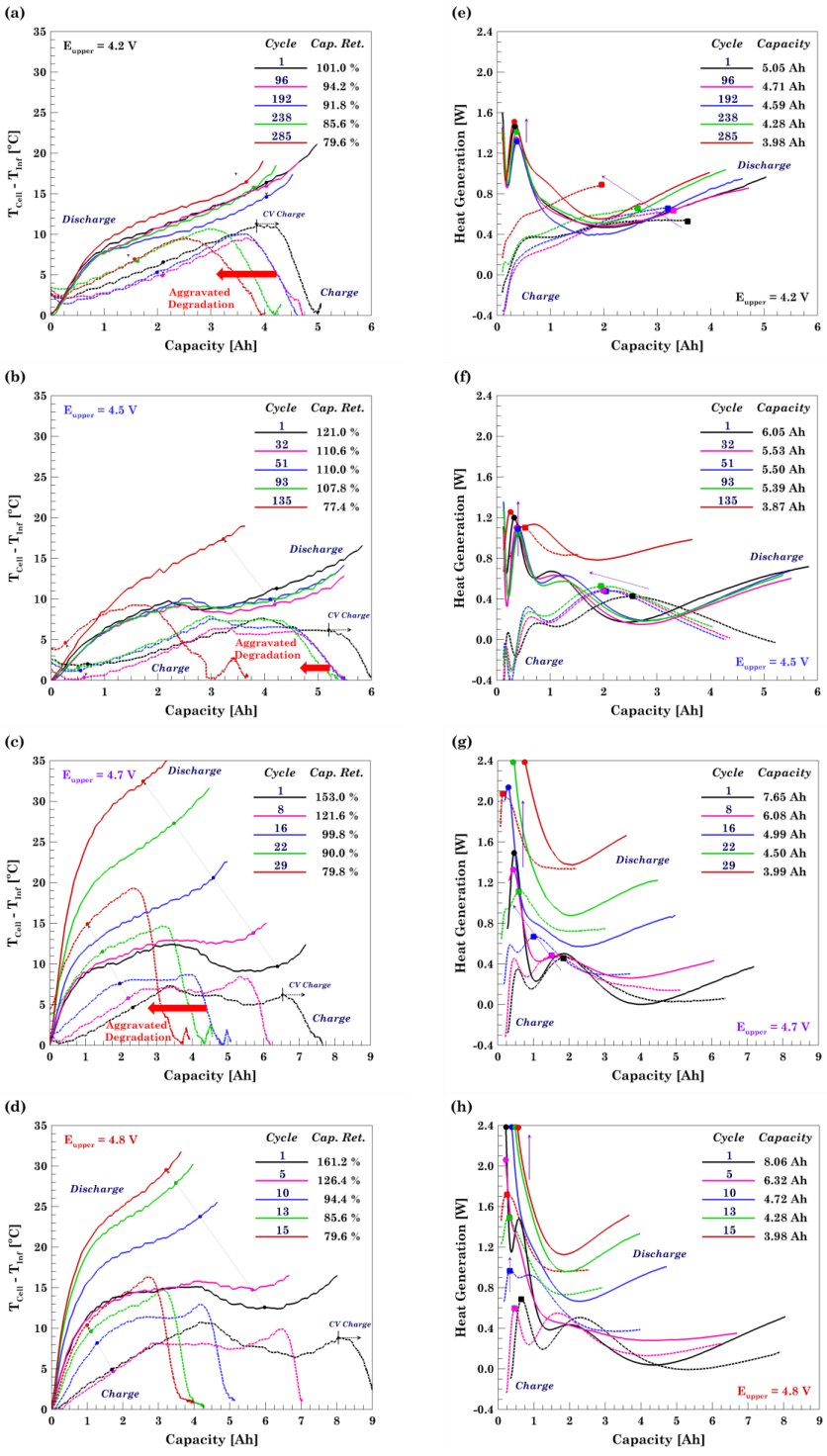

Fig. 8.6 Temperature profiles for the charge/discharge process at different degradation levels for the (a) 4.2 V; (b) 4.5 V; (c) 4.7 V; and (d) 4.8 V. Heat generated curves for the (e) 4.2, (f) 4.5, (g) 4.7, and (h) 4.8 V cells are obtained via an inverse heat transfer method. Voltage undershoot effect from the cells charged up beyond 4.6 V induces a larger heat generation particularly for the discharge process. Horizontal peaks slippage indicates capacity loss with cycling and vertical slippage represents the degradation effect on the cell.

One similar trend observed in all the plots is that as the capacity decreases, there is a slippage of the peaks towards left. This is considered a characteristic feature of the aging process and it is associated with a reduction of capacity utilization.[239] The dV/dQ curve signifies the temporal variation of resistance and the peaks represents the transition between phases in the electrodes. It can be observed the phase transitions occur early with an increase in the upper cutoff voltage denoting that the changes are occurring at a faster rate. Voltage undershoot is reflected as a large initial peak indicating a fast increase in the cell internal resistance due to pore clogging and less available electrolyte to transport Li-ions. The U-shape of the dV/dQ plot implies that the cell internal resistance is larger when the cell is fully discharged and fully charged and it keeps increasing as the cell is driven far away from the recommended voltage window and it decreases in the 0-100% SOC range.

8.4.2 Thermal Response

Thermal response for the charge and discharge cycles in Fig. 8.5a-d is shown in Fig. 8.6a-d. It can be inferred from all the plots that the temperature of the cell increases with an increase in the capacity fade and the number of cycles. It should also be noted that the cell temperature rise during each cycle is related to Joule heating. For the charge cycle, the temperature first increases and reaches a maximum until the end of the CC charge process then starts decreasing in the CV phase. Temperature decay in the CV phase occurs due to a drop in the Joule heating (i^2R_{Int}) as a consequence of the charging current decay. The thermal signature difference between charge and discharge is due to the fact that entropic heat is endothermic during charge and exothermic during discharge, whereas the irreversible heat is always exothermic for both cases. Thus, the total heat generated during the discharge is always greater than the charge one.

As the cell degradation aggravates, the maximum temperature increment also increases. For instance, the temperature increment for the 4.5 V cell, at the end of the discharge, is 19.2 ^{o}C after 20% CF as compared to the 15.2 ^{o}C from the initial cycle. Hence, it can be inferred that side reactions also contributes to temperature increment. For the cells charge up to 4.7 V and 4.8 V, the maximum temperature rise is approximately 35 ^{o}C. However, for cells cycled up to relatively lower cut off voltages, the maximum temperature rise is approximately 20 ^{o}C. Hence, charging the cell to a higher upper cutoff voltage will increase the cell temperature. The effect of the voltage undershoot phenomenon, in the cells charged beyond 4.6 V, associated with electrolyte

deterioration is reflected as a fast temperature rise. The generated gases within the cell, from the reaction between the electrolyte and LCO electrode, increase the internal pressure, lead to swelling and raise the internal temperature. Although swelling is more severe in the 4.8 V cell, the temperature increment is smaller than the 4.6 and 4.7 V cells. Overcharge gases separate the electrodes and electrochemically secludes them, reducing the reactions and the heat generated.

Heat generation (Fig. 8.6e-h) directly correlates with the dV/dQ (Fig. 8.5e-h) curve and its peaks. The heat generation peaks, at the beginning of the charge/discharge, align with the fast internal resistance rise. The irreversible heat associated with the Joule heating effect dominates the cell thermal response. When the voltage undershoot occurs in the 4.6 and 4.7 V cells, the additional peak in the dV/dQ curve translates as a new peak in the heat generation curve. As the SOC increases the heat generation decreases cause the internal resistance also decreases. At the end of the charge, heat generation and cell temperature rise again.

In regards to the safety aspects, indistinctly of the upper cutoff voltage, an aged cell represents a treat to safety only when is aged no more than 16-17% CF. One cell aged beyond this degradation threshold may generate more heat but it will do it for a shorter time not allowing the cell to rise its temperature to a point where thermal runaway may take place.

8.4.3 Destructive Physical Analysis

Cell swelling is a well-known characteristic of overcharge in a pouch cell due to electrode degradation and gas evolution. The average thickness of a fresh cell (3.7 V) is around 8.5 mm. A slight increase in the cell thickness is observed for the cell cycled under the aging dominated (4.2 V) and the slight overcharge regime (4.3 - 4.5 V). On the other extreme, the cell cycled up to 4.8 V experienced a 300% increase on its thickness, Fig. 8.7a-b. At higher voltages, electrolyte reduces at the LCO cathode and produces gases in between the LCO-separator interface. Moreover, the Li-plating on anode also reacts with electrolyte contributing to the gas generation. Gas generation along with the physical constrains imposed by the pouch edge creates a bubbling effect that bends and separates the electrodes around the center. Physical alteration of the electrodes-separators assembly poses a safety concern because the electrodes can get in contact and produce an internal short circuit that could be disastrous if the cell is in an overcharged condition.

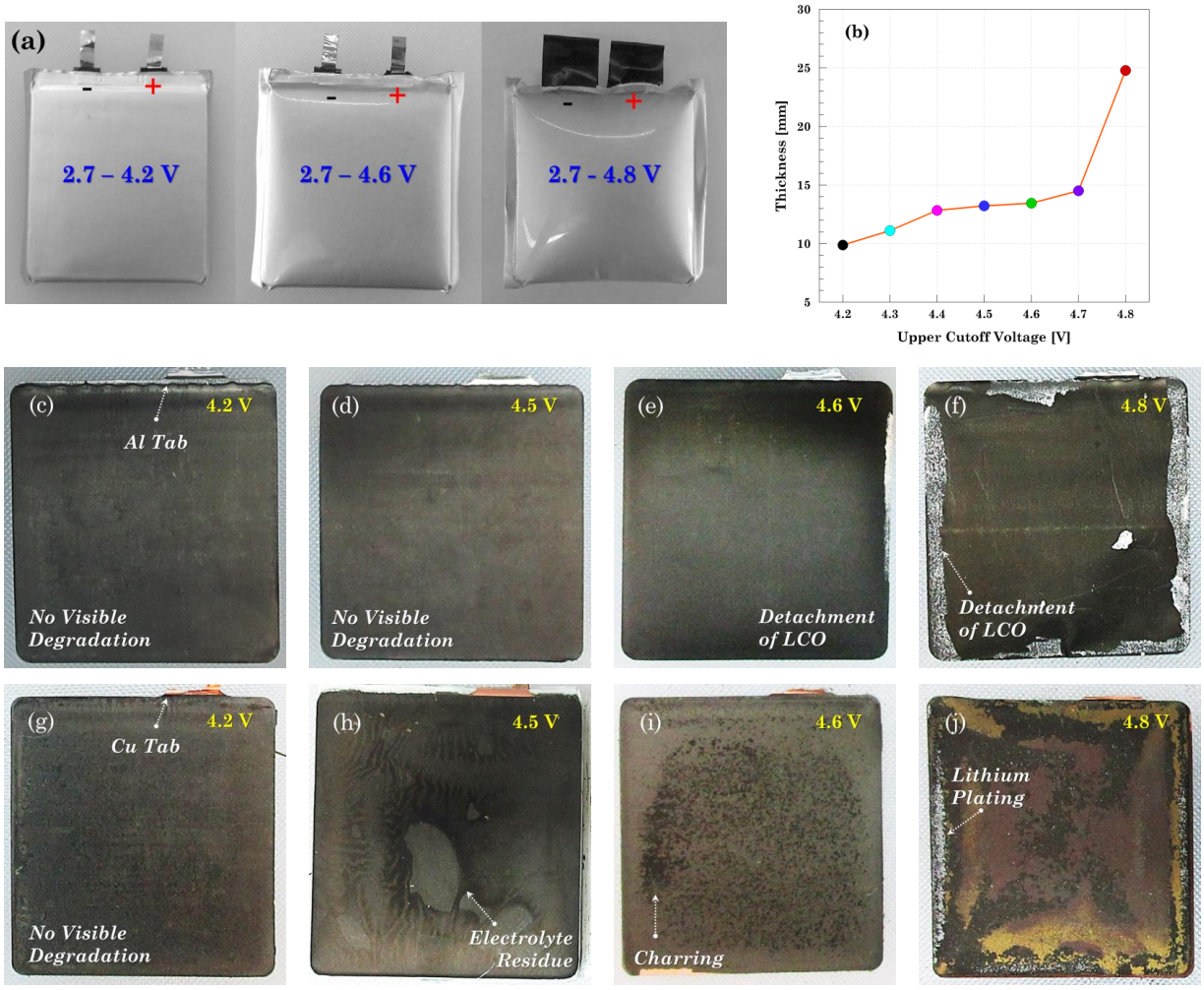

Fig. 8.7 Destructive physical analysis of the cells aged under overcharge condition at the end of the cycle life. (a) Volume expansion and (b) thickness of the cell increase with the extent of the upper cutoff voltage. LCO, (c)-(f), and graphite, (g)-(j), electrodes retrieved after cell autopsy of overcharged cells. No visual evidence of degradation is found in the electrodes extracted from the aging dominated and the slight overcharge regime. The sand-like pattern on graphite from the 4.5 V cell is left by the liquid electrolyte. The marks in the 4.7 V cell are created by micro-internal shorting caused by lithium plating dendrites. In the extreme overcharge condition, 4.8 V cell, degradation starts from the electrode edge to the center.

Cell DPA also includes analyzing the condition of the cell components. For safety reasons, DPA is conducted in a fully discharged condition. No visual degradation is observed for the cells cycled up from 4.2 to 4.5 V, see Fig. 8.7c-d, g-h. However, for the cells cycled to higher voltages, delamination of the LCO active material can be observed. The cathode of cell cycled to 4.8 V shows the highest amount of delamination, particularly in the zones next to edges. The cathode material from the electrode is heavily transferred to the separator. While performing the cell

autopsy it was also observed that the extraction of the cathode from the separator got more difficult for the highly overcharged cell. Overdelithiation of cathode leads to destabilization of LCO microstructure leading to particle cracking and cobalt migration to the separator and anode.[240] Similarly, images of graphite electrodes extracted from all the cells are shown in Fig. 8.7g-h. The anode degradation evidence is visually more significant as compared to the cathode one. As the voltage window is extended, the extent of degradation also increases. A closer look at the anode of cell cycled up to 4.8 V reveals traces of lithium deposit around the edges. Moreover, different degree of delithiation is also observed thus strengthening the results of non-uniform temperature distribution over the cell and the physical deformation of the electrode due to electrolyte bubbling. A small trace of lithium plating and charring (dark spots) is observed in cells overcharged to 4.6 and 4.7 V. The occurrence of lithium plating on cells charged beyond 4.6 V also corroborates the inference of voltage undershoot observed in voltage-capacity curves being an indicator of lithium plating.

8.4.4 SEM/EDS

DPA does not provide insights on morphological and chemical changes that occur in the LIB, this becomes evident in the samples from the 4.2 to 4.5 V cells shown in Fig. 8.7c-d, g-h. Micrographs of representative samples extracted from the graphite and LCO electrodes are shown in Fig. 8.8 and Fig. 8.9. SEM image of a pristine electrode is taken as a reference to analyze the extent of degradation.

Considering the pristine condition of the graphite electrode as a reference, Fig. 8.8a, cell degradation is clearly visible as the value of upper cutoff voltage for cycling is increased. Thickening of the SEI layer can be appreciated in the 4.2 and 4.3 V samples as a layer covering the active particle and fulfilling the spaces in between the graphene layers, Fig. 8.8b-c. This feature is characteristic of the normal aging process. As the upper cutoff voltage extends, electrolyte starts reacting and residues of electrolyte deposits on the graphite surface. Lithium plating also happens and contributes to electrolyte deterioration. Pores clogging become more evident in the graphite samples from the cells charged up beyond 4.5 V, Fig. 8.8e-h, supporting the voltage undershoot hypothesis. The cells charged up to 4.6 and 4.7 V exhibit needle-like structures over the graphite electrode surface, Fig. 8.8g. The dendritic structures are one the morphological forms that Li

plating typically adopts.[241] Dendrites penetrate the porous separator and eventually induced and internal short circuit creating the charring spots on the graphite anode as shown in Fig. 8.7i.

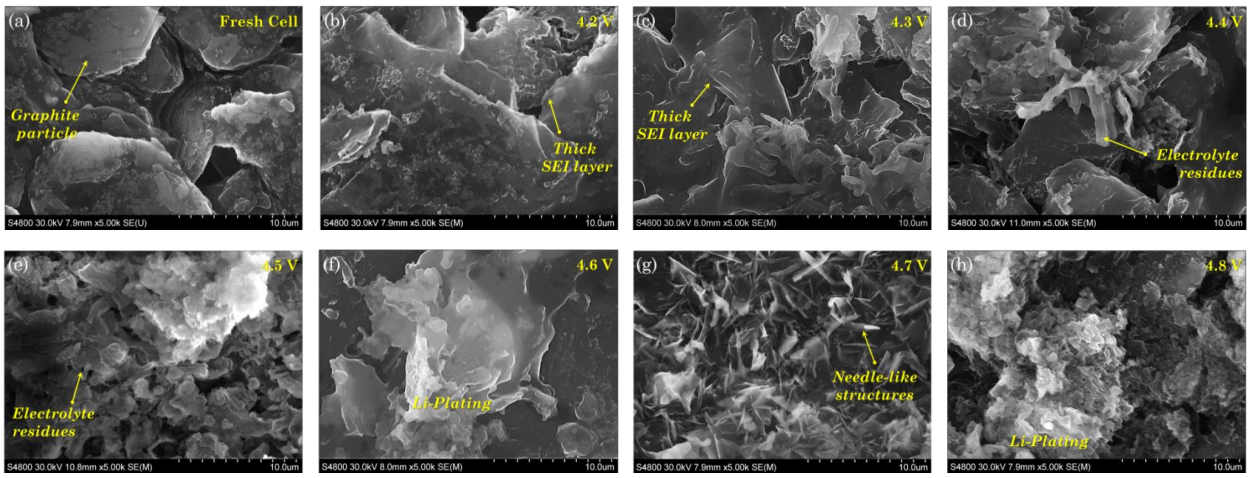

Fig. 8.8 Micrographs of graphite electrode samples extracted from aged cells at different cutoff voltages. (a) Pristine electrode; (b) aging dominated regime characterizes by SEI growth; (c)-(e) slight overcharge regime characterizes with deposits of electrolyte and further SEI thickening; (f)-(h) overcharge dominated and extreme overcharge regimes exhibit different morphologies of Li-plating covering the electrode surface. Scale bar for all images is 10 μm.

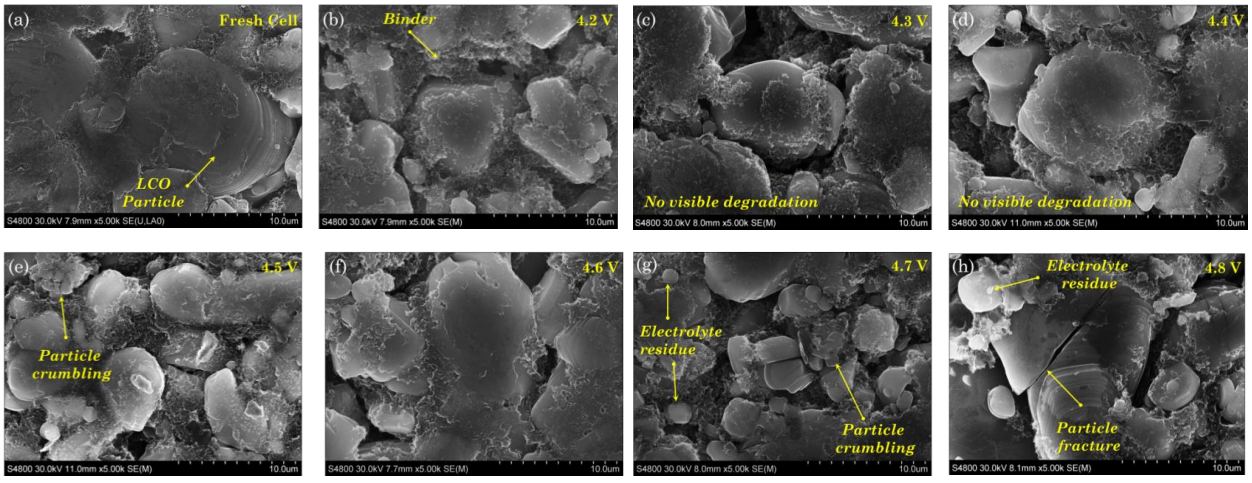

Fig. 8.9 Micrographs of LCO electrode samples extracted from aged cells at different cutoff voltages. No evidence of fracture is found on samples from the (a) pristine electrode; (b) aging dominated regime cell; and (c)-(e) slight overcharge regime cells. Fracture and delamination predominantly happen in the cells under (f)-(g) overcharge dominated, and (h) extreme overcharge condition. Scale bar for all images is 10 μm.

A demarcation of LCO particle and binder material has been shown in the fresh cell image, Fig. 8.9a. No visible degradation is found in the LCO samples extracted from the cells aged between

4.2 and 4.6 V, Fig. 8.9b-e, only isolated zones where the active particle crumbles. As the upper cutoff voltage is increased beyond 4.7 V, Fig. 8.9b-e, fracture occurs due to a continuous overdelithiation of LCO active material mechanically compromising the microstructure and resulting in delamination of the electrode. Residues of electrolyte are found in the sample under overcharge condition, 4.6-4.8 V cells that could only be observed at large scale.

Table 8.1 Electrodes composition extracted from the EDS test of graphite and LCO electrodes at different overcharge voltages for the samples shown in Fig. 8.8 and Fig. 8.9[a]

E_{upper} (V)	anode								cathode						
	C	**O**	**F**	**Al**	**P**	**Cu**	**Co**		**C**	**O**	**F**	**Al**	**P**	**Cu**	**Co**
4.2	76.4	18.5	2.7	1.4	0.5	0.5	0.0		31.3	18.8	6.8	5.3	0.3	0.0	37.5
4.3	58.0	35.0	5.0	0.8	0.7	0.4	0.1		32.9	19.8	7.3	6.1	0.7	0.1	33.1
4.4	40.3	45.4	3.1	8.0	0.8	2.2	0.2		33.6	19.7	7.8	2.2	0.7	0.0	36.0
4.5	36.3	50.6	5.1	5.7	1.9	0.2	0.2		32.8	19.8	8.2	2.3	0.8	0.0	36.1
4.6	45.2	40.8	8.6	3.2	1.3	0.7	0.2		31.5	14.7	9.6	5.2	0.2	0.1	38.8
4.7	37.2	53.7	3.8	1.4	2.8	0.8	0.4		34.8	19.1	5.3	4.3	0.2	0.1	36.3
4.8	28.4	49.0	15.5	3.1	2.6	0.9	0.6		35.1	19.6	6.0	2.7	0.1	0.1	36.4

[a]The values listed correspond to the wt % of each particular element found in the samples.

Degradation at the electrode level is complemented with a chemical composition analysis; see Table 8.1, on the graphite and LCO samples shown in Fig. 8.8 and Fig. 8.9, respectively. EDS analysis of anode shows that the carbon content is high in the pristine electrode and it decreases as the cells are aged independently of the upper cutoff voltage. SEI thickening increases the amount of oxygen due to the compounds on it, such as lithium carbonate (Li_2CO_3), lithium hydroxide (LiOH), lithium oxide (Li_2O), lithium alkyl carbonate ($ROCO_2Li$, RCOLi) [178], where R is the alkyl group. As the upper cutoff voltage is extended beyond 4.6 V, side reactions between electrolyte and lithium plating rise the content of phosphorous and fluorine producing compounds such as (LiF) and hydrogen fluoride (HF). The small increment in the cobalt content with an increase in the overcharge voltage confirms the occurrence of cobalt dissolution.

EDS analysis of cathode shows a slight rise in carbon content as the voltage window is extended, as a consequence of the electrolyte decomposition. Cobalt content remains quasi-constant

independently of the upper cutoff voltage indicating that main degradation in the LCO electrode is mechanical. Electrolyte reacts with oxygen released by the cathode and slightly increases its content. The cobalt content also decreases and one portion dissolves and migrates to the cathode. The presence of aluminum in both anode and cathode comes from the Al_2O_3 ceramic from the separator.

Table 8.2 Compounds detected in the electrolyte recovered from the cells subjected to cycling under continuous overcharge[b]

chemical structure	name	E_{upper} (V)						
		4.2	4.3	4.4	4.5	4.6	4.7	4.8
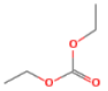	diethyl carbonate	×	×	×	×	×	×	×
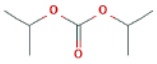	carbonic acid	×	×	×	×	×	-	-
	ethylene carbonate	×	×	×	×	×	×	×
	5-decene	×	×	×	×	×	×	×
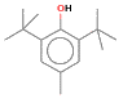	butylatedhydroxy toluene (BHT)	×	×	×	×	×	×	×
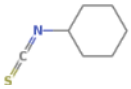	cyclohexyl, isotiocyanate	×	×	×	×	×	×	×
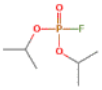	isoflurophate	×	-	×	-	-	-	-
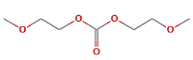	ethanol,2 methoxy carbonate	-	-	-	-	×	×	×
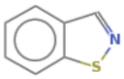	1,2-benzisothiazole	-	-	-	-	-	×	×

[b] The crosses indicate the identification of the compounds.

8.5 GC/MS

The composition of electrolyte obtained during DPA is analyzed via GC/MS technique and the electron impact ionization spectrums are analyzed using the in-built NIST library. The

chromatograms corresponding to the cell cycled under the aging dominated regime, 4.2 V, and the extreme overcharge regime, 4.8 V, are shown in Fig. 8.10. The chromatograms obtained reveal several peaks corresponding to a specific compound. The presence of diethyl carbonate, ethylene carbonate and butylated hydroxytoluene (BHT) is detected in all cells. Therefore, these components are an integral part of the initial electrolyte composition. BHT is a widely used additive to improve the cycling performance of the cells.[242] Presence of diisopropyl carbonate is also observed in all aged cells. A previous study by Kamui et al. also found the presence of dipropyl carbonate for overcharged and overdischarged cells.[243] From electrolyte solution analysis presence of isofluorphate is observed, therefore, suggesting that $LiPF_6$ salt also degrades with overcharge.

The list of compounds detected after analyzing the GC/MS spectrums for all the cells is listed in Table 8.2. Electrolyte solvents such as ethyl carbonate (EC), diethyl carbonate (DEC) are present in all cells. The carbonic acid solvent is stable until 4.6 V. Beyond that, it decomposes particularly when the graphite potential becomes negative. Two of the byproducts from the overcharge reaction, 4.6-4.8 V cells, are ethanol,2 methoxy carbonate, and 1,2-enzisothiazole. Although the study of electrolyte composition is carried to observe the change in decomposition compounds with an increase in the cycling upper cutoff voltage, the complexity of the produced molecules led to not identifying several peaks in the ionization spectrum. Even more, most of the gaseous byproducts get dispersed when the cell is opened.

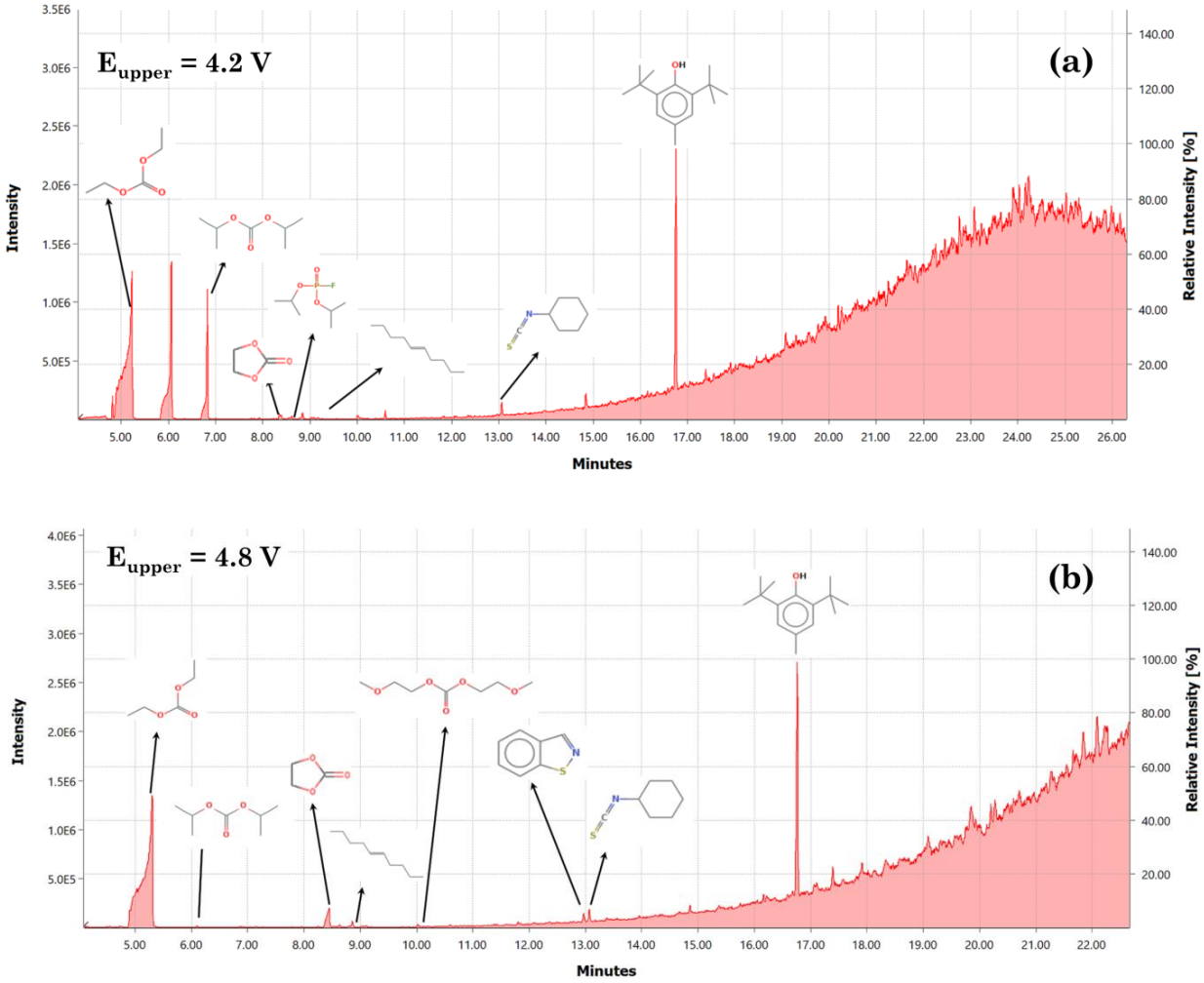

Fig. 8.10 GC/MS Chromatograms of electrolyte for the cell cycled in the (a) aging dominated regime, 4.2 V; and (b) extreme overcharge regime, 4.8 V.

9. CELL LEVEL DEGRADATION: AGING AND OVERDISCHARGE INTERPLAY IN POUCH CELLS

Relevant Publications and/or Working Papers

1. D. Juarez-Robles, A. Arun-Vyas, T. Transue, J. Jeevarajan, P.P. Mukherjee, 2019, *Degradation Mechanisms on Cycling at Different Overdischarge Levels,* working paper

Overdischarge is a potential problem in large battery packs since cells are discharged at the same rate, despite having different capacities. Although a single overdischarge does not necessarily cause a safety hazard, it forces electrodes outside their safe potential range and adversely affects the cell components integrity. This work aims to fill the knowledge gap about, what would happen if aging-induced and overdischarge –induced degradation mechanisms simultaneously occur.

The aim is accomplished by aging graphite/LCO pouch cells at four lower cutoff voltages: 2.7 V (normal discharge), 1.5 V (slight overdischarge), 0.0 V (reverse potential onset), and -0.5 V (deep overdischarge). The cells aged above the onset of reverse potential – the condition where anode potential becomes larger than the cathode potential – have an extended cycle life with usual SEI growth and Li plating as the main degradation mechanisms. On the other hand, the cells aged under reversal condition ($E_{lower} \leq 0.0$ V) exhibit a short cycle life. The interplay between Li plating, LCO particle crumbling, and dissolution of Cu current collector contributes to the fast degradation of the cell. The analysis is complemented with a comparative study of various SOH indicators is presented including an internal resistance based dimensionless SOH number, Φ_R. The proposed degradation number is found to be a good indicator of aggravated degradation in cells. The results prove that overdischarge is a benign abuse test per se but it can turn into a malign condition when alternated with a continuous charging. The interplay between the degradation mechanisms of aging and overdischarge poses a threat not only to cell integrity but also to user health.

9.1 Introduction

9.1.1 Safety

Lithium-ion batteries (LIBs) have turned into a keystone, as a power source, in the development of portable systems mainly due to their specific power and specific energy.[244] Their widespread usage on daily life applications along with their potential to catastrophic failure turns the safety aspects into a priority.[136] Unfortunately, highly publicized events of LIBs failure have drawn attention to the health risks involved. For instance, the failure on the Samsung Galaxy Note 7 batteries, due to manufacturing and design issues, lead to overheating and catching fire.27 Another incident involved Boeing 787 Dreamliner when one flight landed in Boston and smoke was discovered in the cabin from the auxiliary power unit going into thermal runaway.[245] Both of these incidents involved the batteries having an unintended internal short circuit (ISC), a direct contact of the cell electrodes, resulting in catastrophic failure and threatening human safety.[246] ISC can be induced via mechanical,[48] thermal,[247] and electrochemical[24] abuse, typically for research purposes. However, unintended ISC can occur due to mishandling from the user or if the cell is not appropriately cycled either by driving the cell above (overcharge) or below (overdischarge) the safe voltage window. To prevent ISC due to overcharging and overdischarging, battery management systems (BMS) monitor the cells to attempt detection of faulty cells within a battery before they become problematic.[195] BMS can also ensure that the cells are charged and discharged appropriately considering every cell within a battery will have different maximum charge and discharge capacities.[248] Since there are thousands of cells in a battery pack used in electric vehicles (EV), it would be unpractical and unreasonable for a BMS to monitor each cell individually. An electrical load unbalancing not only affects the electrochemical performance of the single cells but also its thermal response. Jeevarajan et al. showed that a single unbalanced cell in a series string can result in high temperatures throughout the string and a possible catastrophic event.[231, 249] For that reason, it's important not only to have good control of the LIBs but also to develop a good understanding of this failure, more specifically during overdischarge, and the safety implications.

9.1.2 Overdischarge

Overdischarge is a phenomenon that occurs when a cell is discharged beyond the lower safe voltage limit determined by the electrode chemistry coupling.[250] Overdischarge is a potential problem in large battery packs since cells are discharged at the same rate, despite having different

capacities. Consider three lithium-ion cells at arbitrary states of charge, two fully charged and one 50% of the state of charge (SOC). If these are connected in series and then connected to an electrical load, the partially discharged cell will fully discharge before the other two and will be forced into polarity reversal by the other cells if the load is left on. Although this does not necessarily cause a safety hazard, it forces electrodes outside their normal potential range and adversely affects the cycle life.[52] Lai et al. showed that even a single overdischarge, if extreme enough, can permanently damage the LIB through ISC.[251] Jeevarajan et al. showed that overdischarging a cell within a battery pack arrangement, either series or parallel, can propagate the degradation in the surrounding cells as a result of compensating for the overdischarged cell.[249]

Overdischarge-induced degradation mechanisms on fresh cells have been previously studied. Maleki et al. showed that overdischarge is the factor that leads to swelling in Li-ion pouch cells due to the decomposition of the solid electrolyte interface (SEI) layer and the gases emitted from it.[201] Fear et al. showed that extreme overdischarge results in the dissolution of the copper (Cu) current collector from anode and deposition on the cathode, separator, and the anode surface.[252] They found that Cu dissolution was C-rate dependent and it takes place when the full cell voltage becomes negative and the anode potential is greater than 3.54 V vs. Li/Li^+. Li et al. showed that mixing cathode materials, in their experiment LCO ($LiCoO_2$) and NMC ($LiNi_{1/3}Mn_{1/3}Co_{1/3}O_2$), greatly reduced the potential for copper dissolution and deposition as well as the swelling.[253]

9.1.3 Cycling

LIBs undergo degradation even under normal cycling operation as shown by He et al. on their study of cycling of A123 18650 cylindrical cells that reduced their capacity by 20% after 1750 cycles.[158]. The major occurring degradation mechanisms are loss of lithium inventory and active material and degradation of the ionic and electronic elements.[210] Side reactions occurring between graphite and electrolyte lead to the formation of the SEI film at the surface of electrodes.[144] SEI prevents further corrosion of graphite and electrolyte reduction but its continuous growth over time may affect the pore size and structure, wettability of electrolyte, contact resistance of the negative and positive electrodes, as well as the separator porosity. Lithium plating is another side reaction consisting of the deposition of Li-metal at the surface of the anode. With continuing charging, due to the decreasing vacancy sites for Li intercalation and the limited solid-state diffusion in graphite,

the intercalation rate in graphite decreases.[254] This leads to accumulation of more Li-ions on the surface and thus leads to anode potential below 0.0 V vs. Li/Li^+.[143] Lithium plating increases at lower temperature[218] because of slower diffusion and increases with an increase in charging rate[255] as higher currents lead to an increase in the diffusion of Li-ions while the rate of diffusion of Li decreases. Lithium plating also leads to several safety issues like ISC and thermal runaway. Under extreme conditions, the changes in electrodes morphology due to constant intercalation and deintercalation induce mechanical stresses resulting in structural damage and cracking.

9.1.4 Current Work

Although there are extensive studies on aging-induced and overdischarge-induced degradation, there still a knowledge gap about what would happen if a LIB is continuously aged under overdischarge condition. The objective of this work is to understand the degradation mechanisms of Li-ion pouch cells when cycling at different overdischarge levels. The study aims to provide insights about the possible interaction between the dissolution of Cu from the current collector and the Li plated on graphite. The interaction between cycling and overdischarge is characterized by the electrochemical performance of the full cell and morphological changes of the electrodes/separator.

9.2 Experimental Details

Commercial Li-ion pouch cells (Wanma) obtained from a reputable vendor, with a lithium cobalt oxide (LCO) cathode and graphite (C) anode having 5.0 Ah rated capacity are used in this study. The cell has 23 double side layers of graphite, 22 double layers of LCO and two single sides coated layer at the extremes. The graphite/LCO electrodes are intercalated with a polypropylene/alumina (PP/Al_2O_3) separator in between. The electrochemical tests are carried out at ambient temperature using a battery tester (Arbin, BT-2000). The sampling rate for all tests is 1 Hz.

9.2.1 Cases of Study

As early described, pushing the cell to a high depth of discharge can induce dissolution of the anode copper substrate. The onset potential for copper dissolution depends upon the electrodes active material coupling, cell configuration, and discharging rate. An upper voltage bound for this onset can be obtained by discharging the cell at a low C-rate and it ranges between -0.5 and -1.4

V.[252] In order to confirm the Cu oxidation potential for this particular electrodes material coupling, a third electrode is incorporated in the cell. A small reference electrode (RE) made of copper wire with lithium titanate (LTO, $Li_4Ti_5O_{12}$) active material on its flatted tip is prepared by following the steps proposed by Minter et al..[256] The procedure ensures having a stable reference electrode potential (1.564 vs. Li/Li^+) throughout the different stages of overdischarge indicated in Fig. 9.1a. Three-electrode cell preparation and the RE insertion is conducted in an argon-filled glovebox (MBraun, H_2O < 0.5 ppm, O_2 < 0.5 ppm). Once the reference electrode is cycled and charged up to 50% SOC, it is inserted in the pouch cell, with the copper wire extending out of the cell, and sealed with epoxy to avoid electrolyte evaporation. The cell is fully charged to 4.2 V, prior extremely overdischarging it at a C/10-rate. The cell voltage and the electrode potentials are simultaneously monitored and the results are shown in Fig. 9.1a. Normal cycling occurs when the cell is operated within the manufacturer recommended voltage window, i.e., E = [4.2, 2.7] V. This range represents the optimal electrochemical conditions where the cell will give the longest lifetime while operating safely. Slight overdischarge takes place when the cell is discharged beyond the lower recommended cutoff without reaching the reverse potential point, i.e., E = [2.7, 0.0] V. The reverse potential point represents the condition where anode potential becomes larger than the cathode potential, as shown in Fig. 9.1b. This condition is used as partway between the slight and the deep overdischarge conditions.

9.2.2 Cycling Protocol

Cycling test is designed in a way that allows studying the cumulative effect of cycling at different overdischarge levels. Four lower cutoff voltages are judiciously selected according to the prior analysis: E_{lower} = 2.7, 1.5, 0.0 and -0.5 V. Aging dominated case, E = [2.7, 4.2] V, corresponds to cycling under the manufacturer recommended voltage window, where mostly Li^+ lithiation/delithiation processes and SEI thickening should take place. The second case consists of a slight overdischarge condition, E = [1.5, 4.2] V, under which delithiation is expected to come along with SEI decomposition. The reverse potential onset, E = [0.0, 4.2] V, is selected as the third case of study. Under this condition, lithium inventory from graphite is almost depleted and SEI layer damage becomes severe. The fourth case of the study consists of a deep overdischarge condition, i.e., a discharge process far beyond from the reverse potential condition, E = [-0.5, 4.2] V. The selection of this condition is special since cyclability needs to be ensured. Previous studies

have shown there is a DoD (depth of discharge) threshold after which the cell cannot longer be cycled [180, 252]. For this particular cell, the threshold voltage corresponds to the global minimum voltage from Fig. 9.1b, E = -0.832 V (5.218 Ah ≈ 104% DoD). Thus, at -0.5 V the cell already crossed the reverse potential condition without crossing the cell shutdown threshold. Cycling along with the overdischarge condition consists of cycling the cell at a C/10-rate under the baseline voltage window followed by 1C-rate cycles at each of the four cases above described. The initial low C-rate charging at the beginning is included to ensure a fully charged condition on the first cycle. Aging under overdischarge test is stopped when the cell exhibited a 20% capacity fade (CF) with respect to the nominal capacity (5 Ah) or in case of failure.

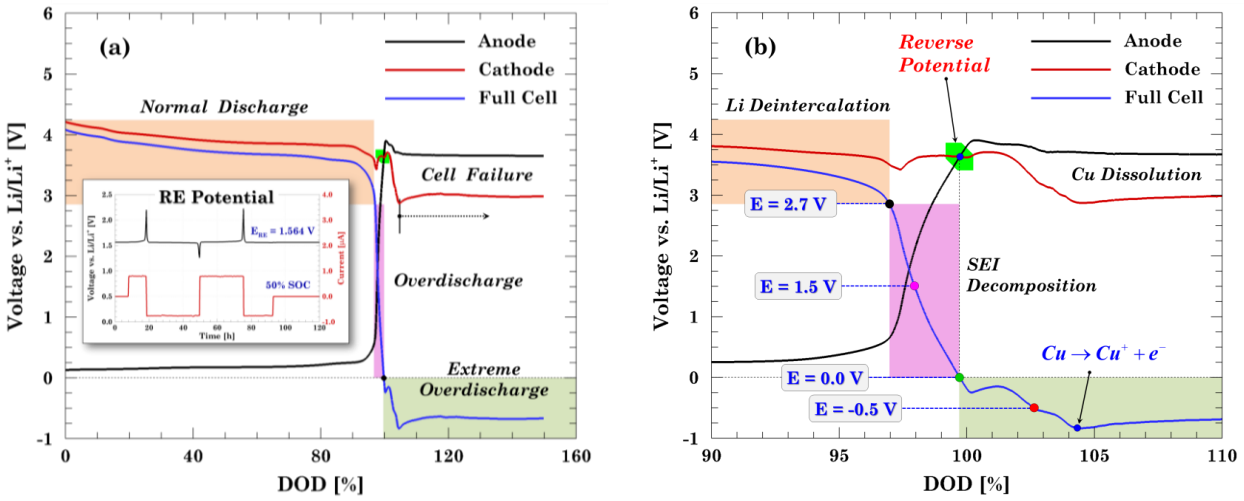

Fig. 9.1 Selection of the lower cutoff voltage for the aging test under overdischarge conditions. (a) LTO reference electrode lithiation and potential determination prior to insertion in the Wanma pouch cell. RE allows measuring the electrodes potential and full cell voltage of the pouch cell. (b) Degradation phenomena associated with each overdischarge stage. The reverse potential is the condition where the anode potential becomes larger than the cathode one. At the extreme overdischarge condition, the dissolution of copper and its deposition on the cathode surface shuts down the cell. Based upon these conditions, four lower cutoff voltages are selected: 2.7 V (normal discharge), 1.5 V (slight overdischarge), 0.0 V (reverse potential onset) and -0.5 V (deep overdischarge).

The cell internal resistance (IR) is measured at the end of the charge, $R_{Int,C}$, and discharge, $R_{Int,D}$, processes using the in-built function from the battery system. The IR function applies 10 current pulses with a 1C-current amplitude (5A) for a period of 100 ms. The cell is allowed to reach thermal and electrochemical equilibrium by resting it for 25 minutes prior to applying the train

pulses. On every cycle, both IR values are collected and used to define the following non-dimensional parameter.

$$\Phi_{\boldsymbol{R}} = \frac{\boldsymbol{R}_{\boldsymbol{Int,C}} - \boldsymbol{R}_{\boldsymbol{Int,D}}}{\boldsymbol{R}_{\boldsymbol{Int,D}}} \qquad \text{Eq. 9.1}$$

Φ_R was previously defined as a state of health (SOH) indicator. The internal resistance takes its maximum values when the cell is fully charged and fully discharged. In between the two SOC extremes, the internal resistance decreases. As the cell degrades, the IR at the two extreme conditions will increase and Φ_R will account for those changes.

The cell and environmental temperature are recorded with a T-type thermocouple (Omega) attached to the pouch cell surface. Heat generation is estimated from the thermal response of the cell using the inverse heat transfer method proposed by Mistry et al..[174] Details of the calculation and the method are included in the first part of this work where aging under different overcharge extremes is studied.

9.2.3 Destructive Physical Analysis

At the end of the cycle life, the cells are subjected to a destructive physical analysis (DPA) in the argon-filled glove-box to determine the failure mechanisms. The inert environment helps to preserve the evidence of degradation induced on each of the cell components for further analysis. Appendix C describes the step-by-step procedure to extract the electrodes and the separator. All the cells are open in a fully discharged condition to reduce the ISC hazards. First, pictographic evidence of the individual electrodes is taken. Then, representative samples from the electrodes and the separator are collected and analyzed via Scanning Electron Microscopy (SEM) (Hitachi S4800) and Energy Dispersive X-Ray Spectroscopy (EDS) techniques. A 30 kV acceleration voltage and 10 μA current are used to get the SEM images of the electrodes. A 10 kV acceleration voltage and 5 μA and low vacuum conditions are used to get the SEM images of the separator.

9.3 Results and Discussion

9.3.1 Cycling Performance

The protocol used to age the cells under an overdischarge condition is exemplified in Fig. 9.2a with the cycling profile corresponding to the cell cycled in the voltage range of [0.0, 4.2] V. The cycling protocol shows that extending the lower cutoff voltage from 2.7 to 0.0 V takes a short time, i.e., no significant capacity is gained. The plot also shows the uneven temperature rise between the charge and discharge process. Under normal cycling conditions, the temperature at the end of the discharge is greater than the one at the end of the charging process mainly due to the different intercalation rates of lithium in graphite and LCO.[173] In this particular case, the temperature difference is roughly 20 ^{o}C.

The effect of changing the lower cutoff on the cycle life is directly reflected on the capacity fade plot, Fig. 9.2b. The initial discharge capacity for each of the four cells shows a negligible capacity increment, from 5.00 Ah to 5.33 Ah, when the lower cutoff voltage is extended from 2.7 to -0.5 V. The number of times the cell can be cycled gets also reduced when the lower voltage is increased. Fig. 9.2c-f shows the charge/discharge capacity (Q) and the coulombic efficiency (η) for the cycle life of the four cycling conditions analyzed. On each plot, it is indicated the apparent cycle where the cell starts degrading at a faster rate based on the faster capacity fade and the maximum coulombic efficiency. The cell operated under the recommended voltage window takes 287 cycles to reduce its capacity 20% with respect to the nominal capacity, Fig. 9.2c. After 165 cycles, the coulombic efficiency exhibits an unsteady trend due to the degradation taking place within the cell. Similarly, for the 1.5 V case, the total number of cycles reduced to 220, Fig. 9.2d, and the unsteady coulombic efficiency occurs at the 145 cycle. In both cases, the main degradation mechanism is the SEI thickening. A significant reduction in the total number of cycles happens once the cell is driven to a reversal condition. The cell cycled at 0.0 V requires only 28 cycles to achieve the 20% CF, Fig. 9.2e, and the cell starts degrading faster just after 8 cycles. The cycle life gets reduced even more to 14 cycles for the deep overdischarge case, Fig. 9.2f, and it degrades faster after 6 cycles. The test was stopped after the cell failed due to internal shorting. Even though lithium plating and copper dissolution simultaneously occur within the cell, the main cause for the cell failure is the cell swelling which finally leads to direct contact between the electrodes.

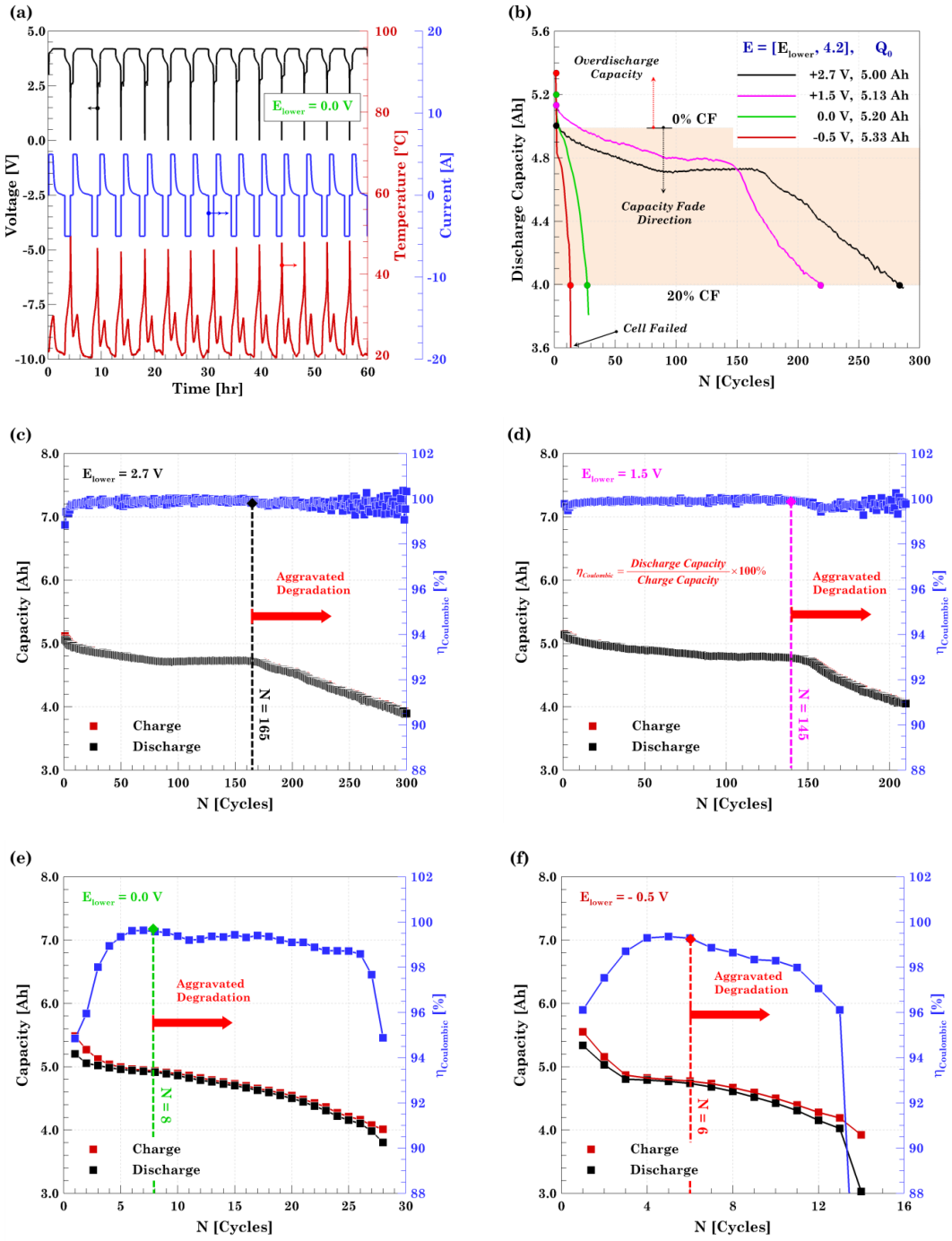

Fig. 9.2 Long-term and cycling life of cells aged under different overdischarge conditions. (a) Representative cycling protocol corresponding to the cell aged under the onset of the reverse potential condition, E = [0.0, 4.2] V. (b) Capacity fade definition and cycle life comparison based on the discharge capacity. The discharge capacity from the first cycle is also included. Charge/discharge capacity and coulombic efficiency for (c) aging dominated case, 2.7 V; (d) slight overdischarge case, 1.5 V; (e) reverse potential onset case, 0.0 V; and (f) deep overdischarge case, -0.5 V. The red dashed line represents the cycle at which degradation exacerbates.

SOH estimation has a significant relevance on the safety aspects for primary use applications of LIBs and its capability to be recycled and used in a secondary application.[3] Unlike previous works, the present analysis focus on analytically elucidating the moment where degradation aggravates and SOH decays. An initial attempt is a differential analysis of the cycle life parameters from Fig. 9.2c-f. First, discharge capacity and coulombic efficiency are fitted using third- and sixth-order polynomials, respectively; then, the derivative of fitting curves is calculated. The inflection point ($d^2Q/dN^2 = 0$) from the differential capacity curves, Fig. 9.3 a-b, indicates the point where the capacity fade rate increases. In a similar fashion, the maximum point from the differential coulombic efficiency ($d\eta/dN = 0$) can be interpreted as a SOH indicator. Before this point, the low coulombic efficiency is due to a reduction of lithium inventory caused by the SEI formation.[257] Once the cell crosses the maximum point, η decreases again due to the accumulated degradation. The flat parabolic trend of the coulombic produces the multiple zeros found in the dη/dN curves, Fig. 9.3 c-d. From all those zeros, the closest one to the cycle indicated in Fig. 9.2 is the one selected as the onset for faster degradation.

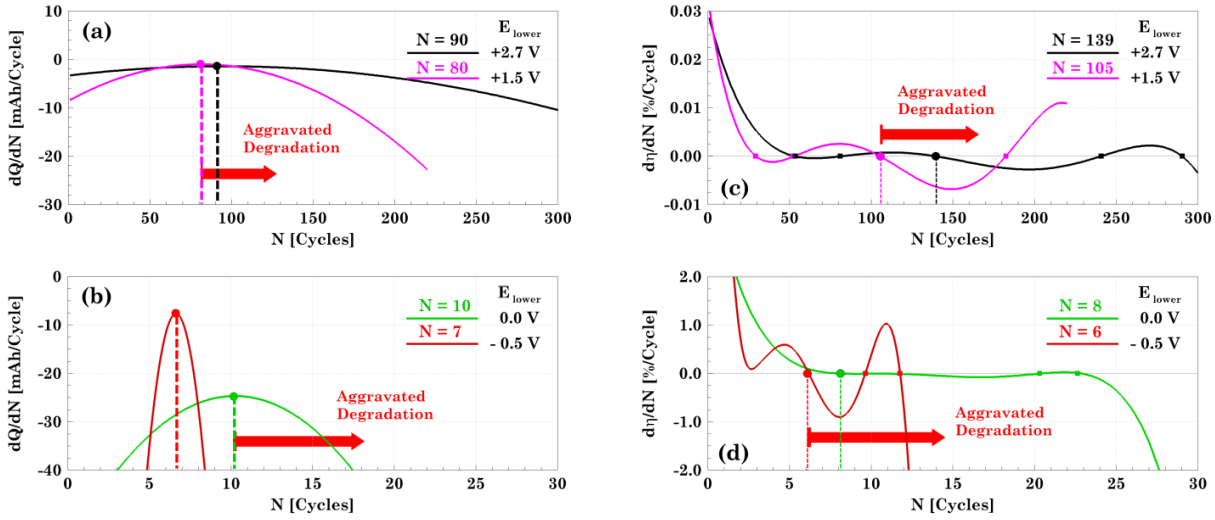

Fig. 9.3 (a), (b) Differential capacity and (c), (d) differential coulombic efficiency for the cycle life of the cells aged under overdischarge conditions. The inflection points on the differential capacity can be interpreted as the onset of fast degradation. The cycle where aggravated degradation takes place is the closest one to the cycle indicated in Fig. 9.2. The maximum coulombic efficiency, represented by the zeros, is used as a SOH indicator.

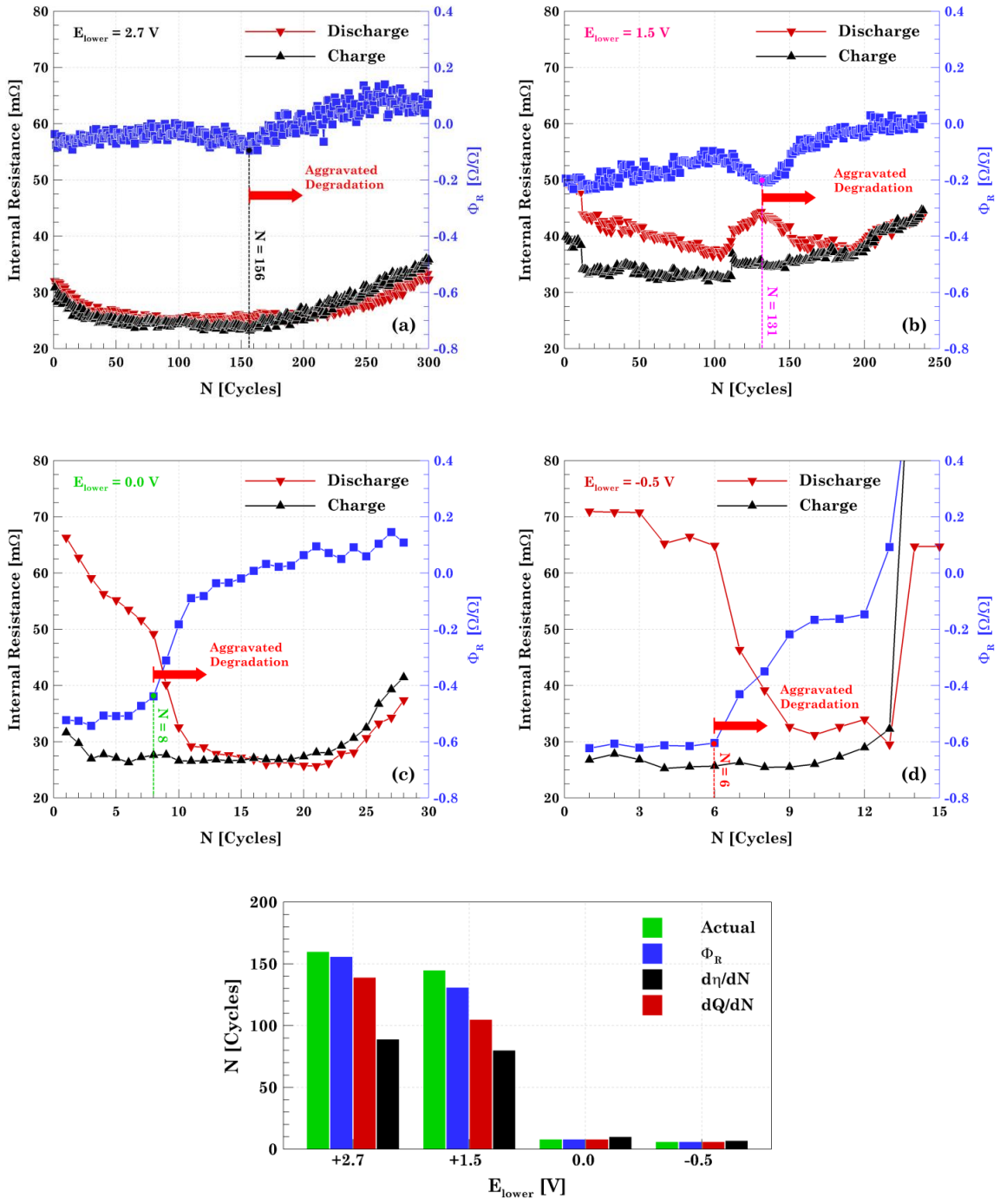

Fig. 9.4 Charge/discharge internal resistance evolution with cycling and degradation number for the cells aged at different overdischarged levels, E_{lower} = (a) 2.7 V, (b) 1.5 V, (c) 0.0 V, and (d) -0.5 V. Extending down the lower cutoff voltage increases the IR at the end of the discharge process, while the IR at the end of the charge remains constant. Accelerated degradation occurs when Φ_R increases at a faster rate.

Even though IR has been previously used to investigate the effect of resistance on degradation and capacity fade,[172] its SOC dependence can influence the derived conclusions. IR maximizes when the cell is fully charged and fully discharged and it decreases in between. [258] Under normal cycling conditions, both IR values are almost equal, as shown in Fig. 9.4a, throughout the whole cycling life. As the lower cutoff voltage is extended, Fig. 9.4b-d, the charge IR remains quasi-constant and it only increases at the end of the cycling life. Meanwhile, the discharge IR shows a significant increment at the beginning of the test that depends on the extent of the overdischarge and it decreases as the cell ages. Two facts can be inferred from Fig. 9.4a-d, first, that the IR value depends not only on the SOC but also on the extent of the cutoff voltages; and second, that the IR does not always increases with aging.

Based on both IR values, a third SOH estimator, Φ_R, defined by Eq. 9.1, is calculated and shown in Fig. 9.4a-d. At the beginning of the aging test, the cells cycled in the safe voltage window satisfy the condition that $R_{Int,D} > R_{Int,C}$ and consequently $\Phi_R < 0$. Defining $\Phi_R = 0$ as the onset of aggravated degradation makes sense if the cells are overcharged since $R_{Int,C}$ increases faster than $R_{Int,D}$ and at some point $R_{Int,C} > R_{Int,D}$. For the 0.0 and -0.5 V cells, $R_{Int,D} >> R_{Int,C}$, thence $\Phi_R << 0$. Even if the cell is degrading at a faster rate, Φ_R may not be necessarily zero, Fig. 9.4c-d, and it cannot be used to estimate as a reference. Instead, the trough from the Φ_R curve represents the onset of aggravated degradation, Fig. 9.4a-b. After this point, Φ_R rises at a faster rate because the cell degradation increases $R_{Int,C}$. The indicated cycle in Fig. 9.4c-d is selected following the same rule. The three SOH indicators are compared in Fig. 9.4e. Predictions made with Φ_R approximates better to the actual degradation onset, especially for the 2.7 and 1.5 V cells. For the cells aged under reversal conditions, all three predictors, dQ/dN, dη/dN, and Φ_R are close to the actual point of failure.

The cycle predictions made with the SOH indicator, Φ_R, are taken as a reference to further inspect the electrochemical, Fig. 9.5, and thermal, Fig. 9.6, variations throughout cycling. Voltage and temperature profiles at five cycles corresponding to first cycle (0% CF), last cycle (20% CF), and the cycle where faster degradation starts (Φ_R prediction), and two more cycles in between the last three points.

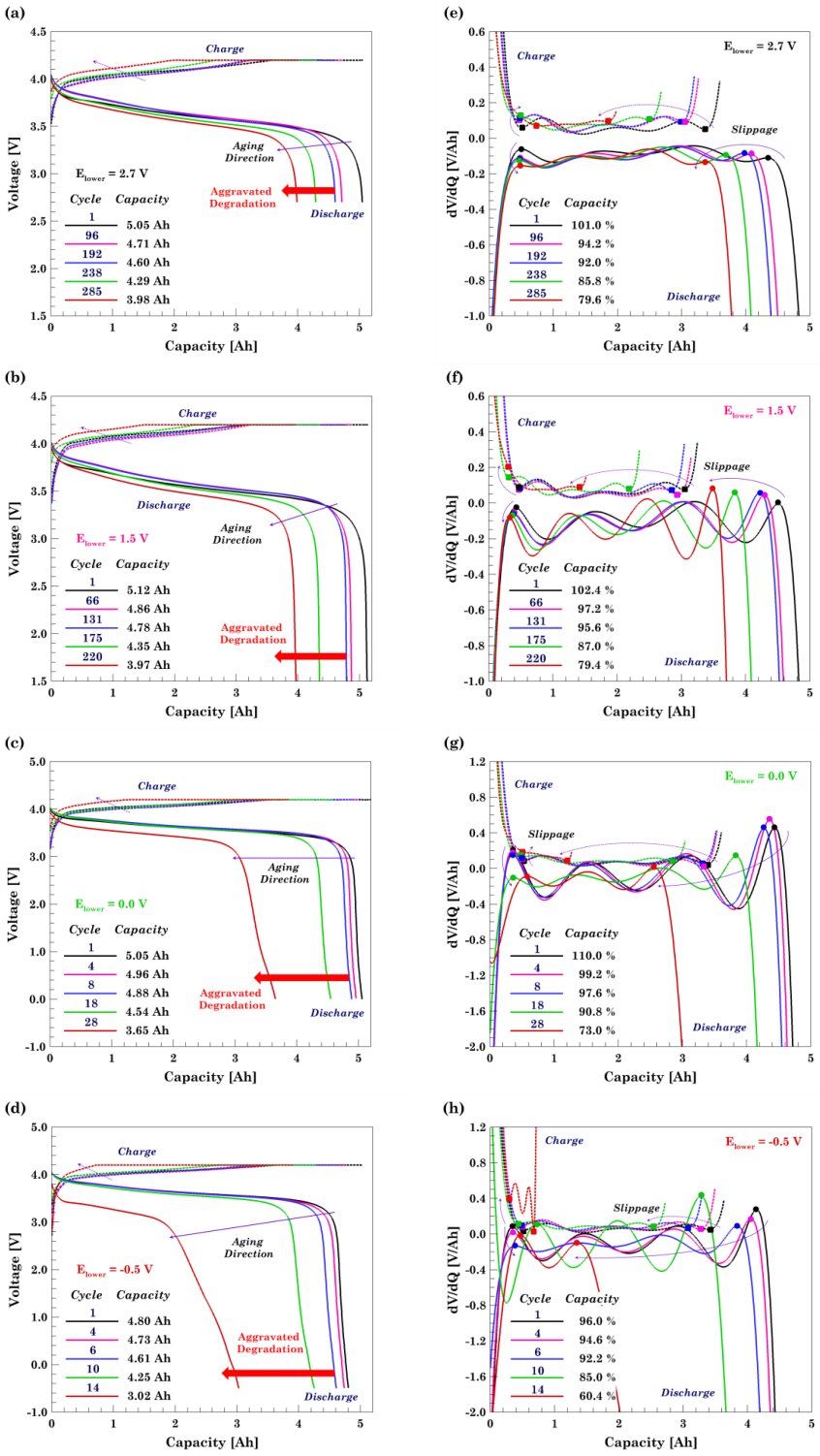

Fig. 9.5 Charge/discharge voltage profiles at different degradation levels for the (a) 2.7 V; (b) 1.5 V; (c) 0.0 V; and (d) -0.5 V cells. Differential voltage curves are obtained by differentiating the 7th order polynomial fitting curves associated to the each of the voltage curves. Horizontal peaks slippage in the differential voltage curves indicates the capacity loss rate.

Charge and discharge voltage profiles for the four cells under analysis are shown in Fig. 9.5a-d. The discharge curves show how the capacity slowly decreases before the Φ_R cycle predicted. Once the cell crosses this cycle the capacity reduces at a faster rate. For instance, the 1.5 V cell takes 131 cycles to reduce its capacity from 5.12 to 4.78 Ah, Fig. 9.5b. When degradation aggravates, it takes only 89 cycles to reduce its capacity from 4.78 to 3.97 Ah. Cycling the cell under reversal condition, 0.0 and -0.5 V cells, significantly increase the CF rate, Fig. 9.5c-d. For instance, the -0.5 V cell takes only 14 cycles to reduce its capacity from 4.08 to 3.02 Ah. A comparison between the charge/discharge curves from the 2.7 and the -0.5 V cells do not show any significant difference. Only the discharge curve for the last cycle (3.02 Ah) from the -0.5 V cell exhibits a slight trend change after at the end of the discharge. The fast voltage decay is mainly due to the fast anode potential rise and the decomposition of the SEI layer.

The differential voltage (dV/dQ) curves from Fig. 9.5e-h are obtained by differentiating the 7^{th} order polynomial fitting curves associated with each of the voltage curves. The dV/dQ plots can be interpreted in two different ways, either as the transition between phases in the electrodes or as the temporal variation of the resistance as a function of the SOC. In order to ease the plot reading the results for charge and discharge are shown in a mirror way.

From the phase transition point of view, the dV/dQ peaks corresponds to the phase transition from graphite. [169] The small peaks from the 2.7 V cell indicate a slow phase transition, Fig. 9.5e. As the cell ages, the peak intensity increases (vertical slippage) due to a non-uniform lithiation and a simultaneous presence of multiple phases. The most representative feature of the aging phenomena is the horizontal slippage of the peaks. [170, 239] The slippage magnitude increases with the extent of the lower cutoff voltage, Fig. 9.5g-h. A comparison of the dV/dQ curves between the charge and discharge process confirms the fact that the side reactions only take place during overdischarge, i.e., no matter the lower cutoff voltage, the dV/dQ plots for charging are similar, Fig. 9.5e-h. The dV/dQ plots also represent the temporal variation of the IR. At the two fully charge and fully discharge conditions, |dV/dQ| becomes larger confirming the fact that the internal resistance is larger at these two extremes. The resistance magnitude increases as the cell ages particularly at the end of the cycle life due to the degradation imposed by the overdischarge.

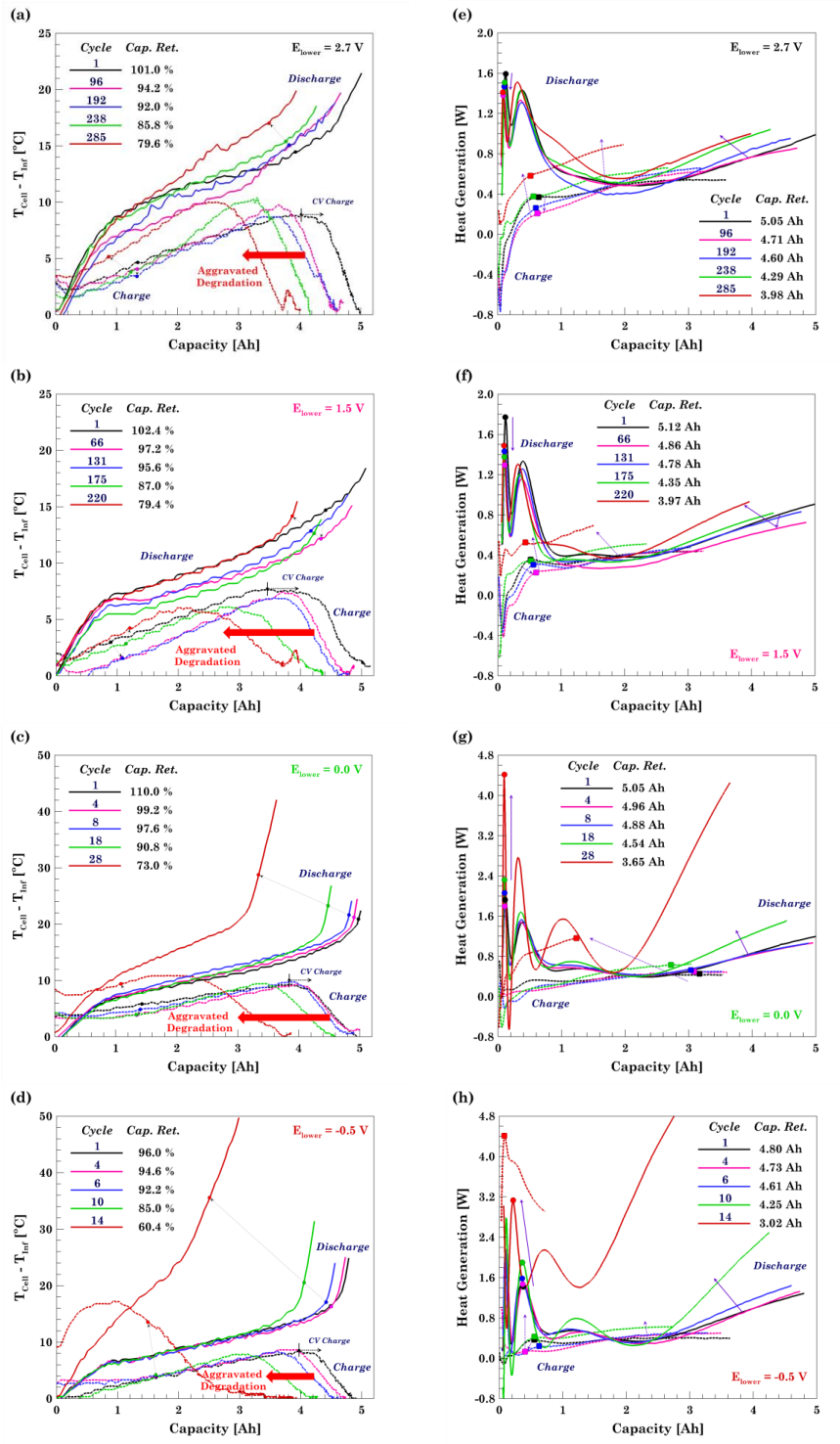

Fig. 9.6 Temperature profiles for the charge/discharge process at different degradation levels for the (a) 2.7 V; (b) 1.5 V; (c) 0.0 V; and (d) -0.5 V. Heat generation curves are obtained via an inverse heat transfer method. The maximum temperature during both, the charge and discharge processes, increases as the cell ages and it aggravates by decreasing the lower cutoff voltage. Horizontal peaks slippage indicates capacity loss with cycling and vertical slippage represents the degradation effect on the cell.

9.3.2 Thermal Response

The temperature increment response for the charge/discharge curves shown in Fig. 9.5a-d is used to estimate the heat generation, Fig. 9.5e-h, for the charge/discharge process. An initial and expected inference is that the temperature increment during discharge is always greater than the charge one. The temperature gap arises from the fact that entropic heat is endothermic during charge and exothermic during discharge. The irreversible heat in the other hand is always exothermic for both cases. Even more, during the CV charge temperature drops as a consequence of the decaying current applied. Hence, from the safety point of view, the discharge process represents a more threatening condition that aggravates as the cell is cycled under overdischarge. Thence, the maximum temperature developed by the cell is achieved in the last cycle no matter the lower cutoff voltage.

The maximum temperature increment for the 2.7 and 1.5 V cells are 21.6 and 18.5 ^{o}C, respectively, Fig. 9.6a-b, and they take place during the first cycle of aging test. The value increases to 41.0 ^{o}C for the cell aged under the onset of reversal potential, Fig. 9.6c, however this time, the maximum temperature increment occurs in the last cycle. As the cell is driven into a continuous reversal condition, the gases released due to the LCO degradation increases the internal pressure and causes cell swelling and an additional temperature increment. Swelling not only affects the pouch but also the electrodes/separator assembly configuration. In the -0.5 V cell, the disarrangement of the assembly caused an ISC due to direct contact between the electrode. Then the cell skin temperature rises up to 106.0 ^{o}C corresponding to a temperature increment of 83.63 ^{o}C, Fig. 9.6d. Once again, the maximum temperature increment occurs in the last cycle. The thermal results imply that if the cell is cycled above the onset of reversal potential, the maximum temperature will occur in the first cycle when both active materials are available for reacting. However, if the cell is cycled near or under a reversal condition, then degradation and side reactions will be the ones leading the temperature rise.

In order to complement the thermal analysis, heat generation plots are estimated from an inverse heat transfer problem using the ambient and cell temperature profiles, Fig. 9.6e-h. A comparison between the dV/dQ and heat generation plots exhibits some similarities. The link between both results is internal resistance. One of the major contributors to irreversible heat is the Joule heating

(i^2R_{Int}) that depends on the current applied and internal resistance. During the charging process, the heat generated remains quasi-constant cause the IT resistance does not change. In the case of the discharge process for the 2.7 and 1.5 V cells, the maximum heat generated occurs at the beginning of the discharge and decreases as the cell ages, Fig. 9.6e-f. A similar trend is found in the cells aged under reversal condition, 0.0 and -0.5 V cells, Fig. 9.6g-h, however this time the heat generated becomes steeper at the end of the discharge. This implies that the additional degradation such as SEI decomposition and LCO mechanical degradation is the cause behind the rapid temperature rise.

9.3.3 DPA

The thermal and electrochemical results can be supported by a physical inspection of the cell components. Fig. 9.7a-d shows the final condition of the four cells after their capacity faded 20%. Since the 2.7 V cell did not swell, it is not included in this figure. As the lower voltage is extended, the cell volume expansion turns out more severe indicating gas generation from the reaction between the electrolyte and the LCO electrode, Fig. 9.7a-b. In the case of the -0.5 V cell, a small charring spot can be observed on the left side of the pouch from Fig. 9.7c. The continuous cycling under reversal condition leads to mechanical degradation and its reaction with the electrolyte generating the gases that expand the cell. The gas production happens in between the electrodes creating a bubbling effect that disarrange the electrodes/separator assembly. Misalignment of adjacent graphite and LCO electrodes leads to an ISC. Even though the temperature ramps up to 106.0 ^{o}C, the cell didn't go into thermal runaway. The cell vented through the charring spot causing the dent on its center. The extremely overdischarged three-electrode cell is also included as part of the analysis, Fig. 9.7d, to put in perspective, the difference between overdischarging a cell in a continuous way and extremely overdischarge it one time. Even though the extremely overdischarged cell is dead at the end of the test, no evidence of swelling is found. This highlights an important point, overdischarge is a benign abuse test per se but it turns into a malign test when combined with charging. The interplay between the degradation mechanisms of aging and overdischarge poses a threat to cell integrity and operator health.

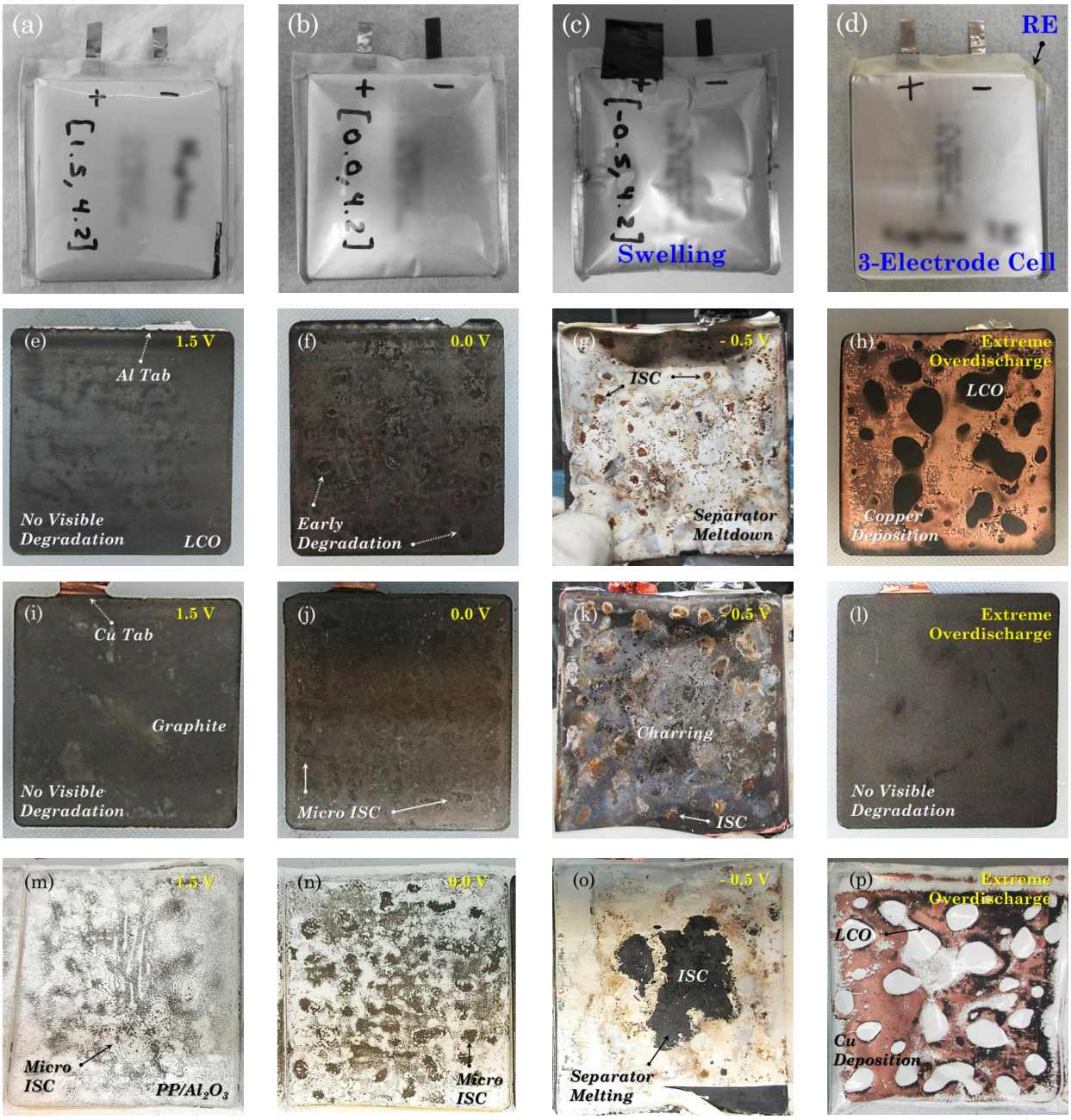

Fig. 9.7 Destructive physical analysis of the cells aged under overdischarge condition at the end of the cycle life. (a)-(c) Cell condition prior to conducting the DPA test. Swelling increases with the extent of the lower cutoff voltage. (d) The extreme overdischarge cell is included as a reference for the DPA analysis. LCO, (e)-(g) LCO and (i)-(l) graphite electrodes and (m)-(p) separator samples retrieved after cell autopsy of overdischarged cells. No pictographic evidence for the 2.7 V cell is included since it did not show any swelling and no visual evidence of degradation is found in the electrodes and separator.

The cell has technically 23 double-side coated layers for each of the electrodes as well as two separators. It will be unpractical to include the whole set of pictographic evidence, instead of a representative sample from the LCO, Fig. 9.7e-h; graphite, Fig. 9.7i-l; and separator, Fig. 9.7m-p, are analyzed. Before analyzing the aged cells, the extreme overdischarge components are inspected to establish a baseline for the condition where overdischarge dominates. The second baseline is the pristine condition that basically comprises the electrodes and separator with no degradation. As the cell is overdischarged, graphite anode is excessively delithiated until the lithium inventory depletes, then SEI starts decomposing by giving the lithium present on it to intercalate into the LCO cathode. [253] When there is no lithium left in the SEI, the Cu current collector starts oxidizing and the Cu-ions start migrating to the cathode where they deposit. [153, 259] Copper deposition, with its characteristic pink color, can be appreciated in the LCO electrode and separator from Fig. 9.7h and Fig. 9.7p, respectively. The graphite electrode resembles the pristine graphite with the only difference that this one does have any lithium intercalated on it, Fig. 9.7l.

Getting back to the aged cells, no visible degradation is found on any of the electrodes from the 1.5 V cells, Fig. 9.7e,i, only the separator exhibit some brown-ish spots mostly due to micro ISC caused by sparse Li plating spots. For the 0.0 V cell, the spots where ISC takes place becomes more populated on all the three components, Fig. 9.7f,j,n. The idea that overdischarge promotes the formation of Li plating may sound counterintuitive cause Li deposition occurs during charging. However, the degradation imposed by the overdischarge process increases the cell IR and during the charging process, the increased overpotential can drive the anode potential below zero and promote Li plating.[260] In the case of the cell aged under reversal condition, -0.5 V cell, the ISC becomes so severe that it causes charring on the graphite electrode, Fig. 9.7k, and separator meltdown, especially around the center of the cell, Fig. 9.7o. After the PP from separator melts, it sticks to the LCO electrodes making hard to separate them, Fig. 9.7g,o.

9.3.4 SEM/EDS

The actual degradation on the cell components is further investigated by extracting representative samples and analyzing their morphology, Fig. 9.8, Fig. 9.9, and Fig. 9.10, and composition, Table 9.1 and Table 9.2. The morphology of the fresh graphite electrode is shown in Fig. 9.8a. Prior to any cycling, the inner layers from the platelet graphite particle are well defined. The electrode

composition is mostly carbon from the active particle and the conductive additive. The presence of aluminum comes from the ceramic coating from the separator, Table 9.1. Once lithium intercalates/deintercalates during normal cycling, the interspaces get covered with a thin SEI film that becomes thicker with aging, Fig. 9.8b. The SEI layer consists of a mixture of different compounds such as lithium fluoride (LiF), lithium hydroxide (LiOH), lithium carbonate (Li_2CO_3), lithium oxide (Li_2O), lithium alkyl carbonate ($ROCO_2Li$, RCOLi) [178]. The formation of these compounds increase the oxygen and fluorine content and reduces the carbon percentage. When the lower voltage is reduced to 1.5 V, dendrites populate the electrode surface. Even though the electron microscope cannot detect small elements like hydrogen or lithium, the highly reactive nature of lithium leads to the formation of lithium oxide when it reacts with the oxygen from the air. Thus, Li plating increases, even more, the oxygen content and reduces the carbon content as shown in Table 9.1. The small percentage of cobalt of the graphite electrode corroborates the cobalt migration from cathode to anode during the charging process. As the lower voltage is decreased to 0.0 V, lithium plating and SEI growth aggravate, Fig. 9.8d. The composition of the electrode further increases its content of oxygen and fluorine and the presence of cobalt still prevails, see Table 9.1. A special detail from this electrode is the presence of copper. During the initial cycles, the cell voltage may not be sufficient to dissolve the current collector, but as the cell ages and the internal resistance increases, the Cu current collector locally starts dissolving. The simultaneous presence of Cu deposition and Li plating increases the likelihood of triggering an ISC. In the cell aged under reversal condition, all the degradation mechanisms simultaneously occur and their interplay eventually leads to the formation of gases, cell swelling, and ISC. The -0.5 V cell case is special because the electrode surface now is covered with residuals of charring and melted separator, as shown in Fig. 9.8e. Charring increases the carbon content; and the SEO compound decomposition reduces the oxygen content, see Table 9.1. Last but not least, the graphite electrode from the extremely overdischarge cells shows a similar morphology than the fresh cell one. In fact, the absence of intercalated lithium makes the inner layers of the particle more distinguishable. In terms of the composition, the extreme overdischarged anode has similar carbon content than the fresh cell, and as expected there is a presence of Cu from the current collector but there is no oxygen. The result supports the idea that when the anode lithium inventory gets depleted, the SEI decomposes to fulfill the power demanded by the external load.

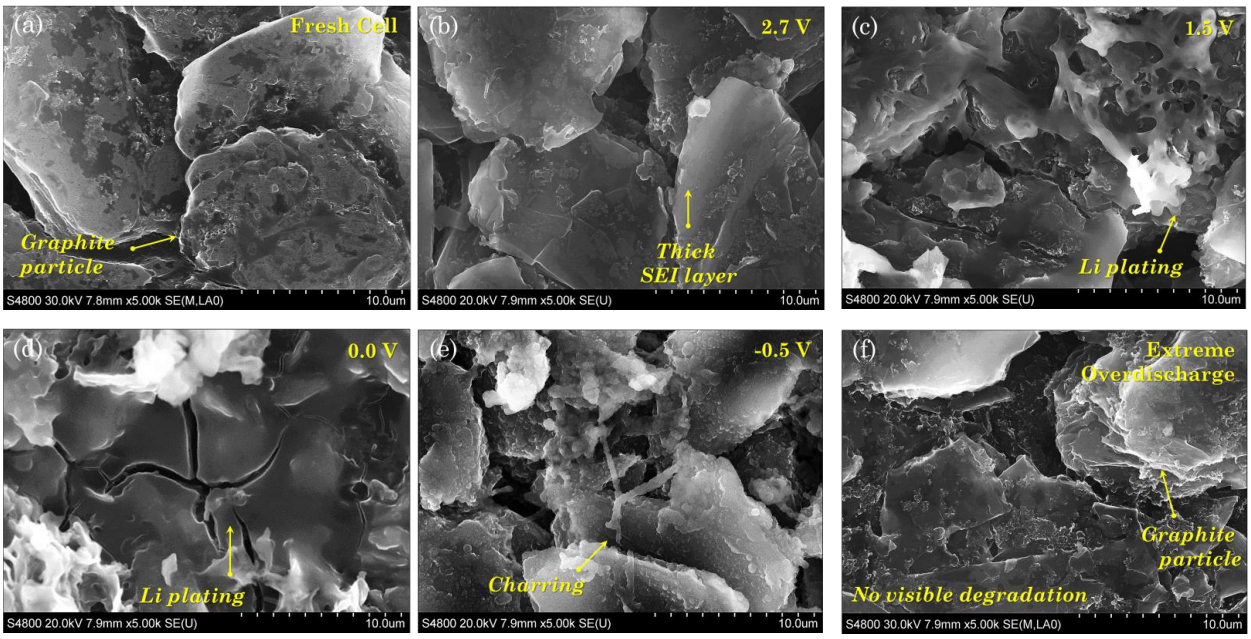

Fig. 9.8 Micrographs of graphite electrode samples extracted from aged cells at different lower cutoff voltages. (a) Pristine electrode. (b) Aging dominated case characterizes by SEI growth. (c) Slight overdischarge case characterizes by Li plating presence and further SEI thickening. (d) The onset of reverse potential case exhibits different morphologies of Li-plating covering the electrode surface. (e) Deep overdischarge case exhibits charring on the particle surface caused by ISC. (f) The extreme overdischarge electrode only shows the graphite particles without any deposits or evidence of the SEI layer. Scale bar for all images is 10 μm.

Table 9.1 Electrodes composition extracted from the EDS test of graphite and LCO electrodes at different overdischarge voltages for the samples shown in Fig. 9.8 and Fig. 9.9[a]

E_{lower} (V)	Anode							Cathode						
	C	**O**	**F**	**Al**	**P**	**Cu**	**Co**	**C**	**O**	**F**	**Al**	**P**	**Cu**	**Co**
FC	95.9	0.0	1.8	1.4	0.9	0.0	0.0	31.9	18.7	5.3	4.0	0.0	0.0	40.1
2.7	76.4	18.5	3.2	1.4	0.5	0.0	0.0	31.3	18.8	6.8	5.3	0.3	0.0	37.5
1.5	69.2	25.2	3.9	0.8	0.7	0.0	0.2	31.5	19.4	8.3	2.5	0.8	0.0	37.4
0.0	48.6	39.6	8.5	1.2	1.2	0.9	0.1	36.4	22.8	10.2	1.9	0.5	0.0	28.1
-0.5	71.4	12.1	14.4	0.6	0.9	0.6	0.0	34.4	24.7	9.8	2.1	1.0	0.1	27.9
EO	86.1	0.0	8.3	1.7	1.6	2.3	0.0	0.0	11.3	1.7	14.6	0.3	64.1	8.0

[a]The values listed correspond to the wt % of each particular element found in the samples.

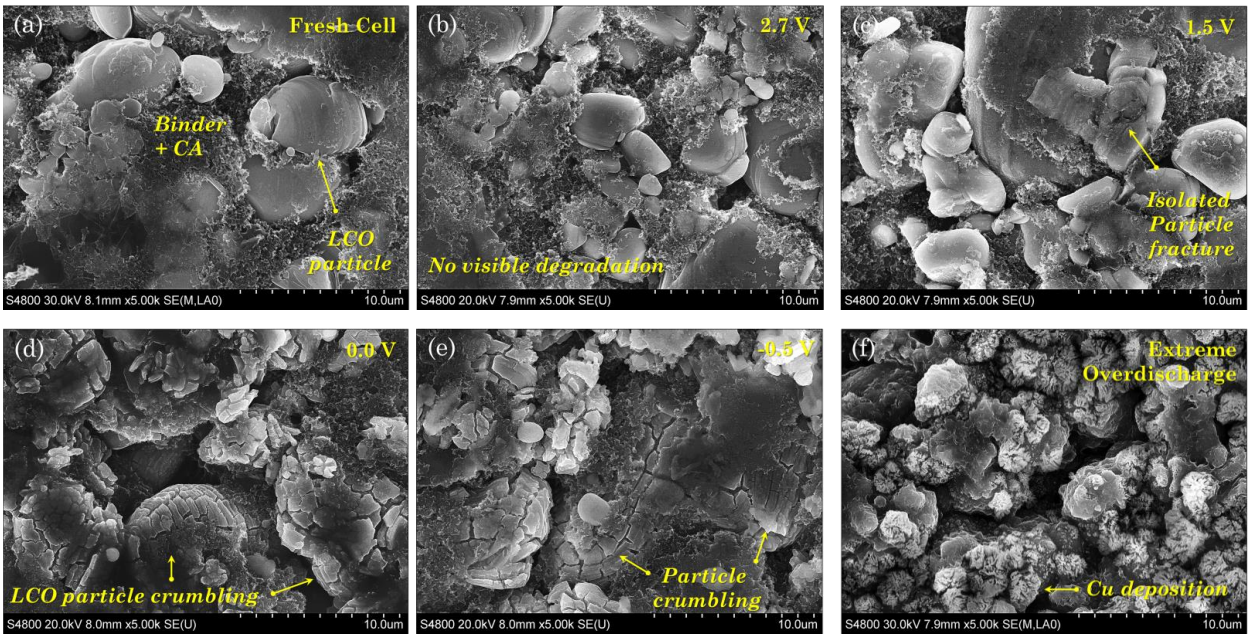

Fig. 9.9 Micrographs of LCO electrode samples extracted from aged cells at different lower cutoff voltages. No evidence of fracture is found in the samples corresponding to the (a) pristine electrode and the (b) aging dominated case cell. (c) Slight overdischarge case shows sparse LCO particles with an early presence of fracture. (d)-(e) LCO particle crumbling predominantly happen in the cells overdischarge under reversal condition due to electrochemical soaking. (f) The LCO electrode from the extreme overdischarge cell exhibited the characteristic Cu deposition on its surface. Scale bar for all images is 10 μm.

The morphology of a fresh cathode is shown in Fig. 9.9a. Its composition confirms LCO is the active material and it has an aluminum current collector. In this figure, the LCO active particle and the secondary phase (binder+conductive additive) are well defined. If the cell is aged under normal conditions, Fig. 9.9b, no significant change in the morphology and composition, Table 9.1, is observed in the micrograph and the EDS results, respectively. Sparse spots with crumbled LCO particles are found when the cell is slightly overdischarged, Fig. 9.9c. Severe LCO particle crumbling occurs when the cells are cycled down to 0.0 and -0.5 V due to electrochemical soaking, Fig. 9.9d-e. In other words, under normal discharge conditions, Li-ions migrate from anode to cathode to occupy one of the available reaction sites of LCO. However, if the cell is extremely overdischarged, the LCO particle is not able to allocate all the Li- and few Cu-ions migrating from the anode. Therefore, the active particle starts swelling and with continuous cycling it eventually crumbles.[64] The structural disintegration of the LCO particles not only increases the transport resistance in the solid phase but also reduces the capacity retention.[259, 261] In terms of the

composition, the Co content decreases as the lower voltage decreases. Particle crumbling exposes its interior and raises the oxygen content. Finally, the LCO electrode, from the extremely overdischarged cell, exhibits the deposition of copper onto its surface, Fig. 9.9f. The Cu deposits hinder the detection of the underneath LCO electrode when the composition is estimated.

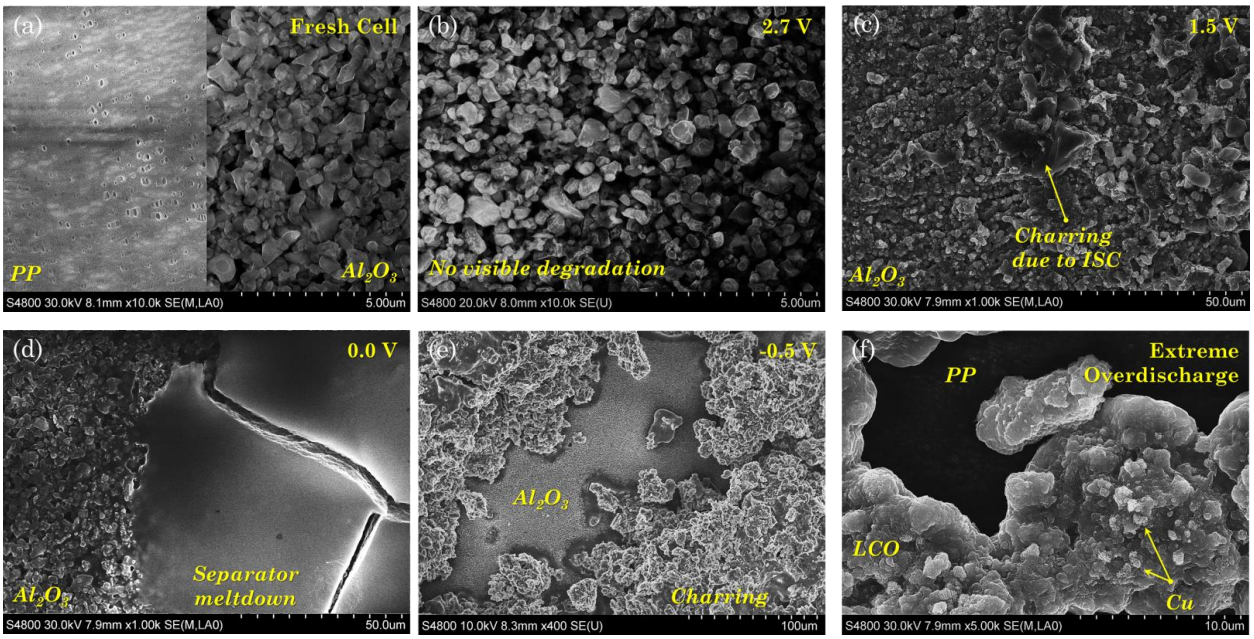

Fig. 9.10 Micrographs of separator samples extracted from aged cells at different cutoff voltages. (a) The separator is made of PP with Al_2O_3 ceramic layer. The PP side is facing the LCO electrode while the Al_2O_3 is facing the graphite one. (b) Aging dominated case separator shows no evidence of degradation. (c) Slight overdischarge case exhibits some deposits in the ceramic layer due to ISC. (d) The onset of reverse potential case exhibits a larger presence of deposits mainly on the Al_2O_3 layer. (e) The intensive ISC from the cell aged under the deep overdischarge condition induces charring and separator meltdown. (f) The extreme overdischarge cell did not show any significant degradation on the Al_2O_3 side but it did show LCO incrustations with Cu deposited on it. The scale bar is different on each panel to enhance the representative degradation details.

The separator from this cell is made of PP facing the LCO electrode and alumina facing the graphite electrode, Fig. 9.10a. The composition indicated in Table 9.2 corresponds to the alumina side. The propylene, $(C_3H_6)_n$, separator side only shows carbon content. In the case of the 2.7 V cell, no significant change with respect in the separator is found, Fig. 9.10b, except for the small presence of carbon and cobalt. Micro ISC becomes visible in 1.5 V cell in the form of deposits on the alumina side, Fig. 9.10c, and it's more evident on the 0.0 V cell, Fig. 9.10d. The deposits

coming from the anode contains SEI and Li plating residuals that increase the oxygen content and reduce the Al percentage. In the case of the -0.5 V cell, Fig. 9.10e, the high temperature caused by the ISC cause charring on the graphite electrode which later attached to the separator. Charring residuals increase the carbon content and significantly reduce the Al one. One of the most significant results is the presence of copper. ISC most of the time is attributed to Li plating, however, if the cell is overdischarged, under a reversal condition, then the dissolved Cu also comes into play in the degradation scene. One of the main differences between an extreme overdischarge and a continuous overdischarge is reflected on the separator where the copper dissolved deposits on the cathode and PP separator surface. During the DPA, the LCO active material detaches from the electrode and sticks on the PP separator. This can be easily proved by looking at the Co and Cu content on the separator from this cell.

Table 9.2 Electrodes composition extracted from the EDS test of separator at different overdischarge voltages for the samples shown in Fig. 9.10[b]

E_{lower} (V)	Separator						
	C	**O**	**F**	**Al**	**P**	**Cu**	**Co**
FC	0.0	41.2	9.5	47.9	1.3	0.0	0.0
2.7	8.8	43.9	1.5	45.1	0.6	0.0	0.1
1.5	27.1	37.8	3.4	28.1	1.3	0.0	2.3
0.0	7.0	50.4	3.1	38.6	0.8	0.0	0.2
-0.5	27.4	58.0	8.5	4.6	1.1	0.2	0.2
EO	0.0	21.2	7.3	17.3	2.4	24.9	26.9

[b]The values listed correspond to the wt % of each particular element found in the samples.

10. MODULE LEVEL DEGRADATION: AGING

Relevant Publications and/or Working Papers

1. D. Juarez-Robles, J. Jeevarajan, P.P. Mukherjee, 2019, *Degradation-Safety Analytics (DSA) in Li-ion Cells. Part 6. Aging Effect on Non-Balance Modules at Different Voltage Windows*, working paper

Li-ion batteries (LIBs) have become one of the most preferred technologies to be used in electric vehicles (EV) and hybrid-electric vehicles (HEVs) due to their nominal voltage, high energy density and extended cycle life. Tesla has adopted this energy storage technology on its EVs. For instance, the S and X EV models have reached autonomy of 370 km and 475 km, respectively. Model 3 has a nominal voltage of 350 V and a capacity of 230 Ah, reaching a maximum power of 80.5 kWh. The battery pack used in the standard Model 3, with a 50kWh power, has 2976 2170-cells. One of the major drawbacks of the Li-ion technologies is the high cost, the special packing, the necessity of protective circuits to avoid overcharge/overdischarge and also the use of thermal management systems.

The use of modules is necessary to implement Li-ion batteries in large applications such as the car batteries above discussed. The cells within the module can be arranged in a series-parallel configuration depending on the desired nominal voltage, capacity or power. Even though most of the cells come from the same batch, there is still a cell-to-cell variation on their capacity and voltage. Those differences may appear negligible when the module is fresh but they can amplify as the module ages. In order to compensate those differences a battery management system (BMS) can be coupled to the module.

A battery management system is an external device that helps to prevent overcharging and overdischarging the module. The main functions of the BMS are (a) disconnect or switch off the external load when the cell voltage drops below or goes above the safe voltage window; (b) disconnect the system in case of overheating; and (c) most importantly, balancing the cells.

It this work, the long-term performance of a 9P3S Li-ion module is investigated. The module is cycled without a BMS under two different voltage windows.

10.1 Results – Module

10.1.1 Setup

The module configuration will be 3P9S (9 series of 3 batteries in parallel). Fig. 10.1 shows a prototype of the final version of the module and how the batteries will be interconnected. Under this configuration the capacity of the module will be 10.2 Ah and its nominal voltage will be E_{ab} = 37.8 V, assuming that all the cells are charged up to 4.2 V, simultaneously.

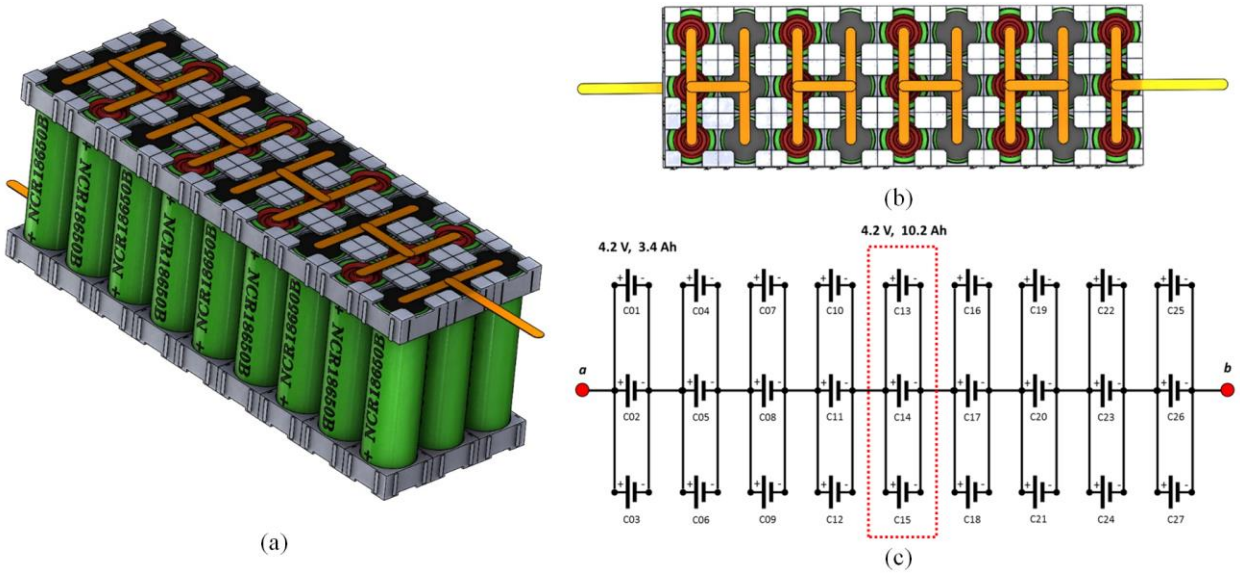

Fig. 10.1 Module setup (3P9S). Anode (Black), Cathode (Red), Nickel strips (Yellow), 18650 separators (Gray). (a) Schematic of the module; (b) physical connection; and (c) electrical circuit.

In Fig. 10.2 (a) is shown a general view of the whole module (3P9S). The initial voltage measure in this module was 32.5 V. The connection of the module was done by using nickel strips (width = 7.5 mm). The distance between the cells is 2 mm, as shown in Fig. 10.2 (c). In order to ensure a firm connection between the voltage cables and the module, an extra piece of nickel tab will be weld on each bank. This tab will extend out of the modules, and cables will be connected to them. Prior the welding, cables will be soldered to the nickel tab. Thus, we can avoid heating the cell.

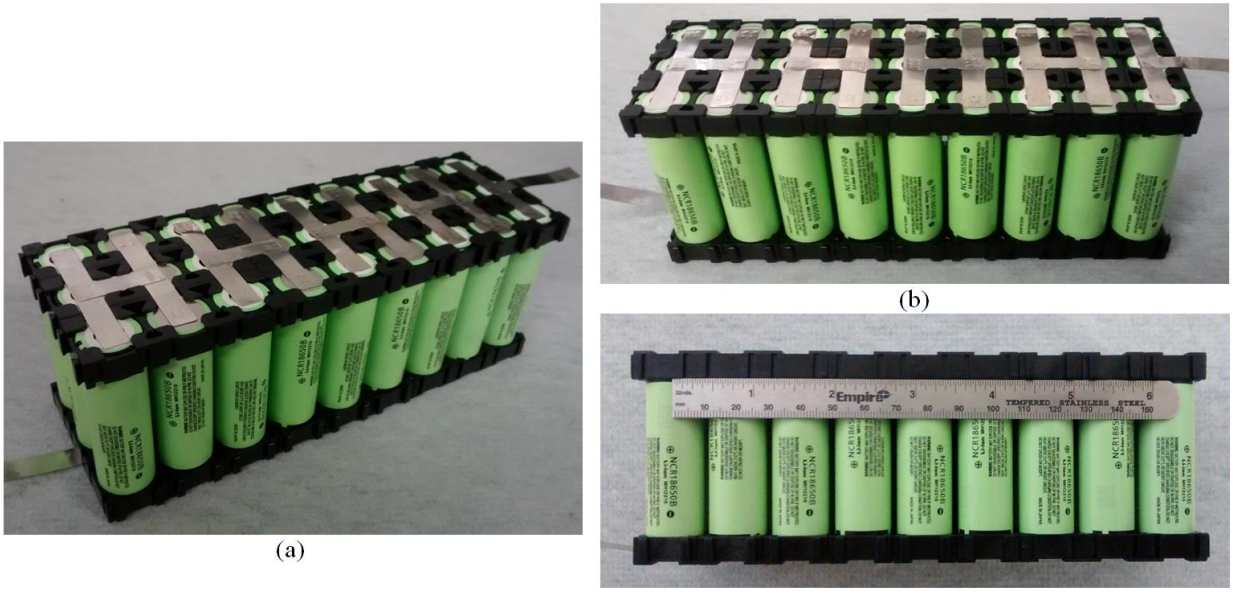

Fig. 10.2 Module setup (3P9S). (a) Isometric view; (b) top view – connection of the cells; and (c) cells' interspace.

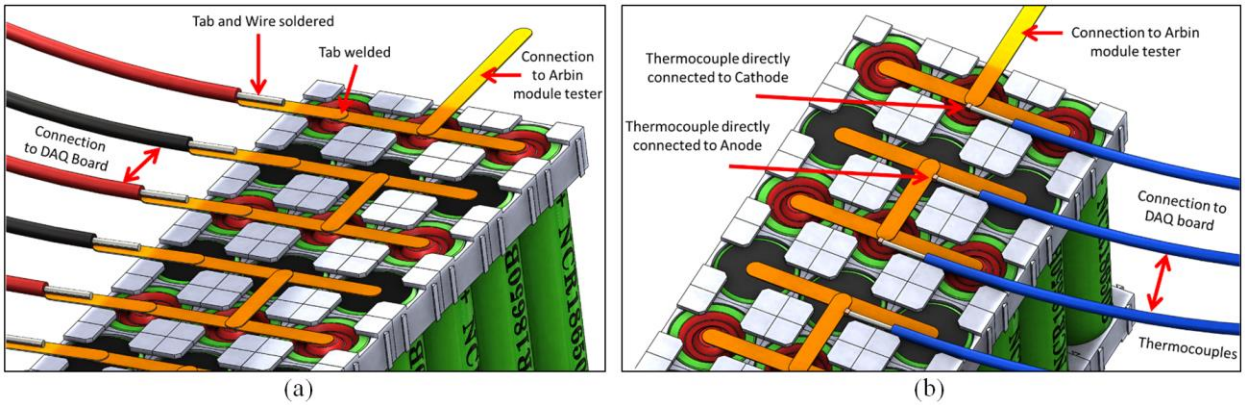

Fig. 10.3 Amplification of the banks' connection to the module tester. Simultaneous measurement of (a) voltage, and (b) temperature along with the cell voltage.

A slight modification in both modules was made. The wires soldered were trim to reduce some space and simplify the connections.

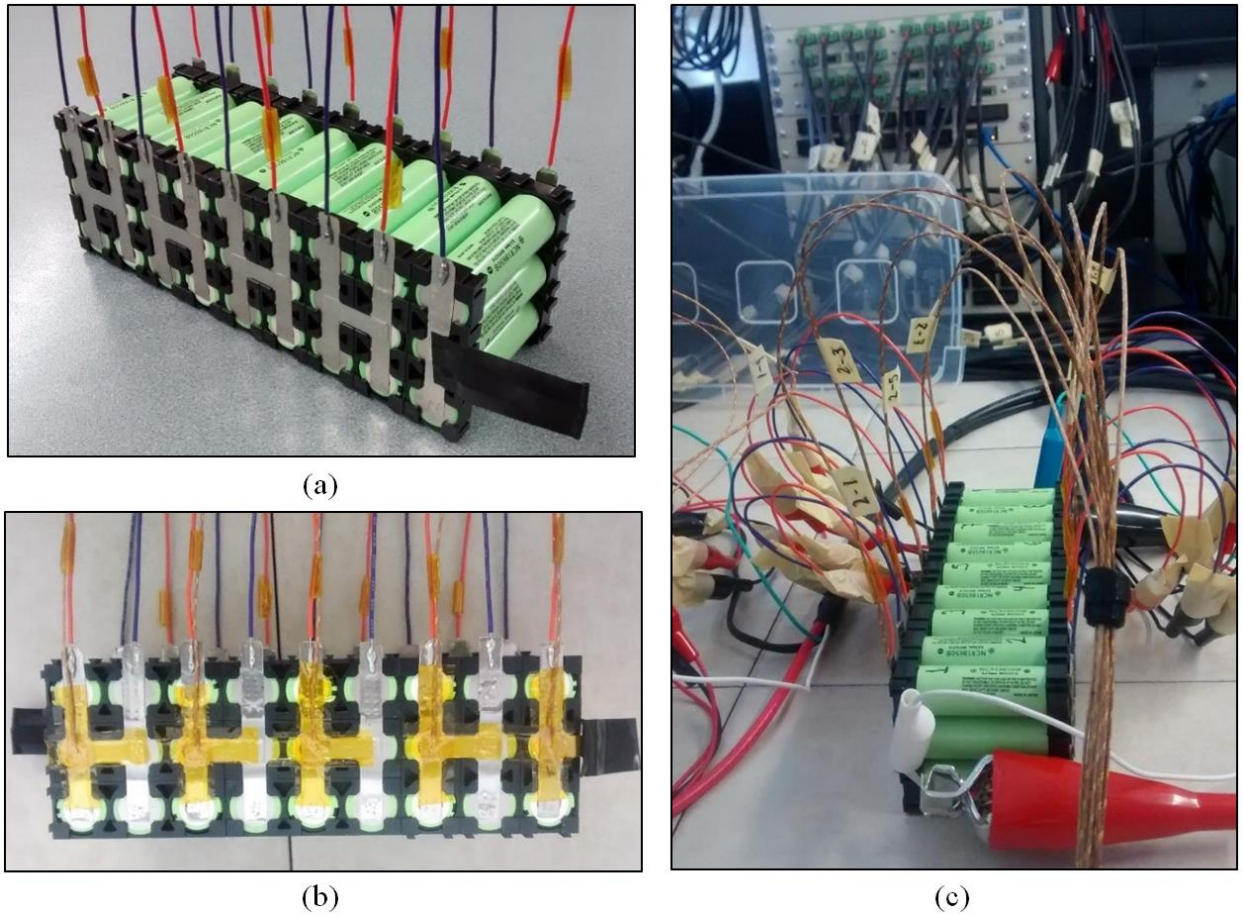

Fig. 10.4 Module 2 connection. (a) Tabs and wires attached to the module. (b) Thermocouples attached to the anode from the central cell of the banks. (c) Connection to the module tester and the DAQ board.

10.1.2 Connection

Arbin Channel 1 is used to test (charge/discharge) a particular bank of the module. In the next figure, this bank corresponds to Bank 7. For that reason, the power and the sensor cables are connected only to this particular bank. Arbin Channel 2 is used to monitor the full Module voltage (direct connection) and also the voltage on the 9 banks (indirect connection). This channel is only resting during the test.

The system of auxiliary voltages monitors only the voltage on each of the banks. It collects all the values and then transmitted them via Hub to the PC from the module tester. Prior to the test, Channel 2 is linked to the auxiliary voltage system, thus 10 measurements are collected

simultaneously (1 Module, 9 banks). In this case, only one channel from the module tester is connected and the voltage and temperature are monitored via the Auxiliary system.

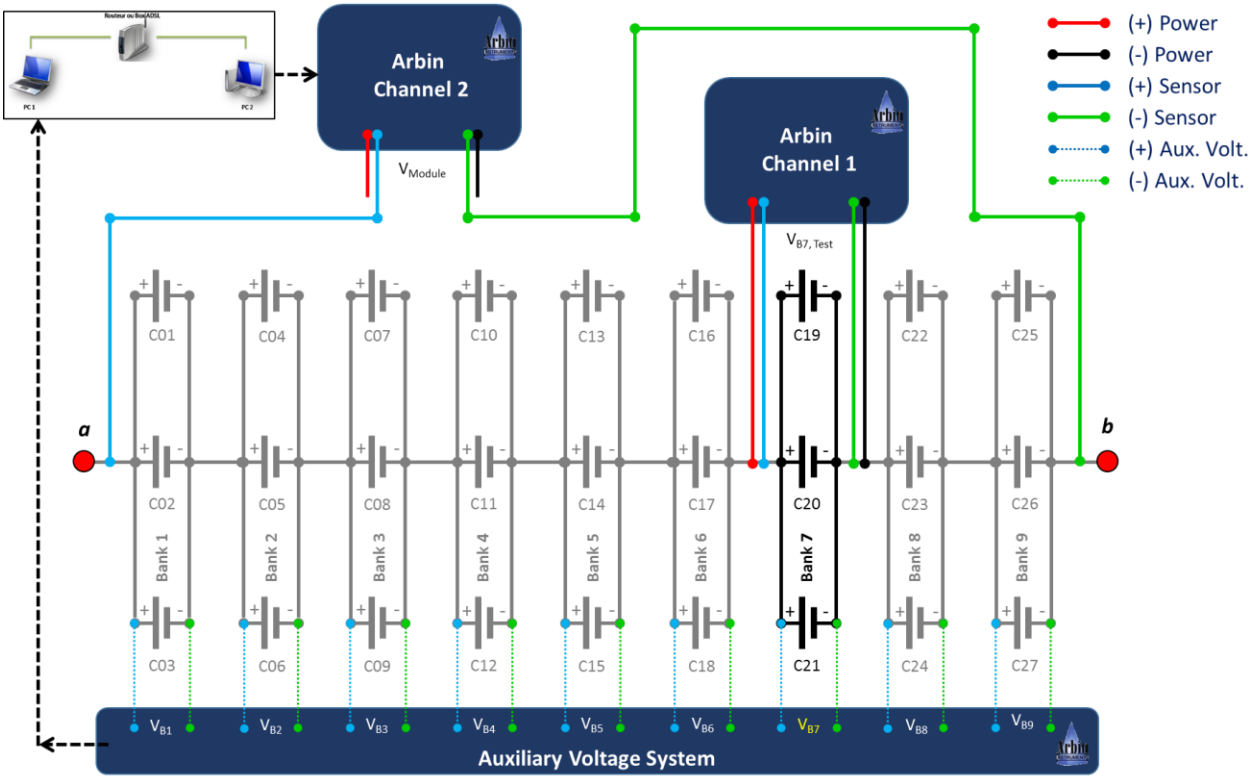

Fig. 10.5 Schematic of the connection used to test the modules. This connection allows measuring the module voltage as well as temperature and voltage on each of the banks.

10.1.3 Test of Individual Banks

If any individual bank has to be tested (charge/discharge/internal resistance measurement) individually, then, the second channel comes to play. Under this condition, the power cables are never connected to the module during this test. It is important to remark that the power cables from Arbin Channel 2 should NOT be connected to the terminals of the module while the power cables from Arbin Channel 1 are still connected. The ground from all the channels is shared by all the channels in the module tester. Connecting two sets of power cables in the module will cause a short.[231]

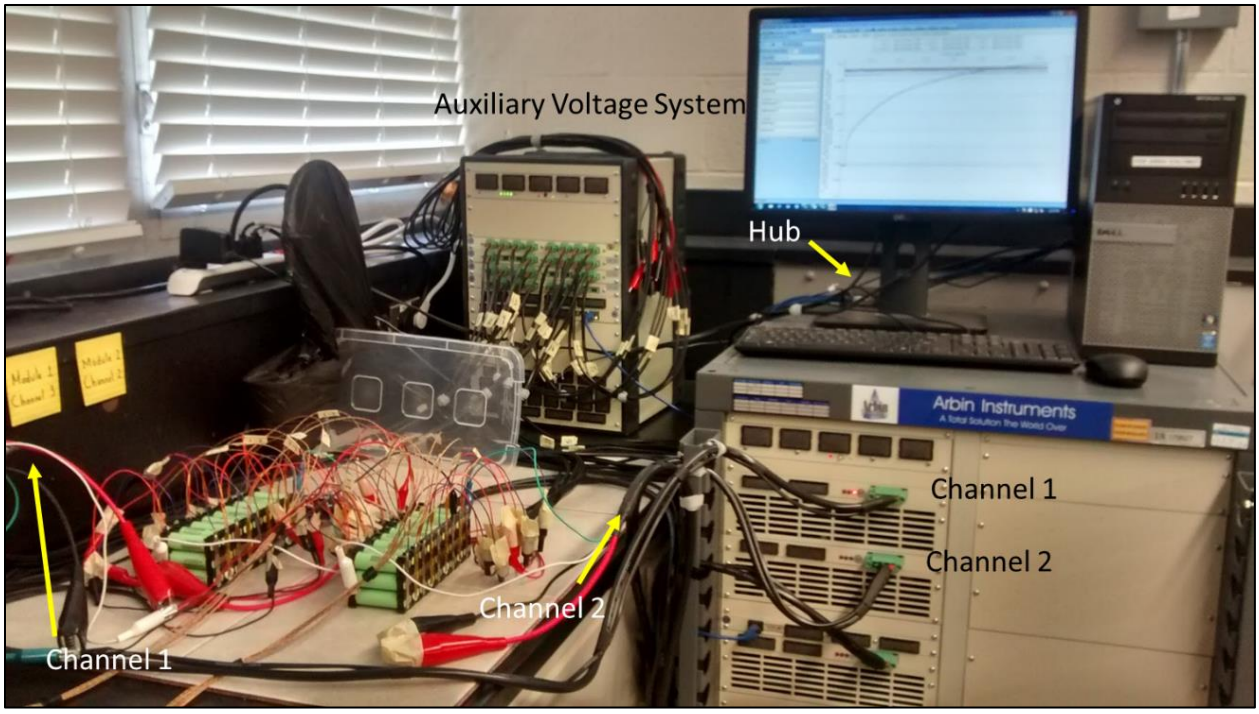

Fig. 10.6 Connection of the modules to the Arbin system.

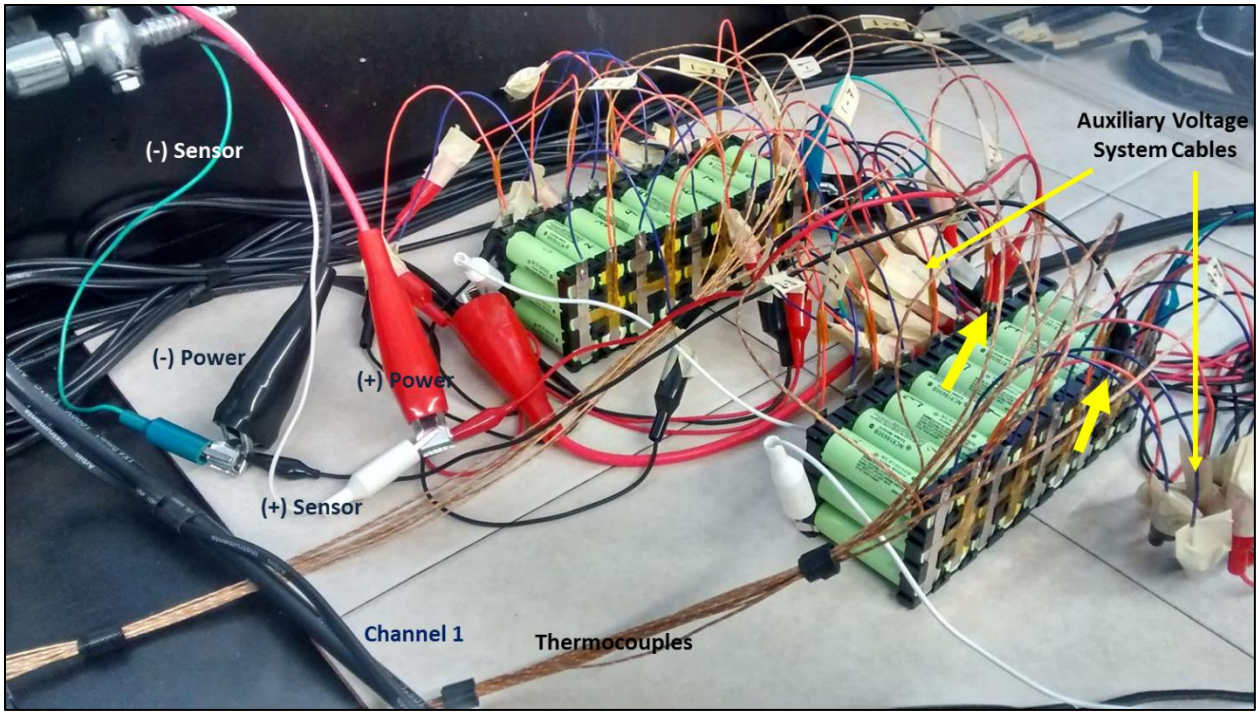

Fig. 10.7 Auxiliary voltages connection and temperature measurements. The connectors are insulated with tape to avoid any possible shorting.

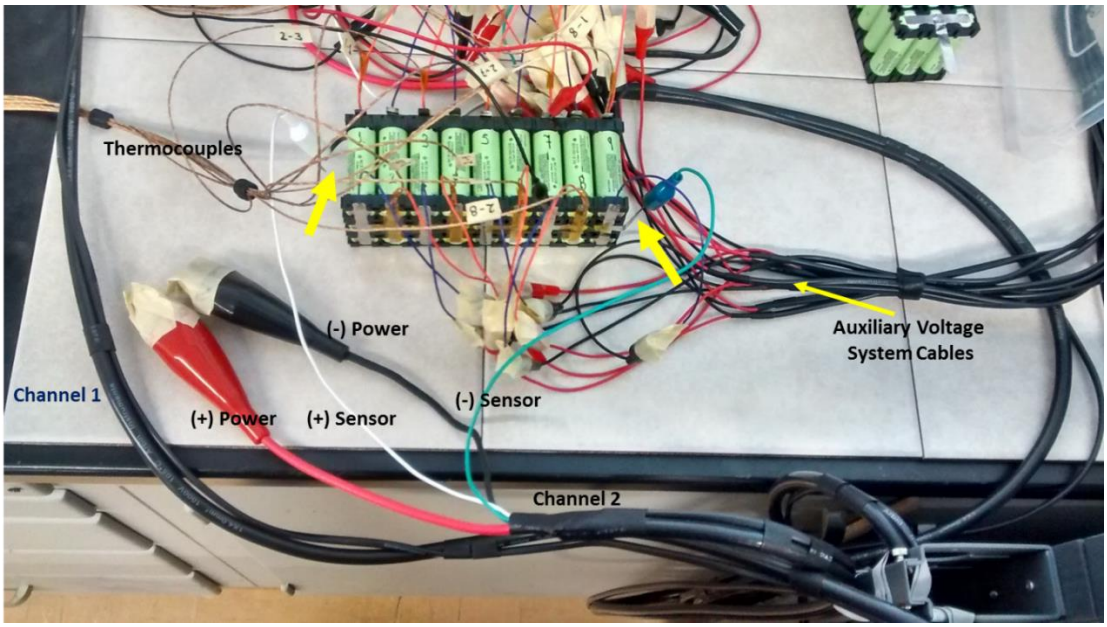

Fig. 10.8 Auxiliary voltages connection and temperature measurements for individual testing of the banks.

10.1.4 Module Preparation Test

Prior cycling the modules, they are tested using the following conditioning test in order to measure the capacity and the internal resistance of the whole module.

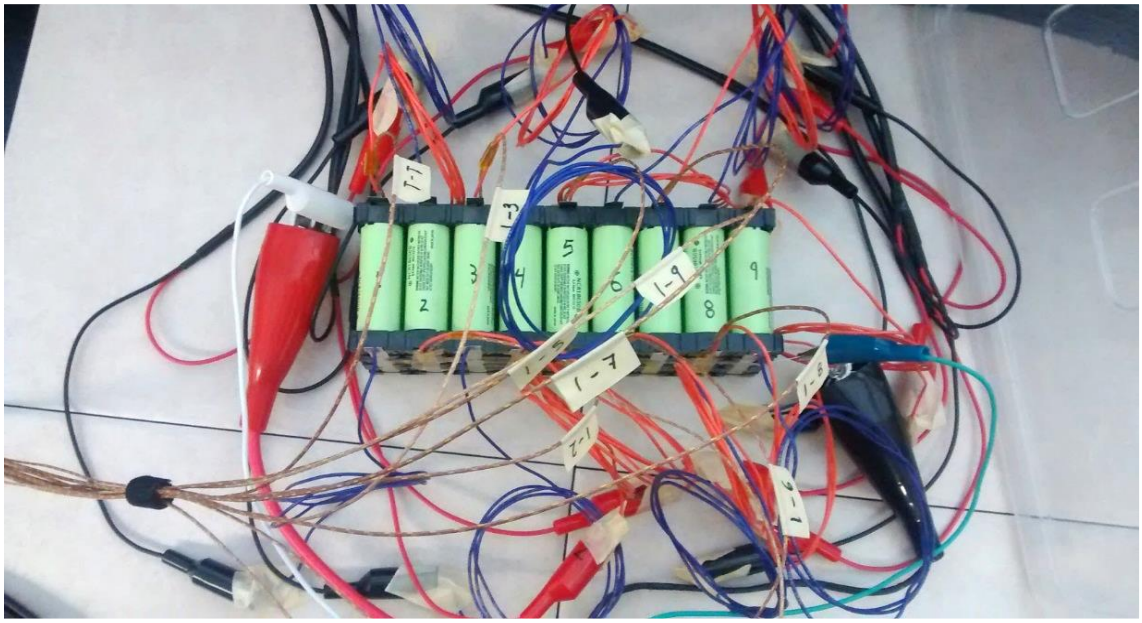

Fig. 10.9 Current setup for testing the module using the Conditioning test protocol. Banks are numbered from left to right (1-9).

Conditioning Test for Modules (3P9S)

1. CCCV charging up to 37.8 V (1C) with a cutoff current of 500 mA.
2. Rest 30 minutes.
3. CC discharging at 1C until voltage is less than 27 V.
4. Rest 30 minutes.
5. CCCV charging up to 37.8 V (1C) with a cutoff current of 500 mA.
6. Rest 30 minutes.
7. Discharge CC at 1C to capacity of 5.1 Ah (50% SOC).
8. Apply current pulse (100 ms at 1.5C) to determine internal resistance of cell.
9. CC discharging at 1C until voltage is less than 27 V.
10. Rest 30 minutes.
11. CCCV charging protocol up to 37.8 V with a cutoff current of 500 mA.
12. Rest – End test.

The results for the first cycle of the conditioning test on the module are shown in Fig. 10.10. The nominal capacity of the module is 10.2 Ah. The internal resistance obtained, during the second cycle, for this module is 133 mΩ. The module does exhibit a typical CCCV charge and CC discharge.

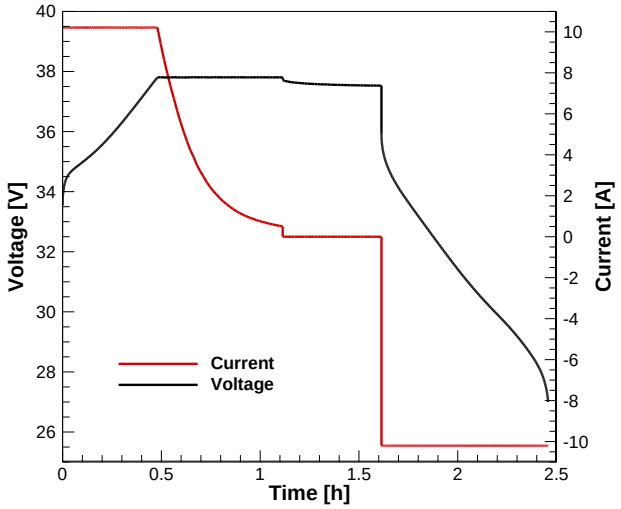

Fig. 10.10 Module 1 response during preparation test for the first cycle.

The module voltage as well as the voltage and temperature on each of the 9 banks were simultaneously monitored. Temperature response for each of the banks was recorded using the Data Acquisition (DAQ) board from National Instruments. While, the voltage response was

measured using an Auxiliary voltage System. Ideally all the cells are equal; hence the response of each of the banks is expected to be similar. However, this initial test revealed that the banks voltage was not the same. It is important to remark how the banks on the extreme (Bank 1 and 9) are the ones that exhibit a larger variation in voltage during cycling.

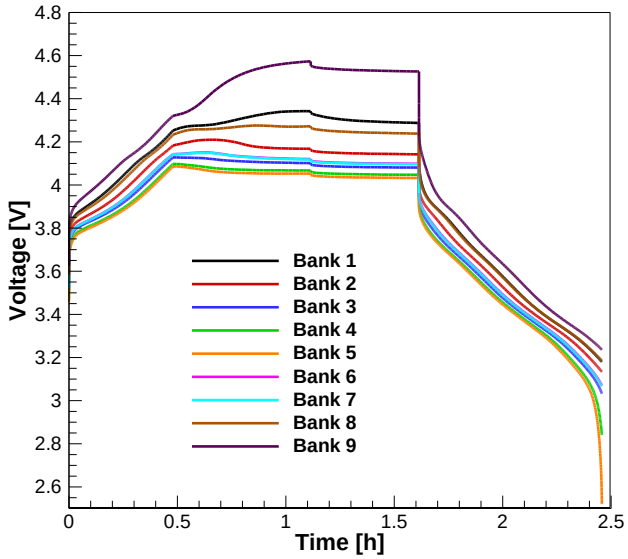

Fig. 10.11 Voltage response for each of the banks for the first cycle of the conditioning test of Module 1.

This issue caused that some banks get overcharged during the charging process (Banks 1 and 9), as well as overdischarging (Bank 5) during the discharge process. In order to avoid this problem, the voltage on each of the banks was measured. The values obtained are shown in Table 10.1.

Table 10.1 Initial voltage on each of the banks for the three different modules.

	Bank 1	**Bank 2**	**Bank 3**	**Bank 4**	**Bank 5**	**Bank 6**	**Bank 7**	**Bank 8**	**Bank 9**
Module 1	3.445	3.365	3.308	3.102	2.854	3.326	3.325	3.425	3.512
Module 2	3.61	3.61	3.61	3.61	3.61	3.61	3.61	3.61	3.61
Module 3	3.61	3.61	3.608	3.61	3.608	3.61	3.61	3.61	3.61

The discrepancies among banks in the same module could be due to a difference in the State of Charge (SOC) of the cells conforming the banks. In order to reduce these differences, a voltage shift by mean of charging/discharging in the individual banks was performed. At this point only two modules (1 and 2), were tested. Even if the initial voltage in all banks is the same, as happens

in Module 2, during the CV charge, some of the banks reached a higher voltage. More specifically, the banks on the extremes (1, 2 and 8, 9).

A second approach consisted on constrain the upper and lower voltage of the banks during charging and discharging, respectively. This idea was discarded after test it since the module cannot be fully and properly charged.

Table 10.2 Final voltage on each of the banks at the end of the CV charging process.

Control	Bank 1	Bank 2	Bank 3	Bank 4	Bank 5	Bank 6	Bank 7	Bank 8	Bank 9
Module 1	4.2265	4.2085	4.1922	4.1884	4.1819	4.1994	4.1943	4.2148	4.2094
Module 1 (Banks)	4.2001	4.1861	4.1757	4.1706	4.1668	4.1802	4.1778	4.1891	4.1923
Module 2	4.2073	4.2025	4.1970	4.1968	4.1955	4.1980	4.1995	4.2021	4.2009

The banks voltage can be equalized temporarily for a particular SOC. However, if the module is cycled the differences in voltage and SOC appears again. Considering this fact, a more realistic constrain was stablished, the banks voltage will be monitored and a maximum 30 mV voltage difference among banks will be allowed.

10.1.5 Modules Cycling

The cycling of the modules consists on charging and discharging the modules until they reach a 20% of capacity fading. The main difference in the protocols is the voltage window in which they will be cycled. The Normal Voltage Window (24.3 ~ 37.8 V) assumes that each of the banks will be cycled between 2.7 ~ 4.2 V, which corresponds to the safe voltage window provided by the manufacturer. A second operating window, denominated Reduced Voltage Window (26.1 ~ 36.0 V), assumes that each of the banks will be cycled between 2.9 ~ 4.0 V. Table 10.3 shows the two protocols in a detailed way.

The stopping criteria will be the capacity fading. The test will be stopped if the capacity of the module drops below 20 % with respect its initial capacity. The internal resistance of the module

will be obtained every 25 cycles. The results obtained for the module during the first cycles are shown next.

Table 10.3 Cycling protocols used for the modules.

Ba. Normal Voltage Window (24.3 – 37.8V)	**Bb. Reduced Voltage Window (26.1 – 36.0V)**
1. Constant Current (CC) charging at 1C (10.2A) up 37.8 V (9 x 4.2V) 2. Constant Voltage (CV) charging at 37.8 V with a cutoff current of 500 mA 3. Resting for 5 minutes 4. CC discharging at 1C to 24.3V (9 x 2.7V) 5. Resting for 5 minutes 6. Repeat step 1	1. Constant Current (CC) charging at 1C (10.2A) up 36.0 V (9 x 4.0V) 2. Constant Voltage (CV) charging at 36.0 V with a cutoff current of 500 mA. 3. Resting for 5 minutes 4. CC discharging at 1C to 26.1V (9 x 2.9V) 5. Resting for 5 minutes 6. Repeat step 1

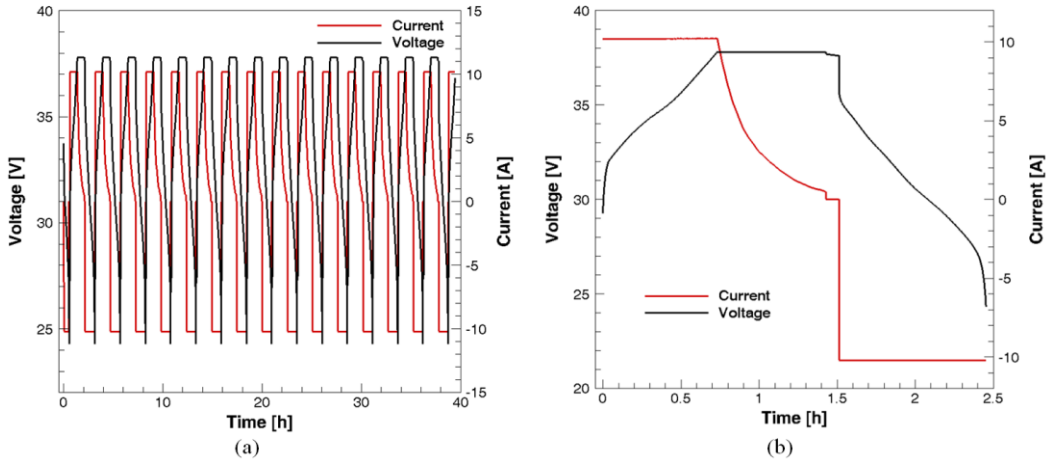

Fig. 10.12 Cycling of Module under the Normal voltage window. (a) First 15 cycles, (b) charge and discharge profiles during the 15th cycle.

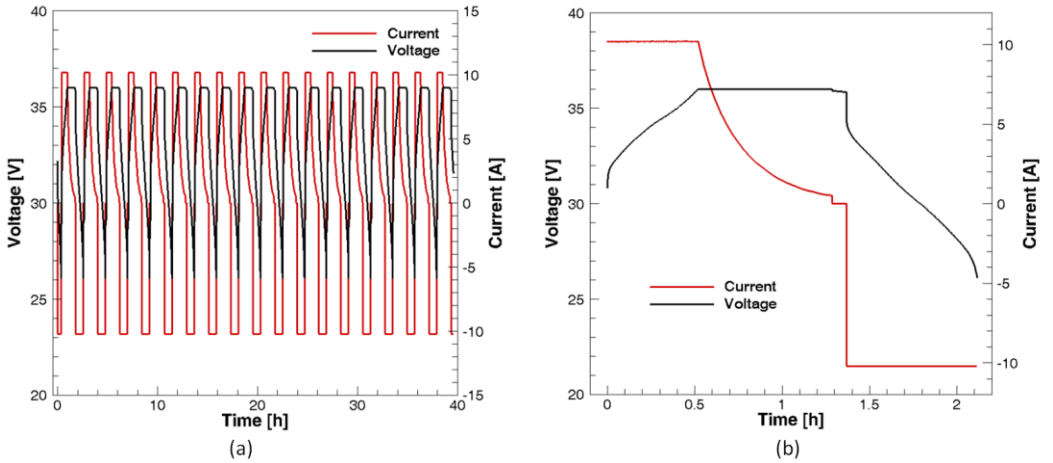

Fig. 10.13 Cycling of Module under the Reduced voltage window. (a) First 18 cycles, (b) charge and discharge profiles during the 17th cycle.

Fig. 10.14 and Fig. 10.15 show the voltage response of the banks. The voltage difference between banks remains below 10 mV during the CC charging or discharging. This difference becomes significant at the end of the CC charging and discharging.

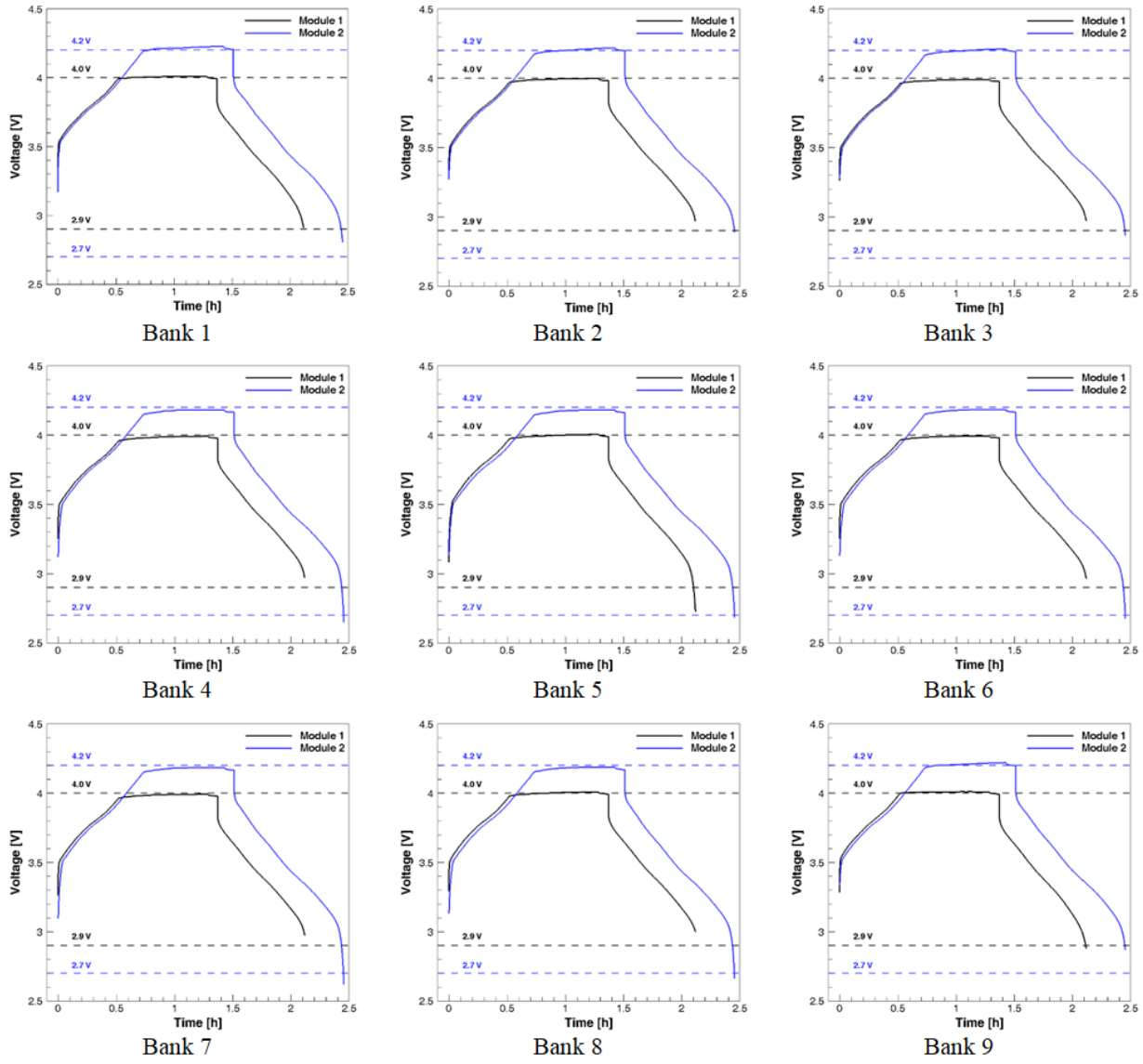

Fig. 10.14 Banks voltage during the 15th cycle for the Module 1 (Reduced) and 17th cycle for the Module 2 (Normal).

Fig. 10.14 provides a clear idea about which banks overpass the voltage limits during the CC charging and discharging. For Module 1 (Reduced), the Banks 1, 2, 5, 8, and 9 overpass the 4.0 V during the CC charging without reaching the 4.3 V. However during the CC discharging only

Banks 5 and 9 went below 2.9 V. In particular Bank 5 had been showing a consistent low voltage during the discharge. The voltage difference between Bank 5 and the rest of the banks at the end of discharge is roughly 180 mV. It is important to mention that out of this range, the difference remains almost constant and lower than 40 mV.

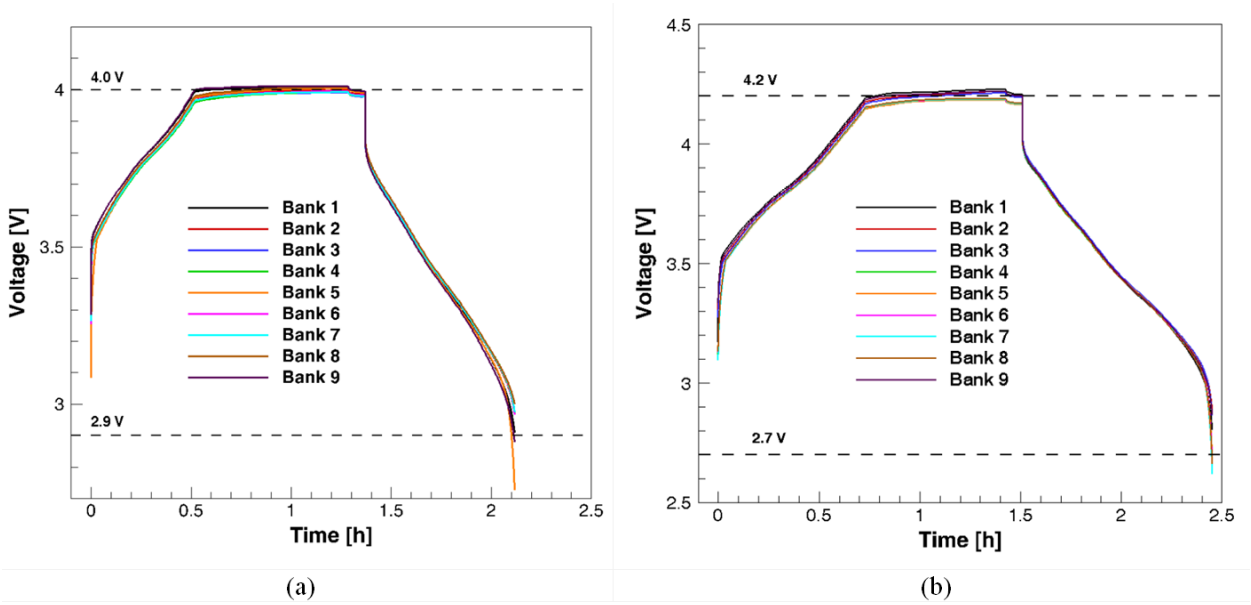

Fig. 10.15 Comparison of all the banks voltage during the cycles (a) Module 1 – Reduced voltage window at cycle 15, (b) Module 2 – Extended voltage window at cycle 17.

A similar analysis can be done in the Module 2 (Normal) cycled in the normal voltage window. During the CC discharging 5 modules drops below 2.7 V, Banks 4, 5, 6, 7 and 8. However during the charging only 4 Banks (1, 2, 3, and 9) increased their voltage above 4.2 V.

Fig. 10.15 shows in a clear way that the voltage difference between banks is very small (in fact less than 40 mV). The difference got magnified at the end of the CV charge and CC discharge. Fig. 10.14 also shows that the cycling is uneven throughout the banks. Theoretically each of the banks should have an identical cycling curve.

10.1.6 Module Test Results

As a brief update, the discharge capacity and the internal resistance for both modules is shown in Fig. 10.16 . The capacity fading percentage for Module Ba is 36.31 % while for Module Bb is 20.61 %.

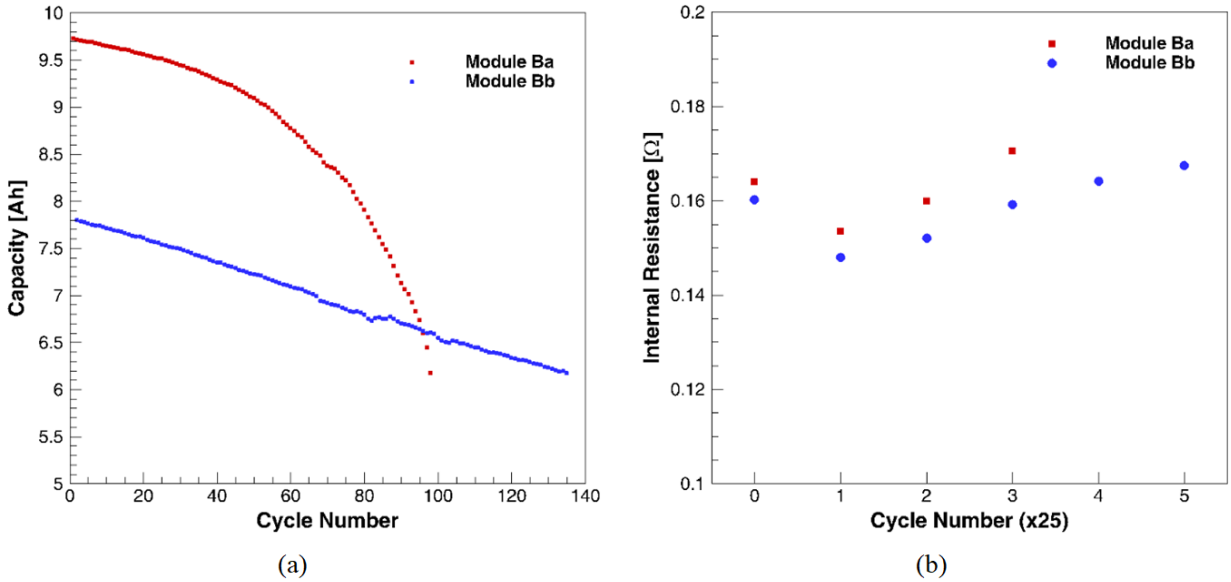

Fig. 10.16 Cycling of Module Ba (Normal voltage window) and Module Bb (Reduced voltage window). (a) Capacity fading, and (b) Internal resistance, measured every 25 cycles.

Fig. 10.17 shows the evolution of the maximum and minimum voltage and temperature on each of the cycles. As discussed in the two last reports, the banks that exhibit the most degradation (larger and lower) are the banks 1 and 9. In both modules, the bank 9 exhibits the larger and the smaller voltage during the charging and the discharging, respectively. Even more, bank 9 from module Ba has been overdischarged in the last two cycles reaching a negative voltage. It is important to remark that this low voltage only happens for some seconds until the CC voltage discharge ends. This overdischarged condition is also reflected as a raise in temperature, where the bank 9 reaches a temperature above of 160 ^{o}C and during the 2 hours resting it only get back to 75 ^{o}C.

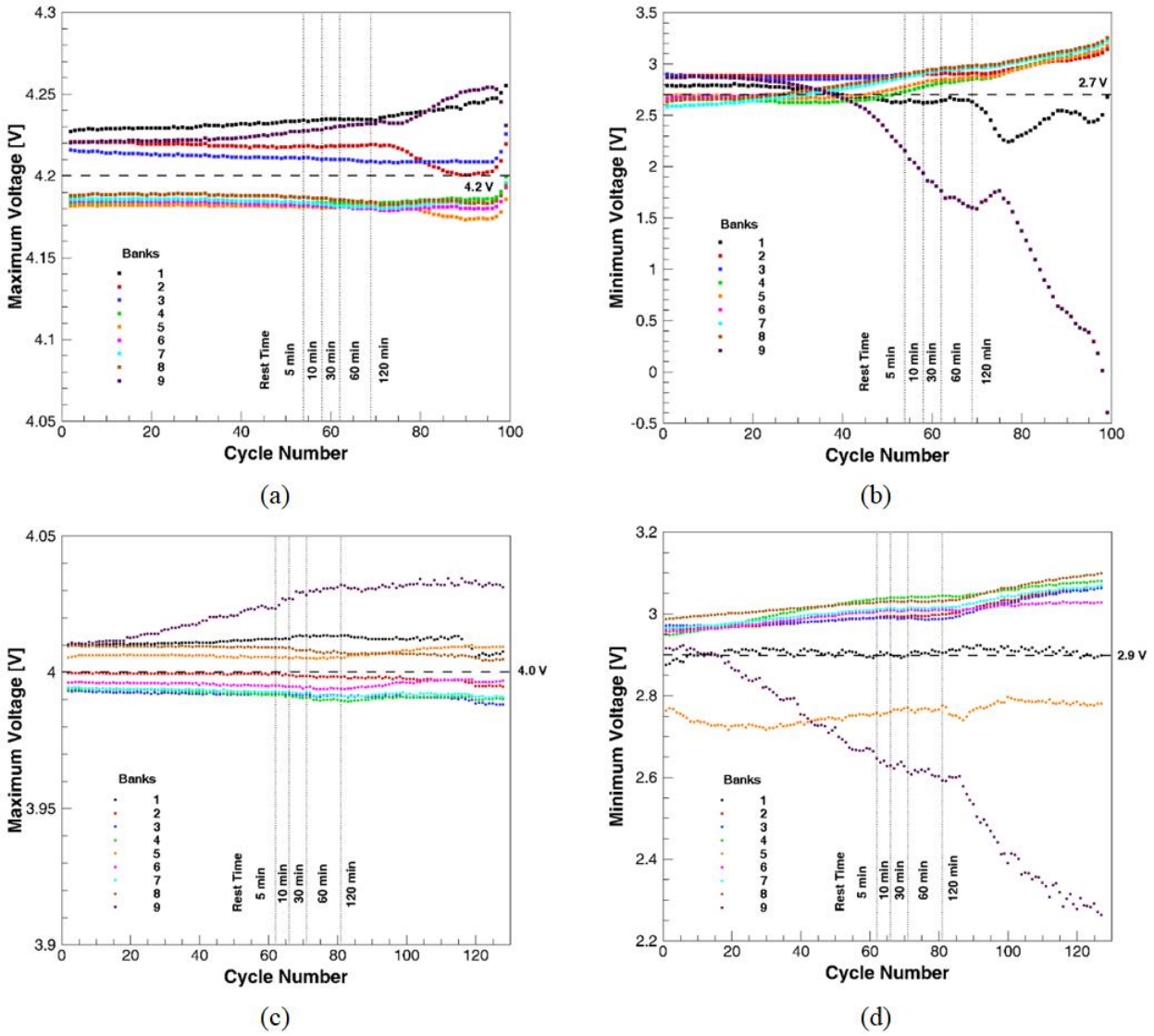

Fig. 10.17 (a) Module Ba, maximum voltage after CCCV charging. (b) Module Ba, minimum voltage after CC discharging. (c) Module Bb, maximum voltage after CCCV charging. (d) Module Bb, minimum voltage after CC discharging.

The effect of changing the resting time is also reflected in the banks' temperature. The extra time allows the module to dissipate part of the heat generated to the environment. It is also important to remark how the banks in the middle are the ones that reach the largest temperatures.

One hypothesis about why the banks show this behavior is the unbalanced capacity (not only voltage) on the banks prior the test started. A second hypothesis is a thermal-electrochemical coupling effect where the electrochemical differences produce a difference in the thermal behavior and vice versa[262], causing a cascade effect.

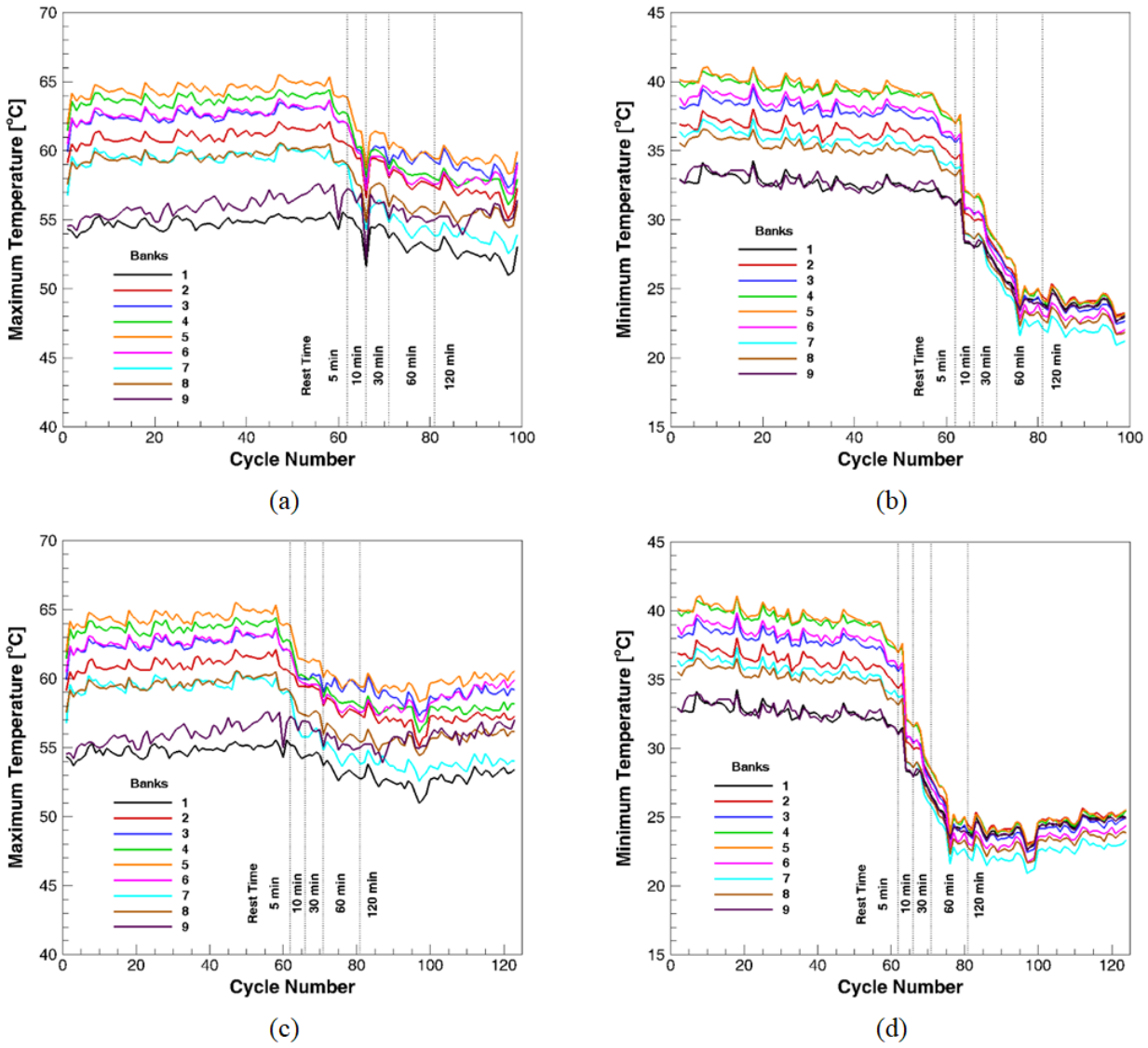

Fig. 10.18 (a) Module Ba, maximum temperature after CCCV charging. (b) Module Ba, minimum temperature after CC discharging. (c) Module Bb, maximum temperature after CCCV charging. (d) Module Bb, minimum temperature after CC discharging.

The results for Module Bb, Fig. 10.18, show that the Bank 9 started being overdischarged in the same way that it happens with the Module Ba. This difference is caused by an increased in the internal resistance of this bank which leads to a larger and smaller voltage during the charging and discharging process, respectively. Bank 5 exhibited some difference in voltage with respect the rest of the banks from the beginning of the test. However, this difference does not seem to be causing any problem. Unlike the Module Ba, Bank 1 from Module Bb does exhibit a constant voltage across cycles.

After being stopped, Module Ba was tried to charge it back, however, the Bank 9 had failed already. The failing happened during the last cycles and the temperature rose up to 164.5 ºC. The internal resistance of the individual banks will be calculated and they will be left fully charged at the end of the test.

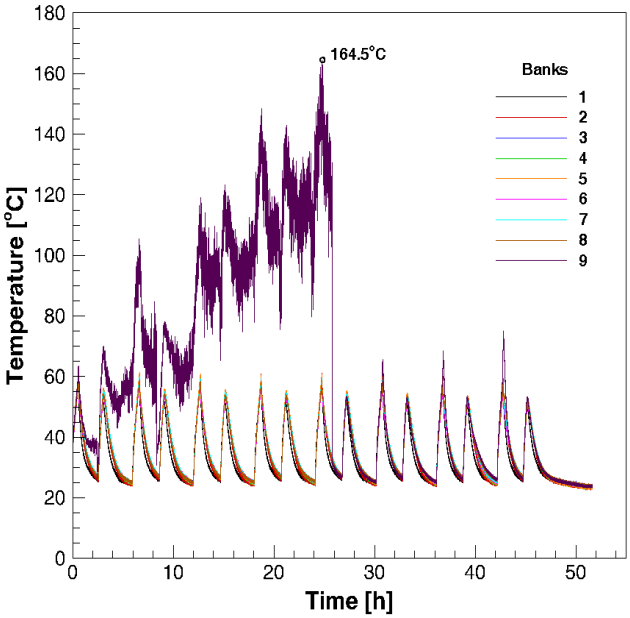

Fig. 10.19 Temperature response of all the banks from Module Ba during the last cycles before failure of Bank 9.

For the remaining banks the temperature oscillated between 25 and 70 ºC. The difference between two consecutive peaks in the temperature response is due that one of the peaks is for charging and one for discharging. This temperature response was larger in the discharging process than in the charging process. Temperature decreases during the resting after charging/discharging finished. During the last 5 cycles the temperature in Bank 9 ramp up from 60 to 164.5 ºC before it failed.

10.1.7 Modules: Banks Capacity and Internal Resistance

Each of the banks was subjected to a conditioning test. In this test, the banks were fully charged at a C-rate of C/3 up to 4.2 V, using a CCCV protocol with a cutoff current of 50 mA. Then, the banks were discharged down to 3.0 V using a CC protocol. During the second discharge, the bank was stopped at 50% of the initial capacity and the internal resistance was obtained. The test was stopped and left at 50% of the SOC.

Table 10.4 Individual capacity and internal resistance of the banks.

	Module Ba (2.7 ~ 4.2 V)		**Module Bb** (2.9 ~ 4.0 V)	
	Capacity [Ah]	**Internal Resistance [mΩ]**	**Capacity [Ah]**	**Internal Resistance [mΩ]**
Bank 1	5.957536301	113.4748310	6.426549332	131.9743544
Bank 2	6.800682536	114.4714728	6.960731346	127.4185926
Bank 3	6.859037935	120.7186058	6.942244618	130.9872568
Bank 4	6.595555166	**130.6930482**	6.930519538	130.5601299
Bank 5	7.084760565	115.7528758	6.110443934	140.2214915
Bank 6	6.886428911	123.5568076	6.588731345	138.2385045
Bank 7	7.077979323	115.3257415	7.026397351	127.7125776
Bank 8	6.47587806	**135.1064295**	6.53387699	**143.9331919**
Bank 9	-	-	5.456312503	**158.3237350**

The values obtained for the internal resistance seems to be abnormal. The typical internal resistance for these particular cells is ~45 mΩ (at 50% SOC). On one of the banks, the cells are connected in parallel; hence the expected internal resistance will be ~15 mΩ. After analyzing the actual results, the difference between both results may be due to the fact that the internal resistance was measured at different SOC (16.66%).

Even though the results provide interesting results about each of the banks. The banks with the larger internal resistance exhibit the lowest temperatures during charging/discharging and at the same time the minimum and maximum voltage during the discharging and charging process, respectively. At the end, Bank 9 from Module Ba was removed and a new tab was welded to it for further tests. Bank 9 failed during cycling due to overdischarging caused by an unbalanced in the bank's capacity.

10.1.8 Internal Resistance of the Module

The internal resistance of the whole module was measured during the conditioning test conducted prior and after they were cycled. The results are shown in Table 10.5, column 4. It is important to remark that the internal resistance in the module Ba, after cycling, was taken by having only 8 banks since the 9th one was removed. The effect of cycling at different voltage windows can be observed from these results. The module Ba tested at the voltage window provided by the

manufacturer exhibited a larger internal resistance than the one tested in the reduced voltage window.

Table 10.5 Internal resistance of the modules prior and after cycling.

Module	Test	No. Banks	Module Internal Resistance [mΩ]	Bank Internal Resistance* [mΩ]	Cell Internal Resistance** [mΩ]
Module Ba	Before cycling	9	**140.49293**	15.61032	46.83096
Module Ba	After cycling	8	**171.23533**	21.40441	64.21323
Module Bb	Before cycling	9	**137.32814**	15.25868	45.77604
Module Bb	After cycling	9	**155.88218**	17.32024	51.96072

So far, it is known the internal resistance from the full module. However, if we assume that all the banks and all the cells have the same internal resistance, then we can back calculate what should be the internal resistance for each bank and each cell on them. This assumption is not at all true, however, it will allow comparing if the internal resistance of the banks is in the same order than the ones measured directly from the banks, see Table 10.4. In the same way we can compare these ideal values for the internal resistance of the cell with some of the values obtained previously in the cells from Section B.

The ideal values for the internal resistance of the banks and the cells are shown in columns 5 and 6 from Table 10.5. The values for the internal resistance of the cells seem to be consistent with all the previous results. However, the ideal values of the internal resistance of the banks (15.0 – 21.4 mΩ) do not seem to match (or at least have the same order of magnitude) with the experimental results (113 – 160 mΩ).

11. SUMMARY AND OUTLOOK

Degradation is a natural phenomenon that cannot be avoided but it can be controlled if it's properly understood. The degradation phenomenon is a relevant issue for energy storage systems. A large amount of battery components, chemistry variety, and multiple architectures for every single component makes it harder to predict the overall cell behavior. Under normal conditions, the cell degrades at a low rate until it cannot longer power the external electrical load. However, when the cell is subjected, intentional or unintentionally, to abnormal operating conditions, then it degrades faster and the component starts interacting in a non-desired way. The high reactive and flammable nature of the cell components poses a threat not only to the cell integrity but also to user safety.

In this work, it is proposed a methodological method to investigate the degradation mechanisms behind the failure in lithium-ion cells. The methodology is a comprehensive program where all the variables involved in the cell performance are contrasted and used to elucidate the possible cause behind a specific cell failure. The experimental basis of this approach sets the pathway to study the abnormal behavior of new chemistries' coupling in a single cell or a module configuration. A few questions that the present work aims to explain are:

- *Electrode level degradation*: Where degradation starts. Degradation not necessarily depends on the operating condition; the intrinsic mechanical properties of the anode/cathode active materials can be the source of poor electrochemical performance.
- *Cell level degradation*: How does the voltage window affect the electrochemical performance. The safe voltage window is a boundary that should not be crossed; otherwise, the cell can fail or its cycle life can get shorten.
- *Module level degradation*: How significant a small voltage or capacity difference can be in the long-term cycling test. Minor manufacture differences from cell-to-cell can be the root behind the poor performance of a module without BMS.
- *The aging effect on the safety aspects*: How different react a fresh cell with respect to a new cell when they are subjected to the same abuse test. Cell internal degradation can play in a benign or malign way depending on the level of degradation and the abnormal condition at which the cell is subjected.

APPENDIX A. IMAGE PROCESSING

Appendix A. **Image Processing of Cracked Electrodes**

Unmodified binary SEM images inherently included excess noise. In addition, conversion to a binary image resulted in void spaces in some cracks – narrow cracks with a width of only a few pixels were specifically vulnerable to this distortion. Consequently, one crack in the gray scale image was incorrectly interpreted as two cracks in the binary image. To resolve these conversion issues, the binary image was subjected to a morphological filtering technique known as closing. The process of closing involves object dilation followed by erosion and was carried out using a 3×3 square structuring element.

Closing first requires the definition of a structuring element. In this case, a 3×3 square structuring element was selected, see Fig. A.1. The structuring element is "laid over" the input image (i.e., the unmodified binary image) with the center pixel coincident with the pixel of interest in the input image. As the structuring element is moved over the entire input image, each pixel of the input image serves as the central pixel of the structuring element exactly once. The structuring element is determined to "fit" the input image if all corresponding input pixels below the structuring element also have a value of 1. On the contrary, if at least one of the input image pixels below the structuring element has a value of one, the structuring element is determined to "intersect" the input image. An example of the structuring element over an input image is shown in Fig. A.1. Once the structuring element is determined to fit or intersect the input image, the operations of erosion and dilation define the subsequent action on the central pixel and the result is output to a modified binary image.

During dilation, if the structuring element intersects the input image, (i.e., one or more underlying input pixels has a value of 1) the input pixel corresponding to the central pixel of the structuring element is given a value of 1 in the output image, otherwise it will be zero. In effect, dilation by a 3×3 structuring element adds a layer of pixels to the boundary of each object in the binary image. The operation then closes gaps less than or equal to two pixels wide. Each pixel in the SEM images

is equivalent to 3.61 μm. Therefore, a 3×3 structuring element was chosen so adjacent cracks with a gap width less than the average diameter of an NMC particle (~10 μm) would be filled.

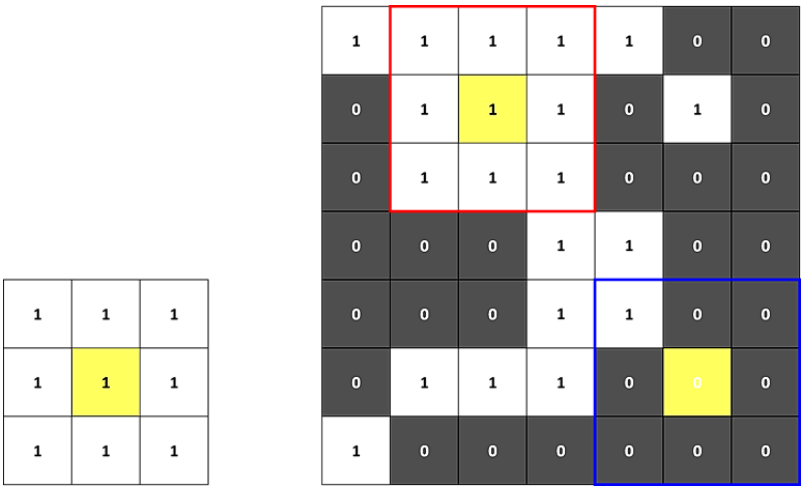

Fig. A.1 The 3×3 structuring element (left) lays over the binary input image (right). The red square outlines an instance when the structuring element fits the input image, whereas the blue square outlines the structuring element intersecting the input image. The pixel of interest is yellow.

Besides filling void spaces in cracks, dilation also amplifies noise in the binary image. To filter noise as well as restore cracks to their true dimensions, erosion was applied to the dilated binary image. During erosion, the same structuring element is passed over the entire image. If the structuring element fits the dilated binary image, (i.e., all input pixels lying below the structuring element have a value of 1) the central pixel is given a value of 1 in the output image. As a result, erosion shrinks the dimension of all connected objects by removing one layer of pixels from the boundary. The advantage of erosion is that small connected objects corresponding to noise in the binary image will be completely omitted from the output image when the structuring element fails to fit in the object for any of its pixels.

The closed binary image was subjected to a final image processing technique to remove noise large enough to evade the process of erosion, which involved removing connected objects of 97 pixels or less from the closed binary image. The end result was a clean binary image comprised of only the electrode crack features.

APPENDIX B. DPA CYLINDRICAL CELLS

Appendix B. **Destructive Physical Analysis**

Destructive physical analysis (DPA) provides insights through visual inspection on the physical degradation of the individual components embedded in the Li-ion cell. The procedure involves a sequence of steps aim to determine any abnormality of the cell and preserving the degradation evidence present on each of the cell components. DPA is especially helpful in cases when the cell undergoes, intentionally or unintentionally, into an electrochemical, mechanical and/or thermal abuse scenario. A physical inspection of the abused cell can help to visualize the starting failure zone. Localized root cause becomes significant in forensic analysis of incidents involving Li-ion cells.

DPA consists of an in-house protocol conducted in an inert Argon-filled glovebox (H_2O < 0.5 ppm, O_2 < 0.5 ppm). The procedure is aimed to be implemented on cylindrical cells. It is recommended to fully discharge the cell prior disassembly when possible. The person conducting the DPA must be familiar with the Li-ion technologies, in particular with architecture of the cylindrical cells. Cells subjected to disassembly may overheat or get internally shorted during the procedure, resulting in an unsafe condition. Additional caution measures must be observed when DPA is conducted on abused cells to reduce the risk of health hazards.

Step 1. The nickel tabs are removed by prying them with narrow tipped pliers. Then, the thin plastic wrapping, surrounding the cell, is removed by making two small cuts with the scalpel and then peeling the plastic by hand.

Step 2. The cell header is removed using a tube cutter. The adjusting screw is turned to bring the cutting wheel and the cell crimping notch into contact. The cell header is gradually cut by rotating the tool around the clamped notch and tightening the adjusting screw.

Step 3. The thin electrical connection between the cell cap and the rest of the cell is snipped with scissors. Caution must be taken to avoid direct contact between the metallic scissors and the cell can since it can externally short the cell.

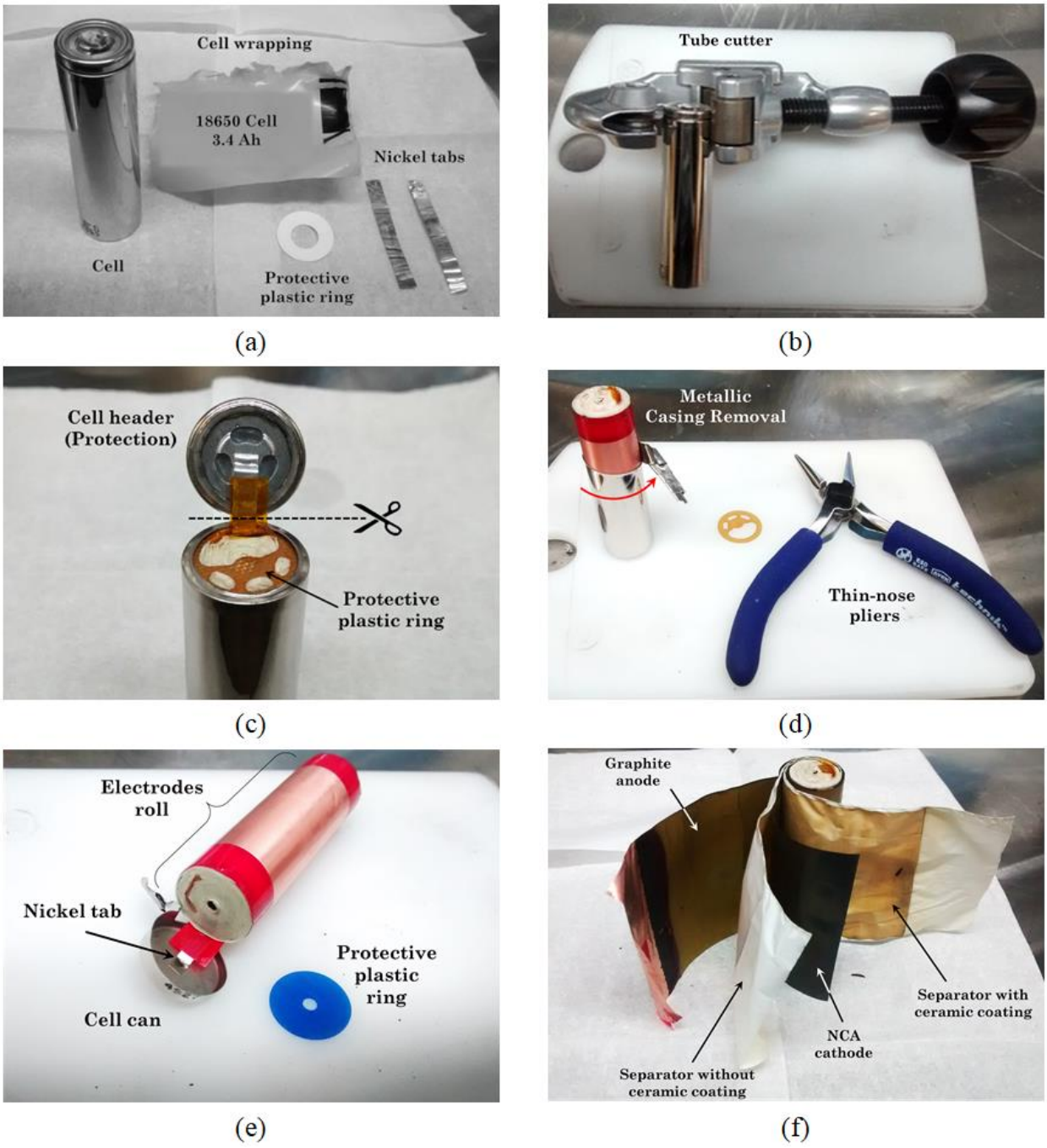

Fig. B.1 In-house procedure used to harvest the cell components while preserving the degradation evidence. (a) Step 1: nickel tabs and plastic wrapping removal. (b) Step 2: cell opening. (c) Step 3: cell header removal. (d) Step 4: metallic casing removal. (e) Step 5: jelly roll extraction. (f) Step 8: electrodes/separators split-up.

Step 4. Starting at the top of the cell where housing is crimped, the protective metal can be removed using a thin-nosed plier and an end-nipper plier by peeling off the metal housing toward the bottom of the cell. The protective plastic located on top of the electrodes is removed.

Step 5. Once the metal housing has been removed to the bottom, the electrical connection located at the bottom of the cell is cut. Then, the blue protective plastic located on the bottom of the jelly roll is removed.

Step 6. If any residual of liquid electrolyte is visible, it is collected in a labeled glass vial. If not liquid electrolyte is found, then, the electrodes are rinsed with isopropyl alcohol (IPA) and the mixture is collected for further composition analysis.

Step 7. The tape holding the electrodes together and the nickel tab placed in between the tape and the copper foil are removed.

Step 8. The two long electrode ribbons and the two separators are unrolled and separated. Take care not to short the electrodes by getting them in direct contact during this process. Pictographically evidence of each electrode and the separator facing it is recommended.

Step 9. The cell components are stored within the inert glovebox in sealing bags. It is recommended to store anode, cathode, separators and the rest of the components in separated bags. By following this procedure, degradation evidence can be preserved in good condition even after one year. If the samples have to be transferred out of the glovebox, then, the sealing bags can be placed under vacuum using a commercial vacuum sealer, and the evidence will not be destroyed.

DPA of Fresh Cell

The results from the Destructive Physical Analysis conducted on the cell are accompanied with pictures to support the evidence of damage on the components. In particular, pictures of the extended electrodes and the separators are taken. Since both sides of the electrodes and the separators are different, it is important to distinguish them. In Fig. B.1, the different faces of the electrodes and separators are labeled in order to facilitate interpretation of the results. The negative electrode, anode, contains Graphite casted on a copper foil. The positive electrode, cathode, contains Nickel Cobalt Aluminum Oxide (NCAO) casted on aluminum foil. Both electrodes are double side coated. However, the casted area is not the same even in the same electrode.

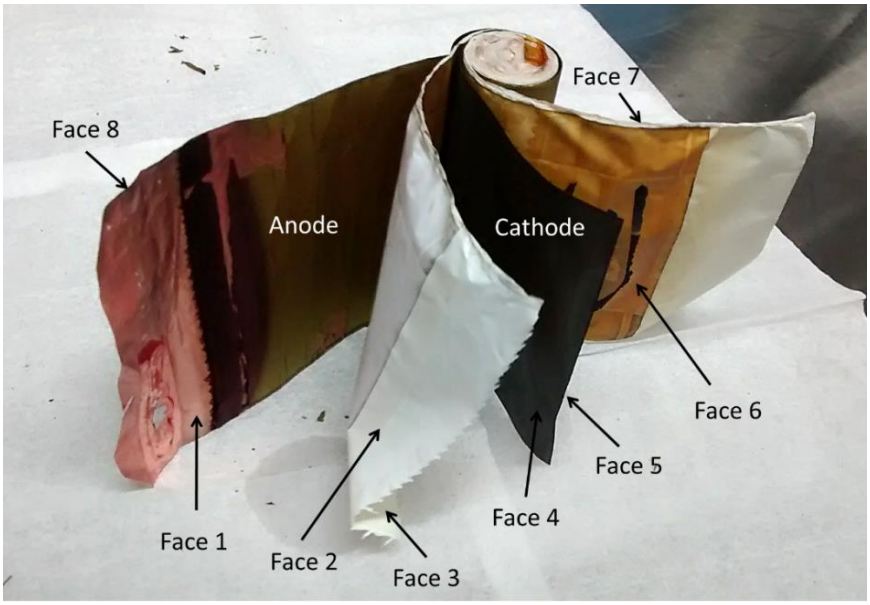

Fig. B.2 Identification of the cell components.

Table B.1 Characteristics of each of the faces on the Li-ion jelly roll.

Face	Zone	Direction	Material
Face 1	Anode	Facing toward the center	Graphite
Face 2	Separator 1	Facing outward the center	No ceramic coating
Face 3	Separator 1	Facing toward the center	With a ceramic coating
Face 4	Cathode	Facing outward the center	NCAO
Face 5	Cathode	Facing toward the center	NCAO
Face 6	Separator 2	Facing outward the center	With a ceramic coating
Face 7	Separator 2	Facing toward the center	No ceramic coating
Face 8	Anode	Facing outward the center	Graphite

The electrodes (graphite and NCAO) and the Polypropylene (PP) separators from a fresh new cell should be close to their pristine state. This cell will be used as a baseline for all the different abuse test experiments. As expected, no damage was found either in the electrodes or the separator. Also, no presence of liquid electrolyte was found. In order to capture the electrolyte properties, the electrodes were rinsed with Isopropanol (IPA) and the mixture was collected. Fig. B.3 shows the pictures taken during the DPA. It is important to remark that during the Physical analysis, both electrodes were extracted and no flaking was observed, see Fig. B.3 (c) and (d).

(a)

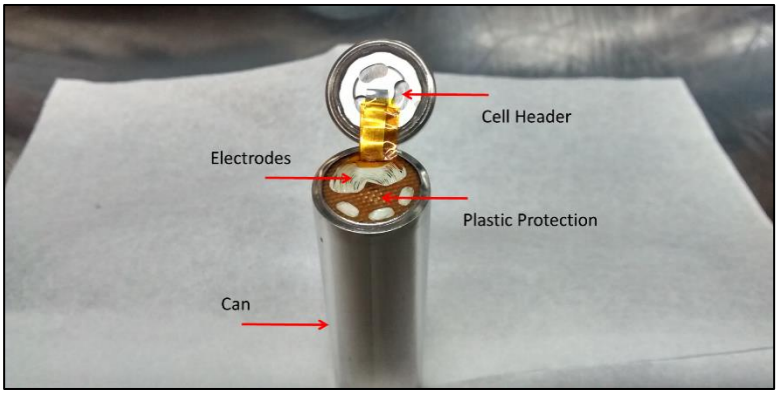

(b)

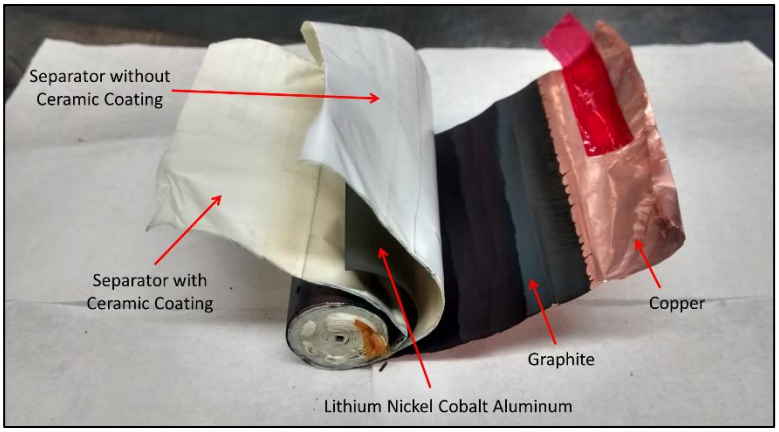

(c)

(d)

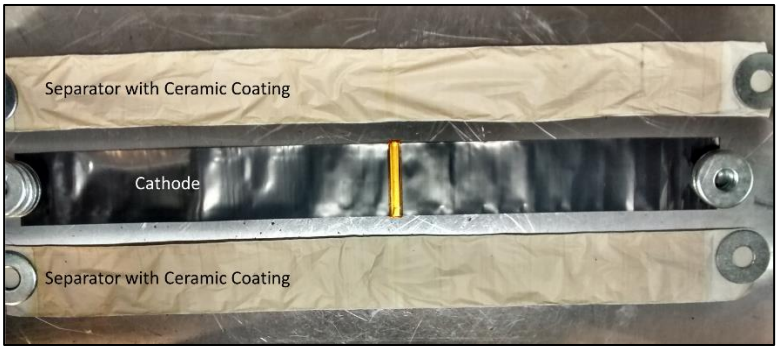

Fig. B.3 Destructive Physical Analysis of a fresh Panasonic cell (3.4 Ah) without cycling. (a) Cell opening by using a tube cutter, (b) electrodes removed from the cell can, (c) double side coated anode, and (d) double side coated cathode.

Since the cell has not been cycled, neither charged nor discharged, the negative electrode exhibits the characteristic purple-darkish color of the unlithiated graphite. Fig. B.3 (d) shows the NCAO electrode and the two separators facing it. In this case, the separators, facing the electrode, possesses a ceramic coating made of a composite of Aluminum Oxide (Al_2O_3) particles and cross-linked ethylene-oxide chains. The solid separator membrane blocks dendrites from the alkali-ion anode and soluble redox species in the cathode side from crossing over to the anode [177]. This ceramic coating spans only the area covered by the cathode electrode as it can be seen in Fig. B.3 (d). The yellow strip on the positive electrode, see Fig. B.3 (d), is the nickel tab that connect cathode and the bottom of the cell can. The yellow color comes from the insulating tape that prevents any possible internal shorting.

APPENDIX C. DPA POUCH CELLS

Appendix C. **Post Mortem Analysis of Pouch Cells**

Post-mortem analysis is a robust and widely-adapted tool used to gain further insights into the failure analysis of a cell. Opening these cells helps in visualizing and characterizing the changes that occurred in the cell components during the test and compare them with that of a fresh cell.

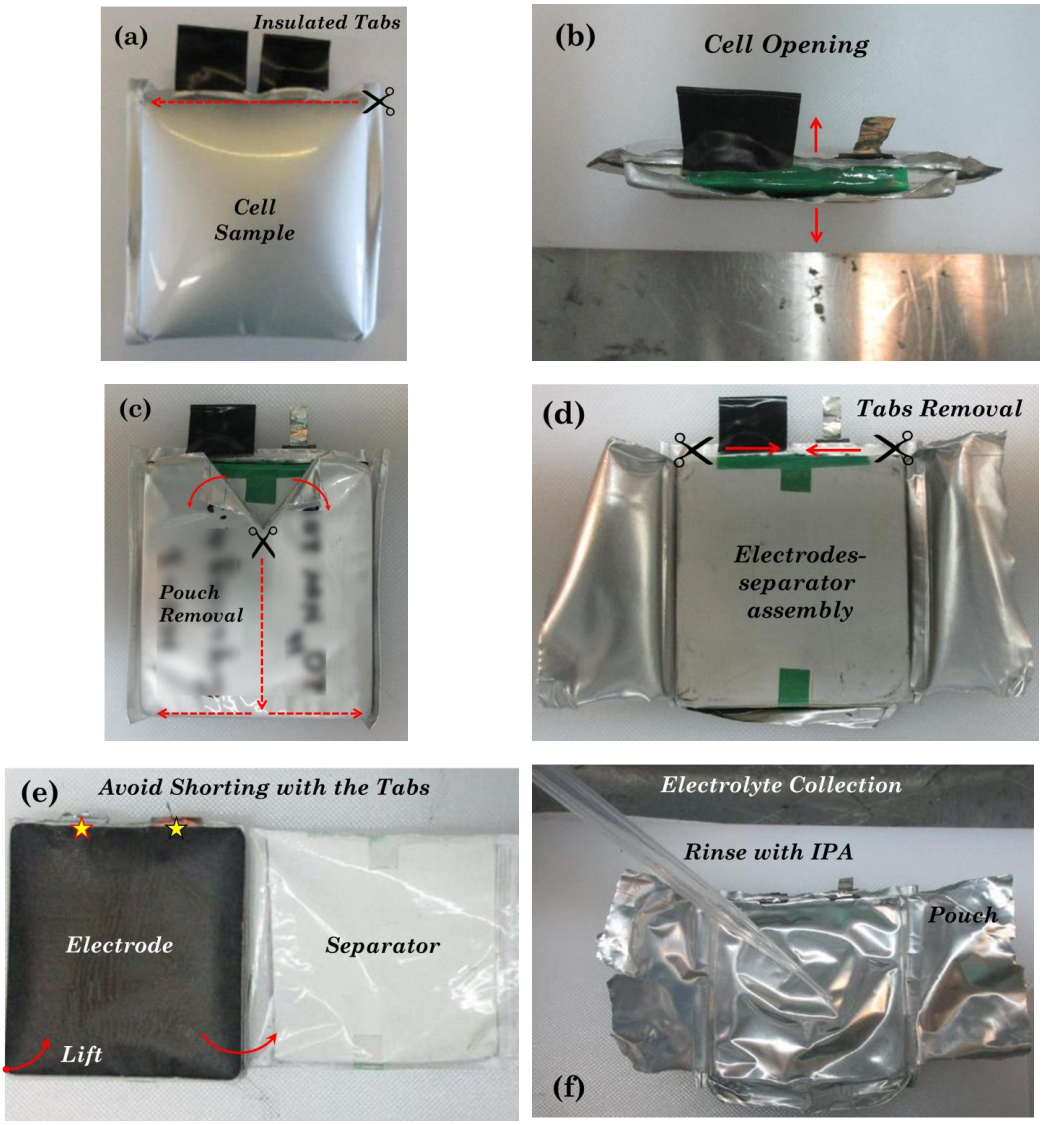

Fig. C.1 Destructive physical analysis of an aged pouch cell. (a) Isolation of the tabs, (b) cut along the width of the pouch, (c) T-shape cut, (d) cut along the length and bottom of the pouch, (e) unwinding the separator and extraction of electrodes, and (f) IPA poured on the pouch to collect electrolyte.

A step by step procedure followed for disassembling the pouch cell is described next.

Step 1. Insulation of tabs. Prior the destructive physical analysis (DPA), the tabs of the pouch cells are isolated with electrical insulation tape. This is an extra precaution that needs to be taken in order to avoid any case of an external short circuit, see Fig. C.1a.

Step 2. Preparation of materials. Sealing bags are used to store the electrodes, separators and other components of the cell. A total of 5 sealing bags, one for each electrode, one for the separator, one for the electrolyte and one for storing the other cell components such as pouch and tabs are labeled based on the things they will house. A glass vial, vial septum, and a vial cap are used to collect the electrolyte of the cell. All the materials, the cell and a media recorder device are transferred to the glovebox.

Step 3. Disassembly of the pouch. After transferring the cell inside the glove box, a plastic board is used to disassemble the cell. This is used to avoid contact of tabs with the metallic floor of the glove box. The process starts with piercing the pouch using a stainless-steel scalpel. This initial cut is made near one of the tabs. Extra care should be taken while using the scalpel to avoid any kind of short circuit and hence it is recommended to keep one of the tabs insulated. The cutting process should be done very slowly and with extra care. Once the cut along the width of the cell is complete, a pair of point-tip plastic tweezers is used to pull up the pouch from the center as shown in Fig. C.1b. After the cut along the length, the pouch is pulled off from the cell forming a T-shaped cut, as shown in Fig. C.1c. The pouch is then cut from the bottom exposing the electrodes-separators assembly, see Fig. C.1d.

Step 4. Tabs removal. The pouch remains connected to the cells through the metallic nickel tabs. A pair of scissors is used to cut the tabs, one by one, and separate the pouch and tabs from the cell, see Fig. C.1d. Extra precaution should be taken while cutting the tabs to avoid short circuit.

Step 5. Disassembly of separator and electrodes. After removing the tapes on the external separator, the electrodes-separator assembly can be unwound. Two separate pairs of plastic tweezers are used to extract cathode and anode. Extra care must be taken while separating the electrodes because the electrodes or the active material on the separator may get in contact with other electrode resulting in a short circuit. An image of unwinding the separator and extraction of electrodes is shown in Fig. C.1e.

Step 6. Electrolyte collection. The electrodes from commercial cells are typically soaked rather than flooded with the electrolyte. In rare occasions, it is possible to get even a few electrolyte drops. However, the electrolyte can be collected by rinsing isopropyl alcohol (IPA) over the disassembled pouch, see Fig. C.1e. The mixture is then carefully poured into the glass vial without spilling any of it. The glass vial is then closed with a septum and cap. As IPA is volatile in nature it is important to seal the electrolyte mixture. A manual crimper is used to seal the glass vial. The collected electrolyte is further analyzed to study the decomposition of electrolyte using gas chromatography and mass spectroscopy.

BIBLIOGRAPHY

1. Administration, U. S. E. I. *Annual Energy Outlook 2018 with Projections to 2050*; 2018.
2. Rahn, C. D. W., C. Y., *Battery Systems Engineering*. First ed.; John Wiley & Sons, Ltd: 2013.
3. Neubauer, J.; Pesaran, A., The Ability of Battery Second use Strategies to Impact Plug-in Electric Vehicle Prices and Serve Utility Energy Storage Applications. *J Power Sources* **2011,** *196* (23), 10351-10358.
4. Juarez-Robles, D.; Hernandez-Guerrero, A.; Ramos-Alvarado, B.; Elizalde-Blancas, F.; Damian-Ascencio, C. E., Multiple Concentric Spirals for the Flow Field of a Proton Exchange Membrane Fuel Cell. *J Power Sources* **2011,** *196* (19), 8019-8030.
5. Kurzweil, P., Lithium Battery Energy Storage: State of the Art Including Lithium-Air and Lithium-Sulfur Systems. Moseley, P. T. G., J.;, Ed. 2015.
6. Alotto, P.; Guarnieri, M.; Moro, F., Redox Flow Batteries for the Storage of Renewable Energy: A Review. *Renew Sust Energ Rev* **2014,** *29*, 325-335.
7. Mousavi G, S. M.; Faraji, F.; Majazi, A.; Al-Haddad, K., A Comprehensive Review of Flywheel Energy Storage System Technology. *Renewable and Sustainable Energy Reviews* **2017,** *67*, 477-490.
8. Xu, K., Nonaqueous Liquid Electrolytes for Lithium-Based Rechargeable Batteries. *Chem Rev* **2004,** *104* (10), 4303-4417.
9. Winter, M.; Brodd, R. J., What are Batteries, Fuel Cells, and Supercapacitors? *Chem Rev* **2004,** *104* (10), 4245-4269.
10. Cairns, E. J.; Albertus, P., Batteries for Electric and Hybrid-Electric Vehicles. *Annual Review of Chemical and Biomolecular Engineering* **2010,** *1* (1), 299-320.
11. Conger, C. How Stuff Works. https://auto.howstuffworks.com/fuel-efficiency/vehicles/lithium-ion-battery-car1.htm.
12. Nitta, N.; Yushin, G., High-Capacity Anode Materials for Lithium- Ion Batteries: Choice of Elements and Structures for Active Particles. *Part Part Syst Char* **2014,** *31* (3), 317-336.
13. Tian, H. X., F.; Wang, X.; He, W.; Han, W.;, High Capacity Group-IV Elements (Si, Ge, Sn) Based Anodes for Lithium-Ion Batteries. *Journal of Materiomics* **2015,** *1*, 153-169.
14. Scrosati, B., Recent Advances in Lithium Ion Battery Materials. *Electrochim Acta* **2000,** *45* (15–16), 2461-2466.

15. Schmitz, R. W.; Murmann, P.; Schmitz, R.; Müller, R.; Krämer, L.; Kasnatscheew, J.; Isken, P.; Niehoff, P.; Nowak, S.; Röschenthaler, G.-V.; Ignatiev, N.; Sartori, P.; Passerini, S.; Kunze, M.; Lex-Balducci, A.; Schreiner, C.; Cekic-Laskovic, I.; Winter, M., Investigations on Novel Electrolytes, Solvents and SEI Additives for Use in Lithium-Ion Batteries: Systematic Electrochemical Characterization and Detailed Analysis by Spectroscopic Methods. *Progress in Solid State Chemistry* **2014,** *42* (4), 65-84.
16. Handbook of Battery Materials, 2nd Edition. *Handbook of Battery Materials, 2nd Edition* **2011**, 1-989.
17. Orendorff, C. J., The Role of Separators in Lithium-Ion Cell Safety.
18. Petibon, R., Study of Electrolyte Additives in Li-Ion Batteries Using Electrochemical Impedance Spectroscopy on Symmetric Cells **2013**.
19. Nitta, N.; Wu, F.; Lee, J. T.; Yushin, G., Li-Ion Battery Materials: Present and Future. *Mater Today* **2015,** *18* (5), 252-264.
20. Aurbach, D.; Talyosef, Y.; Markovsky, B.; Markevich, E.; Zinigrad, E.; Asraf, L.; Gnanaraj, J. S.; Kim, H.-J., Design of Electrolyte Solutions for Li and Li-ion Batteries: A Review. *Electrochim Acta* **2004,** *50* (2–3), 247-254.
21. Li, Q.; Chen, J.; Fan, L.; Kong, X.; Lu, Y., Progress in Electrolytes for Rechargeable Li-Based Batteries and Beyond. *Green Energy & Environment* **2016**.
22. Aurbach, D.; Gamolsky, K.; Markovsky, B.; Gofer, Y.; Schmidt, M.; Heider, U., On the Use of Vinylene Carbonate (VC) as an Additive to Electrolyte Solutions for Li-Ion Batteries. *Electrochim Acta* **2002,** *47* (9), 1423-1439.
23. Etacheri, V.; Marom, R.; Elazari, R.; Salitra, G.; Aurbach, D., Challenges in the Development of Advanced Li-ion Batteries: a Review. *Energ Environ Sci* **2011,** *4* (9), 3243-3262.
24. Larsson, F.; Mellander, B. E., Abuse by External Heating, Overcharge and Short Circuiting of Commercial Lithium-Ion Battery Cells. *J Electrochem Soc* **2014,** *161* (10), A1611-A1617.
25. Chanson, C.; Wiaux, J.-P. *Safety of Lithium-Ion Batteries*; RECHARGE aisbl: Brussels, Belgium, 2013; pp 10-16.
26. Jansen, B., Crash Investigators Trace UPS Plane Fire to Batteries. *USA Today* 24 July, 2013, 2013.
27. Tibken, S.; Cheng, R., Samsung Answers Burning Note 7 Questions, Vows Better Batteries. *CNET* 23 January, 2017, 2017.

28. Matyszczyk, C., Dell Laptop Explodes Again and Again and Again. *CNET* 7 February, 2017, 2017.
29. Finegan, D.; Scheel, M.; Tjaden, B.; Robinson, J.; Di Michiel, M.; Hinds, G.; J L Brett, D.; R Shearing, P., Investigating Lithium-Ion Battery Materials During Overcharge-Induced Thermal Runaway: An Operando and Multi-Scale X-Ray CT Study. *Phys. Chem. Chem. Phys.* **2016,** *18*.
30. Waldmann, T.; Iturrondobeitia, A.; Kasper, M.; Ghanbari, N.; Aguesse, F.; Bekaert, E.; Daniel, L.; Genies, S.; Gordon, I. J.; Loble, M. W.; De Vito, E.; Wohlfahrt-Mehrens, M., Review-Post-Mortem Analysis of Aged Lithium-Ion Batteries: Disassembly Methodology and Physico-Chemical Analysis Techniques. *J Electrochem Soc* **2016,** *163* (10), A2149-A2164.
31. Bandhauer, T. M.; Garimella, S.; Fuller, T. F., A Critical Review of Thermal Issues in Lithium-Ion Batteries. *J Electrochem Soc* **2011,** *158* (3), R1-R25.
32. Schott, T.; Gomez-Camer, J. L.; Bunzli, C.; Novak, P.; Trabesinger, S., The Counterintuitive Impact of Separator-Electrolyte Combinations on the Cycle Life of Graphite-Silicon Composite Electrodes. *J Power Sources* **2017,** *343*, 142-147.
33. Spotnitz, R.; Franklin, J., Abuse Behavior of High-Power, Lithium-Ion Cells. *J Power Sources* **2003,** *113* (1), 81-100.
34. Verma, P.; Maire, P.; Novak, P., A Review of the Features and Analyses of the Solid Electrolyte Interphase in Li-Ion Batteries. *Electrochim Acta* **2010,** *55* (22), 6332-6341.
35. Lisbona, D.; Snee, T., A Review of Hazards Associated with Primary Lithium and Lithium-Ion Batteries. *Process Saf Environ* **2011,** *89* (6), 434-442.
36. Roth, E.; Doughty, D.; Pile, D., Effects of Separator Breakdown on Abuse Response of 18650 Li-Ion Cells. *J Power Sources* **2007,** *174* (2), 579-583.
37. Zhang, S. S., A Review on Electrolyte Additives for Lithium-Ion Batteries. *J Power Sources* **2006,** *162* (2), 1379-1394.
38. Chen, Z. H.; Qin, Y.; Amine, K., Redox Shuttles for Safer Lithium-Ion Batteries. *Electrochim Acta* **2009,** *54* (24), 5605-5613.
39. Feng, X. M.; Ai, X. P.; Yang, H. X., Possible Use of Methylbenzenes as Electrolyte Additives for Improving the Overcharge Tolerances of Li-Ion Batteries. *J Appl Electrochem* **2004,** *34* (12), 1199-1203.

40. Leising, R. A.; Palazzo, M. J.; Takeuchi, E. S.; Takeuchi, K. J., A Study of the Overcharge Reaction of Lithium-Ion Batteries. *J Power Sources* **2001,** *97-8*, 681-683.
41. Roth, E. P., Abuse Response of 18650 Li-Ion Cells with Different Cathodes using EC:EMC/LiPF6 and EC:PC:DMC/LiPF6 Electrolytes. *Ecs Transactions* **2008,** *11* (19), 19-41.
42. Tobishima, S.; Takei, K.; Sakurai, Y.; Yamaki, J., Lithium Ion Cell Safety. *J Power Sources* **2000,** *90* (2), 188-195.
43. Tobishima, S.; Yamaki, J., A Consideration of Lithium Cell Safety. *J Power Sources* **1999,** *81*, 882-886.
44. Golubkov, A.; Fuchs, D.; Wagner, J.; Wiltsche, H.; Stangl, C.; Fauler, G.; Voitic, G.; Thaler, A.; Hacker, V., Thermal-Runaway Experiments on Consumer Li-Ion Batteries with Metal-Oxide and Olivin-Type Cathodes. *Rsc Adv* **2014,** *4*, 3633.
45. Jiang, J. W.; Fortier, H.; Reimers, J. N.; Dahn, J. R., Thermal Stability of 18650 Size Li-Ion Cells Containing LiBOB Electrolyte Salt. *J Electrochem Soc* **2004,** *151* (4), A609-A613.
46. Sun, J.; Li, J. G.; Zhou, T.; Yang, K.; Wei, S. P.; Tang, N.; Dang, N. N.; Li, H.; Qiu, X. P.; Chen, L. Q., Toxicity, a Serious Concern of Thermal Runaway from Commercial Li-Ion Battery. *Nano Energy* **2016,** *27*, 313-319.
47. Larsson, F.; Andersson, P.; Blomqvist, P.; Loren, A.; Mellander, B. E., Characteristics of Lithium-Ion Batteries during Fire Tests. *J Power Sources* **2014,** *271*, 414-420.
48. Hatchard, T. D.; Trussler, S.; Dahn, J. R., Building a "Smart Nail" for Penetration Tests on Li-Ion Cells. *J Power Sources* **2014,** *247*, 821-823.
49. Sahraei, E.; Campbell, J.; Wierzbicki, T., Modeling and Short Circuit Detection of 18650 Li-Ion Cells under Mechanical Abuse Conditions. *J Power Sources* **2012,** *220*, 360-372.
50. Lamb, J.; Orendorff, C. J., Evaluation of Mechanical Abuse Techniques in Lithium Ion Batteries. *J Power Sources* **2014,** *247*, 189-196.
51. Ichimura, M. In *The Safety Characteristics of Lithium-Ion Batteries for Mobile Phones and the Nail Penetration Test*, Intelec 07 - 29th International Telecommunications Energy Conference, 2007; pp 687-692.
52. Chen, J.; Buhrmester, C.; Dahn, J. R., Chemical Overcharge and Overdischarge Protection for Lithium-Ion Batteries. *Electrochem Solid St* **2005,** *8* (1), A59-A62.

53. Kaur, A. P.; Casselman, M. D.; Elliott, C. F.; Parkin, S. R.; Risko, C.; Odom, S. A., Overcharge Protection of Lithium-Ion Batteries above 4 V with a Perfluorinated Phenothiazine Derivative. *J Mater Chem A* **2016,** *4* (15), 5410-5414.
54. Administration, U. S. E. I. *Annual Energy Outlook 2017 with Projections to 2050*; 2017.
55. Goodenough, J. B.; Park, K. S., The Li-Ion Rechargeable Battery: A Perspective. *J Am Chem Soc* **2013,** *135* (4), 1167-1176.
56. Daniel, C., Materials and Processing for Lithium-Ion Batteries. *Jom-Us* **2008,** *60* (9), 43-48.
57. Julien, M., Alain; Zaghib, Karim; Groult, Henri;, Comparative Issues of Cathode Materials for Li-Ion Batteries. *Inorganics* **2014,** *2*, 132-154.
58. Gomez-Camer, J. L.; Bunzli, C.; Hantel, M. M.; Poux, T.; Novak, P., On the Correlation between Electrode Expansion and Cycling Stability of Graphite/Si Electrodes for Li-Ion Batteries. *Carbon* **2016,** *105*, 42-51.
59. Birkenmaier, C.; Bitzer, B.; Harzheim, M.; Hintennach, A.; Schleid, T., Lithium Plating on Graphite Negative Electrodes: Innovative Qualitative and Quantitative Investigation Methods. *J Electrochem Soc* **2015,** *162* (14), A2646-A2650.
60. Balogun, M. S.; Luo, Y.; Qiu, W. T.; Liu, P.; Tong, Y. X., A Review of Carbon Materials and their Composites with Alloy Metals for Sodium Ion Battery Anodes. *Carbon* **2016,** *98*, 162-178.
61. Goldshtein, K.; Freedman, K.; Schneier, D.; Burstein, L.; Ezersky, V.; Peled, E.; Golodnitsky, D., Advanced Multiphase Silicon-Based Anodes for High-Energy-Density Li-Ion Batteries. **2015**.
62. Gao, H.; Xiao, L.; Plümel, I.; Xu, G.-L.; Ren, Y.; Zuo, X.; Liu, Y.; Schulz, C.; Wiggers, H.; Amine, K.; Chen, Z., Parasitic Reactions in Nanosized Silicon Anodes for Lithium-Ion Batteries. **2017**.
63. Wu, X. L.; Guo, Y. G.; Wan, L. J., Rational Design of Anode Materials Based on GroupIVA Elements (Si, Ge, and Sn) for Lithium-Ion Batteries. *Chem-Asian J* **2013,** *8* (9), 1948-1958.
64. Barai, P.; Huang, B.; Dillon, S. J.; Mukherjee, P. P., Mechano-Electrochemical Interaction Gives Rise to Strain Relaxation in Sn Electrodes. *J Electrochem Soc* **2016,** *163* (14), A3022-A3035.
65. Barai, P.; Mukherjee, P. P., Mechano-Electrochemical Stochastics in High-Capacity Electrodes for Energy Storage. *J Electrochem Soc* **2016,** *163* (6), A1120-A1137.

66. Geny, J. F.; Malterre, D.; Vergnat, M.; Piecuch, M.; Marchal, G., Forming Ability and Stability of Amorphous MxSn1-x alloys (M=V, Cr, Mn, Fe, Co, Ni, Cu). *J Non-Cryst Solids* **1984,** *61 & 62*, 1243-1248.
67. Todd, A. D. W.; Mar, R. E.; Dahn, J. R., Combinatorial Study of Tin-Transition Metal Alloys as Negative Electrodes for Lithium-Ion Batteries. *J Electrochem Soc* **2006,** *153* (10), A1998-A2005.
68. Han, Q. G.; Yi, Z.; Cheng, Y.; Wu, Y. M.; Wang, L. M., Simple Preparation of Cu6Sn5/Sn Composites as Anode Materials for Lithium-Ion Batteries. *Rsc Adv* **2016,** *6* (19), 15279-15285.
69. Kepler, K. D.; Vaughey, J. T.; Thackeray, M. M., Copper-Tin Anodes for Rechargeable Lithium Batteries: An Example of the Matrix Effect in an Intermetallic System. *J Power Sources* **1999,** *81*, 383-387.
70. Furtauer, S.; Flandorfer, H., The Cu-Li-Sn Phase Diagram: Isopleths, Liquidus Projection and Reaction Scheme. *Plos One* **2016,** *11* (10), e0165058.
71. Shin, H. C.; Liu, M., Three-Dimensional Porous Copper-Tin Alloy Electrodes for Rechargeable Lithium Batteries. *Adv Funct Mater* **2005,** *15* (4), 582-586.
72. Trahey, L.; Vaughey, J. T.; Kung, H. H.; Thackeray, M. M., High-Capacity, Microporous Cu6Sn5-Sn Anodes for Li-Ion Batteries. *J Electrochem Soc* **2009,** *156* (5), A385-A389.
73. Algul, H.; Uysal, M.; Tokur, M.; Ozcan, S.; Cetinkaya, T.; Akbulut, H.; Alp, A., Three-Dimensional Sn Rich Cu6Sn5 Negative Electrodes for Li Ion Batteries. *Int J Hydrogen Energ* **2016,** *41* (23), 9819-9827.
74. Stein, M.; Chen, C. F.; Mullings, M.; Jaime, D.; Zaleski, A.; Mukherjee, P. P.; Rhodes, C. P., Probing the Effect of High Energy Ball Milling on the Structure and Properties of LiNi1/3Mn1/3Co1/3O2 Cathodes for Li-Ion Batteries. *Journal of Electrochemical Energy Conversion and Storage* **2016,** *13* (3).
75. Mistry, A.; Juarez-Robles, D.; Stein, I. V. M.; Smith, K.; Mukherjee, P. P., Analysis of Long-Range Interaction in Lithium-Ion Battery Electrodes. *Journal of Electrochemical Energy Conversion and Storage* **2016,** *13* (3), 031006-031006.
76. Stein, M.; Mistry, A.; Mukherjee, P. P., Mechanistic Understanding of the Role of Evaporation in Electrode Processing. *J Electrochem Soc* **2017,** *164* (7), A1616-A1627.

77. Ausderau, L. J.; Malabet, H. J. G.; Buckley, J. R.; De Andrade, V.; Liu, Y. J.; Nelson, G. J., Elemental and Chemical Mapping of High Capacity Intermetallic Li-ion Anodes with Transmission X-ray Microscopy. *Jom-Us* **2017,** *69* (9), 1478-1483.
78. Stein, M.; Chen, C. F.; Robles, D. J.; Rhodes, C.; Mukherjee, P. P., Non-Aqueous Electrode Processing and Construction of Lithium-Ion Coin Cells. *JoVE* **2016,** (108), 1-10.
79. Gursoy, D.; De Carlo, F.; Xiao, X. H.; Jacobsen, C., TomoPy: a Framework for the Analysis of Synchrotron Tomographic Data. *J Synchrotron Radiat* **2014,** *21*, 1188-1193.
80. Munch, B.; Trtik, P.; Marone, F.; Stampanoni, M., Stripe and Ring Artifact Removal with Combined Wavelet - Fourier Filtering. *Opt Express* **2009,** *17* (10), 8567-8591.
81. Paganin, D.; Mayo, S. C.; Gureyev, T. E.; Miller, P. R.; Wilkins, S. W., Simultaneous Phase and Amplitude Extraction from a Single Defocused Image of a Homogeneous Object. *Journal of Microscopy-Oxford* **2002,** *206*, 33-40.
82. Schindelin, J.; Arganda-Carreras, I.; Frise, E.; Kaynig, V.; Longair, M.; Pietzsch, T.; Preibisch, S.; Rueden, C.; Saalfeld, S.; Schmid, B.; Tinevez, J. Y.; White, D. J.; Hartenstein, V.; Eliceiri, K.; Tomancak, P.; Cardona, A., Fiji: an Open-Source Platform for Biological-Image Analysis. *Nature Methods* **2012,** *9* (7), 676-682.
83. Munch, B.; Gasser, P.; Holzer, L.; Flatt, R., FIB-Nanotomography of Particulate Systems - Part II: Particle Recognition and Effect of Boundary Truncation. *J Am Ceram Soc* **2006,** *89* (8), 2586-2595.
84. Munch, B.; Holzer, L., Contradicting Geometrical Concepts in Pore Size Analysis Attained with Electron Microscopy and Mercury Intrusion. *J Am Ceram Soc* **2008,** *91* (12), 4059-4067.
85. Holzer, L.; Muench, B.; Wegmann, M.; Gasser, P.; Flatt, R. J., FIB-Nanotomography of Particulate Systems - Part I: Particle Shape and Topology of Interfaces. *J Am Ceram Soc* **2006,** *89* (8), 2577-2585.
86. Liu, Z.; Wood, D. L.; Mukherjee, P. P., Evaporation Induced Nanoparticle – Binder Interaction in Electrode Film Formation. *Phys Chem Chem Phys* **2017,** *19* (15), 10051-10061.
87. Du, Z.; Rollag, K. M.; Li, J.; An, S. J.; Wood, M.; Sheng, Y.; Mukherjee, P. P.; Daniel, C.; Wood, D. L., III, Enabling Aqueous Processing for Crack-Free Thick Electrodes. *J Power Sources* **2017,** *354*, 200-206.

88. Gyenes, B.; Stevens, D. A.; Chevrier, V. L.; Dahn, J. R., Understanding Anomalous Behavior in Coulombic Efficiency Measurements on Li-Ion Batteries. *J Electrochem Soc* **2015,** *162* (3), A278-A283.
89. Thomas, R.; Rao, K. Y.; Rao, G. M., Enhanced Electrochemical Performance of Graphene Nanosheet Thin Film Anode Decorated with Tin Nanoparticles. *Mater Express* **2014,** *4* (1), 65-71.
90. Wang, J.; Karen Chen-Wiegart, Y.-c.; Eng, C.; Shen, Q.; Wang, J., Visualization of Anisotropic-Isotropic Phase Transformation Dynamics in Battery Electrode Particles. *Nat Commun* **2016,** *7*, 12372.
91. Wang, J.; Chen-Wiegart, Y.-c. K.; Wang, J., In Operando Tracking Phase Transformation Evolution of Lithium Iron Phosphate with Hard X-ray Microscopy. *Nat Commun* **2014,** *5*, 4570.
92. Wang, J. J.; Chen-Wiegart, Y. C. K.; Wang, J., In Situ Three-Dimensional Synchrotron X-Ray Nanotomography of the (De) lithiation Processes in Tin Anodes. *Angew Chem Int Edit* **2014,** *53* (17), 4460-4464.
93. Opitz, A.; Badami, P.; Shen, L.; Vignarooban, K.; Kannan, A. M., Can Li-Ion Batteries be the Panacea for Automotive Applications? *Renew Sust Energ Rev* **2017,** *68*, 685-692.
94. Wood, D. L.; Li, J. L.; Daniel, C., Prospects for Reducing the Processing Cost of Lithium Ion Batteries. *J Power Sources* **2015,** *275*, 234-242.
95. de Sa, C.; Benboudjema, F.; Thiery, M.; Sicard, J., Analysis of Microcracking Induced by Differential Drying Shrinkage. *Cement Concrete Comp* **2008,** *30* (10), 947-956.
96. Lura, P.; Pease, B.; Mazzotta, G. B.; Rajabipour, F.; Weiss, J., Influence of Shrinkage-Reducing Admixtures on Development of Plastic Shrinkage Cracks. *Aci Materials Journal* **2007,** *104* (2), 187-194.
97. Kitsunezaki, S., Fracture Patterns Induced by Desiccation in a Thin Layer. *Phys Rev E* **1999,** *60* (6), 6449-6464.
98. Hallett, P. D.; Newson, T. A., Describing Soil Crack Formation using Elastic-Plastic Fracture Mechanics. *European Journal of Soil Science* **2005,** *56* (1), 31-38.
99. Chiu, R. C.; Garino, T. J.; Cima, M. J., Drying of Granular Ceramic Films. I. Effect of Processing Variables on Cracking Behavior. *J Am Ceram Soc* **1993,** *76* (9), 2257-2264.
100. Chiu, R. C.; Cima, M. J., Drying of Granular Ceramic Films. II. Drying Stress and Saturation Uniformity. *J Am Ceram Soc* **1993,** *76* (11), 2769-2777.

101. Routh, A. F., Drying of Thin Colloidal Films. *Rep Prog Phys* **2013,** *76* (4), 046603.
102. Sengupta, R.; Tirumkudulu, M. S., Dynamics of Cracking in Drying Colloidal Sheets. *Soft Matter* **2016,** *12* (13), 3149-3155.
103. Singh, K. B.; Deoghare, G.; Tirumkudulu, M. S., Cracking in Soft− Hard Latex Blends: Theory and Experiments. *Langmuir* **2008,** *25* (2), 751-760.
104. Tirumkudulu, M. S.; Russel, W. B., Cracking in Drying Latex Films *Langmuir* **2005,** *21* (11), 4938-4948.
105. Tirumkudulu, M. S.; Russel, W. B., Role of Capillary Stresses in Film Formation. *Langmuir* **2004,** *20* (7), 2947-2961.
106. Routh, A. F.; Russel, W. B., Horizontal Drying Fronts During Solvent Evaporation from Latex Films. *Aiche J* **1998,** *44* (9), 2088-2098.
107. Routh, A. F.; Russel, W. B., A Process Model for Latex Film Formation: Limiting Regimes for Individual Driving Forces. *Langmuir* **1999,** *15* (22), 7762-7773.
108. Singh, K. B.; Tirumkudulu, M. S., Cracking in Drying Colloidal Films. *Phys Rev Lett* **2007,** *98* (21), 4.
109. Lee, W. P.; Routh, A. F., Why do Drying Films Crack? *Langmuir* **2004,** *20* (23), 9885-9888.
110. Lee, J. H.; Paik, U.; Hackley, V. A.; Choi, Y. M., Effect of Carboxymethyl Cellulose on Aqueous Processing of Natural Graphite Negative Electrodes and their Electrochemical Performance for Lithium Batteries. *J Electrochem Soc* **2005,** *152* (9), A1763-A1769.
111. Lee, J.-H.; Lee, S.; Paik, U.; Choi, Y.-M., Aqueous Processing of Natural Graphite Particulates for Lithium-Ion Battery Anodes and their Electrochemical Performance. *J Power Sources* **2005,** *147* (1-2), 249-255.
112. Moretti, A.; Kim, G.-T.; Bresser, D.; Renger, K.; Paillard, E.; Marassi, R.; Winter, M.; Passerini, S., Investigation of Different Binding Agents for Nanocrystalline Anatase TiO2 Anodes and its Application in a Novel, Green Lithium-Ion Battery. *J Power Sources* **2013,** *221*, 419-426.
113. Wu, Q.; Ha, S.; Prakash, J.; Dees, D. W.; Lu, W., Investigations on High Energy Lithium-Ion Batteries with Aqueous Binder. *Electrochim Acta* **2013,** *114*, 1-6.
114. Li, C.-C.; Wang, Y.-W., Importance of Binder Compositions to the Dispersion and Electrochemical Properties of Water-based LiCoO2 Cathodes. *J Power Sources* **2013,** *227*, 204-210.

115. Targray Technology International Inc., T., Modified Styrene-Butadiene Copolymer Product Data Sheet. Targray: 2012.
116. Wang, Z.; Winslow, R.; Madan, D.; Wright, P. K.; Evans, J. W.; Keif, M.; Rong, X., Development of MnO2 Cathode Inks for Flexographically Printed Rechargeable Zinc-based Battery. *J Power Sources* **2014,** *268*, 246-254.
117. Lacey, M. J.; Yalamanchili, A.; Maibach, J.; Tengstedt, C.; Edström, K.; Brandell, D., The Li–S Battery: an Investigation of Redox Shuttle and Self-Discharge Behaviour with LiNO3-Containing Electrolytes. *Rsc Adv* **2016,** *6* (5), 3632-3641.
118. Khan, Y.; Garg, M.; Gui, Q.; Schadt, M.; Gaikwad, A.; Han, D.; Yamamoto, N. A. D.; Hart, P.; Welte, R.; Wilson, W.; Czarnecki, S.; Poliks, M.; Jin, Z.; Ghose, K.; Egitto, F.; Turner, J.; Arias, A. C., Flexible Hybrid Electronics: Direct Interfacing of Soft and Hard Electronics for Wearable Health Monitoring. *Adv Funct Mater* **2016,** *26* (47), 8764-8775.
119. Ostfeld, A. E.; Gaikwad, A. M.; Khan, Y.; Arias, A. C., High-Performance Flexible Energy Storage and Harvesting System for Wearable Electronics. *Sci Rep-Uk* **2016,** *6*, 10.
120. Auvray, R.; Rosin-Paumier, S.; Abdallah, A.; Masrouri, F., Quantification of Soft Soil Cracking During Suction Cycles by Image Processing. *European Journal of Environmental and Civil Engineering* **2013,** *18* (1), 11-32.
121. Atique, A.; Sanchez, M., Analysis of Cracking Behavior of Drying Soil. In *Environmental Science and Technology, Pt 1*, Dan, Y., Ed. 2011; Vol. 6, pp VI66-VI70.
122. Miller, C. J.; Mi, H.; Yesiller, N., Experimental Analysis of Desiccation Crack Propagation in Clay Liners. *Journal of the American Water Resources Association* **1998,** *34* (3), 677-686.
123. Park, H.; Lee, D.; Song, T., Synthesis of Carboxymethyl Cellulose Lithium by Weak Acid Treatment and Its Application in High Energy-Density Graphite Anode for Li-Ion Batteries. *Ind Eng Chem Res* **2018,** *57* (27), 8895-8901.
124. Cetinel, F. A.; Bauer, W., Processing of Water-based LiNi1/3Mn1/3Co1/3O2 Pastes for Manufacturing Lithium Ion Battery Cathodes. *B Mater Sci* **2014,** *37* (7), 1685-1690.
125. Chong, J.; Xun, S.; Zheng, H.; Song, X.; Liu, G.; Ridgway, P.; Wang, J. Q.; Battaglia, V. S., A Comparative Study of Polyacrylic Acid and Poly(vinylidene difluoride) Binders for Spherical Natural Graphite/LiFePO4 Electrodes and Cells. *J Power Sources* **2011,** *196* (18), 7707-7714.

126. Li, J. L.; Rulison, C.; Kiggans, J.; Daniel, C.; Wood, D. L., Superior Performance of LiFePO4 Aqueous Dispersions via Corona Treatment and Surface Energy Optimization. *J Electrochem Soc* **2012,** *159* (8), A1152-A1157.

127. Man, W.; Russel, W. B., Direct Measurements of Critical Stresses and Cracking in Thin Films of Colloid Dispersions. *Phys Rev Lett* **2008,** *100* (19), 1-4.

128. Zheng, H.; Li, J.; Song, X.; Liu, G.; Battaglia, V. S., A Comprehensive Understanding of Electrode Thickness Effects on the Electrochemical Performances of Li-ion Battery Cathodes. *Electrochim Acta* **2012,** *71*, 258–265.

129. Du, Z.; Wood, D.; Daniel, C.; Kalnaus, S.; Li, J., Understanding Limiting Factors in Thick Electrode Performance as Applied to High Energy Density Li-Ion Batteries. *J Appl Electrochem* **2017,** *47*, 405-415.

130. Chen, C. F.; Barai, P.; Mukherjee, P. P., Diffusion Induced Damage and Impedance Response in Lithium-Ion Battery Electrodes. *J Electrochem Soc* **2014,** *161* (14), A2138-A2152.

131. Barai, P.; Smith, K.; Chen, C. F.; Kim, G. H.; Mukherjee, P. P., Reduced Order Modeling of Mechanical Degradation Induced Performance Decay in Lithium-Ion Battery Porous Electrodes. *J Electrochem Soc* **2015,** *162* (9), A1751-A1771.

132. McGrogan, F. P.; Bishop, S. R.; Chiang, Y. M.; Van Vliet, K. J., Connecting Particle Fracture with Electrochemical Impedance in LiXMn2O4. *J Electrochem Soc* **2017,** *164* (14), A3709-A3717.

133. Badwal, S. P. S.; Giddey, S. S.; Munnings, C.; Bhatt, A. I.; Hollenkamp, A. F., Emerging Electrochemical Energy Conversion and Storage Technologies. *Frontiers in Chemistry* **2014,** *2*.

134. Scrosati, B.; Garche, J., Lithium Batteries: Status, Prospects and Future. *J Power Sources* **2010,** *195*, 2419-2430.

135. Gale, J., Hazardous Materials; Transportation of Lithium Batteries. Administration, P. a. H. M. S., Ed. 2007; Vol. 72, pp 44929-44950.

136. FAA, Lithium Batteries & Lithium Battery-Powered Devices. Safety, F. O. o. S. a. H. M., Ed. 2018; p 57.

137. Finegan, D. P. S., Mario; Robinson, James B.; Tjadenm, Bernhard; Di Michiel, Marco; Hinds, Gareth; Brett, Dan J. L.; Shearing, Paul R.;, Investigating Lithium-Ion Battery Materials During Overcharge-Induced Thermal Runaway: An Operando and Multi-Scale X-ray CT Study. *Phys Chem Chem Phys* **2016**.
138. Balagopal, B.; Huang, C. S.; Chow, M.-Y., Effect of Calendar Aging on Li Ion Battery Degradation and SOH. In *Iecon 2017 - 43rd Annual Conference of the Ieee Industrial Electronics Society*, 2017; pp 7647-7652.
139. Omar, N.; Firouz, Y.; Gualous, H.; Salminen, J.; Kallio, T.; Timmermans, J. M.; Coosemans, T.; Van den Bossche, P.; Van Mierlo, J., Aging and Degradation of Lithium-Ion Batteries. In *Rechargeable Lithium Batteries: from Fundamentals to Applications*, Franco, A. A., Ed. 2015; pp 263-279.
140. Iturrondobeitia, A.; Aguesse, F.; Genies, S.; Waldmann, T.; Kasper, M.; Ghanbari, N.; Wohlfahrt-Mehrens, M.; Bekaert, E., Post-Mortem Analysis of Calendar-Aged 16 Ah NMC/Graphite Pouch Cells for EV Application. *J Phys Chem C* **2017,** *121* (40), 21865-21876.
141. Keil, P. S., Simon F.; Wilhelm, J.; Travi, Julian; Hauser, Andreas; Karl, Ralph C.; Jossen, Andreas;, Calendar Aging of Lithium-Ion Batteries, I. Impact of the Graphite Anode on Capacity Fade. *J Electrochem Soc* **2016,** *163* (9), A1872-A1880.
142. Waldmann, T.; Hogg, B.-I.; Wohlfahrt-Mehrens, M., Li Plating as Unwanted Side Reaction in Commercial Li-Ion Cells - A Review. *J Power Sources* **2018,** *384*, 107-124.
143. Broussely, M., Aging Mechanisms and Calendar-Life Predictions in Lithium-Ion Batteries. 2007; pp 393-432.
144. An, S. J.; Li, J. L.; Daniel, C.; Mohanty, D.; Nagpure, S.; Wood, D. L., The State of Understanding of the Lithium-Ion-Battery Graphite Solid Electrolyte Interphase (SEI) and its Relationship to Formation Cycling. *Carbon* **2016,** *105*, 52-76.
145. Van Havenbergh, K.; Turner, S.; Driesen, K.; Bridel, J. S.; Van Tendeloo, G., Solid-Electrolyte Interphase Evolution of Carbon-Coated Silicon Nanoparticles for Lithium-Ion Batteries Monitored by Transmission Electron Microscopy and Impedance Spectroscopy. *Energy Technol-Ger* **2015,** *3* (7), 699-708.
146. Eddahech, A.; Briat, O.; Vinassa, J. M., Performance Comparison of Four Lithium-Ion Battery Technologies under Calendar Aging. *Energy* **2015,** *84*, 542-550.

147. Grolleau, S.; Delaille, A.; Gualous, H.; Gyan, P.; Revel, R.; Bernard, J.; Redondo-Iglesias, E.; Peter, J.; Network, S., Calendar Aging of Commercial Graphite/LiFePO4 Cell - Predicting Capacity Fade under Time Dependent Storage Conditions. *J Power Sources* **2014,** *255*, 450-458.

148. Ramadass, P.; Haran, B.; White, R.; Popov, B. N., Capacity Fade of Sony 18650 Cells Cycled at Elevated Temperatures Part I. Cycling Performance. *J Power Sources* **2002,** *112* (2), 606-613.

149. Jalkanen, K.; Karppinen, J.; Skogstrom, L.; Laurila, T.; Nisula, M.; Vuorilehto, K., Cycle Aging of Commercial NMC/Graphite Pouch Cells at Different Temperatures. *Appl Energ* **2015,** *154*, 160-172.

150. Waldmann, T.; Wilka, M.; Kasper, M.; Fleischhammer, M.; Wohlfahrt-Mehrens, M., Temperature Dependent Ageing Mechanisms in Lithium-Ion Batteries - A Post-Mortem Study. *J Power Sources* **2014,** *262*, 129-135.

151. Zhang, S., *The Effect of the Charging Protocol on the Cycle Life of a Li-Ion Battery*. 2006; Vol. 161, p 1385-1391.

152. Somerville, L.; Bareno, J.; Trask, S.; Jennings, P.; McGordon, A.; Lyness, C.; Bloom, I., The Effect of Charging Rate on the Graphite Electrode of Commercial Lithium-Ion Cells: A Post-Mortem Study. *J Power Sources* **2016,** *335*, 189-196.

153. Fear, C.; Juarez-Robles, D.; Jeevarajan, J. A.; Mukherjee, P. P., Elucidating Copper Dissolution Phenomenon in Li-Ion Cells under Overdischarge Extremes. *J Electrochem Soc* **2018,** *165* (9), A1639-A1647.

154. Hossain, S.; Kim, Y. K.; Saleh, Y.; Loutfy, R., Overcharge Studies of Carbon Fiber Composite-Based Lithium-Ion Cells. *J Power Sources* **2006,** *161* (1), 640-647.

155. Chen, P.-T.; Yang, F.-H.; Cao, Z.-T.; Jhang, J.-M.; Gao, H.-M.; Yang, M.-H.; David Huang, K., Reviving Aged Lithium- Ion Batteries and Prolonging their Cycle Life by Sinusoidal Waveform Charging Strategy. *Batteries & Supercaps* **2019,** (2019), 1-6.

156. Ramadass, P.; Haran, B.; White, R.; Popov, B. N., Capacity Fade of Sony 18650 Cells Cycled at Elevated Temperatures Part II. Capacity Fade Analysis. *J Power Sources* **2002,** *112* (2), 614-620.

157. Keil, P.; Jossen, A., Charging Protocols for Lithium-Ion Batteries and Their Impact on Cycle Life-An Experimental Study with Different 18650 High-Power Cells. *J Energy Storage* **2016,** *6*, 125-141.

158. He, H.; Liu, Y. D.; Liu, Q.; Li, Z. F.; Xu, F.; Dun, C.; Ren, Y.; Wang, M. X.; Xie, J., Failure Investigation of LiFePO4 Cells in Over-Discharge Conditions. *J Electrochem Soc* **2013,** *160* (6), A793-A804.

159. Li, J.-F.; Lin, C.-H.; Chen, K.-C., *Cycle Life Prediction of Aged Lithium-Ion Batteries from the Fading Trajectory of a Four-Parameter Model*. 2018; Vol. 165, p A3634-A3641.

160. Yang, Q.; Xu, J.; Cao, B.; Xu, D.; Li, X.; Wang, B., State-of-Health Estimation of Lithium-Ion Battery Based on Interval Capacity. In *8th International Conference on Applied Energy*, Yan, J.; Sun, F.; Chou, S. K.; Desideri, U.; Li, H.; Campana, P.; Xiong, R., Eds. 2017; Vol. 105, pp 2342-2347.

161. Koo, B.; Yi, J.; Lee, D.; Shin, C. B.; Park, S., Modeling the Effect of Fast Charge Scenario on the Cycle Life of a Lithium-Ion Battery. *J Electrochem Soc* **2018,** *165*, A3674-A3683.

162. Maheshwari, A.; Heck, M.; Santarelli, M., Cycle Aging Studies of Lithium Nickel Manganese Cobalt Oxide-Based Batteries using Electrochemical Impedance Spectroscopy. *Electrochim Acta* **2018,** *273*, 335-348.

163. Pfrang, A.; Kersys, A.; Kriston, A.; Sauer, D. U.; Rahe, C.; Kaebitz, S.; Figgemeier, E., Long-Term Cycling Induced Jelly Roll Deformation in Commercial 18650 Cells. *J Power Sources* **2018,** *392*, 168-175.

164. Paul, N.; Keil, J.; Kindermann, F. M.; Schebesta, S.; Dolotko, O.; Muehlbauer, M. J.; Kraft, L.; Erhard, S. V.; Jossen, A.; Gilles, R., Aging in 18650-Type Li-Ion Cells Examined with Neutron Diffraction, Electrochemical Analysis and Physico-Chemical Modeling. *J Energy Storage* **2018,** *17*, 383-394.

165. Hagen, M.; Hanselmann, D.; Ahlbrecht, K.; Maca, R.; Gerber, D.; Tubke, J., Lithium-Sulfur Cells: The Gap between the State-of-the-Art and the Requirements for High Energy Battery Cells. *Adv Energy Mater* **2015,** *5* (16).

166. America, P. C. o. N. Lithium Ion Batteries (Li-Ion): Cylindrical Series. https://na.industrial.panasonic.com/products/batteries/rechargeable-batteries/lithium-ion/series/cylindrical-series/CS474?reset=1 (accessed 04/01/2016).

167. Aurbach, D.; Zinigrad, E.; Cohen, Y.; Teller, H., A Short Review of Failure Mechanisms of Lithium Metal and Lithiated Graphite Anodes in Liquid Electrolyte Solutions. *Solid State Ionics* **2002,** *148* (3-4), 405-416.

168. Zhang, S.; Xu, K.; Jow, R., Understanding Formation of Solid Electrolyte Interface Film on LiMn2O4 Electrode. *J Electrochem Soc* **2002,** *149*, A1521-A1526.

169. Bloom, I.; Walker, L. K.; Basco, J. K.; Abraham, D. P.; Christophersen, J. P.; Ho, C. D., Differential Voltage Analyses of High-Power Lithium-Ion Cells. 4. Cells Containing NMC. *J Power Sources* **2010,** *195* (3), 877-882.

170. Dahn, H. M.; Smith, A. J.; Burns, J. C.; Stevens, D. A.; Dahn, J. R., User-Friendly Differential Voltage Analysis Freeware for the Analysis of Degradation Mechanisms in Li-Ion Batteries. *J Electrochem Soc* **2012,** *159* (9), A1405-A1409.

171. Gallagher, K. G.; Dees, D. W.; Jansen, A. N.; Abraham, D. P.; Kang, S. H., A Volume Averaged Approach to the Numerical Modeling of Phase-Transition Intercalation Electrodes Presented for LixC6. *J Electrochem Soc* **2012,** *159* (12), A2029-A2037.

172. Mandli, A.; Kaushik, A.; Patil, R.; Naha, A.; Hariharan, K.; M. Kolake, S.; Han, S.; Choi, W., Analysis of the Effect of Resistance Increase on the Capacity Fade of Lithium Ion Batteries. *Int J Energ Res* **2019**, 1-13.

173. Mistry, A. N.; Smith, K.; Mukherjee, P. P., Electrochemistry Coupled Mesoscale Complexations in Electrodes Lead to Thermo-Electrochemical Extremes. *Acs Appl Mater Inter* **2018,** *10* (34), 28644-28655.

174. Mistry, A.; Palle, H. R.; Mukherjee, P., In Operando Thermal Signature Probe for Lithium-Ion Batteries. *Appl Phys Lett* **2019,** *114*, 023901.

175. Verma, A.; Smith, K.; Santhanagopalan, S.; Abraham, D.; Pierre Yao, K.; Mukherjee, P., *Galvanostatic Intermittent Titration and Performance Based Analysis of LiNi 0.5 Co 0.2 Mn 0.3 O 2 Cathode*. 2017; Vol. 164, p A3380-A3392.

176. Maire, P.; Evans, A.; Kaiser, H.; Scheifele, W.; Novak, P., Colorimetric Determination of Lithium Content in Electrodes of Lithium-Ion Batteries. *J Electrochem Soc* **2008,** *155* (11), A862-A865.

177. Park, K.; Cho, J. H.; Shanmuganathan, K.; Song, J.; Peng, J.; Gobet, M.; Greenbaum, S.; Ellison, C. J.; Goodenough, J. B., New Battery Strategies with a Polymer/Al2O3 Separator. *J Power Sources* **2014,** *263*, 52-58.

178. Wang, F.-M.; Yu, M.-H.; Hsiao, Y.-J.; Tsai, Y.; Hwang, B. J.; Wang, Y.-Y.; Wan, C.-C., Aging Effects to Solid Electrolyte Interface (SEI) Membrane Formation and the Performance Analysis of Lithium Ion Batteries. *Int J Electrochem Sc* **2011,** *6*, 1014-1026.

179. Wu, A.; Tabaddor, M.; Wang, C.; Jeevarajan, J., Simulation of Internal Short Circuits in Lithium Ion Cells. *2013 Ieee Transportation Electrification Conference and Expo (Itec)* **2013**.

180. Guo, R.; Lu, L. G.; Ouyang, M. G.; Feng, X. N., Mechanism of the Entire Overdischarge Process and Overdischarge-Induced Internal Short Circuit in Lithium-Ion Batteries. *Sci Rep-Uk* **2016,** *6*.

181. Abada, S.; Marlair, G.; Lecocq, A.; Petit, M.; Sauvant-Moynot, V.; Huet, F., Safety Focused Modeling of Lithium-Ion Batteries: A Review. *J Power Sources* **2016,** *306*, 178-192.

182. Administration, P. a. H. M. S., Hazardous Materials; Transportation of Lithium Ion Batteries. August 9, 2007 ed.; Transportation, D. o., Ed. 2007; Vol. 72.

183. Jeevarajan, J. A.; Hughes, M. B.; Peck, M. S.; Tipton, B. C.; Bragg, B. J.; Steward, G.; Piao, T.; Waldrop, S., Performance Characterization and Safety Testing of Lithium-Ion Cells and Battery for Space Flight Applications. *Lithium Batteries, Proceedings* **2000,** *99* (25), 694-705.

184. Kalnaus, S.; Wang, Y. L.; Turner, J. A., Mechanical Behavior and Failure Mechanisms of Li-Ion Battery Separators. *J Power Sources* **2017,** *348*, 255-263.

185. Linden, D., Factors Affecting Battery Performance. McGraw-Hill: 2002.

186. Lee, H.; Chang, S.-K.; Goh, E.-Y.; Jeong, J.-Y.; Lee, J. H.; Kim, H.-J.; Cho, J.-J.; Hong, S.-T., Li2NiO2 as a Novel Cathode Additive for Overdischarge Protection of Li-Ion Batteries. *Chem Mater* **2008,** *20* (1), 5-7.

187. Wu, M.-S.; Chiang, P.-C. J.; Lin, J.-C.; Jan, Y.-S., Correlation Between Electrochemical Characteristics and Thermal Stability of Advanced Lithium-Ion Batteries in Abuse Tests—Short-Circuit Tests. *Electrochim Acta* **2004,** *49* (11), 1803-1812.

188. A. Leising, R.; J. Palazzo, M.; Takeuchi, E.; J. Takeuchi, K., Abuse Testing of Lithium-Ion Batteries: Characterization of the Overcharge Reaction of LiCoO2/Graphite Cells. *J Electrochem Soc* **2001,** *148* (8), A838-A844.

189. Hagen, M.; Hanselmann, D.; Ahlbrecht, K.; Maça, R.; Gerber, D.; Tübke, J., Lithium–Sulfur Cells: The Gap between the State- of- the- Art and the Requirements for High Energy Battery Cells. *Adv Energy Mater* **2015,** *5* (16).

190. Balakrishnan, P. G.; Ramesh, R.; Kumar, T. P., Safety Mechanisms in Lithium-Ion Batteries. *J Power Sources* **2006,** *155* (2), 401-414.

191. Electropaedia Battery Protection Methods.

192. Venugopal, G., Characterization of Thermal Cut-Off Mechanisms in Prismatic Lithium-Ion Batteries. *J Power Sources* **2001,** *101* (2), 231-237.

193. Hossain, S.; Kim, Y.-K.; Saleh, Y.; Loutfy, R., Overcharge Studies of Carbon Fiber Composite-Based Lithium-Ion Cells. *J Power Sources* **2006,** *161* (1), 640-647.

194. Cui, W.; He, Y. B.; Tang, Z. Y.; Yang, Q. H.; Xu, Q.; Su, F. Y.; Ma, L., Improvement of Overcharge Performance using Li4Ti5O12 as Negative Electrode for LiFePO4 Power Battery. *J Solid State Electr* **2012,** *16* (1), 265-271.

195. Lu, L. G.; Han, X. B.; Li, J. Q.; Hua, J. F.; Ouyang, M. G., A Review on the Key Issues for Lithium-Ion Battery Management in Electric Vehicles. *J Power Sources* **2013,** *226*, 272-288.

196. Mendoza-Hernandez, O. S.; Ishikawa, H.; Nishikawa, Y.; Maruyama, Y.; Umeda, M., Cathode Material Comparison of Thermal Runaway Behavior of Li-Ion Cells at Different State of Charges including Overcharge. *J Power Sources* **2015,** *280*, 499-504.

197. Xu, F.; He, H.; Liu, Y. D.; Dun, C.; Ren, Y.; Liu, Q.; Wang, M. X.; Xie, J., Failure Investigation of LiFePO4 Cells under Overcharge Conditions. *J Electrochem Soc* **2012,** *159* (5), A678-A687.

198. Finegan, D. P.; Scheel, M.; Robinson, J. B.; Tjaden, B.; Di Michiel, M.; Hinds, G.; Brett, D. J. L.; Shearing, P. R., Investigating Lithium-Ion Battery Materials during Overcharge-Induced Thermal Runaway: an Operando and Multi-Scale X-Ray CT Study. *Phys Chem Chem Phys* **2016,** *18* (45), 30912-30919.

199. Leising, R. A.; Palazzo, M. J.; Takeuchi, E. S.; Takeuchi, K. J., Abuse Testing of Lithium-Ion Batteries - Characterization of the Overcharge Reaction of LiCoO2/Graphite Cells. *J Electrochem Soc* **2001,** *148* (8), A838-A844.

200. Kramer, Y.; Birkenmaier, C.; Feinauer, J.; Hintennach, A.; Bender, C. L.; Meiler, M.; Schmidt, V.; Dinnebier, R. E.; Schleid, T., A New Method for Quantitative Marking of Deposited Lithium by Chemical Treatment on Graphite Anodes in Lithium-Ion Cells. *Chemistry* **2015,** *21* (16), 6062-5.

201. Maleki, H.; Howard, J. N., Effects of Overdischarge on Performance and Thermal Stability of a Li-Ion Cell. *J Power Sources* **2006,** *160* (2), 1395-1402.

202. Nemanick, E. J.; Wand, D.; Matsumoto, J.; Ives, N. In *Effects of Cell Reversal on Li-Ion Batteries*, 230th ECS Conference, Honolulu, HI, ECS: Honolulu, HI, 2016.

203. Li, H. F.; Gao, J. K.; Zhang, S. L., Effect of Overdischarge on Swelling and Recharge Performance of Lithium Ion Cells. *Chinese J Chem* **2008,** *26* (9), 1585-1588.

204. Kishiyama, C.; Nagata, M.; Piao, T.; Dodd, J.; Lam, P.-K.; Tsukamoto, S. In *Improvement of Deep Discharge Capability for Lithium-Ion Batteries*, Symposium, Lithium and lithium-ion battery, Electrochemical Society: 2004; pp 352-359.

205. Mao, Z. 206th Electrochemistry Society Conference, Honolulu, HI, Honolulu, HI, 2006.

206. Kasnatscheew, J.; Borner, M.; Streipert, B.; Meister, P.; Wagner, R.; Laskovic, I. C.; Winter, M., Lithium-Ion Battery Cells under Abusive Discharge Conditions: Electrode Potential Development and Interactions between Positive and Negative Electrode. *J Power Sources* **2017,** *362*, 278-282.

207. Choi, J. A.; Kim, S. H.; Kim, D. W., Enhancement of Thermal Stability and Cycling Performance in Lithium-Ion Cells Through the Use of Ceramic-Coated Separators. *J Power Sources* **2010,** *195* (18), 6192-6196.

208. Guo, L.; Oskam, G.; Radisic, A.; Hoffmann, P. M.; Searson, P. C., Island Growth in Electrodeposition. *J Phys D Appl Phys* **2011,** *44* (44).

209. Au - Ruiz Ruiz, V.; Au - Kriston, A.; Au - Adanouj, I.; Au - Destro, M.; Au - Fontana, D.; Au - Pfrang, A., The Effect of Charging and Discharging Lithium Iron Phosphate-Graphite Cells at Different Temperatures on Degradation. *JoVE* **2018,** (137), e57501.

210. Barré, A.; Deguilhem, B.; Grolleau, S.; Gerard, M.; Suard, F.; Riu, D., A Review on Lithium-Ion Battery Ageing Mechanisms and Estimations for Automotive Applications. *J Power Sources* **2013,** *241*, 680–689.

211. Birkl, C.; Roberts, M.; McTurk, E.; G. Bruce, P.; Howey, D., Degradation Diagnostics for Lithium Ion Cells. *J Power Sources* **2017,** *341*, 373-386.

212. Schuster, S. F.; Bach, T.; Fleder, E.; Mueller, J.; Brand, M.; Sextl, G.; Jossen, A., Nonlinear Aging Characteristics of Lithium-Ion Cells under Different Operational Conditions. *J Energy Storage* **2015,** *1*, 44-53.

213. Arora, P.; E. White, R.; Doyle, M., Capacity Fade Mechanisms and Side Reactions in Lithium-Ion Batteries. *J Electrochem Soc* **1998,** *145* (10), 3647-3667.

214. Ji, Y.; Zhang, Y.; Wang, C.-Y., Li-Ion Cell Operation at Low Temperatures. *J Electrochem Soc* **2013,** *160* (4), A636-A649.

215. Zinth, V.; von Luders, C.; Hofmann, M.; Hattendorff, J.; Buchberger, I.; Erhard, S.; Rebelo-Kornmeier, J.; Jossen, A.; Gilles, R., Lithium Plating in Lithium-Ion Batteries at Sub-ambient Temperatures Investigated by in Situ Neutron Diffraction. *J Power Sources* **2014,** *271*, 152-159.

216. Petzl, M.; Danzer, M., Nondestructive Detection, Characterization, and Quantification of Lithium Plating in Commercial Lithium-Ion Batteries. *J Power Sources* **2014,** *254*, 80–87.

217. Bitzer, B.; Gruhle, A., A New Method for Detecting Lithium Plating by Measuring the Cell Thickness. *J Power Sources* **2014,** *262*, 297-302.

218. Petzl, M.; Kasper, M.; Danzer, M. A., Lithium Plating in a Commercial Lithium-Ion Battery A Low-Temperature Aging Study. *J Power Sources* **2015,** *275*, 799-807.

219. Tewari, D.; Mukherjee, P. P., Mechanistic Understanding of Electrochemical Plating and Stripping of Metal Electrodes. *J Mater Chem A* **2019,** *2019 v.7 no.9* (no. 9), pp. 4668-4688.

220. Dubarry, M.; Truchot, C.; Liaw, B. Y., Cell Degradation in Commercial LiFePO4 Cells with High-Power and High-Energy Designs. *J Power Sources* **2014,** *258*, 408-419.

221. Ecker, M.; Nieto, N.; Käbitz, S.; Schmalstieg, J.; Blanke, H.; Warnecke, A.; Sauer, D. U., Calendar and Cycle Life Study of Li(NiMnCo)O2-Based 18650 Lithium-Ion Batteries. *J Power Sources* **2014,** *248*, 839-851.

222. Yang, X.-G.; Leng, Y.; Zhang, G.; Ge, S.; Wang, C.-Y., Modeling of Lithium Plating Induced Aging of Lithium-Ion Batteries: Transition from Linear to Nonlinear Aging. *J Power Sources* **2017,** *360*, 28-40.

223. Zheng, Y.; Ouyang, M.; Han, X.; Lu, L.; Jianqiu, L., Investigating the Error Sources of the Online State of Charge Estimation Methods for Lithium-Ion Batteries in Electric Vehicles. *J Power Sources* **2017,** *377*, 161-188.

224. Zhang, L.; Zhang, Z.; Redfern, P. C.; Curtiss, L. A.; Amine, K., Molecular Engineering Towards Safer Lithium-Ion Batteries: a Highly Stable and Compatible Redox Shuttle for Overcharge Protection. *Energ Environ Sci* **2012,** *5* (8), 8204-8207.

225. Ren, D.; Feng, X.; Lu, L.; He, X.; Ouyang, M., Overcharge Behaviors and Failure Mechanism of Lithium-Ion Batteries under Different Test Conditions. *Appl Energ* **2019,** *250*, 323-332.

226. Lu, W.; López, C. M.; Liu, N.; Vaughey, J. T.; Jansen, A.; Dennis W., D., Overcharge Effect on Morphology and Structure of Carbon Electrodes for Lithium-Ion Batteries. *J Electrochem Soc* **2012,** *159* (5), A566-A570.

227. Ohsaki, T.; Kishi, T.; Kuboki, T.; Takami, N.; Shimura, N.; Sato, Y.; Sekino, M.; Satoh, A., Overcharge Reaction of Lithium-Ion Batteries. *J Power Sources* **2005,** *146* (1-2), 97-100.

228. Devie, A.; Dubarry, M.; Liaw, B. Y., Overcharge Study in Li4Ti5O12 Based Lithium-Ion Pouch Cell I. Quantitative Diagnosis of Degradation Modes. *J Electrochem Soc* **2015,** *162* (6), A1033-A1040.

229. Arora, P.; Doyle, M.; White, R. E., Mathematical Modeling of the Lithium Deposition Overcharge Reaction in Lithium- Ion Batteries Using Carbon- Based Negative Electrodes. *J Electrochem Soc* **1999,** *146* (10), 3543-3553.

230. Feng, X.; Ouyang, M.; Liu, X.; Lu, L.; Xia, Y.; He, X., Thermal Runaway Mechanism of Lithium Ion Battery for Electric Vehicles: A Review. *Energy Storage Materials* **2017,** *10*, 246-267.

231. Lopez, C. F.; Jeevarajan, J. A.; Mukherjee, P. P., Experimental Analysis of Thermal Runaway and Propagation in Lithium-Ion Battery Modules. *J Electrochem Soc* **2015,** *162* (9), A1905-A1915.

232. Ouyang, M.; Ren, D.; Lu, L.; Jianqiu, L.; Feng, X.; Han, X.; Liu, G., Overcharge-Induced Capacity Fading Analysis for Large Format Lithium-Ion Batteries with LiyNi1/3Co1/3Mn1/3O2+LiyMn2O4 Composite Cathode. *J Power Sources* **2015,** *279*, 626-635.

233. Zhang, Z.; Fouchard, D.; Rea, J. R., Differential Scanning Calorimetry Material Studies: Implications for the Safety of Lithium-Ion Cells. *J Power Sources* **1998,** *70* (1), 16-20.

234. E. Galushkin, N.; N. Yazvinskaya, N.; N. Galushkin, D., Mechanism of Gases Generation During Lithium-Ion Batteries Cycling. *J Electrochem Soc* **2019,** *166* (6), A897-A908.

235. Wandt, J.; Freiberg, A.; Thomas, R.; Gorlin, Y.; Siebel, A.; Jung, R.; Gasteiger, H. A.; Tromp, M., Transition Metal Dissolution and Deposition in Li-Ion Batteries Investigated by Operando X-Ray Absorption Spectroscopy. *J Mater Chem A* **2016,** *4* (47), 18300-18305.

236. Metzger, M.; Strehle, B.; Solchenbach, S.; Gasteiger, H. A., Origin of H2 Evolution in LIBs: H2O Reduction vs. Electrolyte Oxidation. *J Electrochem Soc* **2016,** *163* (5), A798-A809.

237. Remmlinger, J.; Buchholz, M.; Meiler, M.; Bernreuter, P.; Dietmayer, K., State-of-Health Monitoring of Lithium-Ion Batteries in Electric Vehicles by On-Board Internal Resistance Estimation. *J Power Sources* **2011,** *196* (12), 5357-5363.

238. Liu, L.; Zhu, M., Modeling of SEI Layer Growth and Electrochemical Impedance Spectroscopy Response using a Thermal-Electrochemical Model of Li-ion Batteries. *Ecs Transactions* **2014,** *61* (27), 43-61.

239. Bloom, I.; Jansen, A. N.; Abraham, D. P.; Knuth, J.; Jones, S. A.; Battaglia, V. S.; Henriksen, G. L., Differential Voltage Analyses of High-Power, Lithium-Ion Cells: 1. Technique and Application. *J Power Sources* **2005,** *139* (1), 295-303.

240. Kikkawa, J.; Terada, S.; Gunji, A.; Nagai, T.; Kurashima, K.; Kimoto, K., Chemical States of Overcharged LiCoO2 Particle Surfaces and Interiors Observed Using Electron Energy-Loss Spectroscopy. *The Journal of Physical Chemistry C* **2015,** *119* (28), 15823-15830.

241. Lu, W. Q.; Lopez, C. M.; Liu, N.; Vaughey, J. T.; Jansen, A.; Dees, D. W., Overcharge Effect on Morphology and Structure of Carbon Electrodes for Lithium-Ion Batteries. *J Electrochem Soc* **2012,** *159* (5), A566-A570.

242. Liu, R.; Lei, Y.; Yu, W.; Wang, H.; Qin, L.; Han, D.; Yang, W.; Zhou, D.; He, Y.; Zhai, D.; Li, B.; Kang, F., Achieving Low Overpotential Lithium–Oxygen Batteries by Exploiting a New Electrolyte Based on N,N′-Dimethylpropyleneurea. *ACS Energy Letters* **2017,** *2* (2), 313-318.

243. Kumai, K.; Miyashiro, H.; Kobayashi, Y.; Takei, K.; Ishikawa, R., Gas Generation Mechanism due to Electrolyte Decomposition in Commercial Lithium-Ion Cell. *J Power Sources* **1999,** *81-82*, 715-719.

244. Hannan, M. A.; Hoque, M. M.; Hussain, A.; Yusof, Y.; Ker, P. J., State-of-the-Art and Energy Management System of Lithium-Ion Batteries in Electric Vehicle Applications:Issues and Recommendations. *IEEE Access* **2018,** *6*, 19362-19378.

245. Irfan, U. How Lithium Ion Batteries Grounded the Dreamliner. https://www.scientificamerican.com/article/how-lithium-ion-batteries-grounded-the-dreamliner/ (accessed July 18).

246. Kong, L.; Li, C.; Jiang, J.; Pecht, M., Li-Ion Battery Fire Hazards and Safety Strategies. *Energies* **2018,** *11*, 2191.

247. Larsson, F.; Bertilsson, S.; Furlani, M.; Albinsson, I.; Mellander, B. E., Gas Explosions and Thermal Runaways During External Heating Abuse of Commercial Lithium-Ion Graphite-LiCoO2 Cells at Different Levels of Ageing. *J Power Sources* **2018,** *373*, 220-231.

248. Baronti, F.; Fantechi, G.; Roncella, R.; Saletti, R.; Pede, G.; Vellucci, F., Design of the Battery Management System of LiFePO4 Batteries for Electric Off-Road Vehicles. *2013 Ieee International Symposium on Industrial Electronics (Isie)* **2013**.

249. Jeevarajan, J. A.; Strangways, B.; Nelson, T. J., Hazards due to Overdischarge in Lithium-ion Cylindrical 18650 Cells in Multi-cell Configurations. National Aeronautics and Space Administration: 2010.

250. Manthiram, A., An Outlook on Lithium Ion Battery Technology. *ACS Central Science* **2017,** *3* (10), 1063-1069.

251. Lai, X.; Zheng, Y.; Zhou, L.; Gao, W., Electrical Behavior of Overdischarge-Induced Internal Short Circuit in Lithium-Ion Cells. *Electrochim Acta* **2018,** *278*, 245-254.

252. Fear, C.; Juarez-Robles, D.; Jeevarajan, J.; Mukherjee, P. P., Elucidating Copper Dissolution Phenomenon in Li-ion Cells under Overdischarge Extremes. *J Electrochem Soc* **2018,** *165* (9), A1639-A1647.

253. Li, H.-F.; Gao, J.-K.; Zhang, S.-L., Effect of Overdischarge on Swelling and Recharge Performance of Lithium Ion Cells. *Chinese J Chem* **2008,** *26* (9), 1585-1588.

254. Liu, Q.; Du, C.; Shen, B.; Zuo, P.; Cheng, X.; Ma, Y.; Yin, G.; Gao, Y., Understanding Undesirable Anode Lithium Plating Issues in Lithium-Ion Batteries. *Rsc Adv* **2016,** *6* (91), 88683-88700.

255. Cannarella, J.; Arnold, C. B., The Effects of Defects on Localized Plating in Lithium-Ion Batteries. *J Electrochem Soc* **2015,** *162* (7), A1365-A1373.

256. Minter, R. D.; Juarez-Robles, D.; Fear, C.; Barsukov, Y.; Mukherjee, P. P., Three-Electrode Coin Cell Preparation and Electrodeposition Analytics for Lithium-ion Batteries. *JoVE* **2018,** (135), e57735.

257. Uitz, M.; Sternad, M.; Breuer, S.; Täubert, C.; Traußnig, T.; Hennige, V.; Hanzu, I.; Wilkening, M., Aging of Tesla's 18650 Lithium-Ion Cells: Correlating Solid-Electrolyte-Interphase Evolution with Fading in Capacity and Power. *J Electrochem Soc* **2017,** *164* (14), A3503-A3510.

258. Juarez-Robles, D. C., C. F.; Barsoukov, Y.; Mukherjee, P. P., Impedance Evolution Characteristics in Lithium-Ion Batteries. *J Electrochem Soc* **2017,** *164* (4), A837-A847.
259. Zhang, L.; Ma, Y.; Cheng, X.; Du, C.; Guan, T.; Cui, Y.; Sun, S.; Zuo, P.; Gao, Y.; Yin, G., Capacity Fading Mechanism During Long-Term Cycling of Over-Discharged LiCoO2/Mesocarbon Microbeads Battery. *J Power Sources* **2015,** *293*, 1006-1015.
260. Mistry, A.; Fear, C.; Carter, R.; Love, C.; Mukherjee, P., Electrolyte Confinement Alters Lithium Electrodeposition. *ACS Energy Letters* **2018,** *4*.
261. Erol, S.; Orazem, M. E.; Muller, R. P., Influence of Overcharge and Over-Discharge on the Impedance Response of LiCoO2|C Batteries. *J Power Sources* **2014,** *270*, 92-100.
262. Al Hallaj, S.; Selman, J. R., A Novel Thermal Management System for Electric Vehicle Batteries using Phase-Change Material. *J Electrochem Soc* **2000,** *147* (9), 3231-3236.

VITA

Daniel Juárez – Robles

Research Interests

Energy Storage Systems; Degradation; Safety; Li-ion Batteries; Proton Exchange Membrane Fuel Cells; Numerical Methods; Optimization Processes; Education.

Education

- PhD., Mechanical Engineering, Purdue University *, IN, USA, 2017 –2019
- PhD., Mechanical Engineering, Texas A&M University *, TX, USA, 2015 – 2017
- MS on Applied Math, Research Center of Mathematics (CIMAT), Mexico, 2011 – 2013
- MS on Mechanical Engineering, University of Guanajuato, Mexico, 2009 – 2012
- BS on Mechanical Engineering, University of Guanajuato, Mexico, 2003 – 2009
- BS on Mathematics, University of Guanajuato, Mexico, 2001 – 2003, incomplete.

* Moved from Texas A&M to Purdue in Fall 2017 with Prof. Mukherjee

Awards & Honors

- Best Poster Award (A03 Session) in the 233rd Meeting of the Electrochemical Society (ECS), Seattle, WA, 2018.
- Nominee as Student Employee of the Year by Texas A&M Scholarship and Financial Aid, Feb. 2017.
- Best GPA, Graduate Program in Mechanical Engineering of the University of Guanajuato, Nov., 2010.
- Awardee, academic scholarship "DINPO for Young Researchers Formation", Guanajuato, Gto., Jan. 2009 – Dec. 2011.
- Best GPA, Graduate Program in Mechanical Engineering of the University of Guanajuato, Nov., 2009.
- Graduated from the BS degree with the maximum honors, "*Suma Cum Laude*", Feb. 2009.
- Academic Excellency, Undergraduate Program in Mechanical Engineering of the University of Guanajuato, Nov., 2008.
- Participation in the "Mexico – UA Summer Research Program 2008", in the department of "Aerospace and Mechanical Engineering" of the University of Arizona (UA), under the supervision of Dr. Peiwen Li. Topic "CFD Analysis of Flow Uniformity in a Flow Distributor with Multiple Bifurcations", Tucson, AZ, Jun. – Aug., 2008.
- Participation in the "4th State Summer Research Program", organized by CONCyTEG (by its acronym in Spanish, Consejo de Ciencia y Tecnología del Estado de Guanajuato), Guanajuato, Guanajuato, Jul., 2007.
- Best GPA, Undergraduate Program in Mechanical Engineering of the University of Guanajuato, Nov., 2006.

- Best GPA, Undergraduate Program in Mechanical Engineering of the University of Guanajuato, Nov., 2005.
- Participation in the Student International Cultural Exchange between University of Guanajuato and University of Texas A&M, 2004.
- Awardee, scholarship "Diego Bricio Hernández Castaños" by the Math Research Center, Guanajuato, Gto., Sept., 2001.
- Participation in the "XXIII National Contest of Basic Sciences" representing the state of Guanajuato in the math area at the "VII DGETI's Academicals Fest", Mexico, Jul., 2001.
- 1st place in the State Contest of Basic Sciences on the area of Math, at the "Cultural and Academicals Fest 2001" at Dolores Hidalgo, C.I.N., Apr., 2001.
- 3rd place in the National Contest of the XIV Math Mexican Olympiads, representing the state of Guanajuato at Morelia Michoacán, Nov., 2000.
- 1st place in the state contest, Math Mexican Olympiads organized by the Mexican Academy of Sciences, Guanajuato, Nov., 2000.

Academic Experience

- Lecturer (Undergrad level), University of Guanajuato. 2009-2014.
  - Physics II (Sept. – Dec. 2013, Jan. – Apr. 2014, Sept. – Dec. 2014)
  - Numerical Methods (Sept. – Dec. 2013, Jan. – Apr. 2014, May – Aug. 2014, Sept. – Dec. 2014)
  - Experiments design (Sept. – Dec. 2013, May – Aug. 2014)
  - Thermodynamics (May – Aug. 2014)
  - Preparatory course of Physics (Fall 2009, Spring 2010, Winter 2010, Spring 2011)
  - Preparatory course of Pre-calculus (Spring 2010, Spring 2011)
  - Preparatory course of Analytic Geometry (Spring 2011)

- Lecturer (High School), Escuela de Bachilleres "18 de Marzo" high school. 2003 - 2014.
  - Math, Algebra, Analytic Geometry, Differential and Integral Calculus, Probability and Statistics, Applied Math
- Escuela de Bachilleres "18 de Marzo". Thesis advisor to obtain the degree of Electronics Technician.
- Escuela de Bachilleres "18 de Marzo". Member of the thesis committee at the High School thesis defense to obtain the degree of Electronics Technician, Jul. 2011, Jul. 2014.
- Escuela de Bachilleres "18 de Marzo", Academic Secretary, Aug. 2013 - Dec. 2014.

Publications

Published

1. **Daniel Juarez-Robles**, Hernando J. Gonzalez-Malabet, Matthew L'Antigua, Xianghui Xiao, George J. Nelson, Partha P. Mukherjee, "Elucidating Lithium Alloying-Induced Degradation Evolution in High-Capacity Electrodes", ACS Appl. Mater. Interfaces, 2019, 11(1), pp. 563-577. doi: 10.1021/acsami.8b14242
2. **Daniel Juarez-Robles**, Chien Fan Chen, Yevgen Barsukov, Partha P. Mukherjee, "Impedance Evolution Characteristics in Lithium-ion Batteries", J. Electrochem. Soc., 2017, 164 (4) A837-A847, doi: 10.1149/2.1251704jes

3. **Daniel Juarez-Robles***, Kelsey Rollag*, Zhijia Du, David L. Wood III, Partha P. Mukherjee, "Drying Temperature and Capillarity-Driven Crack Formation in Aqueous Processing of Li-Ion Battery Electrodes", ACS Appl. Energy Mater., 2019, 2, 6, 4464-4476, doi: 10.1021/acsaem.9b00704 **Equal Contribution*
4. **Daniel Juarez-Robles***, Conner Fear*, Judith Jeevarajan, Partha P. Mukherjee, "Elucidating Copper Dissolution Phenomenon in Li-ion Cells under Overdischarge Extremes", J. Electrochem. Soc., 165 (9) A1639-A1647, 2018. doi: 10.1149/2.0671809jes **Equal Contribution*
5. **Daniel Juarez-Robles***, Robert D. Minter*, Conner Fear, Yevgen Barsukov, Partha P. Mukherjee, "Three-Electrode Coin Cell Preparation and Electrodeposition Analytics for Lithium-Ion Batteries", J. Vis. Exp., 2018 , (135), e57735, doi: 10.3791/57735 **Equal Contribution*
6. **Daniel Juarez-Robles**, Abel Hernandez, Bladimir Ramos-Alvarado, Francisco Elizalde-Blancas, Cesar E. Damian-Ascencio, "Multiple Concentric Spirals for the Flow Field of a PEMFC", J. of Power Sources, 196, 19, 2011, 8019-8030, doi: 10.1016/j.jpowsour.2011.05.029

Under Review / In Preparation

7. **Daniel Juarez-Robles***, Anjul Arun-Vyas*, Judith Jeevarajan, Partha P. Mukherjee, "Degradation Mechanisms on Cycling at Different Overcharge Levels", Submitted to ACS Appl. Mater. Interfaces., 2019, *Equal contribution; Under Review*
8. **Daniel Juarez-Robles**, Anjul Arun-Vyas, Timothy Transue, Judith Jeevarajan, Partha P. Mukherjee, "Degradation Mechanisms on Cycling at Different Overdischarge Levels", Submitted to ACS Appl. Mater. Interfaces., 2019, *Under Review*
9. **Daniel Juarez-Robles**, Judith Jeevarajan, Partha P. Mukherjee, "Degradation Safety Analytics (DSA) in Li-ion Cells. Part 1. Aging". Submitted to the J. of Electrochem. Soc., 2019. *Under Review*
10. Wenxiu Wang, **Daniel Juarez-Robles**, Partha P. Mukherjee, "Electrochemical Impedance Spectroscopy Based Noninvasive Quantification of Electrolyte Transport Resistance in Porous Electrode Microstructures", Submitted to Physical Chemistry Chemical Physics (2019). *Under Review*
11. Hernando Gonzalez Malabet, **Daniel Juarez-Robles**, Vincent de Andrade, Partha P. Mukherjee, George Nelson, "In Operandeo XANES Imaging of High Capacity Intermetallic Anodes for Li-Ion Batteries", Submitted to ACS Appl. Energy Mater., 2019. *Under Review*
12. **Daniel Juarez-Robles**, Judith Jeevarajan, Partha P. Mukherjee, "Degradation Safety Analytics (DSA) in Li-ion Cells. Part 2. External Short", 2019. *In Preparation*
13. **Daniel Juarez-Robles**, Judith Jeevarajan, Partha P. Mukherjee, "Degradation Safety Analytics (DSA) in Li-ion Cells. Part 3. Overcharge", 2019. *In Preparation*
14. **Daniel Juarez-Robles**, Judith Jeevarajan, Partha P. Mukherjee, "Degradation Safety Analytics (DSA) in Li-ion Cells. Part 4. Drive Cycle", 2019. *In Preparation*

Publications (Co-Author)

1. Aashutosh Mistry, Daniel Juarez-Robles, Malcolm Stein IV, Kandler Smith, Partha P. Mukherjee, "Analysis of Long Range Interaction in Lithium-ion Battery Electrodes", J. Electrochem. En. Conv. and Stor., 2016, 13(3):031006, doi: 10.1115/1.4035198

2. Yuan Yue, Daniel Juarez-Robles, Partha P. Mukherjee, Hong Liang, "Superhierarchical Nickel-Vanadia Nanocomposites for Lithium-ion Batteries", ACS Appl. Energy Materials, 2018. doi: 10.1021/acsaem.8b00163.
3. Yuan Yue; Daniel Juarez-Robles; Yan Chen; Winson C. H. Kuo; Partha P. Mukherjee; Hong Liang, "Hierarchical Structured Cu/Ni/TiO_2 Nanocomposites as Electrodes for Lithium-Ion Batteries", ACS Appl. Mater. Interfaces, 2018, 9, 28695-28703, 2018. doi: 10.1021/acsami.7b10158
4. Peifeng Huang, Ankit Verma, Daniel J. Robles, Qingsong Wang, Partha Mukherjee, Jinhua Sun, "Probing the Cooling Effectiveness of Phase Change Materials on Lithium-ion Battery Thermal Response under Overcharge Condition", Appl. Thermal Eng., 132, 521-530, 2017. doi: 10.1016/j.applthermaleng.2017.12.121
5. Stein IV, M., Chen, C. F., Robles, D. J., Rhodes, C., Mukherjee, P. P., "Non-aqueous Electrode Processing and Construction of Lithium-ion Coin Cells", J. Vis. Exp., 2016, (108), e53490, doi:10.3791/53490.
6. Liu Hong, Li Peiwen, Juarez-Robles D, Wang K and Hernandez-Guerrero A, "Experimental Study and Comparison of Various Designs of Gas Flow Fields to PEM Fuel Cells and Cell Stack Performance", Front. Energy Res., 2014, doi: 10.3389/fenrg.2014.00002
7. Francisco J. Solis, Ignacio Barradas, Daniel Juarez-Robles, "From Backward Approximations to Lagrange Polynomials in Discrete Advection-Reaction Operators", Journal of Differential Equations and Dynamical Systems, pp. 1-13, 2018, doi: 10.1007/s12591-018-0415-9.
8. Liu Hong, Peiwen Li, Jon Van Lew, Daniel Juarez, "Experimental Study of the Flow Distribution Uniformity in Flow Distributors having Novel Flow Channel Bifurcation Structures", Exp. Therm. Flu. Sci., 37, 2012, 142 – 153, doi: 10.1016/j.expthermflusci.2011.10.015
9. Bladimir Ramos-Alvarado, Abel Hernandez-Guerrero, Daniel Juarez-Robles, Peiwen Li, "Numerical investigation of the performance of symmetric flow distributors as flow channels for PEM fuel cells", I. J. Hyd. Ene., 37, 1, 2012, 436 – 448, doi: 10.1016/j.ijhydene.2011.09.080
10. V.H. Rangel-Hernandez, C. Damian-Ascencio, D. Juarez-Robles, A. Gallegos-Muñoz, A. Zaleta-Aguilar, H. Plascencia-Mora, "Entropy Generation Analysis of a Proton Exchange Membrane Fuel Cell (PEMFC) with a Fermat Spiral as a Flow Distributor", Energy, 2011, 36, 8, 2011, 4864-4870, doi: 10.1016/j.energy.2011.05.031
11. Yuting Luo, Luis R. De Jesus, Justin L. Andrews, Abhishek Parija, Nathan Fleer, Daniel Juarez Robles, Partha P. Mukherjee, and Sarbajit Banerjee, "Roadblocks in Cation Diffusion Pathways: Implications of Phase Boundaries for Li-ion Diffusivity in an Intercalation Cathode Material", ACS Appl. Mater. Interfaces, 2018, doi: 10.1021/acsami.8b10604

Conferences (Published)

1. Perez-Raya I., Hernandez-Guerrero A., Elizalde-Blancas F., **Juarez-Robles D.**, Almanza-Huerta L., "3D CFD Analysis of a New Radial Channel for PEMFCs and Comparison with a Traditional Channeled System", Proceedings of IMECE 2010–38660, Vancouver, British Columbia, November, 2010.

2. **Juárez-Robles Daniel**, Hernández-Guerrero Abel, Ramos-Alvarado Bladimir, Rubio-Arana Cuauhtémoc, "Analisis de una PEMFC con Campo de Flujo Radial", XVI Annual International Conference of the Mexican Society of Mechanical Engineers, Monterrey, Nuevo Leon, Mexico, 22-24th September, 2010.
3. Blanco Almanza J. A., **Juárez Robles D.**, Belman Flores J. M., Rubio Maya C., "Modelado de un Compresor Alternativo usando R134a como Fluido Frigorígeno", XVI Annual International Conference of the Mexican Society of Mechanical Engineers, Monterrey, Nuevo Leon, Mexico, 22-24th September, 2010.
4. **Daniel Juarez-Robles**, Abel Hernandez-Guerrero, Bladimir Ramos-Alvarado, Cuauhtémoc Rubio-Arana, "Performance of a PEMFC with a Variable Cross Section Area Flow Field", The Second International Conference on Nuclear and Renewable Energy Resources (NURER), Turkey, 4-7th July 2010.
5. **Daniel Juarez-Robles**, Abel Hernandez-Guerrero, Victor H. Rangel-Hernandez, Cesar E. Damian Ascencio, "Multiple Concentric Spirals for the Flow Field of the PEMFC, Part 2: Entropy Generation Analysis", 5th International Ege Energy Symposium and Exhibition (IEESE-5) – 281, Denizli, Turkey, 27-30th June 2010.
6. **Daniel Juarez-Robles**, Abel Hernandez-Guerrero, Victor H. Rangel-Hernandez, Bladimir Ramos-Alvarado, "Multiple Concentric Spirals for the Flow Field of the PEMFC, Part 1: Performance Comparison", 5th International Ege Energy Symposium and Exhibition (IEESE-5) – 280, Denizli, Turkey, 27-30th June 2010.
7. I. Pérez-Raya, A. Hernández-Guerrero, F. Elizalde-Blancas, **D. Juárez-Robles**, "A Parametric Study of a PEMFC Flow Field using a Constructal Radial Design", Proceedings of ECOS 2010 - 637, Lausanne, Switzerland, June 14-17th, 2010
8. **Daniel Juarez-Robles**, Abel Hernandez-Guerrero, Bladimir Ramos-Alvarado, "Multiple Concentric Spirals for the Flow Field of the PEMFC", ASME District E Early Career Technical Conference (ECTC), Tulsa, Oklahoma, USA, March 25-27th, 2010.
9. Sósimo Emmanuel Diaz Mendez, Abel Hernández Guerrero, José María Rodríguez Lelis, **Daniel Juárez Robles**, "Índice de Impacto Ambiental con Base en Trabajo Perdido Aplicado a la Evaluación de Contaminación de Ríos", VII Congreso Internacional sobre Innovación y Desarrollo Tecnológico, IEEE, Cuernavaca, Morelos, México, 2009.
10. Cano-Andrade Sergio, Hernandez-Guerrero Abel, **Juarez-Robles Daniel**, Rubio-Arana Cuauhtémoc, "Experimental Study for PEMFCs with Conventional and Innovative Channel Configurations", Proceedings of ECOS 2009, Paraná, Brazil, 2009.
11. Ramos-Alvarado Bladimir, Hernández-Guerrero Abel, **Juarez-Robles Daniel**, Rubio-Arana J. C., "Analysis of Flow Distribution in a Symmetric Bipolar Plate for PEMFC", Proceedings of ECOS 2009, Paraná, Brazil, 2009.
12. Bladimir Ramos-Alvarado, Abel Hernandez-Guerrero, **Daniel Juarez-Robles**, Peiwen Li, J. C. Rubio-Arana, "Parametric Study of a Symmetric Flow Distributor", IMECE2009-11149, Proceedings of IMECE 2009, Lake Buena Vista, Florida, USA, 2009.
13. Isaac Perez-Raya, Abel Hernandez-Guerrero, **Daniel Juarez-Robles**, M. Ernesto Gutierrez-Rivera, J. C. Rubio-Arana, "New Radial-Based Flow Configurations for PEMFC's", IMECE2009-12202, Proceedings of IMECE 2009, Lake Buena Vista, Florida, USA, 2009.
14. Bladimir Ramos-Alvarado, Abel Hernandez-Guerrero, **Daniel Juarez-Robles**, Cuauhtemoc Rubio-Arana, "CFD Analysis of a Constructal Flow Distributor as a Bipolar

Plate for PEMFC's", IMECE2009-11113, Proceedings of IMECE 2009, Lake Buena Vista, Florida, USA, 2009.

15. **Juárez Robles D.**, Peiwen Li, Hernández Guerrero A., Ramos Alvarado B., "Distribuidor de Flujo con Multiples Bifurcaciones", XV Annual International Conference of the Mexican Society of Mechanical Engineers, Obregon City, Sonora, Mexico, September 2009.
16. **Juárez-Robles D.**, Hernández–Guerrero A., Damián–Ascencio C. E., Rubio–Arana J.C., "Efecto del Voltaje en una PEMFC con Campo de Flujo en Forma de la Espiral de Fermat", XV Annual International Conference of the Mexican Society of Mechanical Engineers, Obregon City, Sonora, Mexico, September 2009.
17. Ramos Alvarado Bladimir, Hernández Guerrero Abel, **Juárez Robles Daniel**, Rubio Arana J.C., "Análisis Paramétrico de un Distribuidor Simétrico como Colector Difusor de una PEMFC", XV Annual International Conference of the Mexican Society of Mechanical Engineers, Sonora, Mexico, September 2009.
18. Pérez–Raya I. B., Hernández–Guerrero A., **Juárez-Robles D.**, Rubio–Arana J.C., "Estudio de 3 Configuraciones Radiales para los Campos de Flujo de una Celda de Combustible Tipo PEM", XV Annual International Conference of the Mexican Society of Mechanical Engineers, Sonora, Mexico, September 2009.
19. **Juárez-Robles, D.**, Hernández-Guerrero A., Damián-Ascencio C. E., Rubio-Arana, C., "Three Dimensional Analysis of a PEM Fuel Cell with the Shape of a Fermat Spiral for the Flow Channel Configuration", Proceedings of ASME IMECE2008-68101, 2008.
20. **Daniel Juárez Robles**, Abel Hernández Guerrero, "Análisis de una Nueva Geometría para los Canales de Flujo de una Celda de Combustible Tipo PEMFC", Memorias del 4to. Verano Estatal de Investigación del CONCyTEG, Guanajuato, Gto., Aug. 2007.

Book Chapters and Academic Material

1. Book: "Heat Transfer Phenomena and Applications", Chapter 12, "Entropy generation analysis of a proton exchange membrane fuel cell (PEMFC) with a fermat spiral as a flow distributor", V.H. Rangel-Hernandez, C. Damian-Ascencio, **D. Juarez-Robles**, A. Gallegos-Muñoz, A. Zaleta-Aguilar and H. Plascencia-Mora, Edited by Salim N. Kazi, ISBN 978-953-51-0815-3, doi: 10.5772/51979, Intech.
2. Luz A. Aguilera Cortés, Miguel Torres Cisneros, Maximino Antonio González Palacios, **Daniel Juárez Robles**, "Manual de Prácticas de Laboratorio de Cómputo para el Curso Cálculo I", Universidad de Guanajuato, Ident. key: M.CI.L.(1) I 10-08, Mexico, Oct. 2008.

Conference Presentations

- Participation in the International Battery Seminar and Exhibit with the technical presentation "Safety of Fresh and Aged Pouch Format Lithium-Ion Cells and Modules" given on behalf of Dr. Judith Jeevarajan (UL), Fort Lauderdale, FL, March, 2019.
- Participation in the Electrochemical Society (ECS) 233rd Meeting with the poster, "Electrochemical and Microstructural Analysis of Cu_6Sn_5 Alloy Electrodes", Seattle, WA, May 2018. **A03 Best Poster Award*
- Participation in the International Mechanical Engineering Congress & Exposition (IMECE) 2017 with the technical presentation, "Analysis of Cooling Efficacy of Li-Ion Cells under Abuse Conditions", Tampa, FL, November 2017.

- Participation in the Electrochemical Society (ECS) 232nd Meeting with the poster, "Analysis of Plating in Lithium-ion Batteries with Anode Control", National Harbor, MD, October 2017.
- Attendance to the 2017 ESS (Energy Storage Systems) Safety Forum, Santa Fe, NM, February 2017.
- Participation in the International Mechanical Engineering Congress & Exposition (IMECE) 2016 with the technical presentation, "Degradation-Safety Interplay in Li-Ion Cells under External Short-Circuit Scenarios", Phoenix, AZ, November 2016.
- Participation in the Electrochemical Society (ECS) 229th with the technical presentation, "A combined Aging and Abuse Study of Li-ion Cells", San Diego, CA, May 2016.
- Participation in the International Mechanical Engineering Congress & Exposition (IMECE) 2015 with the technical presentation, "Three Electrode Cell Setup for Degradation Analysis in Li-ion Batteries", Houston, TX, November 2015.
- Participation in the Society of Engineering conference hosted at Texas A&M University, as a volunteer staff and with the poster "Aqueous Processing Electrode Fabrication for Li-Ion Batteries", CS, TX, October, 2015.
- Participation in the 2nd Texas A&M Energy Institute Research Workshop, "Non-Fossil-based Technologies for Energy," with the poster October 20, 2015
- Participation as volunteer judge at the 2015 Engineering Summer Undergraduate Research Symposium (USRG/REU Poster session), Texas, August 2015.
- Participation as judge at the Texas Junior Academy of Science, Texas, June 2015.
- Attendance to the Mathematical Congress of the Americas 2013, Guanajuato, Mexico, August 2013.
- Attendance to 45th National Congress of the Mexican Society of Math, Autonomous University of Queretaro, Queretaro, Mexico, October 2012.
- Attendance and participation as speaker in the VII International Congress of Innovation and Technological Development, IEEE, Cuernavaca, Morelos, Mexico, October 2009.
- Assistance and participation as speaker in the XV National Congress of the Mexican Society of Mechanical Engineers (SOMIM), Obregon city, Sonora, Mexico, September 2009.
- Participation in the International Simposium: Green technologies for the production and the susteinable use of energy. Celaya, Gto., March 2009, presenting the following works:
  - CFD Analysis of flow uniformity in a flow distributor with multiple bifurcations
  - Effect of the humidity in the performance of a PEMFC with the shape of Fermat spiral.
  - Effect on the performance of a PEMFC with the shape of Fermat with a reversed inlets and the outlets.
  - Analysis of the performance of a PEMFC with the shape of the Fermat spiral.
- Participation in the "5th TAMU-CONACYT Research Symposium at Texas A&M University", College Station, TX, USA, June 2009 with the poster: "High-performance Electrode Architecture for Lithium-Air Batteries"

Workshops

- Certificate in PROFORDEMS (High School Education Teaching Program). Teaching competences in high school level, 7th generation. Sept. 2013 – Jun. 2014
- "IV Math summer school UVEG - UASLP", San Luis Potosi, Jul., 2012

- "Master CAM 3D", Jan., 2008; "Master CAM", Dec., 2005. "Basic Computerized Numerical Control", Aug., 2005; "Basic Level of AUTOCAD", Sept., 2003
- "Workshop of technical searching of innovative technology", Oct., 2007
- "Starting culture formation and business plan", Aug. – Sept., 2005

Internships

- Academic internship at the Aerospace and Mechanical Engineering department of the University of Arizona (UofA) under the supervision of Dr. Peiwen (Perry) Li. In this internship, the physical and numerical experiments of the thesis' project "Experimentation with PEM Fuel Cells and its Characterization via Neural Networks" were conducted, Tucson, Arizona, Jul. 2010 – Jan. 2011.

Skills

- SEM, FIB and EDS analysis, Vega Tescan 3, Quanta, Fera 2500, Hitachi S-4800
- Electrochemical analysis, Arbin, Biologic, Maccor, MTI
- Technical drawing software, SolidWorks, AutoCad, Mechanical Desktop.
- Computer machining software, CNC, Master CAM.
- Finite volume analysis software, ANSYS FLUENT, GAMBIT
- Mathematical analysis and programming software, C, R, Python, Matlab, EES.
- Handling of Microsoft Office software.

Technical Reviews

- Reviewer for "The Intersociety Conference on Thermal and Thermomechanical Phenomena in Electronic Systems", ITHERM (2 Proposals) Jan. 2018
- Reviewer for the "ASME Journal of Fuel Cell Science and Technology" (9 Proposals) Jun. 2015
- Reviewer for the "Proceedings of Fuel Cell 2008, Sixth International Fuel Cell Science, Engineering and Technology Conference" (2 Proposals) Jun. 2015
- Reviewer for the "ASME, International Mechanical Eng. Congress & Exposition (IMECE)" (2 Proposal) Jun. 2017.
- Reviewer for the "ECOS 2015, 28th international conference on Efficiency, Cost, Optimization, Simulation and Env. Impact of Energy Systems" (1 Proposal) Jun. 2015.

Student Mentoring

- Undergraduate Student
  - Daniel Alejando Angmen- Bernabel, "Design and building of a protonic exchange fuel cell", co – chair with Abel Hernandez – Guerrero Ph.D. August 2014.

PUBLICATIONS

The list of publications related with my dissertation research (accepted before October 3rd, 2019) is provided hereafter.

i. **Daniel Juarez-Robles**, Hernando J Gonzalez-Malabet, Matthew L'Antigua, Xianghui Xiao, George J Nelson, Partha P Mukherjee, "*Elucidating Lithium Alloying Induced Degradation Evolution in High Capacity Electrodes*", ACS Appl. Mater. Interfaces, 2019, 11, 1, 563-577, doi: 10.1021/acsami.8b14242

ii. **Daniel Juarez-Robles**, Chien Fan Chen, Yevgen Barsukov, Partha P. Mukherjee, "*Impedance Evolution Characteristics in Lithium-ion Batteries*", J. Electrochem. Soc., 2017, 164 (4) A837-A847, doi: 10.1149/2.1251704jes

iii. **Daniel Juarez-Robles***, Robert D. Minter*, Conner Fear, Yevgen Barsukov, Partha P Mukherjee, "*Three-electrode Coin Cell Preparation and Electrodeposition Analytics for Lithium-ion Batteries*", J. Vis. Exp., 2018, (135), e57735, doi: 10.3791/57735

iv. **Daniel Juarez-Robles***, Conner Fear*, Judith Jeevarajan, Partha P. Mukherjee, "*Elucidating Copper Dissolution Phenomenon in Li-ion Cells under Overdischarge Extremes*", J. Electrochem. Soc. 2018, 165 (9), A1639-A1647, doi: 10.1149/2.0671809jes

v. **Daniel Juarez-Robles***, Kelsey Rollag*, Zhijia Du, David L. Wood III, Partha P. Mukherjee, "*Drying Temperature and Capillarity-Driven Crack Formation in Aqueous Processing of Li-Ion Battery Electrodes*, ACS Appl. Energy Mater. 2019, 2, 6, 4464-4476, doi: 10.1021/acsaem.9b00704

vi. Yuan Yue, **Daniel Juarez-Robles**, Partha P. Mukherjee, Hong Liang, *"Superhierarchical Nickel-Vanadia Nanocomposites for Lithium Storage"*, ACS Appl. Energy Mater. 2018,1, 5, 2056-2066, doi: 10.1021/acsaem.8b00163

vii. Yuan Yue, **Daniel Juarez-Robles**, Yan Chen, Lian Ma, Winson CH Kuo, Partha Mukherjee, Hong Liang, *"Hierarchical Structured Cu/Ni/TiO_2 Nanocomposites as Electrodes for Lithium-Ion Batteries"*, ACS Appl. Mater. Interfaces 2017, 9, 34, 28695-28703, doi: 10.1021/acsami.7b10158

viii. Aashutosh Mistry, **Daniel Juarez-Robles**, Malcolm Stein IV, Kandler Smith, Partha P. Mukherjee, *"Analysis of Long-Range Interaction in Lithium-Ion Battery Electrodes"*, J. Electrochem. En. Conv. Stor. 2016, 13 (3): 031006, doi: 10.1115/1.4035198

ix. Peifeng Huang, Ankit Verma, **Daniel Juarez-Robles**, Qinsong Wang, Partha P. Mukherjee, "*Probing the Cooling Effectiveness of Phase Change Materials on Lithium-ion Battery Thermal Response under Overcharge Condition*", Applied Thermal Engineering J., 2017, 132, 521-530, doi: 10.1016/j.applthermaleng.2017.12.121

x. Malcolm Stein IV, Chien Fan Chen, **Daniel Juarez-Robles**, Christopher Rhodes, Partha P. Mukherjee, "*Non-aqueous Electrode Processing and Construction of Lithium-ion Coin Cells*", J. Vis. Exp., 2016, (108), e53490, doi:10.3791/53490

xi. Yuting Luo, Luis R. de Jesus, Justin L. Andrews, Abhishek Parija, Nathan Fleer, **Daniel Juarez-Robles,** Partha P. Mukherjee, Sarbajit Banerjee, *"Roadblocks in Cation Diffusion Pathways: Implications of Phase Boundaries for Li-Ion Diffusivity in an Intercalation Cathode Material",* ACS Appl. Mater. Interfaces 2018, 10, 36, 30901-30911, doi: 10.1021/acsami.8b10604

In Preparation or Under Review

xii. **Daniel Juarez-Robles**, Anjul Arun-Vyas, Judith Jeevarajan, Partha P. Mukherjee, "Degradation Mechanisms on Cycling at Different Overcharge Levels", ACS Appl. Mater. Interfaces., 2019, *Ready to send for Review*

xiii. **Daniel Juarez-Robles**, Anjul Arun-Vyas, Timothy Transue, Judith Jeevarajan, Partha P. Mukherjee, "Degradation Mechanisms on Cycling at Different Overdischarge Levels", ACS Appl. Mater. Interfaces., 2019, *Ready to send for Review*

xiv. **Daniel Juarez-Robles**, Judith Jeevarajan, Partha P. Mukherjee, *"Degradation-Safety Analytics (DSA) in Li-ion Cells. Part 1. Aging"*, J. Electrochem. Soc., 2019, *Ready to send for Review*

xv. **Daniel Juarez-Robles**, Judith Jeevarajan, Partha P. Mukherjee, *"Degradation-Safety Analytics (DSA) in Li-ion Cells. Part 2. External Short Test on Fresh and Aged Cells"*, J. Electrochem. Soc., 2019, *In Preparation*

xvi. **Daniel Juarez-Robles**, Judith Jeevarajan, Partha P. Mukherjee, *"Degradation-Safety Analytics (DSA) in Li-ion Cells. Part 3. Overcharge Test on Fresh and Aged Cells"*, J. Electrochem. Soc., 2019, *In Preparation*

xvii. Hernando Gonzalez Malabet, **Daniel Juarez-Robles**, Vincent de Andrade, Partha P. Mukherjee, George Nelson, *"In Operando XANES Imaging of High Capacity Intermetallic Anodes for Li-Ion Batteries"*, ACS Appl. Energy Mater., 2019, *Under Review*

xviii. Wenxiu Wang, **Daniel Juarez-Robles**, Partha P. Mukherjee, *"Electroanalytical Quantification of Electrolyte Transport Resistance in Porous Electrode Microstructures"*, Physical Chemistry Chemical Physics, 2019, *Under Review*